Convenzione tra

UNIVERSITÀ DEGLI STUDI DI TRIESTE

e

UNIVERSITÀ CA' FOSCARI DI VENEZIA

XXXIII CICLO DOTTORATO DI RICERCA IN CHIMICA

IMAGING AND CHARACTERIZATION OF CULTURAL HERITAGE MATERIALS BY ADVANCED ELECTROANALYTICAL TECHNIQUES

Settore scientifico-disciplinare: **CHIM/01**

DOTTORANDA
MARGHERITA DONNICI

COORDINATORE
PROF. ENZO ALESSIO

SUPERVISORE DI TESI
PROF. SALVATORE DANIELE

ANNO ACCADEMICO 2019/2020

Table of Contents

Chapter 1: Introduction

1. Introduction

1.1. A brief history of the chemistry and analytical methods that intertwine with cultural heritage

The study and interpretation of cultural heritage properties using scientific methods date back to the XVIII-XIX century[1,2]. Between 1795 and 1798, the German chemist Martin Heinrich Klaproth, famous for the discovery of uranium, zirconium and titanium among others elements[3], presented the first work on the subject entitled "*Mémoire de numismatique docimastique*" (see Figure 1.1), at the Royal Academy of Sciences and Belles-Lettres in Berlin[1]. In his studies, Klaproth determined, by using a gravimetric technique, the composition of Greek and Roman coins, a variety of metallic objects, pieces of colored Roman glasses from the Villa of Tiberius (Capri, Italy). The latter study is considered the earliest known analysis of archaeological glass[4].

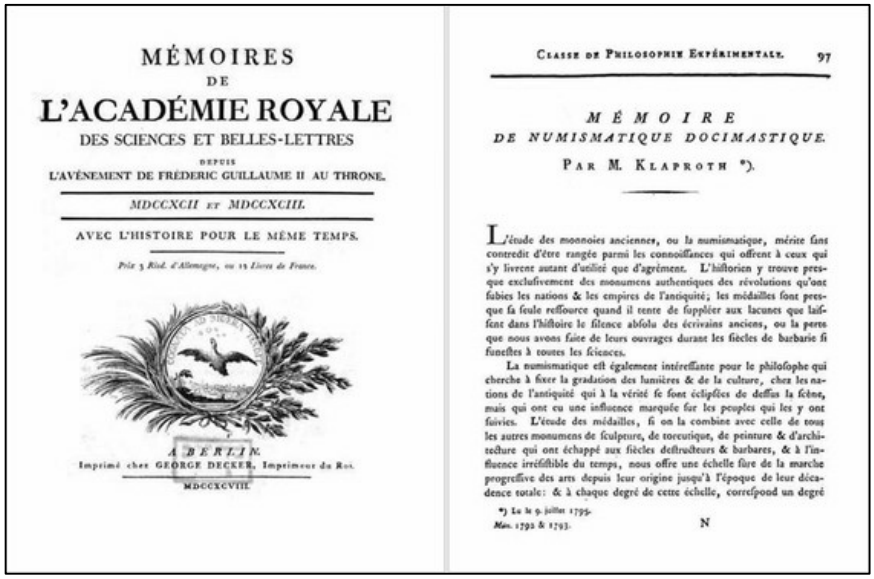

MÉMOIRES
DE
L'ACADÉMIE ROYALE
DES SCIENCES ET BELLES-LETTRES
DEPUIS
L'AVÉNEMENT DE FRÉDERIC GUILLAUME II AU THRONE.
MDCCXCII ET MDCCXCIII.
AVEC L'HISTOIRE POUR LE MÊME TEMPS.
A BERLIN.
Imprimé chez GEORGE DECKER, Imprimeur du Roi.
MDCCXCVIII.

CLASSE DE PHILOSOPHIE EXPÉRIMENTALE. 97

MÉMOIRE
DE NUMISMATIQUE DOCIMASTIQUE.
PAR M. KLAPROTH *).

L'étude des monnoies anciennes, ou la numismatique, mérite sans contredit d'être rangée parmi les connoissances qui offrent à ceux qui s'y livrent autant d'utilité que d'agrément. L'historien y trouve presque exclusivement des monumens authentiques des révolutions qu'ont subies les nations & les empires de l'antiquité; les médailles sont presque sa seule ressource quand il tente de suppléer aux lacunes que laissent dans l'histoire le silence absolu des écrivains anciens, ou la perte que nous avons faite de leurs ouvrages durant les siècles de barbarie si funestes à toutes les sciences.

La numismatique est également intéressante pour le philosophe qui cherche à fixer la gradation des lumières & de la culture, chez les nations de l'antiquité qui à la vérité se sont éclipsées de dessus la scène, mais qui ont eu une influence marquée sur les peuples qui les y ont suivies. L'étude des médailles, si on la combine avec celle de tous les autres monumens de sculpture, de toreutique, de peinture & d'architecture qui ont échappé aux siècles destructeurs & barbares, & à l'influence irrésistible du temps, nous offre une échelle sûre de la marche progressive des arts depuis leur origine jusqu'à l'époque de leur décadence totale: & à chaque degré de cette échelle, correspond un degré

*) Le 9. juillet 1795.
Mém. 1792 & 1793. N

***Figure 1.1**: First report on the analysis of cultural heritage materials in "Mémoire de numismatique docimastique" (1795). Image reproduced from Ref[4].*

[1] A.M. Pollard and C. Heron. Archaeological chemistry, 2nd ed. RSC Cambridge, UK (**2008**).
[2] R. Mazzeo. Analytical Chemistry for Cultural Heritage In: *Top Curr Chem* (Z), 374, Springer (**2016**).
[3] R.E. Oesper, *Journal of Chemical Education* (**1959**) 36, 6, A368 – A370.
[4] M. H. Klaproth, *Mémoires de l'academie royale des sciences et belles-lettres. Classe de philosophie expérimentale* (**1798**) 3–16.

Another important step forward in the history of chemistry applied to the cultural heritage field was done by Humphry Davy in 1815. He, best known for his work on laughing gas and his intuition about the electrical nature of chemical affinity[5], examined ancient pigments collected from archaeological sites of Pompeii and Rome (Italy). He was able to discern among natural and synthetic pigments, the latter called Egyptian Blue, which were produced by the fusion of copper, silica and sodium carbonate[1]. Davy taught chemistry at the Royal Institution (London, UK) and one of his students was the young Michael Faraday, who is considered the father of the electromagnetism[6]. Faraday, besides his main discoveries, studied also archeological materials. He provided the first evidence on the use of lead glaze in antiquity, by performing investigations on Roman pottery glazes. This study was reported in the journal *Archaeologia* in 1867[1]. Theodore William Richards, Nobel prize in Chemistry (1914) for his work concerning exact determinations of the atomic weights of several chemical elements, performed one of the earliest analyses on archaeological ceramics, published in *American Chemical Journal* in 1895[7]. Out of curiosity, it is interesting to note that Richards' scientific interests also concerned with electrochemistry. His investigations of the electromotive forces, exhibited by liquid amalgams, allowed the extraction of Gibbs energy data, which paved the road for the subsequent Nernst heat theorem and the third law of thermodynamics[7,8]. Despite the number of well-known chemists, who provided the very first contributions in the scientific cultural heritage investigations, the systematic involvement of science, in general, and analytical chemistry in particular, in the cultural heritage field, as well as the acknowledgement of this subject from the international scientific community, as a new scientific branch, occurred only in the 1950s[1,2]. In 1958 the journal *Archaeometry* was founded; it was edited by the

[5] D. Knight. Humphry Davy: science & power, Cambridge University Press, (**1998**).
[6] G. Moshenska, *Ambix* (**2015**) 62:3, 266-286.
[7] D. R. Herschbach, *Angew. Chem. Int. Ed*. (**2014**), 53, 13982 – 13987.
[8] Theodore William Richards 1868—1928, Biographical Memoir, National Academy of Sciences, Washington D.C. (**1974**).

Research Laboratory for Archaeology and History of Art of the Oxford University[9]. The term "archaeometry" comes from *archaeos*- in Greek "ancient", and, *-metron* from Greek "measure", coined by Christopher Hawkes in Oxford to describe the increased emphasis on dating, quantification and physicochemical investigations of archaeological materials[1,10]. As stated by G. Clark in the first Bulletin of the Research Laboratory for Archaeology and the History of Art, (Oxford)[11]:

> "*The best evidence of scientific activity lies in the publication of results. […] Today, as our attention turns to investigating how these early societies functioned and how and why they changed […], we need to study the archaeological material with all the resources that modern science is able to make available*."

The very first articles in this journal concerned the study of the composition of coins by X-Ray Fluorescence[12], the magnetic dating of Chinese pottery[13], and the Neutron Activation Analysis applied to trace element determination in pottery and coins[14].

Successively to these first recognitions of the new scientific field, there are nowadays several international journals (i.e., Journal of Cultural Heritage, Studies in Conservation, Heritage Sciences, Archaeometry and ArcheoSciences - *revue d'archéométrie*) (from the Database: Journal Citation Report) specifically devoted to the studies performed worldwide of a variety of ancient materials. These journals are classified within the Analytical Chemistry subject category. However, there are variety of other journals, belonging to other subject

[9] L. Campanella, A. Casoli, M.P. Colombini, R. Marini Bettolo, M. Matteini, L.M. Migneco, A. Montenero, L. Nodari, C. Piccioli, M. Plossi Zappalà, G. Portalone, U. Russo, M.P. Sammartino, Chimica per l'arte, Zanichelli (**2007**).
[10] I. Liritzis, N. Laskaris, A. Vafiadou, I. Karapanagiotis, P. Volonakis, C. Papageorgopoulou, M. Bratitsi, *Scientific Culture* (**2020**) 6 (1) 49.
[11] G. Clark, The Bulletin of the Research Laboratory for Archaeology and the History of Art, Oxford. Editor, E. T. Hall. 1 (1). Spring, (**1958**). Proceedings of the Prehistoric Society, 24, 233-234.
[12] C.M. Kraay, (**1958**). *Archaeometry*, 1(1), 21–22.
[13] M.J. Aitken, *Archaeometry* (**1958**) 1(1), 16–20.
[14] E.T. Hall, *Archaeometry* (**1958**), 1(1), 1–15.

categories, host articles, which support professionals for their interventions and investigations on ancient materials to acquire information on the following main aspects[9]: (i) attribution (origin, provenance and dating), (ii) composition (material identification and conservation state assessment), (iii) preservation (optimal substances to be used in restoration/conservation treatments). Within this scenario, the chemical analytical science played and still play an important role.

The analysis of cultural heritage is intricate and challenging in itself for several reasons. Among others, we can mention the intrinsic chemical complexity of artworks, due to the heterogeneity of their compositions and the alteration and degradation processes to which they are unavoidably subjected[2,15]. Moreover, it is important to underline that for cultural heritage materials, the maintenance of the sample integrity is a crucial aspect. Therefore, the analytical techniques to be employed for their investigations must be carefully chosen. On the other hand, the analytical procedures to be applied strictly depend on the type of information aimed to be acquired and the problem it intends to solve[16]. These aspects imply that the adequate scientific sequence of planned techniques should start from the less invasive up, eventually, to the more destructive[2,9,17]. In this context, it is possible to define and distinguish the concepts of invasiveness and destructiveness. A technique is defined as *invasive* when the removal of a sample is necessary to gain the searched information. Conversely, the *non-invasive* techniques represent those for which the information can be acquired without the removal of the sample from the object, and, hence, leave the object in essentially the same state before and after the analysis[18]. The *micro-invasive* analysis aims at removing the minimum amount of material from the sample without essentially modify the overall structure and appearance. Parallelly,

[15] M.Matteini, A. Moles, La chimica nel restauro, 3rd ed., Nardini Firenze (**1993**).
[16] E. Ciliberto, G. Spoto, Modern Analytical methods in Art and Archaeology, In the Chemical Analysis Series, John Wiley & Sons (**2001**) 155.
[17] D. Pinna, M. Galeotti, and R. Mazzeo, Scientific Examination For the Investigation of Paintings. A Handbook For Restorers (**2011**).
[18] A. Adriaens, (**2005**). *Spectrochim. Acta - Part B At. Spectrosc.* 60, 1503–1516.

another classification of the techniques exists depending on their degree of destructiveness, and it is related to the extent at which the sample is consumed or damaged after the analysis. One can refer to *micro-destructive* analysis when a few micro- (or even nano-) grams of material is taken from the sample to be analyzed and not anymore recovered. On the other hand, if the sample removed is not completely destructed during the analysis and remains available for further studies, the technique is termed *non-destructive*[17]. Examples of the main techniques employed for the analysis of cultural heritage materials and their classification are shown in Figure 1.2.

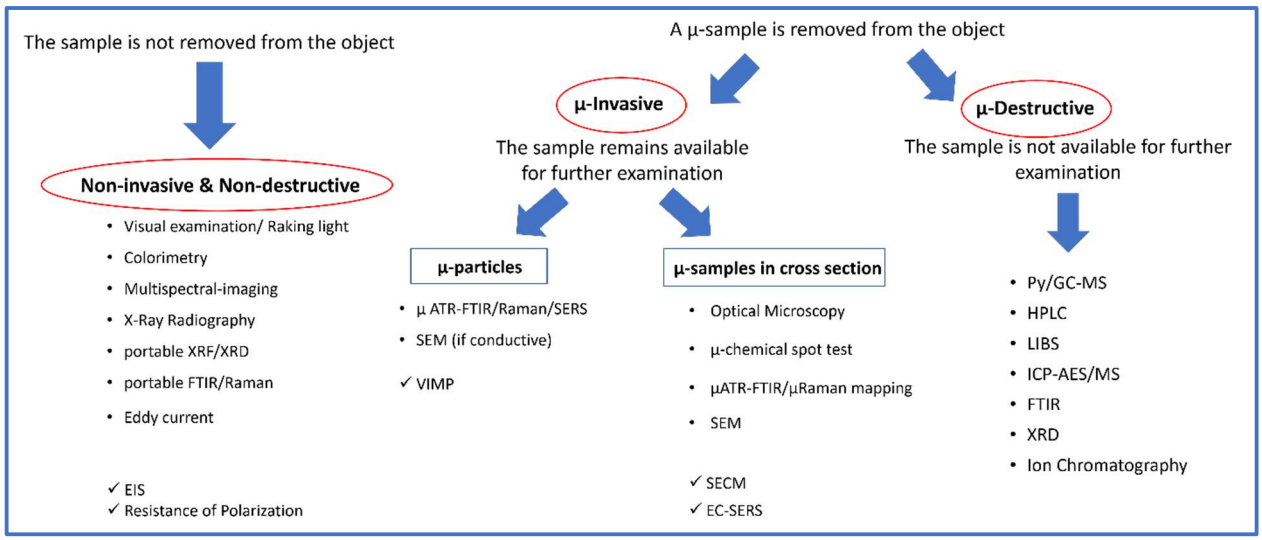

***Figure 1.2**: Schematic summary of some of the analytical techniques employed in the cultural heritage analysis; information elaborated from Ref. [17]. For the entire name of each analytical techniques refers to the list of acronyms. The symbol ✓ indicates the electrochemical techniques.*

As is evident, in general, most of them are based on spectroscopic techniques, as they can be used in an essentially non-invasive way. Their use has increased substantially in the last 10 years, especially for the availability of portable devices[19]. However, the recent scientific research in the cultural heritage field leans towards the development and improvement of

[19] F. Rosi, L. Cartechini, D. Sali, C. Miliani, *Physical Sciences Reviews* (**2019**) *4*(11), 20180006.

micro-invasive analytical techniques, with the purpose of maximizing the amount of information extractable from the minimum amount of sample (at the micro- or, even, nano-scale)[2]. Indeed, micro-invasive techniques are employed when the sampling issue is less crucial and the use of object fragments for the analysis is less restricted[16]. Upon the removal of the micro-sample, it can follow two paths: (i) be analyzed as it is (μ-particles) or (ii) be embedded in epoxy resin to form cross sections. The choice of which paths has to be followed depends on the information aimed to be gained. There are cases in which the information can be extracted directly from μ-particles, other cases in which a detailed stratigraphic characterization of the samples is the only way to achieve the desired information, especially when the constituent materials must be identified and spatially located, for example, along a cross-section[2]. In these types of analyses, high spatial resolution techniques are capable of providing the spatial distribution, readable from the resulting image, of the chemical species present in extremely small specimens[16].

In the class of the non-destructive and micro-invasive techniques, more recently, several electrochemical techniques have also taken hold and expanded their applications (see, for instance those shown in Figure 1.2 with the symbol ✓). Electrochemical techniques are gaining increasing attention thanks to their advantageous characteristics, such as fast analysis, high sensitivity, cost-effective instrumentations and the possibility to perform studies of complex and multicomponent matrices, as is the case of cultural heritage objects[20].

Since the present thesis is concerned mainly with the use of electrochemical techniques, in the next section, the state of art of application of these techniques in cultural heritage studies is reviewed.

[20] A. Domenéch-Carbò. Analytical Archaeometry, Selected Topics, Chapter 7: Electrochemical techniques (**2012**).

1.2. Electrochemistry at disposal of cultural heritage inquiries

Historically, since the XIX century, electrochemical techniques have been mainly applied to recover artifacts in their original metallic state. Friedrich Rathgen (1862-1942), director of the Chemical Laboratory of the Royal Museums of Berlin, began to apply electrolytic reduction process to corroded objects, a method originally proposed by Adolf Finkener, a chemist at the Bergakademie in Berlin[21]. Rathgen applied the first treatments on archaeological bronze and iron pieces[22] with the aim of "cleaning" the corroded object surface and thus regaining the clean metal. Although very appreciated at that time, those treatments were very drastic, resulting in the removal of the entire corrosion patina. In subsequent years, the ethics and criteria for the restoration of metal objects have been questioned, and moved towards the recognition of the importance of corrosion products as part of the history of the object[23]. From the first half of XX century, the philosophy of restoration of metallic objects started changing, and moved towards the stabilization of the active corrosion and their treatment to prevent further deterioration. Therefore, the radical electrolytic reduction was gradually abandoned, while the "consolidative reduction" was introduced in which galvanostatic conditions were still employed, but with lower currents[24]. This process, apart from being time-consuming, was not selective, involving the whole object. The electrolytic approach was improved somewhat by using the potentiostatic reduction process[25]. Following the new philosophy, other specific and sophisticated electrolytic methods have been developed

[21] M. Gilberg, *Journal of the American Institute for Conservation* (**1987**) 26(2), 105–120.

[22] F. Rathgen. The preservation of antiquities. Cambridge University Press, Cambridge (**1905**).

[23] R. Bertholon, La limite de la surface d'origine des objets métalliques archéologiques : caractérisation, localisation et approche des mécanismes de conservation. Thèse de doctorat, Sciences de l'Homme et Société. Université Panthéon-Sorbonne - Paris I (**2000**).

[24] H.J. Plenderleith, A.E. Werner. The Conservation of Antiquities and Works of Art, 2nd edn, Oxford University Press, 267-270 (**1971**).

[25] I.A. Carradice, S.A. Campbell, *Studies in Conservation* (**1994**) 39(2), 100–106.

for the stabilization of archaeological artifacts without compromising the overall characteristics of the materials surfaces. For instance, to extract chloride ions from iron objects, a pulsed potential was applied to the metal[26]. Other studies were devoted to investigate the kinetics of the material deterioration and their protection by, for instance, electrodepositing protective films on the surfaces, thus preventing further corrosion. This scheme was applied to the case of silver tarnishing[27]. A variety of electrochemical stabilization methods and surface treatments, together with investigations to get insights on their mechanism action, have been extensively applied to lead[28] and copper artifacts[29]. Polarization resistance measurements (Rp) or polarization curves have been used for the evaluation of the protection of different natural or artificial patinas on bronze monuments[30]. Rp information demonstrated to be of great help to restorers and conservators in choosing the most appropriate substances to employ for their work, since it is a non-destructive technique that can provide quantitative values of corrosion rates in a short time[31]. Electrochemical Impedance Spectroscopy (EIS) has recently gained an increasing interest thanks to the development of new systems that allow to perform investigation of anti-corrosion coatings for the protection of metals in a non-invasive way[31].

Besides the stabilization and anti-corrosion treatments to solve conservation issues, electrochemistry is nowadays widely used for analytical purposes. For example, voltammetric techniques have been used for the identification and discrimination of metals in alloys or components of corrosion layers[32,33]. Voltammetric techniques devoted to the identification of materials of historical interest were firstly employed in the 2000 when Doménech-Carbó

[26] F. Dalard, Y. Gourbeyre, C. Degrigny, *Studies in Conservation* (**2002**) 47:2, 117-121.
[27] M. C. Bernard, E. Dauvergne, M. Evesque, M. Keddam, H. Takenouti, *Corrosion Science* (**2005**) 47, 663–679.
[28] B. Schotte, A. Adriaens, *Studies in Conservation* (**2006**) 51:4, 297-304.
[29] I.D. MacLeod, *Studies in Conservation* (**1987**) 32:1, 25-40.
[30] C. Bartuli, R. Cigna, O. Fumei, *Studies in Conservation* (**1999**), 44(4), 245–252.
[31] E. Cano, D. Lafuente, D.M. Bastidas, *Journal of Solid State Electrochemistry* (**2010**)14:381–391.
[32] V. Costa, E. Balliana, K. Leyssens, A. Adriaens. Identification of copper alloys constituting cultural artefacts using electrochemical techniques. In: Degrigny C, Van Lang R, Joosten I, Ankersmith B (eds) Metal 07. Proceedings of the interim meeting of the ICOMCC Metal WG, vol 5. Rijksmuseum Amsterdam, Amsterdam (The Netherlands), 22–25 (**2007**).
[33] C. Degrigny, *Journal of Solid State Electrochemistry* (**2009**) 14(3), 353–361.

applied the voltammetry of immobilized particles (VIMP) to identify pigments in paint samples[34,35]. VIMP is of particular interest in artifacts analysis[36,37,38] because: (i) only micro/nanograms of sample are required; (ii) it displays high sensitivity; (iii) it provides quick information on the composition and oxidation state of the various compounds; (iv) it can be used *in-situ*; (v) it is easy-to-build set-up; (vi) it is low cost.

More recently, imaging methods, based on electrochemical techniques and applied to cultural heritage materials, have also been developed. In particular, scanning electrochemical microscopy (SECM) has been applied to study the patina on copper-based samples[39] with the aim of characterizing the deterioration processes and to mapping the precursor sites of corrosion. The great advantage of SECM applied in the cultural heritage materials relies in its ability to return an easy-to-interpret image spatially localizing redox active species. In fact, although still limited, the number of publications concerning SECM and cultural heritage is growing.[42,40,41,42,43,44,45,46]

A summary of the above-mentioned electrochemical methods is reported in Table 1.1.

[34] A. Domenech-Carbo, M. T. Domenech-Carbo, M. Moya-Moreno, J. V. Gimeno-Adelantado, F. Bosch-Reig, *Anal. Chim. Acta* (**2000**) 407, 275.
[35] A. Domenech, M. T. Domenech, J. V. Gimeno, F. Bosch, M. C. Sauri, S.Sanchez, *Analyst* (**2001**) 126, 1764.
[36] A. Domenech-Carbo and M. T. Domenech-Carbo, *Pure Appl. Chem*. (**2017**) 90(3), 447-461.
[37] A. Domenech-Carbo, Electrochemistry in Archaeology and Art Conservation, *Isr. J. Chem.* (**2020**) 60.
[38] G. Domingos da Silveira, F. Di Turo, D. Dias, J.A. Fracassi da Silva, J Solid State Electrochem (**2020**) 24:2633–2652.
[39] L. Guadagnini, C. Chiavari, C. Martini, E. Bernardi, L. Morselli, D. Tonelli, *Electrochimica Acta* (**2011**) 56, 6598– 6606.
[40] G. Sciutto, S. Prati, R. Mazzeo, M. Zangheri, A. Roda, L. Bardini, G. Valenti, S. Rapino, M. Marcaccio, *Anal. Chim. Acta* (**2014**) 831, 31–37.
[41] G. Sciutto, M. Zangheri, S. Prati, M. Guardigli, M. Mirasoli, R. Mazzeo, A. Roda*, Anal. Chem. Cult. Herit*. (**2016**) 374, 213–240.
[42] S. Varvara, G. Caniglia, J. Izquierdo, R. Bostan, L. Găină, O. Bobis, R.M. Souto, *Corrosion Science* (**2020**) 165, 108381.
[43] S. Liu, M. Shi, Y. Zhou, R. Li, Z. Xie, D. Hu, M. Zhang, G. Hu, *Journal of Cultural Heritage* (**2020**) 46, 176-183.
[44] A. Doménech-Carbo´, M.T. Doménech-Carbo´, M.L. Pérez, M. Herrero-Cortell, *Forensic Science International* (**2015**) 247, 79–88.
[45] A. Doménech-Carbó, M.T. Doménech-Carbó, M. Silva, F.M. Valle-Algarra, J.V. Gimeno-Adelantado, F. Bosch-Reig and R. Mateo-Castro, *Analyst* (**2015**) 140, 1065.
[46] L. Iannucci, J.F. Rìos-Rojas, E. Angelini, M. Parvis, and S. Grassini, *Eur. Phys. J. Plus* (**2018**) 133: 522.

***Table 1.1**: Summary of the main electrochemical techniques applied in the cultural heritage analysis up-to-date.*

Electrochemical Technique	**Subject of Study**	**Aim of the technique**	**Ref.**
Potentiostatic/galvanostatic techniques	Metal objects, Alloys	Stabilization treatments	22, 24-26
Polarization techniques	Metal objects, Alloys, Patina, Inhibitors	Evaluation of: inhibitors efficiency, corrosion processes, patina stability, rate of surface corrosion	31-33
Electrochemical Impedance Spectroscopy (EIS)	Metal objects, Alloys, Patina, Coatings	Evaluation of coatings and corrosion progression	31
Voltammetric techniques	Pigments, dyes, ceramics, inhibitors…	Redox properties and identification of the materials, assessment of provenance and dating	32-35
Scanning Electrochemical Microscopy (SECM)	Protein-based binders, metals/alloys, patina, coatings	Redox properties of the materials, corrosion monitoring, patina and its treatment evaluation	42-46

Chapter 2: Aim of the thesis

2. Aim of the thesis

Techniques and methodologies devoted to the study of materials of historic/artistic interest need to be carefully chosen, as the maintenance of the sample integrity is a crucial aspect that must be taken into strong consideration by scientists working in this field. However, micro-invasive techniques have recently gained increasing attention in conservation science as they represent a good compromise between the sample integrity and the necessity of acquiring fundamental and decisive information on the composition of materials, their history, and how to preserve them from further degradation phenomena. Electroanalytical techniques, under certain conditions, can be included in the above-mentioned category.

In view of these considerations, the main goal of this thesis was to develop strategies, based, primarily, on dynamic electroanalytical techniques, for investigating and characterizing different types of substrates of historic/artistic interest. To this purpose, several electrochemical techniques were employed, from one side, to characterize metal-based materials; from the other side to propose new systems and approaches to study materials, which can suffer from contact with liquid electrolytes.

Voltammetry of immobilized particles (VIMP) has been considered to gain information on the redox properties of the materials investigated, as it enables to analyse artifacts, essentially, by a non-destructive sampling. In this thesis, VIMP has been employed with the aim of developing a new strategy for discriminating ancient coins displaying a basic primary patina (made of cuprite) on the basis of the corrosion patterns they undergone.

A further focus of this thesis was to investigate copper-based materials in a more complex corrosion status (presence of primary cuprite together with brochantite). The goal was to study the effect of alternative, to classical and poorly environmentally and human safe, corrosion inhibitors. Alternative compounds can be obtained from natural products. Specifically, decanoic

acid and its sodium salts have been considered here, as potential eco-friendly inhibitors. Classical polarisation curves and voltammetric techniques have been applied to the solid substrates or solutions, mimicking possible interaction between samples and environmental chemical species. Voltammetry performed with microelectrodes have also been employed to get insights on mechanisms involved in corrosion phenomena. Complementing electroanalytical evidences with other analytical techniques, such as Raman and FT-IR spectroscopies as well as scanning electron microscopy (SEM), enabled to gain elemental, molecular and structural information.

As scanning electrochemical microscopy (SECM) enables to investigate and monitor chemical corrosion phenomena with high spatial resolution, it was employed with the aim of assessing the stability of the corroded copper-based materials in their pristine conditions and after they underwent treatments with inhibitors. SECM was also used for imaging the local reactivity of the entire sample stratigraphy and to get information of chemical species released.

In addition to the above procedures, and with the aim of attempting the use of miniaturised electrochemical cells for local analyses, an innovative strategy was also investigated, based on the use of microcapillary (MC) techniques. In particular, MCs filled with conductive hydrogels have been developed with the objective of applying it to study materials that suffer the contact with liquid solutions. With the purpose to tailor the electrode surface or the content of MCs with more selective compounds, conducting polymers, presenting intrinsic chiral activity, have been considered. These could be useful to detect, in a very selective way, molecules present in natural compounds like natural resins, mainly composed by terpenoids, generally added to drying oils and often employed as final protective films in paintings.

2.1. Overview of the thesis

Chapter 1 presents a brief history of how scientific methodologies have been developed starting from the past up to the present days to study and restore materials of cultural heritage interest. Moreover, some general aspects, concerning the variety of analytical techniques and methodologies that are employed in the field have also been reviewed. Emphasis is given to the electroanalytical techniques and methodologies.

Chapter 2 illustrates the aims of the research.

Chapter 3 reviews theoretical background of electrochemical techniques and mass transport to electrodes of various geometries and sizes, including conventional and microelectrodes. Basic principles of scanning electrochemical microscopy and microcapillary techniques are also described.

Chapter 3 describes the experimental aspects of the work done. It includes: reagents and solutions employed; the procedure for preparation of agarose hydrogel; the preparation of the roof cladding specimens; the methods of fabrication of microelectrodes, micropipettes, and their characterization by voltammetry; all the instruments and cells employed.

Results & Discussion is devoted to the presentation of the results obtained from the research activity and their discussion. It is divided in the following chapters:

- ***Chapter 5*** describes the use the VIMP technique based on repeated square–wave voltammetric scans recorded on carbon electrode modified with small particles of copper/bronze picked-up from ancient coins. This methodology was applied to a set of

16 copper/ bronze coins produced between 1709 and 1962. Voltammetric data suggested the possibility of establishing a chronological ordering of the coins.

This part of the work was performed at Universitat de Valencia (Spain) under the supervision of Professor A. Domenéch-Carbó.

- ***Chapter 6*** includes several aspects concerning: the general behavior of Cu^{2+} ions and decanoic acid (HC10) in aqueous and 50% (v/v) ethanol/water (E/W) media and their mutual interactions; the electrochemical, spectroscopic and SEM characterization of the roof cladding specimens either untreated or treated with the inhibitors; the characterization by SECM of the top surfaces and cross sections of the roof claddings, untreated and treated with HC10 and benzotriazole (BTA). These investigations are presented and discussed in the following specific sections:

  - ***Section 6.1*** deals with the voltammetric behavior of Cu^{2+} and HC10 in water and 50% (v/v) E/W mixture. The measurements have been performed using a Pt microdisk, this to avoid effects due ohmic drop in the ethanol-rich media. In the E/W mixture, the interaction between Cu^{2+} and HC10 was elucidated by a detailed analysis of the voltammetric responses. The results obtained proved useful to clarify some aspects of the mechanisms which could be involved when the corroded roof claddings are treated with the inhibitors and the stability of the coatings when the samples are immersed in synthetic acid rain.

  - ***Section 6.2*** compares the protective effects of HC10, sodium decanoate (NaC10) and BTA (the latter for comparison), on bare copper and roof cladding samples. The sample surfaces modifications after treatments have been assessed

by examining the color change, the contact angle, the morphology and chemical structure of the samples. The efficiency of the treatments against corrosion, when the samples come in contact with acid rain, has been assessed by open circuit potential (OCP) and potentiodynamic polarization (PDP) measurements. This part of the PhD project was carried out in the Laboratoire Archéomatériaux et Prévision de l'Altération (LAPA) at the Commissariat à l'énergie atomique et aux énergies alternatives (CEA), in Gif sur Yvette (France) under the supervision of Dr. Delphine Neff.

- ***Section 6.3*** examines in detail the reactivity of the top layer and cross section of the roof cladding samples untreated and treated with HC10 and BTA. This study has been performed by using SECM to get information on the reactivity with high spatial resolution. The ability of the inhibitors to prevent further corrosion of the various layers of patina was assessed in aqueous media containing NO_3^-, SO_4^{2-} and Cl^-, which are characterized by different complexing ability towards copper ions. The stability of the various layers composing the patina has been assessed by the amount of Cu^{2+} and Cu^+ released in the solution.

- ***Chapter 7*** examines the properties of agarose hydrogel as medium to perform voltammetric measurements, using the electroactive redox probes $[Ru(NH_3)_6]^{3+}$ and $[Fe(CN)_6]^{4-}$ or Ag^+ ions and a Pt microdisk electrode. The hydrogel containing the redox probe and various electrolytes are employed for MC contact measurements above platinum and gold substrates. To demonstrate the suitability of the above microprobe for more practical applications, proof-of-concept measurements are also presented to characterize micro areas of metallic silver deposited on to the surface of a pencil graphite

lines deposited on a paper material. It is suggested that this approach can be used to characterize ancient paper decorated with metallic nanoparticles.

- ***Chapter 8*** deals with the use of chiral oligomer-film, electrodeposited onto the surface of a gold disk electrode, starting from the chiral monomer (*S*)-BT_2T_4, as substrate to discriminate chiral analytes. The chiral oligomer film is studied by voltammetry and SECM, using the chiral redox probes ferrocene (Fc), (*S*)-(-), (*R*)-(+) and racemate of *N*,*N*-dimethyl-1-ferrocenylethylamine (FcEA) ((*S*)-FcEA, (*R*)-FcEA and *rac*-FcEA).

Chapter 9 summarizes the main conclusions that can be drawn from the various research activities presented in the previous chapter and sections, and formulates some proposals for future developments/applications of the methodologies developed in the thesis.

Chapter 3: Theory

3. Theory

3.1. Electroanalytical Techniques and Methods

Electroanalytical techniques involve the measurement of electrical quantities such as current, potential and charge, and their relationship to chemical parameters[1]. They can be classified on the basis of whether net current flows or not in the electrochemical cell, as well as on the basis of the nature of charge carriers (ions or electrons) involved. The main types of techniques are illustrated in Figure 3.1. For a first general classification, the techniques can be grouped in two classes: one regarding the transport properties of ions in the electrolyte (charge transport), and the other regarding the electrochemical equilibria and the charge transfer (electrons) at the electrode/electrolyte interface. Techniques based on the charge transport are mainly (i) conductometry, i.e., the measure of the ionic conductivity of a solution, and (ii) electrophoresis, where the variations in charge transport are used to separate ions.

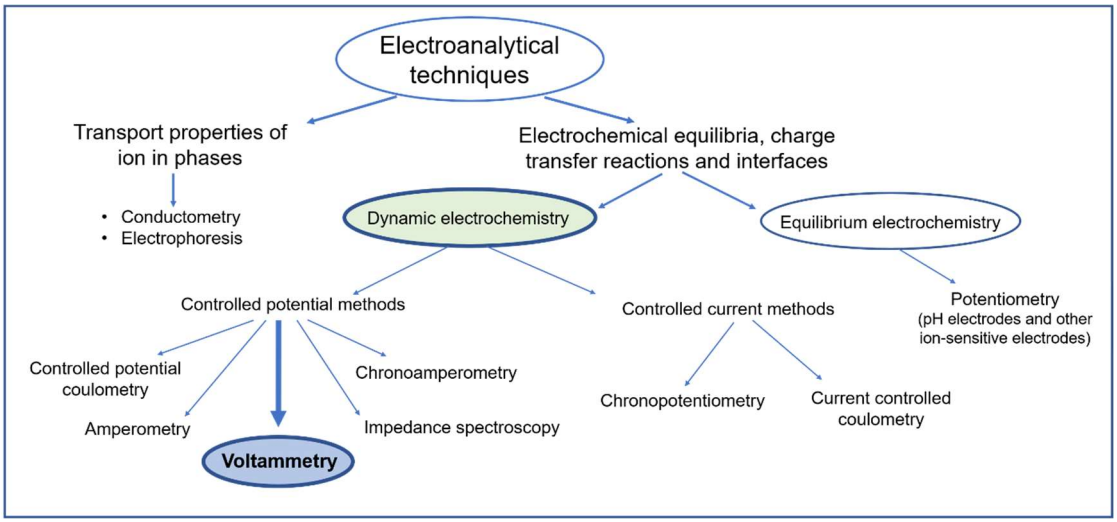

***Figure 3.1**: Schematic overview of electroanalytical techniques elaborated from Ref.* [1].

[1] F. Scholz, *ChemTexts* (**2015**) 1:17.

When dealing with the electrochemical equilibria one can further divide the techniques based on: (i) processes occurring at the electrode without affecting the electrochemical equilibrium (equilibrium electrochemistry, i.e. potentiometric techniques, pH measurements, potentiometric measurements with ion-selective electrodes); (ii) processes occurring shifting the electrochemical equilibrium with the help of an excitation - potential or current changes, which fall in the class of dynamic techniques. Dynamic electroanalytical techniques are numerous and they depend on the excitation potential and how it is applied to a so-called working electrode.

Electroanalytical techniques based on measuring the transport properties of ions and the potentiometric techniques are routinely used in classical electroanalysis. For both electroanalysis or investigation studies of electrode processes, voltammetry is more frequently used. The present thesis will mostly focus on the dynamic electroanalytical techniques and in particular, on voltammetry.

Historically, voltammetric techniques emerged in the first half of the nineteenth century, following the experiments made by Heyrovsky in 1922. He showed that it was possible to obtain information on the nature of the species in the solution, reduced at the electrode surface, by measuring the current while changing the potential of a dropping mercury electrode (DME). This technique, named polarography, was used for analytical applications, especially regarding metal ions. In 1940 the term voltammetry was first introduced to describe experiments, similar to those made at a DME, performed at a solid working electrode[2]. Many variations of the basic polarography were developed and established during the 1940s and the early 1950s.

Under the term voltammetry, the driving force for charge transfer (usually electron transfer) is represented by the applied potential, and the resultant flowing current denote a

[2] A.J. Bard, C.G. Zoski, *Anal Chem* (**2000**) 72, 346A–352A.

measure of the reaction rate[3]. If the potential is held, or stepped, to a value at which a faradaic process takes place, involving the electrode and a solution species, then current flows[4].

The current is the rate at which charge passes through the electrode/solution interface. Current originating from a faradaic process is a direct measure of the rate of the process and, if the rate is proportional to concentration, it is also a measure of the concentration of solute species. The integrated current, or charge, is a measure of the total amount of material converted to another form. In a typical voltammetric experiment, the amount of material actually removed, or converted to another forms, can be made quite small, so that, even for very small sample volumes, voltammetric techniques may be considered non-destructive. Although the amount of material converted can be very small, large changes in concentration occur at the electrode surface during a redox reaction. Considering the general redox reaction:

$$Ox + ne^- \leftrightarrows Red \qquad (3.1)$$

the concentration of the species involved, changes with time; reactions at the electrode/solution interface create sharp concentration profiles that extend away from- or into- the electrode[4]. The time dependence of the concentration profiles near the electrode is displayed experimentally by currents that vary with time. This time dependence is a central feature of voltammetry, every voltammetric experiment contains time as a parameter[4].

The voltammetric techniques can differ for: (i) the potential signal applied, (ii) the type of mass transport occurring, and (iii) the current response recorded[1]. For example, linear

sweep voltammetry (LSV) utilizes a linear potential waveform (Figure 3.2a) which originates the corresponding current response shown in Figure 3.2b. Cyclic voltammetry

[3] P.R. Unwin. Introduction to Electroanalytical Techniques and Instrumentation. In: Encyclopedia of Electrochemistry. A.J. Bard (Ed.) (**2007**).
[4] J.G. Osteryoung, R.A. Osteryoung, *Anal. Chem.* (**1985**) 57**,** 101–110.

(CV), utilizes a triangular potential waveform (Figure 3.2c) which give rise to the current response shown in Figure 3.2d.

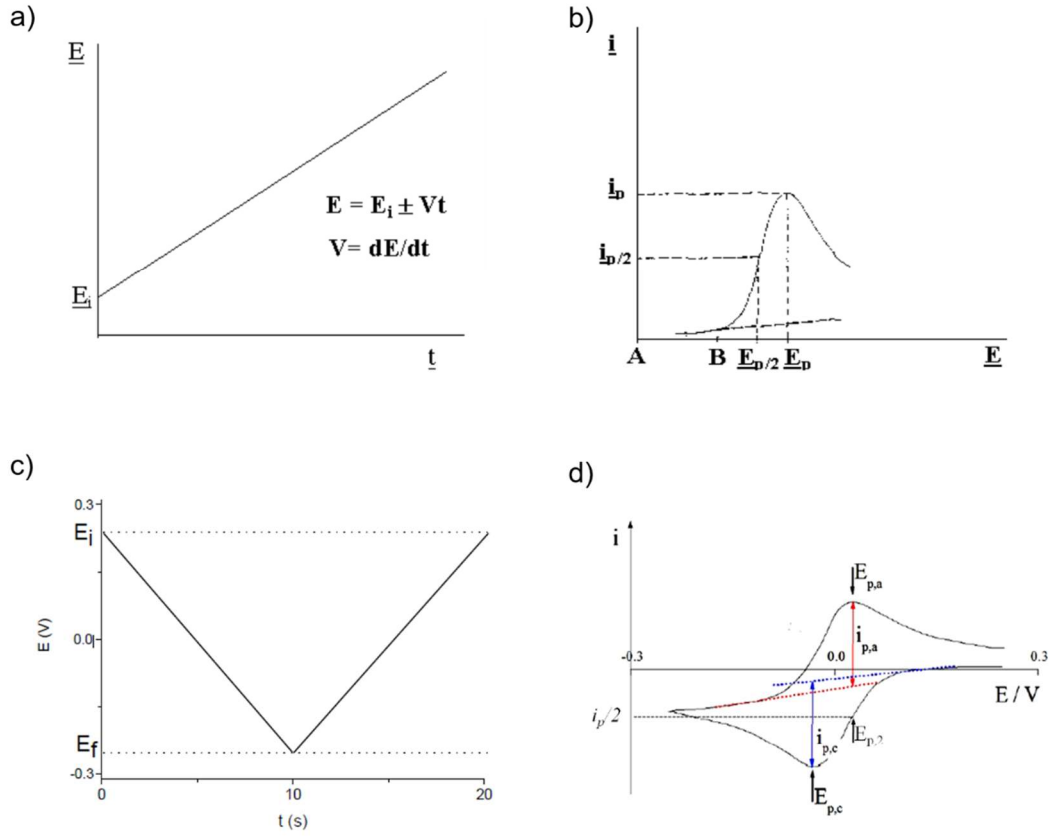

***Figure 3.2**: Waveform applied to the working electrode in LSV (a) and CV (c) experiments with the corresponding I vs E plots, (b) and (d), respectively.*

In pulse voltammetry, the time dependence appears as the width in time of the potential step that is applied to an electrode to cause the faradaic process to occur. Techniques of pulse voltammetry are based on chronoamperometry, the measurement of current as a function of time after applying a potential pulse, as shown in Figure 3.3.

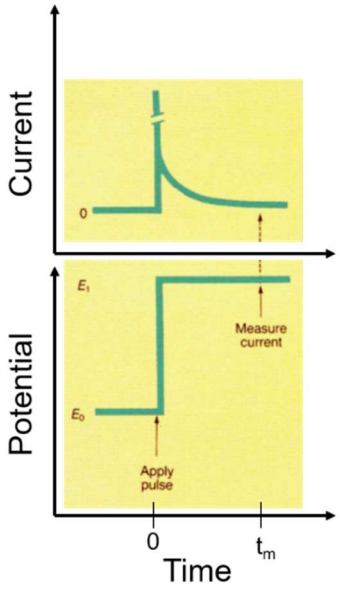

***Figure 3.3**: Potential pulse and current response showing sampling of the current at time t_m after pulse application. Image elaborated from Ref* [4].

In pulsed techniques, such as differential pulse voltammetry (DPV) or square wave voltammetry (SWV), pulses of potential are applied linearly or with a staircase waveform, respectively[5] (for details see next paragraph). The pulsed techniques aim at decreasing the contribution of the capacitive current arising from charging the electrical double-layer capacitance at the electrode/solution interface[6].

Faradaic processes, associated to the electron transfer occurring at the electrode/solution interface, are also accompanied by the mass transport in the solution. In what follows the main theoretical aspects concerning with the latter phenomenon, the electrode geometry, and their effects on current/time or current/potential responses are briefly illustrated.

[5] A. Domenéch-Carbò. Analytical Archaeometry, Selected Topics, Chapter 7: Electrochemical techniques (**2012**).
[6] S. Daniele, C. Bragato. In: Environmental Analysis by Electrochemical Sensors and Biosensors, Chapter 15, L. Moretto, K. Kalcher (eds.) (**2014**).

3.2. Mass transport and electrode geometry

The majority of electrochemical methods rely on mass transport conditions governed by diffusion[7]. Under diffusion-controlled conditions, the flux of the electroactive species and, consequently, the concentration profiles, depend on the electrode geometry. Here, the electrode geometry considered are those illustrated in Figure 3.7.

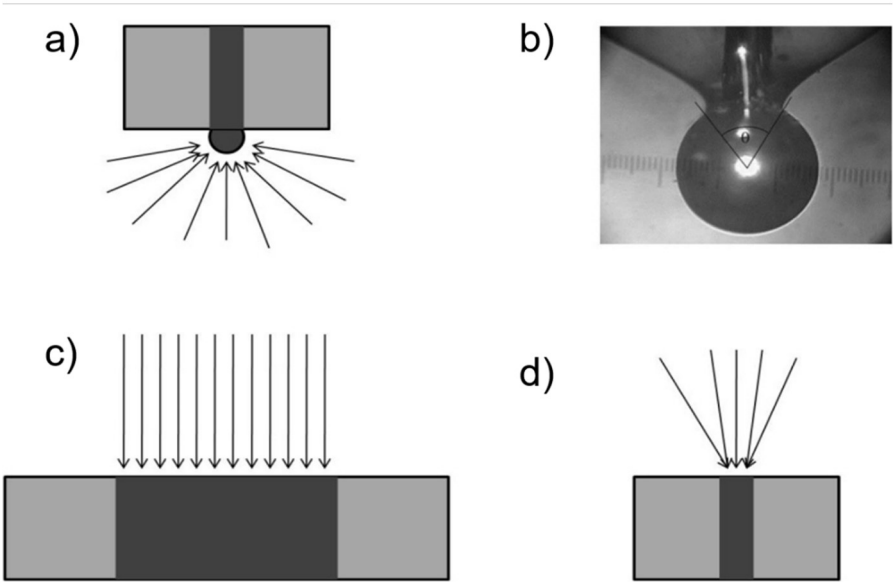

Figure 3.7*: a) Diffusion trajectories at hemisphere electrode; b) dropping mercury electrode; c) planar macroelectrode and d) microdisk electrode.*

Starting from the random walk theory, it is possible to describe the diffusion by formulating differential equations for flux and concentration of a substance as a function of time and position in the space close to the electrode surface. The equations describing these processes are known as Fick's equations. Let *r* denotes the position in the three dimensional space, *t* the time, *J(r, t)* and *C(r, t)* are the local flux (expressed in mol cm^{-2} s^{-1}) and the concentration (in

[7] A.J. Bard, L.R. Faulkner. Electrochemical Methods - Fundamentals and and Applications, Wiley (**2001**).

mol cm^{-3}) of a substance spatially diffusing. Fick's first law establishes that the flux is proportional to the concentration gradient $\nabla C\,(r,t)$ through this equation:

$$\boldsymbol{J(r,t) = -D\nabla C(r,t)} \tag{3.5}$$

where the parameter D is the diffusion coefficient (typically in $m^2\ s^{-1}$ or $cm^2\ s^{-1}$) of the chemical species under consideration. Fick's second law regards the variation of concentration with time, described by the following equation:

$$\boldsymbol{\frac{\partial C(r,t)}{\partial t} = D\nabla^2 C(r,t)} \tag{3.6}$$

The Laplacian operator, ∇^2, depends on the electrode geometry.

Fick's second law provides the so-called concentration profiles. In order to solve this differential equation and to specify it for the system considered (geometry, electroanalytical technique etc.), it is necessary making some assumption on: (i) the initial conditions for every point in space at $t=0$ and (ii) the boundary conditions at the physical contour of the system, for any time t. The form of the Laplacian and the above conditions will be specified for each case separately, on the basis of the electrode geometries shown in Figure 3.7.

3.2.1. Mass transport to planar electrode

The flux (J), associated with an electrode having a planar geometry (Figure 3.7c) of infinite dimension, where the diffusion takes place only along the direction perpendicular to the surface (x), is given by the first Fick's law in one-dimension[7]:

$$J\,(x,\,t) = -D\,[\frac{\partial C(x,t)}{\partial t}\,] \qquad (3.7)$$

where D is the diffusion coefficient, and t the time. The current I, is then expressed by:

$$I = -\,nFAJ(x,\,t) \qquad (3.8)$$

where F is Faraday constant (96500 $Cmol^{-1}$), n the number of electrons, A is the electrode surface. Combination of Eqs. 3.7 and 3.8 give rise to:

$$I = -nFAD\,\frac{\partial C(x,t)}{\partial t} \qquad (3.9)$$

Considering the following reversible electrode process:

$$Ox \;+\; ne^{-} \;\leftrightarrows\; Red \qquad (3.10)$$

From the second Fick's law, it is possible to derive:

$$\frac{\partial C(x,t)}{\partial t} = D_{Ox}\,[\nabla^2 C\,(x,t)] \qquad (3.11)$$

Considering the process (Eq. 3.10), let us make the assumptions that: (i) only the species *Ox* is initially present in the solution and (ii) the potential is stepped from an initial value, where no electrode reaction occurs, to one potential value sufficiently negative so that the concentration of *Ox* at the electrode surface is equal to zero. Hence, under these boundary conditions, the

solution to Eq 3.11 provides the concentration profile of the specie in the solution. For *Ox* the following expression holds:

$$C(x,t)=C_{Ox}\, erf[\frac{x}{2\cdot\sqrt{D_{Ox}t}}] \qquad (3.12)$$

Figure 3.8 shows different concentration profiles for the specie *Ox* depending on the pulse length.

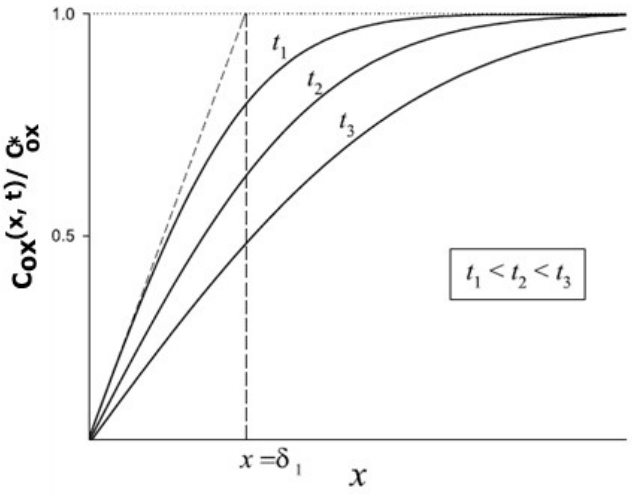

Figure 3.8*: Concentration profiles at different pulse times for the specie Ox.*

As Figure 3.8 evidences, the *Ox* concentration increases with the distance (*x*) from the zero value to the value in the bulk of the solution. This distance is the diffusion layer (δ), which, for a generic species *i*, can be calculated by:

$$\delta_i = \sqrt{\pi D_{0x} t} \qquad (3.13)$$

Considering the flux at the electrode surface and Eq. 3.9, the following relationship can be obtained:

$$\frac{I}{nFA} = D_{Ox}\left[\frac{\partial COx\,(x,t)}{\partial x}\right] \qquad (3.14)$$

Combining Eq 3.14 and Eq 3.12, the Cottrell equation can be obtained[7]:

$$I = \frac{nFAD_{Ox}^{1/2}\,C_{Ox}^{b}}{\pi^{1/2}t^{1/2}} \qquad (3.15)$$

where C^{b}_{Ox} is the concentration of *Ox* in the bulk of the solution and the other symbols have their customary meaning. A typical current *versus* time plot is shown in Fig 3.9 for planar (black line) and hemispherical electrode geometries (red line).

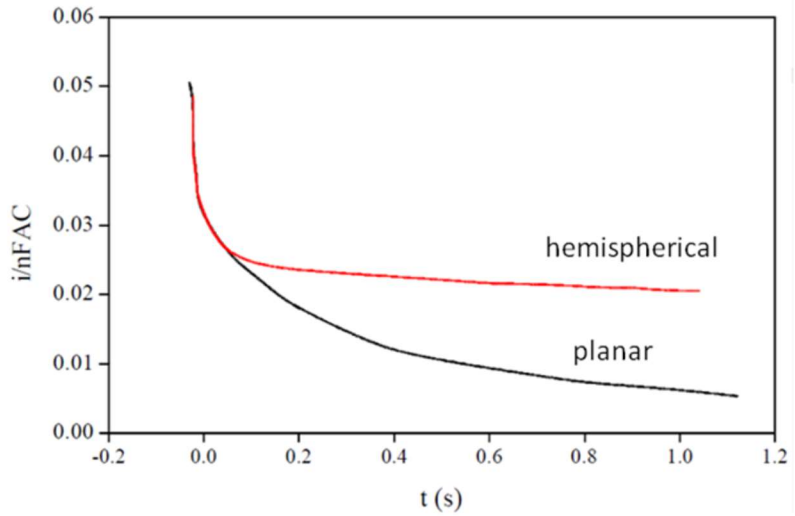

***Figure 3.9**: Current versus time response in a chronoamperometric experiment for electrodes with different geometries: planar (black line) and hemispherical (red line).*

3.2.2. Mass transport to spherical electrodes

The sphere and hemisphere electrodes (Fig. 3.7b,a), can be treated analytically, and the mathematical solution allows to explain, also, qualitatively the mass transport properties of microelectrodes. This mathematical case was solved many years ago because of the importance of spherical electrodes in the classical polarographic experiments with a dropping mercury electrode[8] (Fig. 3.7b).

Let us consider a potential step experiment at an electrode with the geometry of a sphere with radius r_0, placed in a solution containing an electroactive species at a concentration $C_b(r, t)$ and the supporting electrolyte. The experiment involves stepping the potential from an initial value, where no electrode reaction occurs, to one potential value sufficient to completely reduce or oxidize the electroactive species at the electrode surface. The process involves electron transfer across the electrode/solution interface and the rate at which this takes place is described by the heterogeneous electron transfer rate constant. If this rate constant is large, mass transport will control the current recorded. Let us assume that mass transport occurs via diffusion only, and accordingly, Fick's laws govern the system. With this geometry, Fick's second law can be expressed in terms of spherical coordinates:

$$\frac{\partial C(r,t)}{\partial t} = D\left[\frac{\partial^2 C(r,t)}{\partial r^2} + \frac{2}{r}\frac{\partial C(r,t)}{\partial r}\right] \qquad (3.16)$$

where $C(r, t)$ denotes the concentration at the position r and time t; r is the radial distance from the center of the electrode. The initial and boundary conditions are:

$$C(r, 0) = C^b \quad (t = 0), \qquad (3.17)$$

[8] D. MacGillavry, E. K. Rideal, *Trav. Chim. Pays-Bas* (**1937)** 56, 1013-1021.

$$\boldsymbol{lim_{r\to\infty}\, C\,(r,t) = C^b \quad (t > 0)},\tag{3.18}$$

$$\boldsymbol{C(r_0,t) = 0 \quad (t > 0)}.\tag{3.19}$$

where C^b represents the concentration of the electroactive species in the bulk and r_0 is the radius of the spherical electrode.

Initially, the concentration of the electroactive species, C^b, is constant throughout the cell (Eq. 3.17). As the potential is switched on, the bulk value is assumed to be reached at the cell boundaries (Eq. 3.18), whereas on the electrode surface the concentration is zero at all times (Eq. 3.19), since the species is completely reduced. Equation (3.16) can be solved using Laplace transform techniques[7]. The solution to the latter equation, combined with flux equation, at the electrode surface provides:

$$\boldsymbol{I(t) = nFADC^b\left(\frac{1}{a} + \frac{1}{\sqrt{\pi Dt}}\right)}\tag{3.20}$$

where the symbols have their usual mining, while the geometrical electrode area, A, is equal to $4\pi r_0^2$. Eq. (3.20) contains both time independent and time dependent terms, which prevail in two limiting regimes, depending on whether the experimental time scale is short or long. At sufficiently short times, the thickness of the diffusion layer of the reactant is much smaller than the electrode radius. The spherical electrode, hence, appears planar to a molecule at the edge of this diffusion layer. Under these conditions, the electrode acts as a conventional macroelectrode (Fig. 3.7c) and mass transport is dominated by the linear diffusion to the electrode surface[7]. At these short times, the dependence of the current response on the term $t^{-1/2}$ in Eq. (3.20) becomes

significantly larger, hence, the current response initially decays in time according to the Cottrell equation[7]:

$$\boldsymbol{I(t) = nFAC^b\sqrt{\frac{D}{\pi t}}} \qquad (3.21)$$

At long times, the transient contribution given by the second term of Eq. (3.20) has decayed down to the point at which its contribution to the overall current is negligible. At these long times, the spherical character of the electrode becomes important and the mass transport process is dominated by the spherical diffusion.

The current accomplishes a time-independent steady state value given by the equation:

$$\boldsymbol{i_{ss} = \frac{nFADC^b}{r_0}} \qquad (3.22)$$

The steady state response is typical of the radial diffusion and this is due to the fact that the electrolysis rate is equal to the rate at which molecules diffuse to the electrode surface.

Since *short* and *long* times are relative terms, it is useful to determine the times over which transient and steady state features predominate and how this time regime is affected by the electrode radius. This can be accomplished by considering the ratio of the steady state current (Eq. 3.22), to the transient current contribution (Eq. 3.21). In this way, a dimensionless parameter is obtained ($\frac{\sqrt{\pi Dt}}{r_0}$) which can be used to calculate a lower time limit at which the steady state contribution will dominate over the total current to a specific extent. For example, the time required for the steady state contribution to be ten times larger than the transient one is 8×10^5 s, taking as a typical value of $D = 10^{-5}$ cm^2/s, for an electrode with $r_0 = 5$ mm (typical of a conventional, *i.e.*, macroelectrode). However, reducing the electrode radius by a factor of a

thousand to 5 μm means that a steady-state current can be observed for times longer than 0.8 s. Since the steady-state response becomes more dominant with the increasing of the time, steady state current is measured for microelectrodes in electrochemical experiments run at conventional time scales. It is important to highlight that there is no theoretical barrier to observe steady-state responses for any size of electrode. However, for conventional millimetric-dimension electrodes, the time taken is too long to be experimentally evidenced. Moreover, unintentional convection, i.e., caused by building vibrations, or natural convection play a significant role in the mass transport process at these long-time scales.

A similar mathematical treatment can be used for a hemispherical microelectrode. The only difference in the mathematics relies on the surface area *A,* which becomes: $A = 2\pi r_0^2$. All the general equations, results and considerations equally apply.

The results obtained for both spherical and hemispherical electrodes are in general achieved for electrodes enough small, such as the diffusion regime converges towards the electrode surface. These conditions hold for microelectrodes.

3.3. Microelectrode: introduction and theory

A microelectrode is generally defined as an electrode with at least one dimension sufficiently small, typically less than 50 μm and can possess various geometries, as shown in Figure 3.10. Microelectrodes have, according to IUPAC, at least one dimension called critical dimension in the range of 10 nm – 25 μm[7,9]. To accomplish the features which characterizes the microelectrode behavior, apart from the electrode size and shape, the component time is a key factor and it depends on the electroanalytical technique employed in the measurements. The thickness of the diffusion layer developed around the electrode surface is governed by the time

[9] K. Štulik, C. Amatore, K. Holub, V. Mareček, W. Kutner, *Pure and Applied Chemistry* (Technical Report) (**2000**) 72, 1483-1492.

parameter. From this point of view, according to IUPAC, a microelectrode is "any electrode whose characteristic dimension is, under the given experimental conditions, comparable to or smaller than the diffusion layer thickness"[9]. In the following sub-paragraphs, the diffusion mass transport that controls the current at the microelectrodes of different size and geometries will be presented.

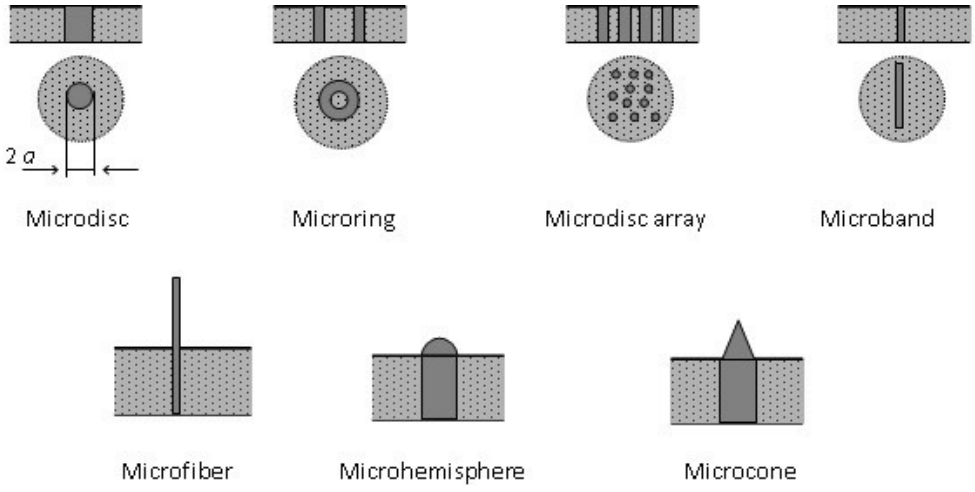

***Figure 3.10**: Most common geometries of microelectrodes and microelectrode arrays.*

After the introduction of microelectrodes, around the 1980s, they were subject of a considerable development and application into electroanalytic methodologies based on amperometry as well as voltammetry[9,10,11,12]. The advantages of employing microelectrodes in analytical chemistry come from their distinct properties: (i) low ohmic drop; (ii) high Faradaic to capacitive current ratio; (iii) high rate of diffusion to the microelectrode surface under steady state conditions; (iv) quick achievement of steady state currents; (v) possibility to operate with

[10] M. I. Montenegro, M. A. Queirós, J. L. Daschbach, Microelectrodes: Theory and Applications, Eds., Proceedings of the NATO ASI Series E197, Kluwer Academic Press (**1990**).
[11] M. R. Deakin, D. Wipf, R. M. Wightman, *J Electrochem Soc* (**1986**) 133, C135–C135.
[12] M. Fleischmann, S. Pons, D. R. Rolison, P. P. Schmidt, Ultramicroelectrodes, Datatech Systems Inc., Morganton, NC, p. 363. (**1987**)

electrochemical cells in the two-electrode configuration and in small volume of sample[9,11,12]. Thanks to their properties, microelectrodes have been employed in many fields of electroanalysis, ranging from environmental[13,14], food[15], biomedical[16,17,18], to material science[19] and even at micro-locations, *i.e.*, in-vivo measurements[16]. During the last decade, microelectrodes have been employed to characterize and detect metal and metal oxide nanoparticles (MNPs) (*i.e.*, silver, gold, platinum, copper, nickel, iridium, titanium and their oxides), which are nowadays widely used in electronics, medicine, energy production and consumer goods. For these studies, various detection strategies have been developed, most of them based on the frequency of impact of the MNPs with the microelectrode surface[20,21,22,23,24,25,26]. The small electrode surface limits the number of nanoparticles that can interact with it, thus simplifying the interpretation of the electrochemical responses. The peculiar properties of microelectrodes and their theoretical achievements have had a significant impact in the development of the new electroanalytical techniques such as Scanning Electrochemical Microscopy (SECM) and Microcapillary Amperometry/ Voltammetry, which can be included within the Scanning Probe Microscopy (SPM) techniques.

[13] F. Davis, S. P. J. Higson, *Environ. Sci.: Processes Impacts* (**2013**), 15, 1477–1489.
[14] F. Tan, J. P. Metters, C. E. Banks, *Sensors and Actuators B: Chemical* (**2013**), 181, 454–462.
[15] K. Peckova, J. Barek, *Curr. Organic Chem.* (**2011**), 15, 3014–3028.
[16] S. Marinesco, O. Frey, (**2013**), *Neuromethods* (eds S.Marinesco and N.Dale) vol. 80, Microelectrode Biosensors, 3–25.
[17] X. P. Sun, Y. L. Luo, F. Liao, W. Lu, G. Chang, *Electrochim. Acta* (**2011**), 56, 2832–2836.
[18] O. Ordeig, J. del Campo, F. X. Munoz, C. E. Banks, R. G. Compton, *Electroanalysis* (**2007**), 19, 1973–1986.
[19] C. M. Li, W. H. Hu, *J. Electroanal. Chem.* (**2013**), 688, 20–31.
[20] A. Boika, S. N. Thorgaard, A. J. Bard, *J. Phys. Chem. B* (**2013**), 117, 4371–4380.
[21] X. Y. Xiao, A. J. Bard, *J. Am. Chem. Soc.* (**2007**), 129, 9610–9612.
[22] S. J. Kwon, F. R. F. Fan, A. J. Bard, *J. Am. Chem. Soc.* (**2010**), 132, 13165– 13167.
[23] S. J. Kwon, H. J. Zhou, F. R. F. Fan, V. Vorobyev, B. Zhang, A. J. Bard, *Phys. Chem. Chem. Phys.* (**2011**), 13, 5394–5402.
[24] E. J. E. Stuart, N. V. Rees, J. T. Cullen, R. G. Compton, *Nanoscale* (**2013**), 5, 174–177.
[25] E. J. E. Stuart, Y. G. Zhou, N. V. Rees, R. G. Compton, *RSC Advances* (**2012**), 2, 6879–6884.
[26] Y. G. Zhou, N. V. Rees, J. Pillay, R. Tshikkudo, S. Vilakazi, R. G. Compton, *Chem. Commun.* (**2012**), 48, 224– 226.

3.3.1. Mass transport to microdisk electrodes

From a manufacture point of view, the fabrication of microelectrodes with disk geometry embedded in an infinite insulating plane (Fig. 3.7d) is easier than the creation of spherical microelectrodes. However, the derivation of a rigorous expression to predict the current response is complicated, because the surface is not uniformly accessible (Fig. 3.7d). In fact, the flux of the material reacting at the surface is unequal across the electrode surface[27] because the electrolysis taking place at the outer circumference of the disk reduces the flux of the material to the central part of the disk[28,29].

Early approaches to mathematically solve this issue used either simplifications[30] or digital simulation procedures[31] attempted to get a solution to the chronoamperometry problem, analogous to the Eq. (3.20). To a first approximation, one might expect the results for a disk to be very similar to those previously examined for spherical electrodes. In particular, there should be close analogy between the results for a hemisphere and a disk, and it has been demonstrated[32,33]. Thus, for small values of Dt/a^2, where a is the radius of the disk, it would be expected that the Cottrell equation still describes the current as a function of time. For large values of Dt/a^2, a hemispherical diffusion layer can be proposed over the disk, and steady state behavior would be expected[34].

Y. Saito was the first to give insights into the steady state nature of the current at the microdisk electrode[35]. To mathematically solve the problem for a disk, the second Fick's law for the *Ox* species needs to be written in cylindrical coordinates[7]:

[27] J. Albery, S. Bruckenstein, *J. Electroanal. Chem.* (**1983**), 144, 105-112.
[28] K. B. Oldham, *J. Electroanal. Chem.* (**1981**), 122, 1-17.
[29] J. Newman, *J. Electroanal. Soc.* (**1966**), 113, 501-502.
[30] Z. G Soos, P. J. Lingane, *J. Phys. Chem.* (**1964**), 68, 3821-3828.
[31] J. B. Flanagam, L. Marcoux, *J. Phys. Chem.* (**1973**), 77, 1051-1055.
[32] J. O. Howell, R, M. Wightman, *Anal. Chem.* (**1984**), 56, 524-529.
[33] Z. Galus, J. O. Schenk, R. N. Adams, *J. Electroanal. Chem.* (**1982**), 135, 1-11.
[34] A. Dayton, J. C. Brown, K. J. Stuttus, R. M. Wightman, *Anal. Chem.* (**1980**), 52, 946-950.
[35] Y. Saito, *Rev. Polarogr. Jpn.* (**1968**), 15, 177-187.

$$\frac{\partial C_{Ox}}{\partial t} = D_{Ox}\left[\frac{\partial^2 C_{Ox}}{\partial r^2} + \frac{1}{r}\frac{\partial C_{Ox}}{\partial r} + \frac{\partial^2 C_{Ox}}{\partial z^2}\right] \qquad (3.23)$$

where r is the radial direction with the origin at the center of the disk, and z is the direction perpendicular to the electrode surface, as depicted in Figure 3.11.

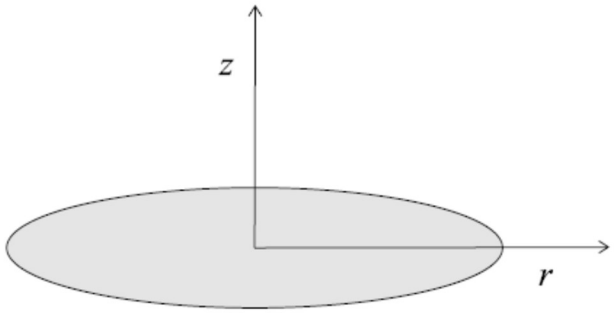

Figure 3.11*: Graphical representation of cylindrical coordinates for a microdisk electrode.*

The solution of Eq. 3.23 is very complex. Approximate numerical solutions have been provided to predict with good accuracy the current *versus* time responses for this electrode geometry. Among them, the one proposed by Shoup and Szabo[36] (Eq. 3.24) covers the entire range of time in a single equation as a function of the dimensionless parameter τ:

$$I(\tau) = \frac{4nFAD_{Ox}C_{Ox}^{b}}{\pi a} f(\tau) \qquad (3.24)$$

where $f(\tau)$ is expressed by:

$$f(\tau) = 0.7854 + 0.8862\,\tau^{1/2} + 0.2146\,e^{-0.7823\tau^{-1/2}} \qquad (3.25)$$

[36] D. Shoup, A. Szabo, *Journal of Electroanalytical Chemistry* (**1982**) 140, 237-408.

And $\tau=4D_{Ox}t$ / a^2; being a the radius of the microdisk.

For $t \rightarrow 0$, Eq. 3.24 is reduced to the Cottrell equation; while for $t \rightarrow \infty$, Eq. 3.24 converts to:

$$I = i_{ss} = 4\, n\, F\, D_{Ox}\, \boldsymbol{C_{Ox}^{b}}\, a \qquad (3.26)$$

Eq. (3.26) and Eq. (3.20), for a hemispherical electrode are equal when $\boldsymbol{a_{disc} = \frac{\pi}{2} a_{hemisphere}}$.[28]

The above equations hold for a potential step experiment. In voltammetry, the potential changes, usually in a linear way, up to a given value (in LSV) and eventually it can be reversed and returned linearly to the starting value (in CV). In these techniques, the transition from planar to radial diffusion for a given microelectrode and electrode geometry, is accomplished by reducing the scan rate. The faster the transition, the smaller the characteristic length of the microelectrode. Figure 3.12 reports, for instance, a series of CVs obtained at a microdisk electrode at different scan rates (v). It is evident that at high v, the CV displays the peak-shaped voltammogram as for macroelectrodes; at low v, the CV becomes sigmoidal with the forward and backward curves overlapping one another. This is due to the formation of a stationary diffusion layer produced by the relatively high diffusion mass transport. The current at the stationary state is essentially independent from the scan rate and the diffusion-limited current corresponds to that assessed by a large potential step experiment described above. Theoretical modeling of the current-potential profiles at microelectrodes is usually difficult, and because of the complexity of the task, numerical solutions or digital simulation procedures have often been applied. The only exception is for the spherical microelectrodes for which Eq. (3.20) can be used.

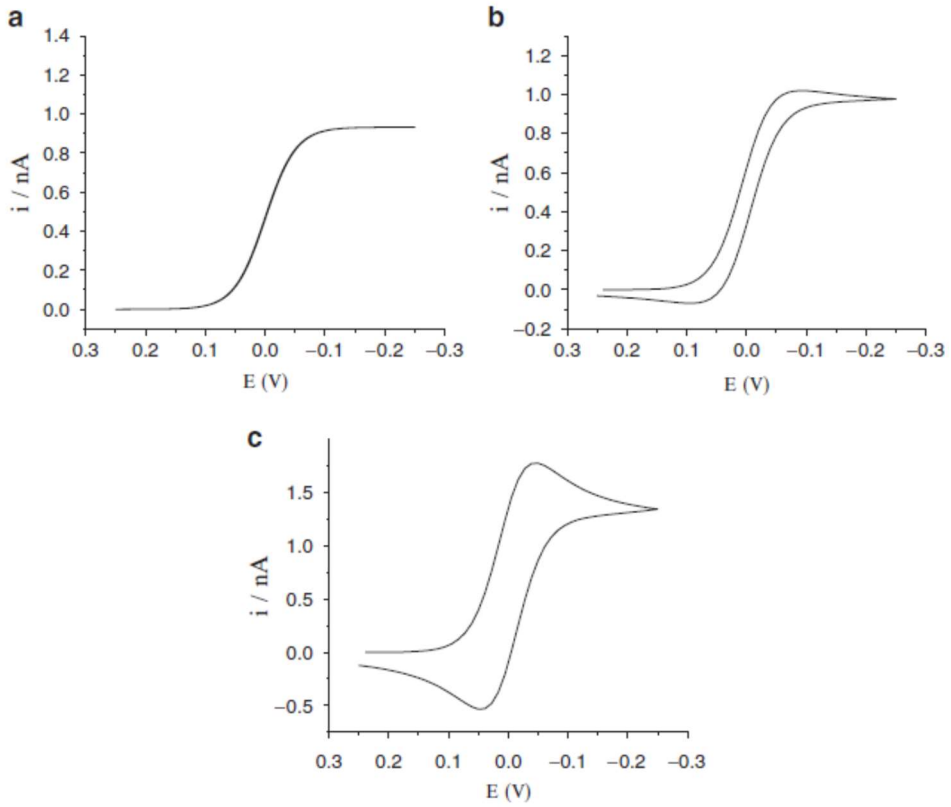

***Figure 3.12**: Simulated CVs for a microdisk with radius of 12.5 µm at different scan rates: a) 1 mV/s; b) 200 mV/s; c) 2 V/s.*

For disk and cylindrical microelectrode geometries, mathematical expressions for the voltammograms have been derived as function of the parameter p which contains the typical dimension of the specific microelectrode. Since the peak or maximum current characterizes quantitatively the voltammograms, relevant expressions are reported in Table 3.1.

***Table 3.1**: Voltammetric peak current for different electrode geometries.*

Electrode geometry	*Peak or maximum current*
Microdisk	$I = 4nFDC\,a[0.34\exp(-0.66p^{d})+0.66-0.13\exp(-11/p^{d})+0.351p^{d}]$
Microcylinder	$I = n^2F^2CAr_0\,v/(RT)\,(0.446/p+0.335/p^{1.85})$
p^{d}	$p^{d} = (nFa^2v/RTD)^{1/2}$
$p^{1.85}$	$p^{1.85} = (nF\,r_0\,v/RTD)^{1/2}$

In general, for large values of the parameter *p*, the equations reported in Table 3.1 are identical to the equation for planar diffusion. For small values of *p*, these equations approach those for the steady-state current displayed in Table 3.1 for the corresponding microelectrode geometry.

3.4. Voltammetry of immobilized microparticles and square-wave voltammetry

The voltammetry of immobilized particles (VIMP), also known with his first historic name of abrasive stripping voltammetry, was developed by Scholz et al.[37] in the 1980s for the identification of solid materials. Right after, the technique has had a rapid establishment due to its practicability, rapidity, easiness of use and high sensitivity. VIMP is part of the wider class of solid-state electrochemistry techniques, where the electrode reaction starts at the three-phase junction (electrode/electrolyte solution/solid particles) and then spread across the solid particles by the gradient of the electrochemical potential. The so-generated fluxes of both electrons and ions in the solid particles obey the Fick's laws of diffusion[38]. The electrochemical reactions progress via electron-hopping between immobile redox centers in the solid, accompanied by the migration of charge-balancing electrolyte cations through the solid (electron diffusion and cation diffusion, respectively). The redox conductivity is maintained even in the case where electron diffusion and cation diffusion are hindered. This technique usually exploits the electrochemical method of the square wave voltammetry (SWV). Figure 3.4 reports the principal parameters on which SWV is based. At each potential step, two small, oppositely oriented potential pulses are imposed. The duration of the two pulses (pulse width) is identical and defined as $t_p = \tau/2$, where

[37] F. Scholz, L. Nitschke, G. Henrion, *Fresenius' Zeitschrift Für Analytische Chemie* (**1989**) 334(1), 56–58.
[38] M. Lovric, F. Scholz, *J Solid State Electrochem* (**1997**) 1: 108-113.

τ is the duration of the step (Figure 3.4a). The square wave is characterized by a pulse height, E_{sw}, termed square wave amplitude, and the ΔE, which is the pulse width. Usually, the pulse width is expressed in terms of the square wave frequency, $f = 1/2t_p$. The scan rate can be defined as the product of the frequency and the scan increment $v = \Delta E /2t_p = f\Delta E$. The first and the second pulses are termed as *forward* and *reverse pulse*, respectively, thus, the total resulting wave-form can be considered as a staircase scan, each tread of which is superimposed by a symmetrical double pulse, one in the forward direction and one in the reverse (Fig 3.4b).

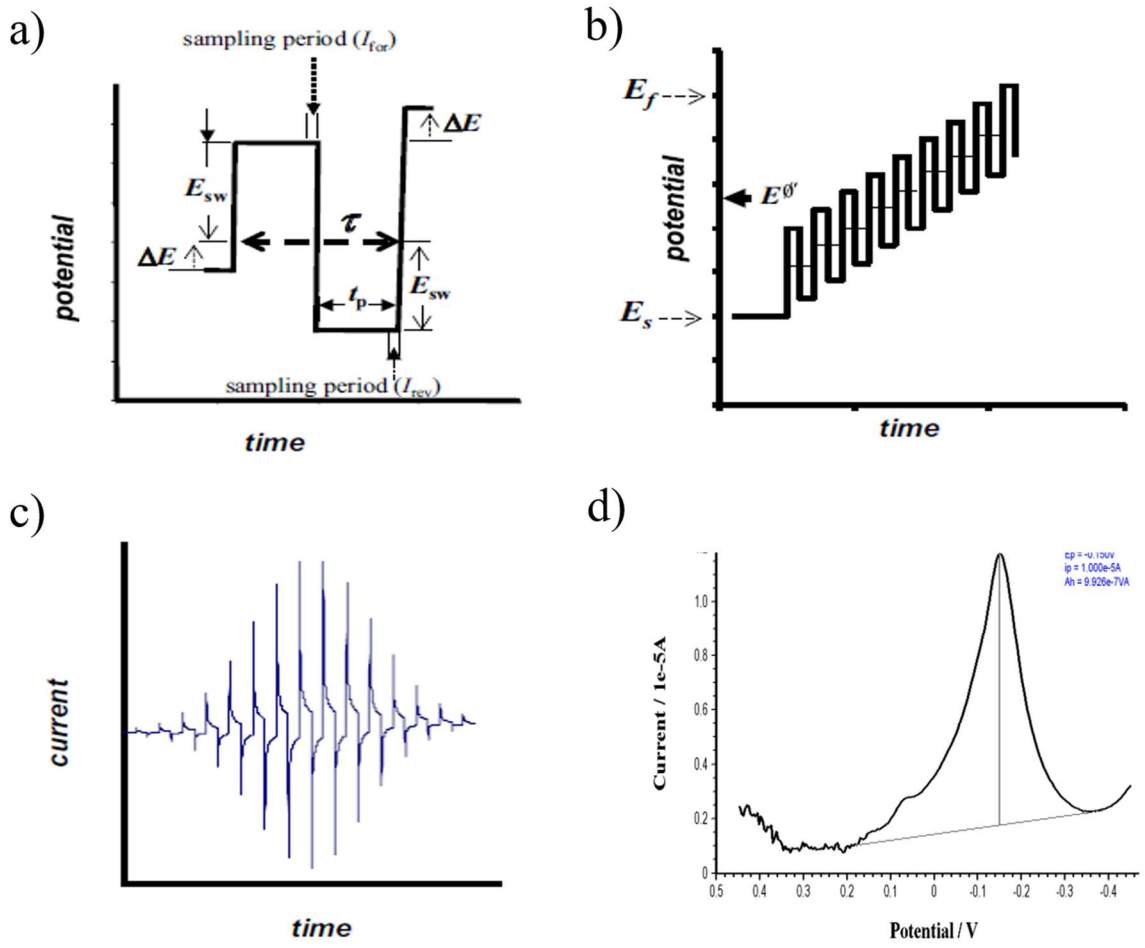

***Figure 3.4**: Graphical representation of different parameters involved in the SWV. a) single potential cycle of SWV; b) potential modulation; c) variation of the current versus time; d) typical SW voltammogram.*

The idea behind imposing two oppositely oriented potential pulses is to drive the electrode reaction in both anodic and cathodic directions in order to gain mechanistic

information. The resulting current variation recorded versus time (Figure 3.4c) give rise to the typical graph current versus potential shown in Fig 3.4d.

Current values are taken twice per cycle, at the end of each potential pulse only. The forward current, I_f, arises from the first pulse per cycle, which is in the direction of the staircase scan. The reverse current, I_r, is taken at the end of the second pulse, which is in the opposite direction. A current difference ΔI is calculated as I_f - I_r. Forward and reverse currents are diagnostic, hence they are taken separately. Consequently, the result of a single SWV run is constituted by three curves: two experimentally measured (forward and reverse), and the third calculated net current *versus* the potential on the corresponding staircase tread.

The peak-like shape of net SW component is advantageous in analytical context as it provides readily measurable parameters 'peak height' and 'peak position'[39]. These parameters can be used for the discrimination of different compounds as the reduction and oxidation peaks is phase-characteristic. However, there are some factors that influence the recorded peak[40]: (i) type of electrodes used as reference (Ag/AgCl, SCE) and as working (graphite, gold, platinum); (ii) electrolytic solution; (iii) particle size and distribution. Moreover, it is important to recall that faradic background processes contribute and control the detection limits of this technique[4]. At solid electrodes or near background limits, the effects on the forward and reverse current can be significant, but they are often suppressed effectively in the difference of the currents[7]. However, the theoretical treatments of SWV are more complex and it is out of the aims of this chapter. In general, it is possible to summarize the advantageous characteristics of VIMP: (i) it combines the capabilities of the pulse voltammetric methods, like the background suppression, the sensitivity intrinsic of the differential pulse voltammetries and a wide range of time scales; (ii) it gives a quick and reliable response; (iii) in comparison with traditional voltammetric

[39] V. Mirceski, S. Skrzypek, L. Stojanov, *ChemTexts* (**2018**) 4:17.
[40] A. Doménech-Carbó, M.T. Doménech-Carbó, V. Costa. Electrochemical Methods in Archaeometry, Conservation and Restoration. Springer Berlin Heidelberg (**2009**).

techniques (such as Differential Pulse Voltammetry, DPV), SWV offers a background suppression, faster scan times and applicability to a wider range of electrode materials[7].

3.4.1. VIMP applications

Among the fields the VIMP technique has been applied, like biochemistry, food chemistry, pharmaceutical chemistry[41,42,43], it has proved to be very useful for the study of the corrosion layer of archeological objects and artifacts because of its capability to work with micro/nano samples[44,45].

Application to the study of metal objects exploiting VIMP, is made by gently pressing the tip of the paraffin-impregnated graphite lead on their surface (Figure 3.5a), thus resulting in a micro-invasive sampling in which only few nanograms of the corrosion patina are sampled[46,47]. Then, the electrode is immersed in the electrochemical cell with a suitable electrolyte (Fig. 3.5b) and the voltammetric response of the samples attached to the electrode's surface can be recorded (Fig. 3.5c) and used for identification[44] and quantification purposes[48].

[41] S. Muñiz-Calvo, J.M. Guillamón, I. Domínguez, A. Doménech-Carbó, *Food Anal. Methods* (**2017**) 10, 1408–1418.
[42] I.N. Jovanovića, L. Čižmek, Š. Komorsky-Lovrić, *Electrochimica Acta* (**2016**) 208, 273-281.
[43] A. Doménech-Carbó, M. Martini, L. Machado de Carvalho, C. Viana, M.T. Doménech-Carbó, M. Silva, *Journal of Pharmaceutical and Biomedical Analysis* (**2013**) 80, 159-163.
[44] A. Doménech-Carbó, *J Solid State Electrochem* (**2010**) 14(3):363–379.
[45] V. Costa, K. Leyssens, A. Adriaens, N. Richard, F. Scholz, *J Solid State Electrochem* (**2010**) 14(3):449–451.
[46] D. Blum, W. Leyffer, R. Holze, *Electroanalysis* (**1996**) 8(3):296–297.
[47] A. Doménech-Carbó, M.T. Doménech-Carbó, M.A. Peiró-Ronda, *Electroanalysis* (**2011**) 23(6):1391–1400.
[48] F. Arjmand, A. Adriaens, *J Solid State Electrochem* (**2012**) 16(2):535–543.

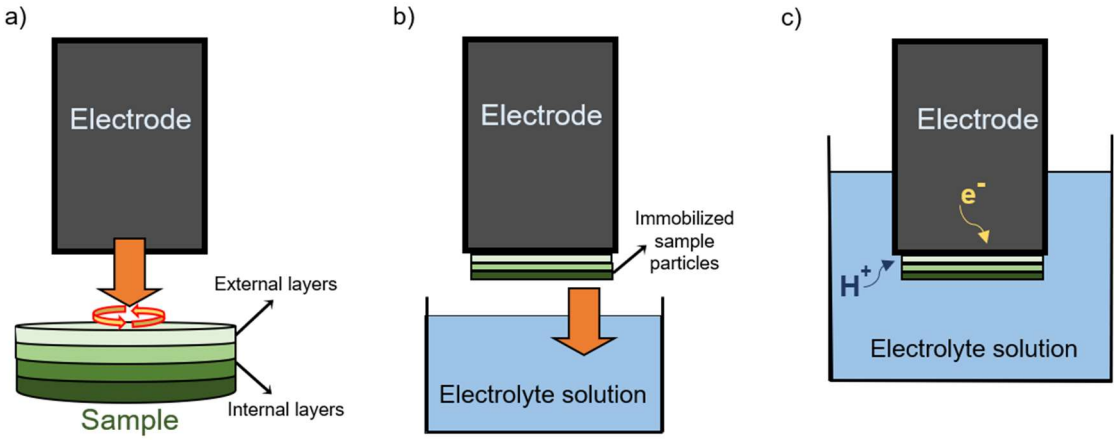

***Figure 3.5**: Scheme of the VIMP operational sequence. a) Abrasive transference of the sample onto the electrode surface; b) immersion of the sample-modified electrode into the electrochemical cell; c) application of the suitable voltammetric method.*

The early applications of the VIMP technique to copper/bronze artifacts were focused on the identification of corrosion products of their patinas[44,49,50,51]. Further applications of the VIMP technique on copper-based objects, allowed the discrimination of provenances and minting processes[52,53,54,55], as well as dating[56,57,58] on the basis of the antecedent idea proposed by Scholz on dating ceramics[59] and further developed and applied on lead artifacts by Doménech-Carbó[60].

[49] N. Souissi, L. Bousselmi, S. Khosrof, E. Triki, *Mater Corros* (**2004**) 55(4):284–292.
[50] A. Doménech-Carbó, M.T. Doménech-Carbó, I. Martínez-Lázaro, *Microchim Acta* (**2008**) 162(3-4):351–359
[51] D. Satovic, S. Martinez, A. Bobrowski, *Talanta* (**2010**) 81(4-5):1760–1765.
[52] F. Di Turo, N. Montoya, J. Piquero-Cilla, C. De Vito, F. Coletti, G. Favero, A. Doménech-Carbó, *Anal Chim Acta* (**2017**) 955:36-47.
[53] A. Doménech-Carbó, M.T. Doménech-Carbó, E. Montagna, C. Álvarez-Romero, Y. Lee, *Talanta* (**2017**) 169:50–56.
[54] A. Doménech-Carbó, M.T. Doménech-Carbó, C. Álvarez-RomeroT. Pasíes-Oviedo, M. Buendía, *Electroanalysis* (**2019**) 31(6):1164–1173.
[55] A. Doménech-Carbó, J. Bernabeu-Aubán, *J Solid State Electrochem* (**2019**) 23(10):2803–2812.
[56] A. Doménech-Carbó, *J Solid State Electrochem* (**2017**) 21(7):1987–1998.
[57] A. Doménech-Carbó, F. Scholz, *Acc Chem Res* (**2019**) 52(2):400–406.
[58] F. Di Turo, N. Montoya, J. Piquero-Cilla, C. De Vito, F. Coletti, G. Favero, M.T. Doménech-Carbó, A. Doménech-Carbó, *Electroanalysis* (**2018**) 30(2):361–370.
[59] F. Scholz, U. Schröder, S. Meyer, K.Z. Brainina, N.F. Zakharchuk, N.V. Sobolev, O.A. Kozmenko, *J Electroanal Chem* (**1995**) 385:139–142.
[60] A. Doménech-Carbó, M.T. Doménech-Carbó, M.A. Peiró-Ronda, *Anal Chem* (**2011**) 83:5639–5644.

3.5. Polarization curves

The open circuit potential (OCP) is the potential at which an electrode spontaneously establishes in the absence of external current. For a single electrode the OCP is equal to the equilibrium potential. The OCP of a system undergoing corrosion is called *corrosion potential* (E_{corr}) and its value is determined by kinetics. Indeed, it depends on the rates of the anodic and cathodic partial reactions occurring. According to Faraday's law ($I = n\,F\,dN/dt$), (where I is the current, n the number of electrons, F is the Faraday's constant and N the amount of substance in mols), the rate of a reaction is proportional to the current density flowing through the electrode/electrolyte interface. By measuring the current density as a function of the potential applied, we can gain information on the kinetics of the electrochemical reactions occurring. In this way, one obtains the so-called polarization curves, by controlling the potential gets potentiostatic polarization curves, $i=f(E)$, whereas, by controlling the current density gets galvanostatic polarization curves, $E=f(i)$. The potentiostatic polarization curves can be registered either by imposing a constant potential, or a linear potential scan, thus obtaining a potentiodynamic polarization curve. Depending on the potential sweep rate and the characteristics of the electrochemical systems, such curves may or may not correspond to steady state current conditions[61]. Experimentally, one can determine the kinetic parameters i_0, β_a and β_c, respectively the exchange current density and the Tafel coefficients of the anodic and cathodic reactions (Eqs. 3.2-4).

$$i_a = -i_c = i_0 \qquad (3.2)$$

$$\beta a = \frac{\mathrm{d}E}{\mathrm{d}\ln i\mathrm{a}} \qquad (3.3)$$

$$\beta c = -\frac{\mathrm{d}E}{\mathrm{d}\ln |ic|} \qquad (3.4)$$

[61] D. Landolt. Corrosion and surface chemistry, 1st edn, EPFL Press, (**2007**).

From the experimental curve obtained (log|I| *vs* E, like in Figure 3.6), by extrapolation from the corrosion potential (E_{corr}), it possible to get the corrosion current density (I_{corr}) and, from the slopes of the tangent lines, the Tafel coefficients β_a and β_c. The values of the exchange current density can vary over several orders of magnitude (10^{-12} to 1 A cm^{-2}) depending on the electrolyte composition and the electrode surface. On the other hand, the Tafel coefficients slightly vary between different reactions (typically 20-50 mV)[61].

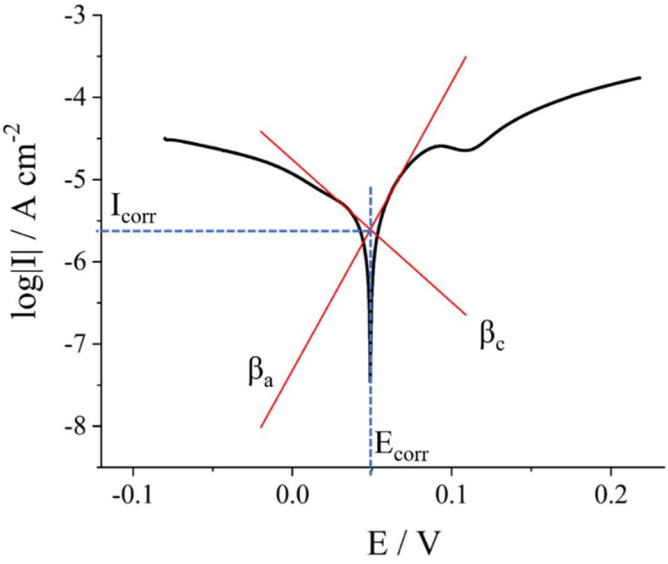

***Figure 3.6**: Potentiodynamic curve (log|I| vs E) experimentally obtained, showing the extrapolation of the corrosion current density (I_{corr}), the corrosion potential (E_{corr}) and the Tafel coefficients for the anodic and cathodic reactions (β_a and β_c).*

3.6. Scanning Probes Microscopies

The introduction of Scanning Probe Microscopies (SPMs) helped gaining and widening the knowledge of local structure and reactivity of surfaces and interfaces. These techniques, developed during the 1980s, use the response of a micro- or nano-probe, while scanned close to or in contact with a surface, to create an image of the topography or some other property of

interest. The family of SPMs includes Scanning Tunneling Microscopy (STM), Atomic Force Microscopy (AFM), Scanning Electrochemical Microscopy (SECM) and Microcapillary (MC). In view of the aims of the present thesis, the theory further presented will be limited to the SECM and MC techniques.

As concerns the SECM technique, the tip is a microelectrode and the tip signal is usually a Faradaic current resulting from oxidation/reduction of species in solution; in some cases, SECM experiments use an ion-selective electrode as tip. Since the performance of a variety of biological and nanotechnological systems is based on electrochemical processes, SECM represents a powerful technique for their full characterization. A further positive aspect of SECM compared with other SPMs is the availability of well-developed quantitative theory.

Microcapillary techniques (MCs) have been introduced, recently, for high-resolution imaging of conducting surfaces, microfabrication and to perform micro- and nano-electrochemistry onto a variety of substrate materials. In MCs, the probe is a laser pulled glass pipette or theta pipette, which is filled with an electrolyte solution, which forms a meniscus at the pipette extremity. As regards single barrelled micropipette, a two-electrode electrochemical cell can be formed by a pseudo-reference/counter electrode, which is immersed in the solution within the pipette, and a working electrode made by the small portion of the substrate that touch the electrolyte solution[62,63].

[62] C. Kranz, *Analyst* (**2014**), 139, 336-352.
[63] N. Ebejer, A. G. Guell, S. C. S. Lai, K. McKelvey, M. E. Snowden, P. R. Unwin, *Annu. Rev. Anal. Chem.* (**2013**), 6, 329-351.

3.6.1. Scanning Electrochemical Microscopy

Historically, the concept of localized electrochemical study took place already since the 1940s, thanks to the pioneer work of Evans[64]. His first experiments concerned potentiometric measurements for probing corrosion processes[67], while Davies [65] recorded amperometric responses in animal biological tissues. During the 1980s the concept of localized analysis was developed by Engstrom and coworkers[66,67,68], who examined, by the use of a microelectrode, the properties of the diffusion layer of a larger active electrode. Few years later, in 1989, Bard and colleagues described the use of a microelectrode tip held by a three-dimensional micro-positioning system. Since then, the term "scanning electrochemical microscopy" has taken hold, and series of papers have been published on principles[69,70], theory and applications[71] of SECM, which have provided the foundations for many of the subsequent development in this field. To provide some examples, SECM has been applied to fundamental electrochemistry, bioanalytical electrochemistry, catalyst screening, corrosion studies, molecular transport, surface patterning and modification[72,73] in direct mode[74,75] and in feedback mode [76,77] (*vide infra*). SECM has been used to investigate electron transfer kinetics at solid/liquid interfaces[78,79], to detect and image areas with different catalytic activities[80,81]. In the latter topic, most of the published articles

[64] U. R. Evans, *Journal of the Iron and Steel Institute* (**1940**), 141, 219–234.
[65] P. W. Davies, F. J. Brink, *Review of Scientific Instruments* (**1942**), 13, 524–533.
[66] R. C. Engstrom, M. Weber, D. J. Wunder, R. Burgess, S. Winquist, *Anal. Chem.* **1986**, 58, 844–848.
[67] R. C. Engstrom, T. Meaney, R. Tople, R. M. Wightman, *Anal. Chem.* (**1987**), 59, 2005–2010.
[68] R. C. Engstrom, R. M. Wightman, E. W. Kristensen, *Anal. Chem.* (**1988**), 60, 652–656.
[69] A. J. Bard, F. R. F. Fan, J. Kwak, O. Lev, *Anal. Chem.* (**1989**), 61, 132–138.
[70] A. J. Bard, M. V. Mirkin, Scanning Electrochemical Microscopy, Marcel Dekker, Inc, New York, (**2001**).
[71] J. Kwak, A. J. Bard, *Anal. Chem.* **1989**, 61, 1794–1799.
[72] S. M. Oja, M. Wood, B. Zhang, *Anal. Chem.* (**2013**), 85, 473-486.
[73] D. Battistel, S. Daniele, D. Fratter, *Electrochim. Acta* (**2012**), 78, 557-562.
[74] L. Stratmann, J. Clausmeyer, W. Schuhmann, *ChemPhysChem* (**2015**),16, 3477–3482.
[75] J. Claumeyer, J. Henig, W. Schuhmann, N. Plumeré, *ChemPhysChem* (**2014**), 15, 151-156.
[76] Y. Kanno, K. Ino, K. V. Inoue, M. Sen. A. Suda, R. Kunikata, M. Matsudaira, H. Abe, C.-Z. Li, H. Shiku, T. Matsue, *J. Electroanal. Chem* (**2015**), 741, 109-113.
[77] X. Wang, Y. Xia, Y. Zhan, L. Nie, F. Cao, J. Zhang, C. Cao, *Acta Metall. Sinica* (**2015**), 51, 631-640.
[78] R. M. Penner, M. J. Heben, T. L. Longin, N. S. Lewis, *Science* (**1990**), 250, 1118-1121.
[79] Y. Wang, J. Velmurugan, M. V. Mirkin, *Isr. J. Chem.* (**2010**), 50, 291-305.
[80] J. Zhou, Y Zu, A. J. Bard, *J. Electroanal. Chem.* (**2000**), 491, 22-29.
[81] S. Jayaraman, A. C. Hillier, *J. Combinat. Chem.* (**2004**), 6, 27-31.

concerned the hydrogen oxidation and the oxygen reduction processes, which are of great importance for fuel cells, bio-fuel cells and air batteries applications[82,83].

The growing interest on SECM is therefore due to the wide spectrum of systems that can be investigated and the information that can be acquired.

3.6.1.1. SECM set-up

Figure 3.13 shows the scheme of a typical SECM experimental set-up. It consists of an electrochemical cell equipped with three electrodes (microelectrode, ME, counter electrode, CE, and reference electrode, RE), a bipotentiostat for the potential control (*versus* the reference electrode) applied to the microelectrode (working electrode) and/or to the substrate, if it is a conductor, and a micropositioner. The investigated substrate is typically placed at the bottom of the cell and the electrolyte solution contains the so-called redox mediator, *i.e.*, an electroactive specie of known electrochemistry, whose response at the microelectrode allows characterizing the substrate properties.

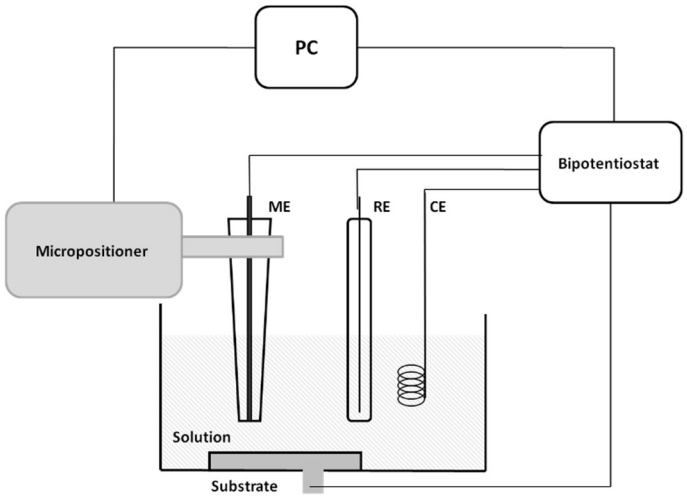

Figure 3.13: *Scheme of a typical SECM set-up.*

[82] F. Li, I. Ciani, P. Bertoncello, P. R. Unwin, J. J. Zhao, C. R. Bradbury, D. J. Fermin, *J. Phys. Chem. C* (**2008**), 112, 9686-9694.
[83] J. W. Lee, H. C. Ye, S. L. Pan, A. J. Bard, *Anal. Chem.* (**2008**), 80, 7445-7450.

3.6.1.2. Operation Modes

There are several operation modes of SECM, and their classification can be based either on the way the tip is moved/kept above the sample or on the interaction of the redox mediator with both the microelectrode and the substrate[70]. In what follows, SECM modes employed in the present thesis are briefly illustrated.

In the *feedback mode* the microelectrode can be approached forward and backward perpendicularly to the sample surface (along the *z* direction), see Figure 3.14. In this way, it is possible to investigate the features of the sample surface by measuring the current variations and obtaining the so-called approach curves[70].

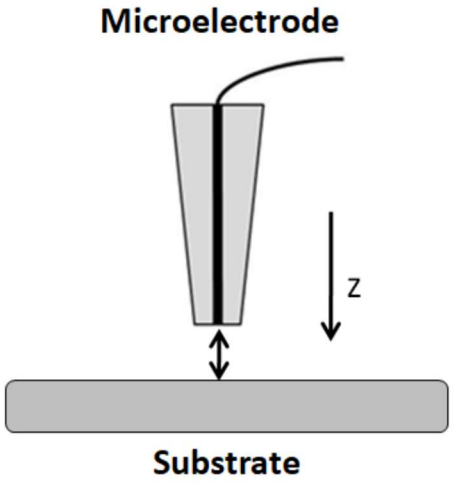

Figure 3.14: *Scheme of the microelectrode when approached to the substrate along the z direction in feedback mode.*

In the *scanning mode* the microelectrode is placed at a fixed distance (along the *z* direction) above the sample and it is displaced parallel to the surface in one and/or two directions (*x* and/or *y*) along the surface (Figure 3.15). The registered current plotted *versus* the spatial coordinates allows imaging the investigated surface in terms of either topography and/or chemical reactivity.

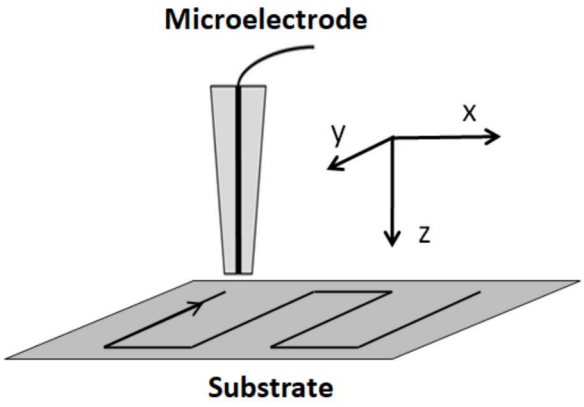

Figure 3.15: *Scheme of the microelectrode when displace over the substrate along the x and y z directions in scanning mode.*

In the feedback mode, the microelectrode act as working electrode in an electrochemical cell containing a solution of the redox mediator. The tip is displaced along the *z* direction perpendicular to the substrate and the response is recorded as a function of the tip-substrate distance. Let us suppose that the redox mediator is a reducible species *O*. If a sufficiently negative potential is applied to a microdisk electrode of radius *a*, the reduction of *O* occurs at a rate governed by the diffusion of *O* to the microelectrode and the species *R* is generated. When the microelectrode tip is in the bulk of the solution, *i.e.,* positioned far away from the target substrate (usually at a distance $d > 10a$, where *d* is the tip-substrate distance, as depicted in Fig. 3.16a), it behaves as a conventional microelectrode.

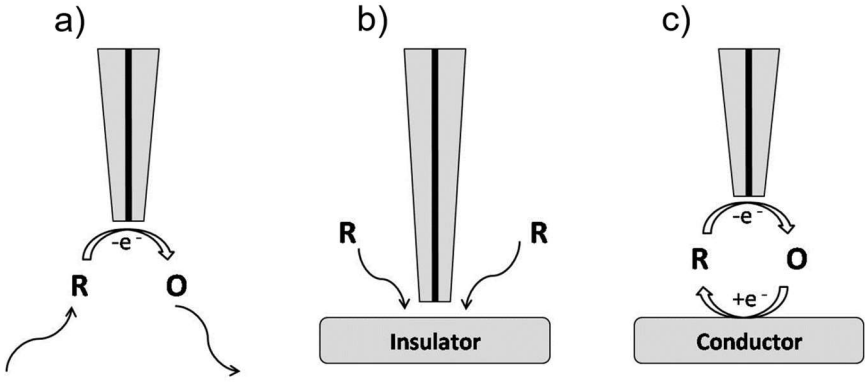

Figure 3.16: *Feedback mode: a) the microelectrode tip is in the bulk of the solution containing the redox reducible mediator O which generates R at the set potential; b) Negative feedback condition; c) Positive feedback condition.*

In this situation, a steady-state current, i_{ss}, is rapidly established due to hemispherical diffusion of the target species, *O*. As the tip is brought close to the substrate, it is possible to differentiate between two feedback effects, depending on the nature of the substrate itself. Considering a substrate inert to species involved in the electrode process (such as an insulating substrate), the diffusion to the microelectrode becomes hindered (Fig. 3.16b), and the registered current, *i*, decreases compared to i_{ss}. Indeed, the closer is the tip to the substrate, the smaller will be *i*. This effect is called *negative feedback*. When the tip approaches a conductive substrate, the *R* species diffuses to the substrate where it may be oxidized back to *O* (Fig. 3.16c) by an electrochemical, chemical or enzymatic reaction. This process generates an additional flux of *O* to the microelectrode tip and, hence, the recorded current increases compared to i_{ss}. The smaller the tip-substrate distance, the larger is *i*. In fact, when the electrode process is rapid, $\boldsymbol{i \rightarrow \infty}$ as $\boldsymbol{d \rightarrow 0}$. This effect is called *positive feedback*.

The feedback effects are displayed by plotting the normalized current i/i_{ss} versus the normalized tip-substrate distance *d/a*. These plots are called *approach curves* and allow the identification of the microelectrode position with respect to the sample surface under investigation. Theoretical approach curves have been derived for several electrode geometries.

To derive the normalized steady-state tip current, also labelled as *i(L)*, for disk-shaped microelectrodes, as a function of normalized tip-substrate distance, $L = d/a$, numerical approaches have been employed[70]. In particular, digital simulation procedures have been considered. From these methods, approximate analytical equations were derived, which are simpler to use from a practical point of view[84].

For a microdisk, Equation (3.27) describes the negative feedback approach curves:

$$\boldsymbol{i(L) = \frac{i}{i_\infty} = \frac{1}{K_1^N + K_2^N/L + K_3^N \, exp(K_4^N/L)}} \qquad (3.27)$$

[84] M. V. Mirkin, F. R. F. Fan, A. J. Bard, *J. Electroanal. Chem.* (**1992**) 328, 47-62.

where K_1^N, K_2^N, K_3^N and K_4^N are constants depending on the *RG* parameter as reported in Table 3.2. The *RG* parameter is defined as the ratio between the overall tip radius to the electrode radius.

***Table 3.2**: K_1^N, K_2^N, K_3^N and K_4^N values for negative feedback approach curves as a function of RG.*

RG	K_1^N	K_2^N	K_3^N	K_4^N
1002	0.132	3.371	0.821	-2.347
100	0.279	3.054	0.686	-2.759
50.9	0.305	2.62	0.667	-2.669
20.1	0.355	2.025	0.628	-2.556
15.2	0.373	1.851	0.613	-2.495
10.2	0.404	1.601	0.588	-2.372
8.13	0.426	1.46	0.568	-2.285
5.09	0.486	1.177	0.512	-2.078
3.04	0.604	0.86	0.395	-1.894
2.03	0.761	0.609	0.238	-2.032

The resulting approach curves have the shape shown in Figure 3.17.

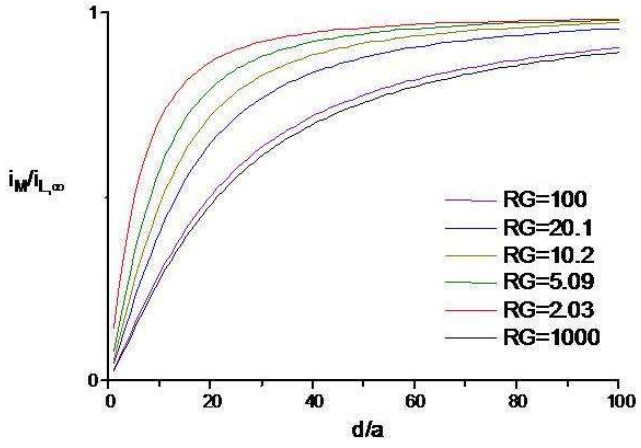

***Figure 3.17**: Theoretical negative feedback approach curves for different RG values.*

From the curves depicted in Figure 3.17 it can be observed that for large L values (*i.e.*, long distances microelectrode/substrate), RG has no influence; this is evident from the relatively low slope of the curves for a certain L value. For small L values, the slope is affected by RG and, in particular, it becomes higher as RG decreases. This indicates a higher sensitivity of the probe in the z direction.

For a microdisk, Equation (3.28) describes the positive feedback approach curves:

$$\boldsymbol{i(L) = K_1^P + \frac{K_2^P}{L} + K_3^P\, exp\left(-K_4^P/L\right)} \qquad (3.28)$$

where K_1^P, K_2^P, K_3^P and K_4^P are constants depending on RG, as reported in Table 3.3.

***Table 3.3**: K_1^P, K_2^P, K_3^P, K_4^P values for positive feedback approach curves as a function of RG.*

RG	$\boldsymbol{K_1^P}$	$\boldsymbol{K_2^P}$	$\boldsymbol{K_3^P}$	$\boldsymbol{K_4^P}$
1002	0.7314	0.77957	0.26298	-1.2907
10.2	0.72627	0.76651	0.26015	-1.41332
5.1	0.72035	0.75128	0.26651	-1.62091
1.51	0.63349	0.67476	0.36509	-1.42897

The resulting approach curves have the shape shown in Fig. 3.18.

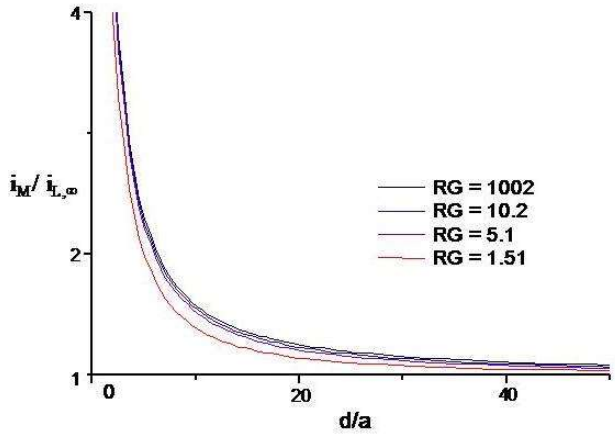

***Figure 3.18**: Theoretical approach curves in positive feedback conditions obtained for different RG values.*

In this case, the *RG* parameter is less influent in determining the shape of the approach curve respect to the negative approach curves. Indeed, either for large or small *L* values, the responses of the working electrode are**,** respectively, slight or much influenced by the presence of the substrate, regardless of the *RG* value. The approach curves are extremely useful from a practical point of view because of the association of each normalized current value with a distance electrode/substrate[85,86]. Therefore, knowing the experimental current and the electrode radius it is possible to determine the distance electrode/substrate by graphic interpolation or exploiting the Equations (3.27) and (3.28).

3.6.2. Microcapillary Techniques

Microcapillary-based techniques have been employed to probe the electrochemistry of small areas of macroscopic surfaces[87,88]. These techniques have enabled to perform individual

[85] I. Ciani, S. Daniele, *Anal. Chem.* (**2004**), 76, 6575-6581.
[86] S. Daniele, I. Ciani, D. Battistel, *Anal. Chem.* (**2008**), 80, 253-259.
[87] C. G. Williams, M. A. Edwards, A. L. Colley, J. V. Macpherson, P. R. Unwin, *Anal. Chem.* (**2009**) 81, 2486-2495.
[88] D. Battistel, G. Pecchielan, S. Daniele, *ChemElectroChem.* (**2014**) 1, 140-146.

measurements at specific surface locations and, initially, have been applied to investigate corrosion or passivation processes on metallic surfaces. Innovation of the techniques has led to scanning microcapillary techniques, which have allowed high-resolution imaging of conducting surfaces, and microfabrication, to perform micro- and nano-electrochemistry onto a variety of substrates materials[89,90].

Micropipettes and nanopipettes have also been exploited as SECM probes to examine chemical and redox phenomena occurring at liquid/liquid interfaces of immiscible solvents. With this setup it was possible to probe electron-transfer and ion-transfer processes across the liquid phase boundary. In these experiments, usually, the pipette was filled with an organic solvent immiscible with the outer aqueous solution; the liquid/liquid interface is formed at the tip extremity. Single-phase experiments, in which the same solvent is used inside and outside the pipette, have been performed in Scanning Ion Conductance Microscopy, (SICM)[91,92]. SICM has recently gained significant attention due to the high-resolution non-contact imaging of biological samples like living cells[62]. By integrating SICM with SECM, it was possible deconvoluting responses related to topography and chemical activity of surfaces[93].

3.6.2.1. Microcapillary systems and methods

In all microcapillary methods the probe is a glass laser-pulled pipette (single channel) or a theta pipette (double channel), which is filled with an electrolyte liquid solution; it usually

[89] P. V. Dudin, P. R. Unwin. J. V. Macpherson, *J. Phys. Chem. C* (**2010**) 114, 13241-13248.
[90] C. Laslau, D.E. Williams, B. Kannan, J. Travas-Sejdic, *Adv. Funct. Mater.* (**2011**) 21, 4607-4616.
[91] P.K. Hansma, B. Drake, O. Marti, S.A.C. Gould, C.B. Prater, *Science* (**1989**) 243, 641-643.
[92] P. Novak, C. Li, A.I. Shevchuk, R. Stepanyan, M. Caldwell, S. Hughes, T.G. Smart, J. Gorelik, V.P. Ostanin, M.J. Lab, G.W. J. Moss, G.I. Frolenkov, D. Klenermann, Y.E. Korchev, *Nat. Methods* (**2009**) 6, 279-281.
[93] D.J. Comstock, J. W. Elam, M.J. Pellin, M.C. Hersam, *Anal. Chem.* (**2010**) 82, 1270-1276.

contains a redox mediator, and forms a thin meniscus at one of the pipette extremities, as shown in Figure 3.19 a,b.

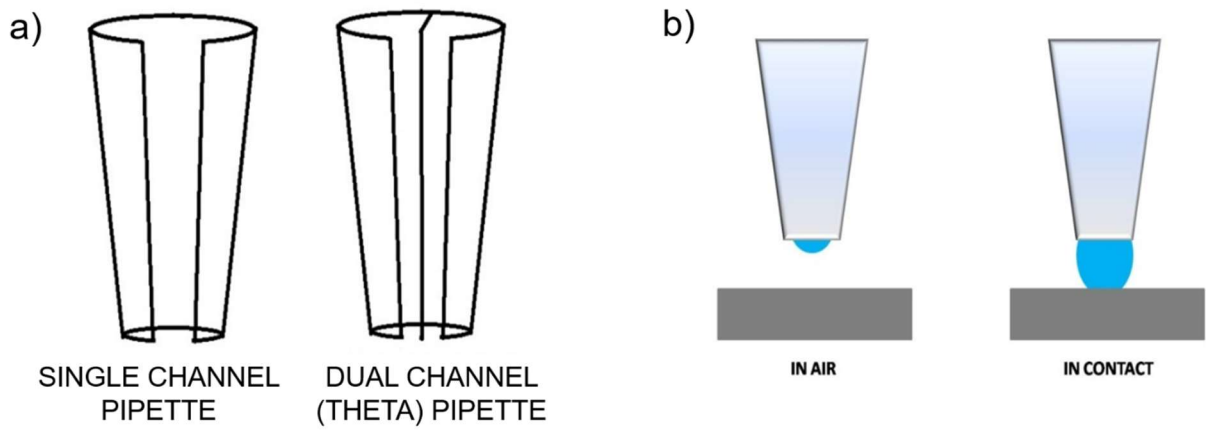

***Figure 3.19**: a) Single channel (left) and double/theta channel (right) pipette. b) Detail of the meniscus when it is in air and in contact with the substrate.*

A two-electrode micro-electrochemical cell is exploited when using a single channel pipette. The pseudo-reference/counter electrode (PRCE) is immersed in the solution within the pipette, while the working electrode is made by the small portion of the substrate touched by the meniscus (Fig. 3.20a). The use of a theta pipette allows obtaining more complex cell systems with multifunction properties (Fig. 3.20b). Pipette-based electrochemical methods were originally developed for high-resolution corrosion studies, which required to confine measurements to a small area. The scheme of the evolution of the set-up for microcapillary techniques and its working principles are presented in Fig. 3.20a,b,c

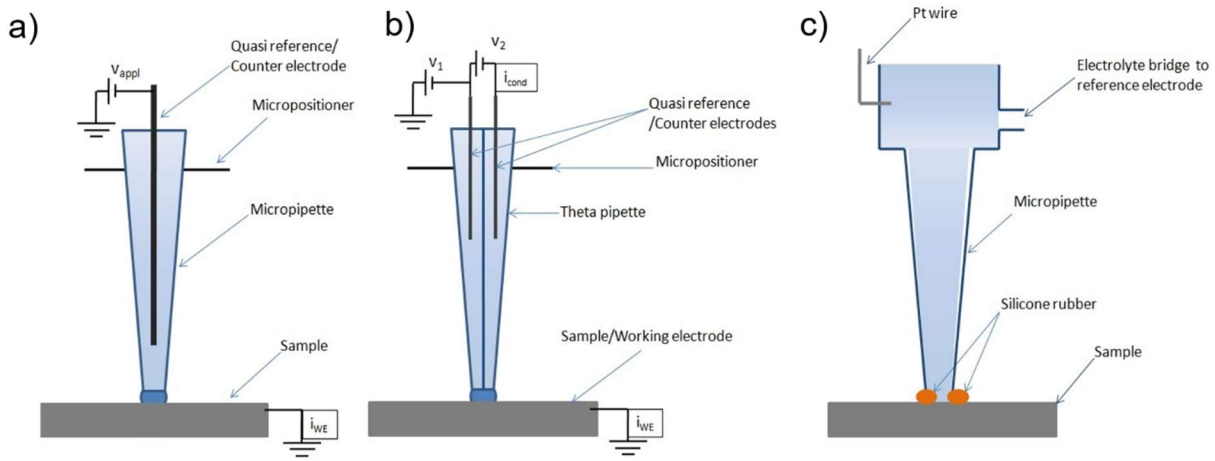

***Figure 3.20**: a) Scheme of the scanning microcapillary technique; b) scheme of scanning electrochemical cell microscopy; c) scheme of the microcapillary technique using a silicone rubber gasket to define the contact area.*

The first set-up employed (Fig. 3.20a,c) is a single-channel pipette probe with a diameter between 100 and 1000 µm, with the end coated with a thick silicone rubber gasket to prevent (solvent) evaporation and to define the electrode area[94,95]. The pipette was mounted on a micro-positioner system, which allowed its easy and precise positioning on the surface. This set-up allowed the electrochemical investigation of localized pitting sites on stainless steel [96,97].

Subsequently, a flow-through microcell reactor was developed for collecting products of reactions carried out at large current densities for off-line analysis of reactions[98]. For this purpose, a dual-channel (theta) capillary, defined by a silicone rubber gasket, was used (Fig. 3.20b). The electrolyte flow was achieved via an external pump, and this approach has been used for metal dissolution and corrosion studies[99,100,101].

[94] M.M. Lohrengel, A. Moehring, M. Pilaski, *Fresenius' J. Anal. Chem.* (**2000**) 367, 334-339.
[95] M M. Lohrengel, A. Moehring, M. Pilaski, *Electrochim. Acta* (**2001**) 47, 137-141.
[96] J.V. Macpherson, P.R. Unwin, *Anal. Chem.* (**2000**) 72, 276-285.
[97] J.V. Macpherson, P.R. Unwin, *Anal. Chem.* (**2001**) 73, 550-557
[98] M. M. Lohrengel, C. Rosenkranz, I Klüppel, A. Moehring, H. Bettermann, B. Van den Bossche, J. Deconink, *Electrochim. Acta* (**2004**) 49, 2863-2870.
[99] S.O. Klemm, J.-C. Schauer, B. Schuhmacher, A. W. Hassel, *Electrochim. Acta* (**2011**) 56, 9627-9636.
[100] S.O. Klemm, J.-C. Schauer, B. Schuhmacher, A. W. Hassel, *Electrochim. Acta* (**2011**) 56, 4315-4321.
[101] S.O. Klemm, S.E. Pust, A.W. Hassel, J. Hüpkes, K.J.J. Mayrhofer, *J. Solid State Electrochem.* (**2012**) 16, 283-290.

The microcapillary electrochemical method has been employed for a variety of applications such as to control the microfabrication of crystal of iron hexacyanides[102,103,104], to investigate the electroactivity of basal plane of highly oriented pyrolitic graphite and aluminum alloy[71], to probe the electrochemistry of individual single-walled carbon nanotubes[87,88], to deposit nanoparticles on nanostructured substrates[105], to explore passive oxide breakdown and pit initiation on Al (111) thin films[106,107], to investigate single metallurgic sites[108] and to understand the behavior of metallic phases and non-metallic heterogeneities in alloys[109].

An innovation of MC is the Scanning Micropipette Contact Method (SMCM, Fig. 3.20b), where micropipette is positioned and displaced over the sample surface. Positioning is achieved by the current spike registered upon the contact between the sample surface and the liquid meniscus. An imaging can be constructed via point-by-point measurements, while the pipette is retracted and then re-approached for the next measurements. More recently, the basic principle described above was extended to the use of double-barrel pipettes fabricated from theta capillaries (Figure 3.18b and 3.20b). In contrast to the single barrel approach, a voltage may be applied between the two reference electrodes, which leads to migration of ions across the meniscus between the two barrels. Again, if the dual-barrel pipette is moved towards the sample surface the meniscus at the end of the barrels comes into contact, while changes the measured ion current. With this approach multiple and simultaneously information on topography, electroactivity and conductivity can be obtained[63].

[102] T.M. Day, P.R. Unwin, J. V. Macppherson, *Nano Lett.* (**2006**) 7, 51-57.
[103] P.V. Dudin, M.E. Snowden, J. V. Macpherson, P. R. Unwin, *ACS Nano* (**2011**) 5, 10017-10025.
[104] D. Yang, L. Han, Y. Yang, L.-B. Zhao, C. Zong, Y.-F. Huang, D. Zhan, Z.-Q. Tian, *Angew. Chem.* (**2011**) 123, 8838-8841.
[105] S.X. Chen, K. Eckhard, M. Zhou, M. Bron, W. Schuhmann, *Anal. Chem.* (**2009**) 81, 7597-7603.
[106] K.R. Zavadil, *ECS Transactions* (**2012**) 41, 133-142.
[107] V. Vignal, H. Krawiec, O. Heintz, R. Oltra, *Electrochim. Acta* (**2007**) 52, 4994-5001.
[108] H. Krawiec, V. Vignal, R. Akid, *Electrochim. Acta* (**2008**) 53, 5252-5259.
[109] H.Y. Ha, C.J. Park, H.S. Kwon, *Corrosion Science* (**2007**) 49, 1266-1275.

The resolution of microcapillary methods depends on the size of the pulled pipette extremity, and the meniscus produced on the substrate surface[110]. The contact radius may vary by up to 10-20% of the pipettes radius, according to the local wetting properties of the substrate[63].

[110] Y.H. Shao, M.V. Mirkin, *Anal. Chem.* (**1998**) 70, 3155-3161.

Chapter 4: Experimental

4. Experimental

4.1. Chemicals

All chemicals were of reagent-grade and used as received. Absolute ethanol ≥ 99.8% was provided by Fisher Scientific, decanoic acid ($CH_3(CH_2)_8COOH$ – HC10, (99%), benzotriazole (BTA, 99%), sodium decanoate ($CH_3(CH_2)_8COONa$ (NaC10, ≥ 98%), acetic acid (CH_3COOH – HAc, ≥ 99.8%), hexaammine ruthenium (III) trichloride ($Ru(NH_3)_6Cl_3$), potassium hexachloroiridate (III) (K_3IrCl_6), potassium chloride (KCl), potassium bromide (KBr), sodium sulfate (Na_2SO_4), copper (II) sulphate ($CuSO_4$), formaldehyde (CH_2O, 37%), disodium carbonate (Na_2CO_3), agarose powder (99%), acetonitrile (anhydrous, 99.9%), tetrabutylammonium hexafluorophosphate ($TBAPF_6$), ferrocene (Fc), (*S*)-(-), (*R*)-(+) and racemate of *N*,*N*-dimethyl-1-ferrocenylethylamine (FcEA) ((*S*)-FcEA, (*R*)-FcEA and *rac*-FcEA), potassium ferro- and ferri-cyanide ($K_4[Fe(CN)_6]$, $K_3[Fe(CN)_6]$) were provided by Aldrich (St. Louis, MO, USA). (Ferrocenylmethyl) trimethylammonium hexafluorophosphate (FA^+) was prepared following the procedure available in the literature[1]. The acetic acid/sodium acetate buffer at pH 4.75 was prepared by using reagents provided by Probus (Barcelona, Spain). Silver nitrate ($AgNO_3$) 0.1 N standard solution were from Vetrotecnica s.r.l. (Padua, Italy). The monomer (*S*)-2,2'-bis(2,2'-bithiophene-5-yl)-3,3'-bibenzothiophene ((*S*)-BT_2T_4) was kindly provided by Prof. Tiziana Benincori (Univensity of Insubria). The synthesis and purification of (*S*)-BT_2T_4 is reported in the literature[2].

[1] M. Silvestrini & P. Ugo, *Anal Bioanal Chem* (**2013**) 405:995–1005.
[2] F. Sannicolò, S. Arnaboldi, T. Benincori, V. Bonometti, R. Cirilli, L. Dunsch, W. Kutner, G. Longhi, P.R. Mussini, M. Panigati, M. Pierini, S. Rizzo, *Angew. Chem. Int. Ed*. (**2014**), 53, 2623-2627.

All the solutions were prepared by using Milli-Q water (Millipore System, Darmstadt, Germany). Nitrogen stream (99. 99% from SIAD, Bergamo, Italy) was used to deoxygenate the electrochemical cell.

When it was required, the working solutions were purged with a pure nitrogen equilibrated to the vapor pressure of the medium, and then kept under the nitrogen blanket throughout the measurements.

4.2. Copper/Bronze coins samples

A series of 16 copper and bronze coins produced between 1709 and 1962 in Belgium, France, Malta, Portugal, Spain, and Swiss were kindly issued from the private collection of Doménech-Francés, (Valencia, Spain). The numismatic characteristics of the coins are summarized in Appendix A1, Table A.1.

4.3. Base electrolyte in the voltammetric study of Cu^{2+} and HC10 in the hydroalcoholic medium

For the study of the voltammetric behavior of Cu^{2+} in the absence and presence of HC10, the base electrolyte was made of 50% (v/v) Ethanol/Water (E/W) mixture and 0.05 M Na_2SO_4 as supporting electrolyte. Stock solutions of 0.1 M $CuSO_4$ and 0.1 M HC10 were prepared in Milli-Q water and pure ethanol, respectively. Proper amounts of these solutions were added directly in the electrochemical cell to achieve the desired concentrations. When necessary, current responses were corrected for dilution effects.

4.4. Preparation of bare and naturally corroded copper samples

Bare copper samples (about 1×1 cm^2) were obtained by cutting 1 mm-thick copper sheet (99% Alfa Aesar). The electric contact was ensured by a tin-welded copper wire. Samples were further embedded in epoxy resin in order to expose only the non-welded side to the solutions. The surface was polished using successive abrasive SiC papers with 500, 800, 1200, 2000 and 4000 grit with a bench-top lapping machine and degreased with ethanol (99% VWR) before each experiment.

Samples of naturally corroded copper having a surface of ca. 1×1 cm^2 were cut from a larger copper plate. The plate originally part of the roof cladding of St. Martin's Church in Metz (France), had undergone long-term (>100 years) atmospheric corrosion. The surface was firstly cleaned with deionized water and dried at ambient conditions to eliminate contamination (dust) and powdery particles.

Each type of sample (bare and naturally corroded) was prepared in triplicate. The side not exposed to the atmosphere was polished using SiC 500 grit paper and an electric contact was created made by tin-soldering a copper wire. The electric contact and the reverse exposed surfaces were finally insulated by using a commercial nail varnish.

4.4.1. Inhibitors treatment conditions

The treatment of both bare and copper roof cladding samples was performed by soaking the samples for 2 hours in the solutions having the composition shown in Table 4.1.

***Table 4.1**: Treatment conditions employed in this study for each type of inhibitor.*

Organic compound	Treatment conditions
Benzotriazole (BTA)	0.25M in 50% E/W solution
Decanoic acid (HC10)	0.17M in 50% E/W solution
Sodium decanoate (NaC10)	0.15M aqueous solution

The concentration of BTA corresponds to the one most in use among conservators[3] (3%w/v in ethanol solution), while for HC10 and NaC10 treatments the concentrations chosen are based on previous studies on the subject[4,5]. The treated samples were air dried for 10-20 minutes prior to analysis.

4.4.2. Preparation of synthetic acid rain

The efficiency of the treatment was evaluated after 24 hours immersion of the samples in a solution mimicking the composition of rain in urban environment[6]. The synthetic acid rain (AR) composition is reported in Table 4.2; the pH of the solution was 3.1.

***Table 4.2**: Composition of the synthetic acid rain employed in this study.*

Compound	Concentration (mM)
H_2SO_4	0.325
HNO_3	0.25
NaCl	1.452
$NaNO_3$	0.25
Na_2SO_4	0.225
$(NH_4)_2SO_4$	0.350

[3] D.A. Scott, Copper and Bronze in Art: Corrosion, Colorants, Conservation, J Paul Getty Museum Pubns (**2002**).
[4] E. Apchain, Apport des traitements carboxylates à la protection des alliages cuivreux, Thèse de doctorat, Matériaux, Université de Cergy Pontoise (UCP) (**2018**).
[5] S. Hollner, F. Mirambet, E. Rocca, and S. Reguer, *Corros. Eng. Sci. Technol*. 45 (**2010**) 362–366.
[6] G. Brunoro, A. Frignani, A. Colledan, and C. Chiavari, *Corros. Sci*. 45 (**2003**) 2219–2231.

4.4.3. Preparation of naturally corroded roof cladding samples in cross sections

Naturally corroded roof cladding samples untreated and treated with HC10 and BTA were first wrapped in a Paraolid B-72 film (provided by Kremer Pigmente, Aichstetten – Germany) to avoid the penetration of the resin inside the corrosion layers. Then, the wrapped samples were embedded in epoxy resin (EpoFix, provided by Struers, Ohio – United States) and let harden for 48 hours. Subsequently, the samples were cut in order to expose their whole stratigraphy. Abrasive SiC papers with increasing grit (500, 800, 1200, 2000 and 4000) were used to polish the cross sections with a bench-top lapping machine. Deionized water was used to remove SiC dust particles.

4.5. Hydrogel preparation

A weighted amount of agarose powder was added in Milli-Q water at room temperature to provide a series of 2% w/v suspensions. The appropriate amounts of the redox probes and KCl or KNO_3, as supporting electrolyte, were then added to obtain the desired hydrogel compositions. The mixtures were slowly heated up to 80 °C in sealed containers to avoid water evaporation. During the heating, the suspensions were gently stirred to avoid the formation of gas bubbles. The mixtures were kept at 80°C until they displayed a clear appearance (Figure 4.1), and afterwards cooled down at room temperature.

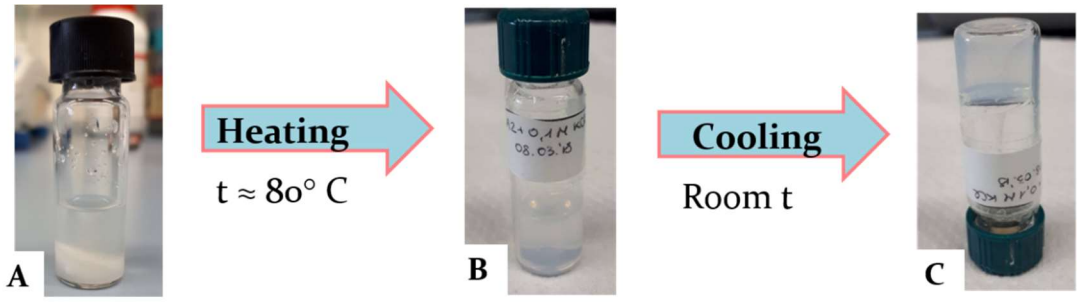

***Figure. 4.1**: Scheme of the hydrogel preparation and photos of the 2% w/v agarose suspension in water (a); after heating at ca. 80°C (b); jellified agarose cooled at room temperature.*

4.6. Apparatus and Instrumentations

4.6.1. Coins surface characterization

The coins surfaces were examined using field emission scanning electron microscopy (Model S-4800, Hitachi Ltd., Tokyo, Japan) operating at 20 kV. The microanalysis of samples was performed with X-ray microanalysis system (SEM/EDX). Secondary electron images of coins were carried out with a Leica M165 stereo microscope using a capture system of high-resolution digital image IC80HD controlled by LAS program.

Sectioning and imaging of trenches of the coins was performed with a FIB-FESEM Zeiss (Orsay Physics Kleindiek Oxford Instruments) model Auriga compact equipment. The operating conditions were: voltage 30 kV, current intensity 500 µA, and current of 20 nA in the FIB for generating the focused beam of Ga ions and a voltage of 3 kV in the FESEM for photographs. X-ray line scans were performed in the trench operating with an Oxford-X Max X-ray microanalysis system coupled to the FESEM controlled by Aztec software. A voltage of 20 kV and a working distance of 6–7 mm was used.

4.6.2. Colorimetric analysis

Considering the relevance of the aesthetic impact of a treatment in the field of conservation, colorimetric analyses were performed on the naturally corroded copper samples by using a portable Minolta CM-2300d spectrophotometer coupled with the SpectraMagic NX software. Reflectance spectra were collected between 360 nm and 740 nm using a standard D65 illuminant at 10° degrees observer angle. An auto average of five flashes on a spot of 8 mm diameter was recorded for each measurement.

4.6.3. Surface morphology examinations

Changes in surface morphology due to the different treatments were evaluated by Optical Microscopy and Scanning Electron Microscopy. Optical observations were made by using an Olympus Light Microscope with 5X, 10X, 20X and 50X magnification lenses in bright field mode.

SEM images were collected with a JEOL JSM-7001F Scanning Electron Microscope. The micrographs were taken using an incident beam of 5 keV at a working distance of 4-6 mm. EDX analysis on the surface is performed in the case of the sample treated with sodium decanoate, using an acceleration voltage of 2 keV at a working distance of 10 mm. A carbon coating was applied prior to the analysis to avoid charging effects.

4.6.4. Contact angle measurements

The change in surface tension of the roof cladding after the treatments with the inhibitors was evaluated by the sessile drop method. For this purpose, a OCA20 Dataphysics Instruments tensiometer equipped with SCA20 software was employed. A drop of 5 µL of distilled water

was placed on the surface and the contact angle value is measured after 10 seconds. An average of 5 drops and standard deviation are reported in the results and discussion section.

4.6.5. μ-Raman spectroscopy

The impact of the inhibitors on the structural composition of the roof claddings' surface was evaluated by performing μ-Raman spectroscopy. Spectra were collected using a Renishaw Invia Reflex spectrometer equipped with a 532nm Nd:YAG laser and CCD detector and coupled with an optical microscope. The spectra were recorded using a 50X objective and a laser power <100 μW on the surface to avoid phase transformation by heating. The spot size examined was of 1 μm diameter and the spectral resolution was 2 cm^{-1}. Spectral calibration was performed by using the main peak of a silicon wafer at 520.5 cm^{-1}. Spectra were processed with the use of Wire 3.4 software and displayed with no baseline correction. Identification of the structure of corresponding phases was based on comparison with synthetic reference compounds or references found in the literature.

4.6.6. Fourier Transform Infrared Spectroscopy (FTIR)

FTIR was employed to examine the sparingly soluble blue product formed in the electrochemical cell during the voltammetric investigation concerning the interaction between Cu^{2+} ions and HC10. The blue precipitate was filtered, rinsed with deionized water, dried at room temperature and then grinded in a mortar together with KBr to form pellets. These were examined by a Perkin-Elmer "Spectrum One" FT-IR Spectrometer (Shelton, CT, USA), equipped with Spectrum software. The spectra were registered with a wavelength resolution of 4 cm^{-1}.

4.7. Electrochemical Measurements

4.7.1. VIMP

Sampling for VIMP measurements was carried out by manually pressing one of the extremities of the graphite electrode bars (Alpino HB, 2.0 mm diameter) onto 3-5 points of the surface of each coin previously selected by the criteria of planarity and color homogeneity. Then, the sample-modified graphite electrode was immersed into the electrolyte (0.25M HAc/NaAc buffer at pH 4.75) and the electrochemical runs were performed by using a CH I660c potentiostat (Cambria Scientific, Llwynhendy, Llanelli UK) coupled to a three-electrode cell with a platinum auxiliary electrode and a Ag/AgCl (3 M NaCl) reference electrode. The measurement of peak current and peak areas was made using the CHI software.

4.7.2. Open circuit potential and Potentiodynamic polarization

Open circuit potential (OCP) and Potentiodynamic polarization (PDP) measurements were performed on the naturally corroded roof cladding samples and, for comparison, on bare copper specimens, either untreated or treated with the various inhibitors. A Bio-Logic Science Instrument potentiostat (Mod. SP-200) controlled by an EC-Lab® software, using an electrochemical cell in a three electrodes configuration was employed. Both bare and naturally corroded samples were used as working electrodes (WEs); a platinum spiral (0.6/250mm) and an Ag|AgCl|KCl (3M) were employed as counter (CE) and reference electrode (RE), respectively. The corrosion tests were performed in the synthetic AR solution (composition reported in Table 4.2). Before PDP measurements, all samples were immersed in the solution in OCP conditions until the potential achieved a constant value (within ± 5 mV). This stage,

typically, required about 1 hour. Potentiodynamic measurements were performed over the range of ±150 mV with respect to OCP, at 1 mV s^{-1}. All tests were performed in aerated solutions without stirring.

4.7.3. Voltammetric study of Cu^{2+} and HC10 in the hydroalcoholic solution

Electrochemical measurements were performed by using a Pt microelectrode (WE) connected to the CHI760B workstation (CH Instruments Inc., Austin, Texas, U.S.A.) controlled with a personal computer via the CHI760b software.

The electrochemical cell was used in the three-electrode configuration, where the reference electrode Ag|AgCl|KCl (KCl, saturated) was separated from the solution by a porous glass frit, containing the same solvent as in the main cell, and a platinum spiral as counter-electrode.

4.7.4. Microelectrodes fabrication and characterization

Platinum microdisk electrodes were prepared by sealing platinum wires of 20 or 25 μm in diameter (Goodfellow, Cambridge, England) within glass capillaries by the use of a P-2000 Laser Puller (Sutter Instrument, Novato, CA, U.S.A). About 1.5 cm of a platinum wire was inserted inside a borosilicate glass capillary, of 0.58 mm (i.d.), 1.0 mm (o.d.) and 10 cm length. The capillary was fixed by the clamps to the laser puller. The protocol for microelectrode fabrication foresees a 40 s heating step (by a CO_2 laser) and a 20 s relaxing step. The parameters set for sealing the platinum wire are summarized in Table 4.3.

***Table 4.3**: Laser puller parameter for sealing platinum wires.*

Parameter	Heat	Filament	Velocity	Delay	Pull
Value	360	5	20	128	0

Heat represents the power of the laser and consequently the amount of energy supplied to the glass; *filament* specifies the scanning pattern of the laser beam (filament = 2 corresponds to 1.9 mm scan length[7]); *velocity* controls the moment when the glass softens and begins to pull apart under a constant load; *pull* controls the force of the hard pull and the higher the pull, the smaller the capillary tip diameter and the longer the taper; *delay* controls the time between the *heat* is turned off and the hard *pull* is activated.

In order to avoid the formation of bubbles, the two ends of the capillary were connected to a vacuum pump, for the entire length of the sealing procedure. The capillary tube, within the melting zone, was cut by a small circular saw, thus obtaining two tips containing the electrode material. The sealing quality and the continuity of the wire were checked by an optical microscope. The electric contact between the platinum fiber and the external circuit was realized with a copper wire soldered by means of indium flakes.

The active surface of the microelectrodes was exposed mechanically by using emery paper (Buehler, Illinois, U.S.A.) of decreasing grain size and alumina suspensions in water of size varying from 1 down to 0.05 μm. The microelectrodes were afterward characterized by cyclic voltammetry (CV) at low scan rates and SECM to evaluate the actual radius of the microelectrodes and the overall tip radius to the electrode radius ratio, RG, respectively, as described below.

[7] P-2000 Laser Puller Guide, Sutter Instruments.

4.7.4.1. Determination of the radius and the RG parameter of the microdisk electrodes

The radius of the platinum microdisk electrodes was determined by recording the steady-state limiting current in water solutions containing, from time to time and depending on the specific study, various redox mediators and using the following equation[8]:

$$I_{ss} = 4\, n\, F\, D\, C^b\, a \qquad (4.1)$$

where n is the number of electrons, F is the Faraday constant, D is the diffusion coefficient of the electroactive species, C^b is the bulk concentration and a is the radius of the microdisk. The steady-state limiting current was obtained from cyclic voltammetry at low scan rates, which provided voltammetric patterns as those displayed in Figures 4.2 and 4.3.

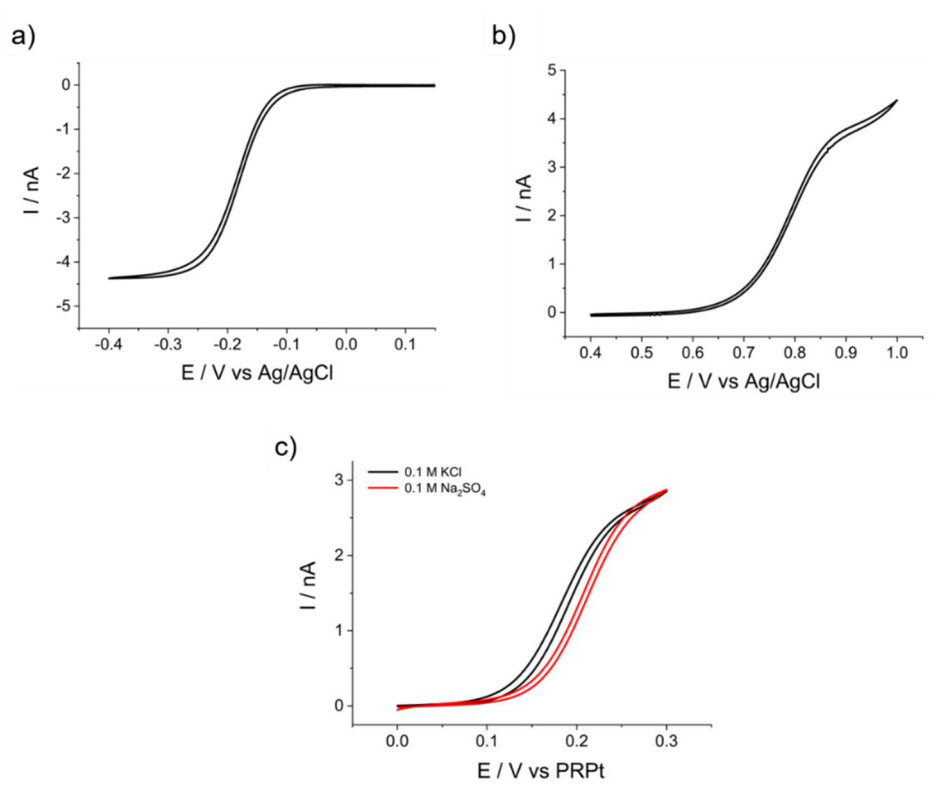

***Figure. 4.2**: CVs recorded at 10 mV s^{-1} in a) 1 mM $Ru(NH_3)_6Cl_3$ + 0.1 M KCl; b) 1 mM K_3IrCl_6 + 0.1 M KNO_3 and c)* 1 mM FA^+ + 0.1 M Na_2SO_4 *(red line) and 1 mM FA^+ + 0.1 M KCl for a laser pulled Pt microdisk electrode.*

[8] Y. Saito, *Rev. Polarogr.* 15 (**1968**) 177–187.

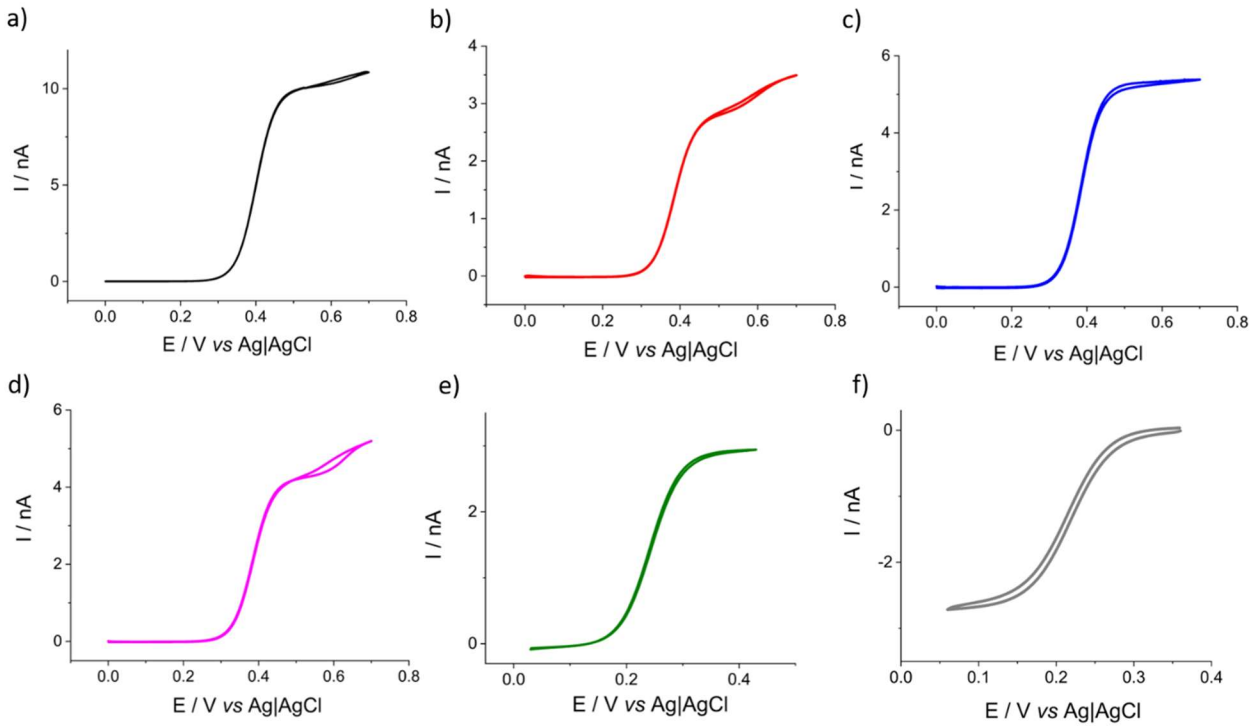

Figure 4.3: *CVs recorded at 5 mV s^{-1} with a Pt microdisk electrode (12.5 µm radius) in the following media: CH_3CN + 0.1 M $TBAPF_6$ solution containing 1 mM Fc (a), 0.6 mM (R)-FcEA (b), 1 mM (S)-FcEA (c), 1 mM rac(±)-FcEA (d) redox mediators; H_20 + 0.1 M KCl solutions containing 1 mM $K_4[FeCN)_6]$ (e), 1 mM $K_3[FeCN)_6]$ (f) redox mediators.*

Table 4.4 reports the half-way potential values ($E_{1/2}$) and diffusion coefficients (D) for each redox mediator measured versus Ag|AgCl and PRPt.

Table 4.4*: Half-wave potentials and diffusion coedìfficients (D) of the redox mediators employed in the SECM measurements versus Ag|AgCl and PRPt.*

Redox couple + supporting electrolyte	***E*$_{1/2}$ *vs* Ag|AgCl / V**	***E*$_{1/2}$ *vs* PRPt / V**	***D* / 10^{-6} cm^2s^{-1}**
$[Ru(NH_3)_6]^{3+}$ / $[Ru(NH_3)_6]^{2+}$	-0.14	-	7.0 [9]
$[IrCl_6]^{3-}$ / $[IrCl_6]^{2-}$	+0.74	-	8.3 [10]

[9] D. Battistel, G. Pecchielan, S. Daniele, *ChemElectroChem*. 1 (**2014**) 140 –146.
[10] J.J. Watkins, H.S. White, *Langmuir* (**2004**), 20, 5474-5483.

FA^{2+}/ FA^{+} + KCl	-	+0.19	5.3 [11]
FA^{2+}/ FA^{+} + Na_2SO_4	-	+0.21	-
Fc^{+}/Fc	+0.400	-	24
R-$FcEA^{+}$/ *R*-FcEA	+0.395	-	12.1
S-$FcEA^{+}$/ *S*-FcEA	+0.390	-	11.5
rac(±)-$FcEA^{+}$/ *rac(±)*-FcEA	+0.395	-	12
$[FeCN)_6]^{3-/4-}$	+0.230	-	6.7

When the microelectrodes were used in SECM measurements the parameter RG of the tips were evaluated by fitting experimental and theoretical approach curves obtained above an insulating (Teflon) substrate and using one or more of the above redox mediators. The SECM tips used in this thesis were characterized by RG values varying between 5 and 10.

4.7.5. Micropipettes fabrication

Micropipettes were pulled from borosilicate capillaries (Sutter) having 1.0 mm (o.d.), 0.58 mm (i.d.) and 150 mm length using the P-2000 Laser Puller system (Sutter Instruments, Novato, U.S.A.). A typical pulling program used in the present work was: *HEAT* = 320, *FILAMENT* = 2, *VELOCITY* = 15, *DELAY* = 128, *PULL* = 100.

After fabrication the pipette was polished flat to reveal openings varying in diameter between 2 and 80 μm. The size of the meniscus generated at the pipette ends were evaluated by cyclic voltammetry (*vide infra*). The pseudo-reference Pt electrode was inserted inside the

[11] E. Coutouli-Argyropoulou, A. Kelaidopoulou, C. Sideris, G. Kokkinidis, (**1999**). *Journal of Electroanalytical Chemistry, 477(2), 130–139.*

microcapillary and then was approached towards the studied substrate surface by a micropositioner. The capillary motion and the meniscus landing were monitored by using an optical microscope. The micropipettes were filled with either the ionic hydrogel or aqueous solutions by capillarity. Contrary to the normal practice [12, 13], the outer walls of the microcapillaries were not silanized.

4.7.6. SECM instrumentation

The SECM apparatus was a CHI920C Scanning Electrochemical Microscope workstation (CH Instruments Inc., Austin, Texas, U.S.A.) The positioner system consisted in a stepper motor combined with a three dimensional closed-loop piezo positioner having the characteristics summarized in Table 4.5:

***Table 4.5**: Micropositioner specifications.*

Parameter	Value
Piezo positional resolution	1.6 nm
Stepper motor resolution	4 nm
X, Y, Z total distance	50 mm

The electrochemical experiments were carried out either in two- or three-electrodes configuration. Typically, in the SECM measurements, the microelectrode tip was a platinum microdisk, while the reference/counter electrodes employed were either a platinum coil or an Ag/AgCl (KCl saturated) electrode, depending on the specific application. Similarly, the SECM cell employed varied upon varying the samples or methods investigated. To avoid external

[12] Y. Shao, M.V. Mirkin, (**1998**) *Anal Chem* 70(15):3155–3161.
[13] J.V. Macpherson, P.R. Unwin, (**1999**) *Anal Chem* 71(20):4642–4648.

interferences, the electrochemical cell or the SECM apparatus was maintained in a Faraday Cage made of aluminum.

Figure 4.4 illustrates the SECM cell used for the investigation of the roof cladding.

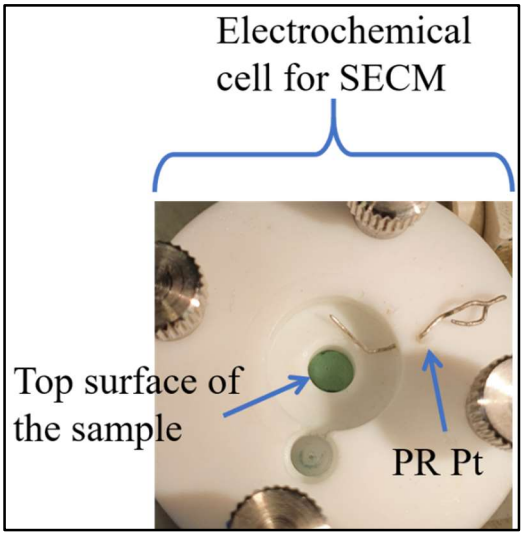

***Figure. 4.4**: Photo of the electrochemical cell used for SECM investigation of the roof cladding samples.*

For the microcapillary experiments, the sample and the micropipette were mounted in a home-made cell as shown in Figure 4.5. The cell was sealed to maintain into the chamber a sufficient level of humidity to prevent solvent evaporation from the thin pipette meniscus. The cell was also equipped with a humidity and temperature sensor to supervise the experimental conditions. A constant flux of humidified nitrogen was injected in the cell to avoid interfering processes due to oxygen, while maintaining the desired humidity level.

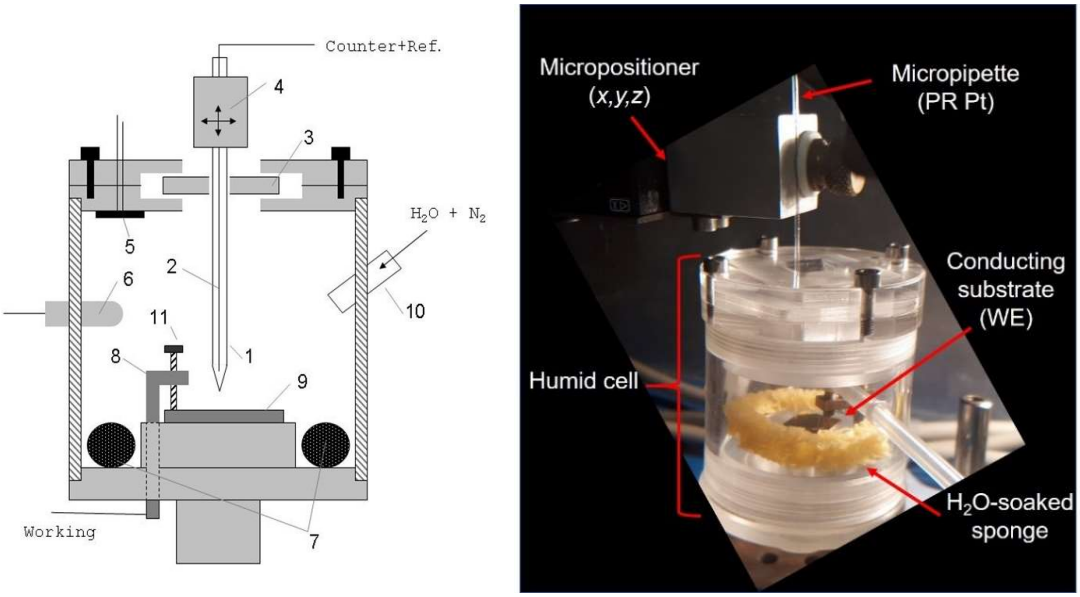

***Figure 4.5**: On the left: schematic representation of the microcapillary cell designed for micropipette experiments in humidity-controlled conditions. 1) Micropipette filled with electrolyte solution; 2) Pt wire (Counter/Quasi reference electrode); 3) mobile plate handling; 4) SECM micropositioning device; 5) humidity sensor; 6) temperature control; 7) water-soaked sponge; 8) external electrical connection; 9) sample under study; 10) air humidified injector; 11) connection screw. On the right: photographic image of the microcapillary cell.*

Results & Discussion

Chapter 5: Dating copper-based coins by multiple-scan voltammetry

5. Dating copper-based coins by multiple-scan voltammetry

A general challenge in studying ancient metals is the achievement of archaeometric information by means of non-destructive techniques applied to the corrosion layers, not only by the intrinsic high value of the artifacts under study but also by the fact that such layers can exert a protective effect over the metallic core[1]. This has motivated the increasingly growing interest in the studies focused on the corrosion of ancient metal objects under different environmental conditions as well as to the effect of the presence of various elements such as Zn, Sn, and Pb[2,3]. Given the variety of corrosion conditions, it is difficult, however, to establish general patterns of long-term aging. Here, the VIMP was applied to study the corrosion layer of copper-based coins in order to determine an in-depth electrochemical profile which would be representative of the composition gradient of the corrosion patina. The method was applied to discriminate a series of 16 copper and bronze coins produced between 1709 and 1962 in Belgium, France, Malta, Portugal, Spain, and Swiss from a private collection (Figure 5.1). The coins, whose numismatic characteristics are summarized in Appendix A1, Table A.1, were always in collection (coll. Doménech-Francés, Valencia, Spain) meaning that they underwent only atmospheric corrosion and/or could have been chemically or mechanically cleaned, being conserved in paper containers. The selection of the coins to be studied was made following two criteria: (i) apparent moderate corrosion with absence of green corrosion products and (ii) variety of provenances and ages. For this reason, the voltammetric responses are dominated by the cuprite signatures which are sensitive to the in-depth variation in the composition, crystallinity, and porosity of this

[1] D.A. Scott. Metallography and Microstructure of Ancient and Historic Metals, The Getty Conservation Institute, Paul Getty Museum, Malibu (**1991**).
[2] C. Chiavari, E. Bernardi, C. Martini, F. Passarini, F. Ospitali, L. Robbiola, *Corrosion Science* (**2010**) 52, 3002–3010.
[3] L. Campanella, O. Colacicchi Alessandri, M. Ferretti, S.H. Plattner, *Corrosion Science* (**2009**) 51, 2183–2191.

component in the patina[4]. The study was complemented and supported by FIB-FESEM and HRFESM-EDX.

***Figure 5.1**: Photographic representation of the 16 copper/bronze coins from the private collection of Doménech-Francés, Valencia, Spain.*

5.1. Samples composition and morphology

The 16 coins, object of this study, were preliminary inspected by visual examination. They presented uniform pale brown to black/brown patinas without green corrosion products,

[4] F. Di Turo, N. Montoya, J. Piquero-Cilla, C. De Vito, F. Coletti, G. Favero, A. Doménech-Carbó, *Analytica Chimica Acta* (**2017**) 955, 36–47

attributable to cuprite-based patinas accompanied by tenorite. This first hypothesis was then completed with HRFESM-EDX analysis of the corrosion patina. Table 5.1 summarizes the elemental components estimated from averaged values measured by HRFESM-EDX, since the direct analysis of the metal bulk implies destructive analysis.

Table 5.1. *Elemental components estimated from values measured by HRFESM-EDX in the corrosion patina of the studied coins.*

Coin	Producer	Date	Cu	Sn	Zn	Pb	Others
M16	Spain	1709	+	–	–	+	–
M14	Malta	1770	+	–	–	+	–
M03	Spain	1798	+	–	–	–	Sb, As
M04	Spain	1803	+	–	–	+	Sb, As
M32	Spain	1840	+	–	–	+	Ag, Sb, As
M20	Spain	1849	+	–	–	–	As
M07	France	1864	+	+	+	–	–
M11	Spain	1868	+	–	–	–	As
M15	Spain	1870	+	+	+	+	As
M13	Portugal	1892	+	+	+	–	–
M12	France	1904	+	+	+	–	–
M06	France	1916	+	+	–	–	–
M08	France	1916	+	+	+	–	–
M30	Spain	1937	+	–	+	–	–
M31	Belgium	1953	+	+	+	–	–
M18	Swiss	1962	+	+	+	–	–

The morphology of the coins was investigated by FIB-FESEM analysis which, in general, show a relatively high variability in the corrosion forms, as illustrated in Figure 5.2. Several coins, such as coin M12 (5cts, Republique Française, 1904), Figure 5.2a, shows an external

uniform layer of 1–2 μm thick, covering the typical faceted internal region. This pattern was observed in the binary bronze coins, the external layer being enriched in Sn relative to the internal, the thickness of the external layer apparently increasing with age, as it can be seen comparing coin M12 with coin M7 (5 cts, Napoleon III, France, 1864) shown in Figure 5.2b. In the case of coin M18 (1 rappen, Swiss, 1962), Figure 5.2c, the trenches show fractures in the external layer of 3–4 μm thick which is followed by a fine layer ca. (0.5 μm thick) placed over the internal faceted region. This coin was constituted by a ternary Cu-Sn-Zn bronze, and the intermediate layer was considerably enriched in Sn, thus suggesting the possibility of a cassiterite-based layer, while the internal region is enriched in Zn, in agreement with the inhibiting effect of tin in the dezincification of brass described for archeological coins by Campanella et al.[3] The oldest coins presented a complex corrosion pattern with fractures crossing the external layer of thickness varying between 5 and 7 μm in the case of coin M3 (4 maravedís, Carolus IV, Spain, 1798) shown in Fig. 5.2d.

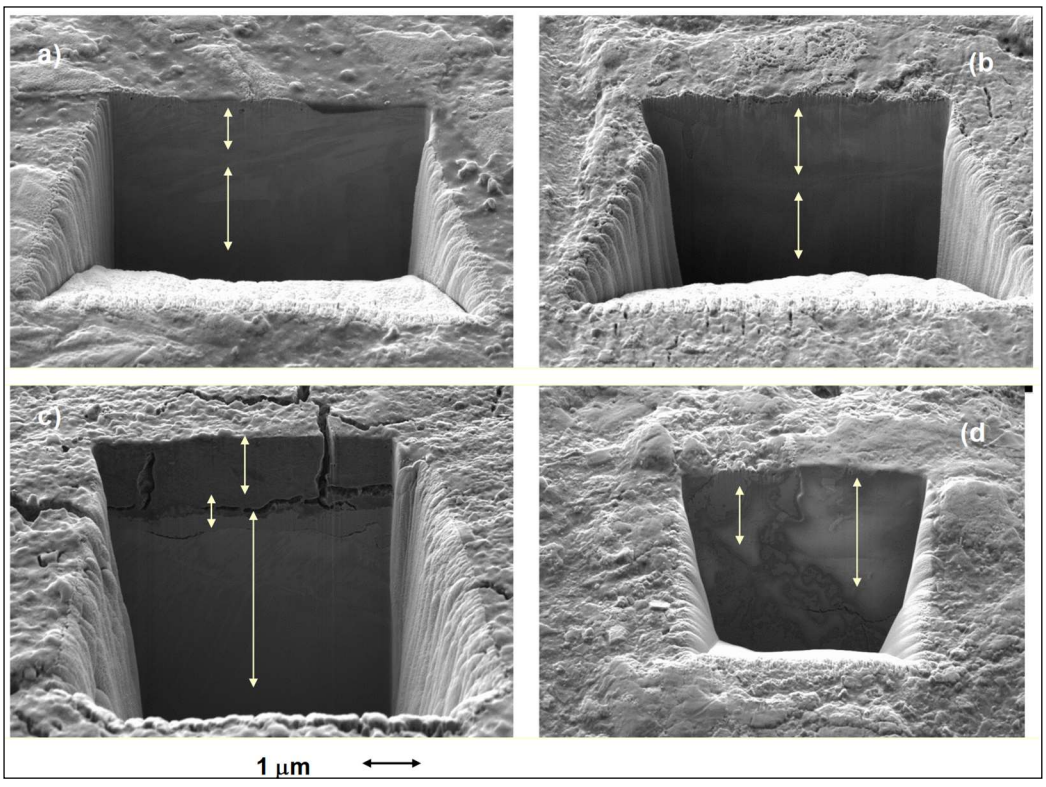

***Figure 5.2**: FIB-FESEM images of trenches on coins: a) M12 (5cts, Republique Françaice, 1904); b) M7 (5 cts, Napoleon III, France, 1864); c) M18 (1 rappen, Swiss, 1962); d) M3 (4 maravedís, Carolus IV, Spain, 1798).*

5.2. Electrochemical features

Voltammetric pattern of Figure 5.3 were obtained superimposing the square wave voltammograms (SWVs) successively registered on material sampled from a spot of coin M08 (10 cts Republique Française, 1916) attached to the graphite electrode in contact with 0.25 M HAc/NaAc aqueous solution at pH 4.75. The first to sixth scans (successively recorded) are depicted for both the negative-going and positive-going scans (Figure 5.3a and b respectively). In the SWVs initiated at +0.45 V in the negative direction, a cathodic peak appears at −0.15 V vs. Ag/AgCl (C_1) whose profile looks like the superposition of two or three highly overlapping waves at peak potentials of ca. −0.05, −0.15, and −0.22 V (C_{1a}, C_{1b}, and C_{1c}, respectively). Forward and backward SWV components display different profiles, as shown in Figure 5.4, thus suggesting that different voltammetric processes are superimposed (notice that the relative shift of forward and backward SWV components can often produce shoulders in the net component erroneously suggesting multiple processes).

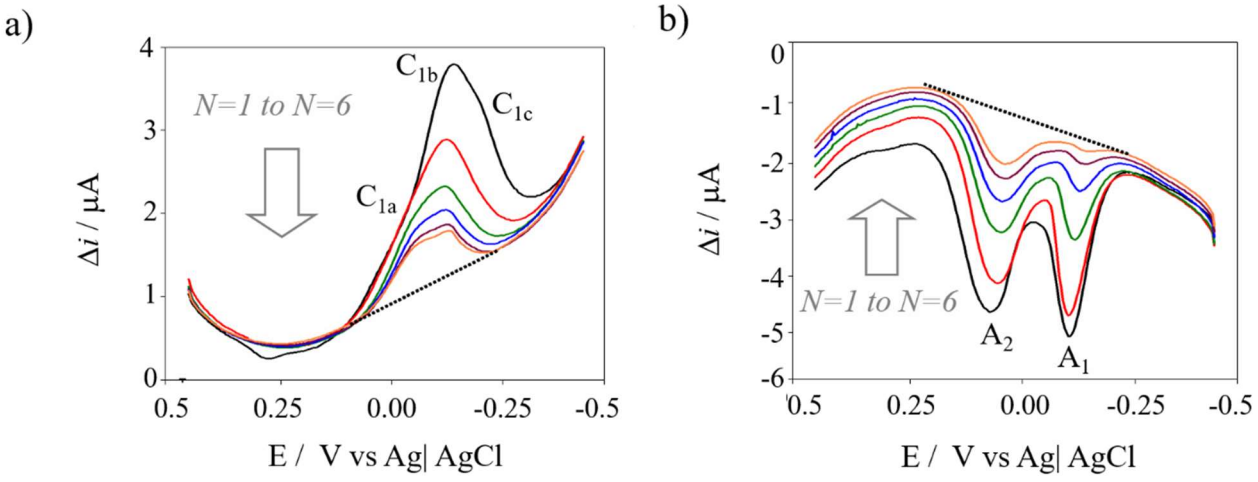

Figure 5.3: *Multiple-(1st to 6th)-scan SWVs of a sample from coin (10 cts Republique Française, 1916) attached to graphite electrode in contact with 0.25 M HAc/NaAc aqueous solution at pH 4.75. Potential scan initiated at a) 0.45 V in the negative direction, b) –0.45 V in the positive direction. Potential step increment 4 mV; square wave amplitude 25 mV; frequency 5 Hz. The dotted lines represent the base lines used for peak area measurements in the 6th scan.*

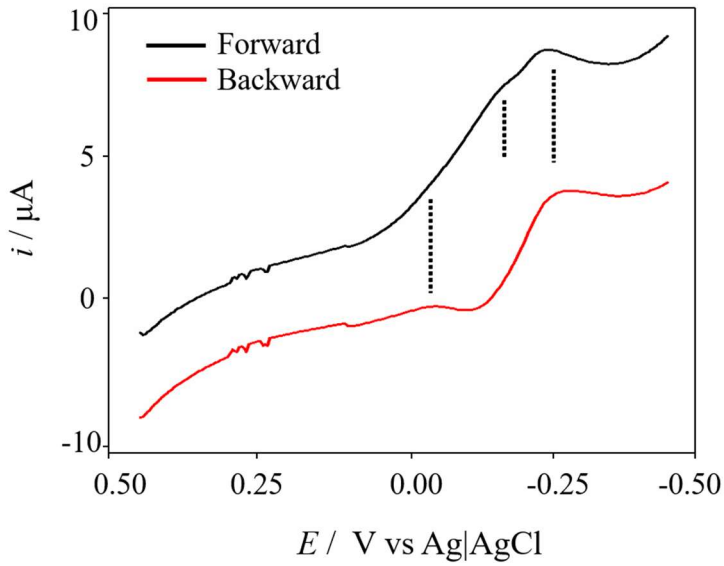

Figure 5.4: *1st scan SWVs of coin M08 (10 cts Republique Française, 1916) attached to graphite electrode in contact with 0.25 M HAc/NaAc aqueous solution at pH 4.75. Potential scan initiated at +0.45 V in the negative direction. Potential step increment 4 mV; square wave amplitude 25 mV; frequency 5 Hz. Separated forward (black line) and backward (red line) components are depicted. The dotted lines mark the shoulders and peaks recorded for each component illustrating their different profiles.*

Upon multiple scans, the peak C_{1c} vanishes, whereas the signal C_{1a} is enhanced relative to the signal C_{1b} whose intensity clearly decreases in successive scans. In the SWVs initiated at −0.45 V in the positive direction, two anodic peaks at −0.12 (A_1) and 0.06 V (A_2) are recorded. The process C_1 can be interpreted, on the basis of VIMP literature[5,6], in terms of the reduction of different cuprite arrangements (differing in the crystallinity and/or grain shape and size) and/or following different electrochemical pathways (vide infra), whereas the processes A_1 and A_2 can be attributed to the oxidative dissolution of two different deposits of metallic copper to Cu^{2+} ions in solution, a frequent feature in the voltammetry of corrosion products[4,7]. These processes can be described as:

[5] A.Doménech-Carbó, M.T. Doménech-Carbó, C. Álvarez-Romero, N. Montoya, T. Pasíes-Oviedo, M. Buendía-Ortuño, *Electroanalysis* (**2017**) 29, 2008–2018.
[6] A. Doménech-Carbó, M.T. Doménech-Carbó, J. Redondo-Marugan, L. Osete-Cortina, J. Barrio, A. Fuentes, M.V. Vivancos Ramon, W. Al-Sekhaneh, B. Martinez, I. Martinez-Lazaro, T. Pasies-Oviedo, *Archaeometry* (**2018**) 60(2):308–324.
[7] A. Doménech-Carbó, M.T. Doménech-Carbó, S. Capelo, T. Pasíes-Oviedo, I. Martínez-Lázaro, *Angew Chem Int Ed* (**2014**) 53(35):9262–9266.

$$Cu_2O_{(solid)} + 2H^+_{(aq)} + 2e^- \rightarrow Cu_{(solid)} + H_2O \quad (5.1)$$

$$Cu_{(solid)} \rightarrow Cu^{2+}_{(aq)} + 2e^- \quad (5.2)$$

Since the negative-going potential scan is initiated at a potential positive enough to oxidize metallic copper, the process described by Eq. (5.1) can be accompanied, in the second and successive scans, by the reduction of Cu^{2+} ions electrochemically generated to Cu metal (i.e., the inverse of the process described by Eq. (5.2)). The maintenance of the signal C_{1a} in successive scans suggests that the relative contribution of this process to the overall signal C_1 increases progressively. In order to evaluate the variation of the voltammetric response in the successive scans, peak areas were measured using the base lines as depicted in Figure 5.3. To obtain peak area values with reasonable accuracy, the number of successive scans was limited to 6. Interestingly, the accumulated values of peak areas (calculated as the sum of the peak areas in each one of the successive scans) ranged between 0.5 and 5 μC, which corresponded to the maximum amounts of removed sample of 2 ng. The areas were determined either for the forward and the forward-backward difference currents (Δi) using both Gaussian and diffusive models (provided by the CHI software) with equivalent results. These were essentially identical to those obtained by measuring the net peak current. Figure 5.5 compares the variation of the area under the signal C_1 with the scan number N in three different spots for coins: (a) M04 (Carolus IV, Spain, 1803), (b) M16 (Phillipus V, Spain, 1709), (c) M06 (Republique Française, 1916), and (d) M18 (Helvetia, Swiss, 1962). In all cases, rapidly descending values of the peak area were obtained. To illustrate this variation, experimental data points are fitted to a function of the type (*area*) = aN^b (taken N as a continuous variable and a,b being constant parameters). The rapid decrease of the peak current/area of C_1 can be interpreted in terms of the exhaustion of the reducible component, mainly cuprite, in successive scans, a feature that can be explained on the

basis of the characteristics of the sampling and the modeling of VIMP processes made by Lovric, Scholz, Oldham, and coworkers[8,9,10,11,12].

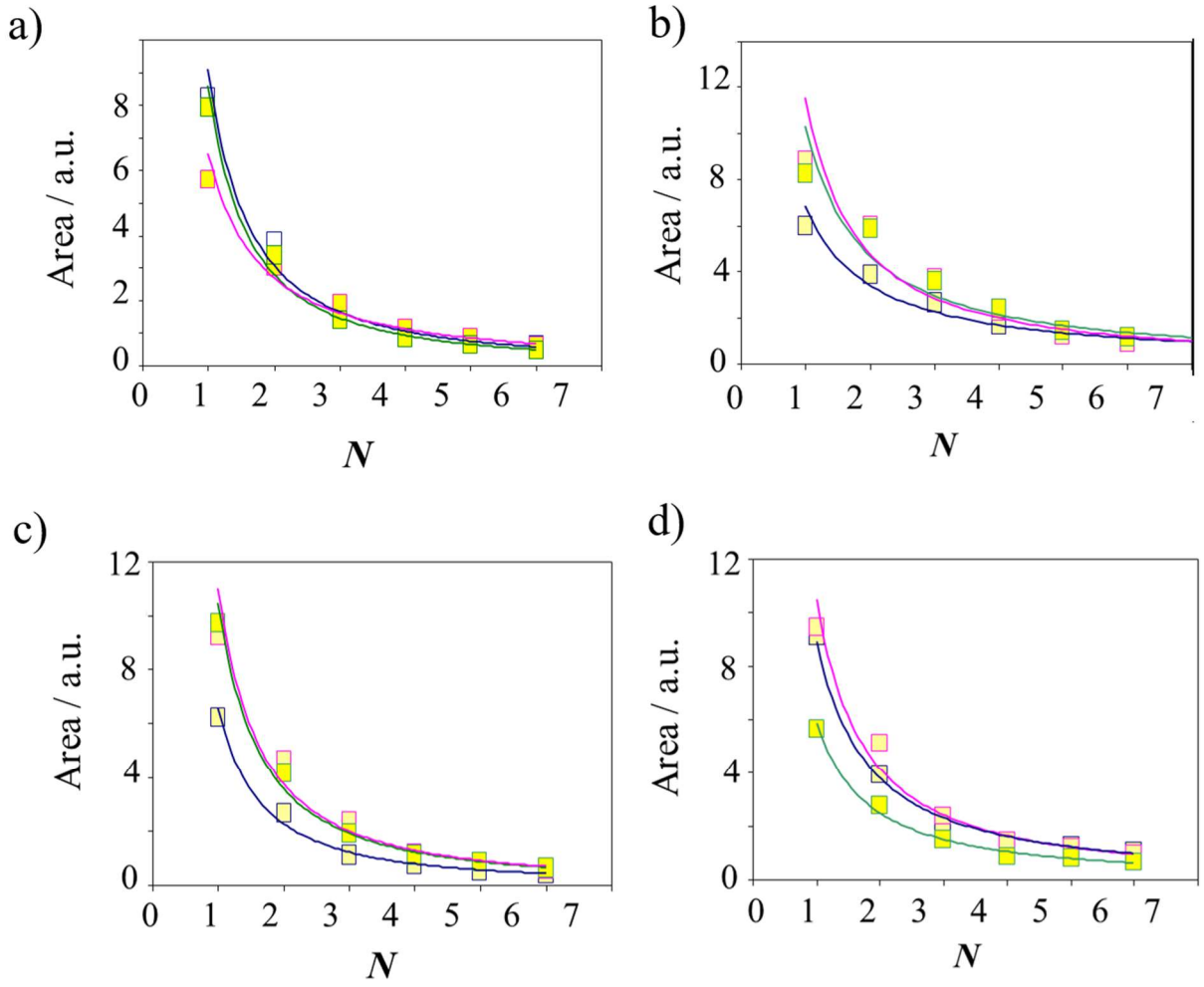

Figure 5.5: *Variation with the scan number N of the area under the signal C_1 (taken from series of SWVs such as in Figure 5.3a) in three different spots for coins: a) M04 (Carolus IV, Spain, 1803); b) M16 (Philipus V, Spain, 1709); c) M06 (Republique Française, 1916); d) M18 (1 rappen, Swiss, 1962). The continuous lines correspond to the fit of experimental points to a potential function taken N as a continuous variable.*

Figure 5.6 shows the secondary electron images of patina plate from coin M31 abrasively transferred onto a graphite bar before (Figure 5.6a) and after (Figure 5.6b-d) the application of 6

[8] M. Lovric, F. Scholz, *J Solid State Electrochem* (**1997**) 1:108–113.
[9] M. Lovric, M. Hermes, F. Scholz, *J Solid State Electrochem* (**1998**) 2:401–404.
[10] K.B. Oldham, *J Solid State Electrochem* (**1998**) 2(6):367–377.
[11] M. Lovric, F. Scholz, *J Solid State Electrochem* (**1999**) 3:172–175.
[12] U. Schröder, K.B. Oldham, J.C. Myland, P.J. Mahon, F. Scholz, *J Solid State Electrochem* (**2000**) 4(6):314–324.

successive negative-going potential scans (as previously illustrated in Figure 5.3a). The original deposit (Figure 5.6a) contains irregular flat copper grains ca. 10 μm sized that, after application of successive potential inputs, become smoothed and narrowed (Figure 5.6b). After the application of successive cathodic inputs, the remaining plates are accompanied by copper nanoparticles distributed more or less homogeneously on the graphite surface (Figure 5.6c) or even over the copper-based plates (Figure 5.6d). These features suggest that under the above experimental conditions, the reduction of cuprite species occurs via intermediates in solution so that metal deposits external to the plates are formed. This means that, ideally, the plates containing a sample of the stratified coin patina are de-laminated upon application of repetitive cathodic inputs, consistently with the modeling discussed in the next section and previous observations on the oxidative dissolution of gold archeological objects in contact with HCl electrolytes[13] and studies on copper/bronze[14] and brass coins[15].

[13] A. Doménech-Carbó, F. Scholz, M. Brauns, S. Tiley-Nel, A. Oliver, G. Aguilella, N. Montoya, M.T. Doménech-Carbó, *Electrochim Acta* (**2020**) 337:135759.
[14] F. Di Turo F, R. Parra R, J. Piquero-Cilla, G. Favero, A. Doménech-Carbó, *J Solid State Electrochem* (**2019**) 23(3):771–781.
[15] M. Di Fazio, A.C. Felici, F. Catalli, M.T. Doménech-Carbó, C. De Vito, A. Doménech-Carbó, *Microchem J* (**2020**) 152:104306.

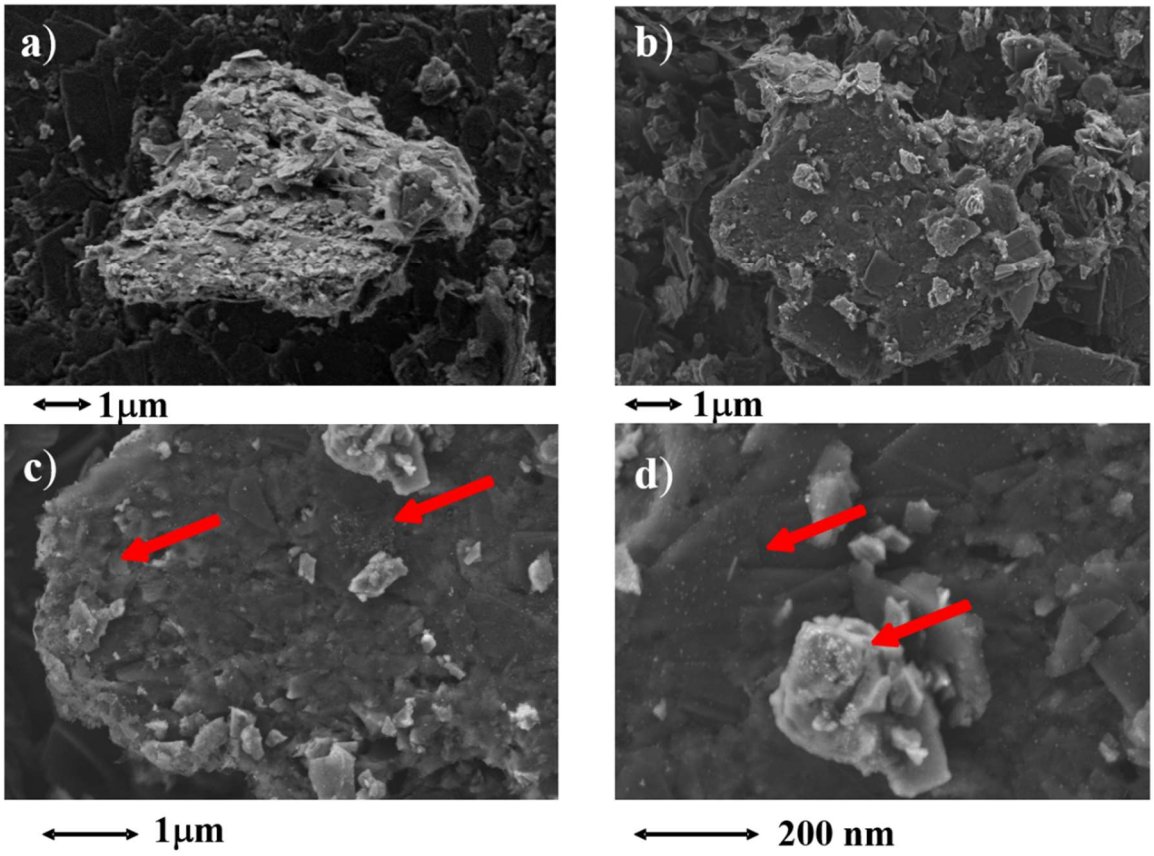

Figure 5.6: *Secondary electron images of patina plates from coin M31 abrasively transferred onto a graphite bar in contact with 0.25 M HAc/NaAc aqueous solution at pH 4.75, a) before and b-d) after application of 6 successive negative-going potential scans. The red arrows mark the regions where high concentration of nanoparticulate copper appears after application of reductive steps.*

5.3. Data modeling

According to the aforementioned model for the electrochemistry of ion-insertion solids[8,9,10,11,12], the proton-assisted reduction of cuprite and other copper corrosion products starts at the three-phase boundary of the graphite electrode/electrolyte/solid sample phases by electron transfer through the electrode/sample interface and the proton transfer through the electrolyte/sample interface. This means that the electrochemical reaction initiates in the more external region of the corrosion layer.

The sampled corrosion products deposited onto the graphite electrode can in principle be formally- and roughly- modeled as composed by k plates forming laminas of average area A, the net charge passed in the first scan will be:

$$q(1) = nkFA\delta(1)\rho(1) \qquad (5.3)$$

where $\delta(1)$ is the thickness of the layer removed in the voltammetric scan and $\rho(1)$ the average molar density of the corrosion product in the first lamina. Assuming that the deposit of copper metal does not interfere in the response in successive scans, as suggested by data shown in Figure 5.6, and that the number of laminas remains essentially constant, the net charge passed in the N-scan will be:

$$q(N) = nkFA\delta(N)\rho(N) \qquad (5.4)$$

where $\delta(N)$ and $\rho(N)$ represent the thickness of the removed layer and the average density of electroactive component in the N lamina. Then, the variation of $q(N)$ with N will be representative of the distribution of the corrosion products in the patina. In turn, the cumulative charge at the N-scan will be:

$$Q(N) = \sum q(N) = nkFA \sum \delta(N)\rho(N) \qquad (5.5)$$

As previously noted, in the case of moderately corroded coins, we can take a simplified view of the corrosion layer as mainly composed by cuprite whose crystallinity and porosity vary with the depth z. This means that, in principle, the density of electroactive component, ρ, can be expressed as a continuous function of z. On the basis of a preliminary study based on the experimental data obtained for our coins (vide infra), three types of ρ(z) functions, potential, exponential, and logarithmic, were tested, to rationalize voltammetric data:

a) Potential model: here, the density function can be expressed as:

$$\rho(z) = \rho_{\text{inn}} - \rho_{\text{surf}}\left(1 - \frac{z}{z_{\text{inn}}}\right)^{\alpha} \qquad (5.6)$$

where ρ_{surf} is the density at the external surface of the patina, ρ_{inn} the corresponding density in the core of the corrosion layers, and α, an adjustable parameter. Then, the charge passed during the first scan for a n-electron process in which a depth z_1 is reached will be:

$$q(1) = nkFA\int_{z=0}^{z_1}[\rho_{\text{innf}} - \rho_{\text{surf}}(1 - \frac{z}{z_{\text{inn}}})^{\alpha}]dz = nkFA[(\rho_{\text{inn}} - \rho_{\text{surf}})z_1 + \frac{\rho_{\text{surf}}}{1+\alpha}\left(\frac{z_1}{z_{\text{inn}}}\right)^{1+\alpha}] \qquad (5.7)$$

The corresponding charge for the N scan will be:

$$q(N) = nkFA\left[(\rho_{inn} - \rho_{surf})(z_N - z_{N-1}) + \frac{\rho_{surf}}{1+\alpha}\left[\left(\frac{z_N}{z_{inn}}\right)^{1+\alpha} - \left(\frac{z_{N-1}}{z_{inn}}\right)^{1+\alpha}\right]\right] \qquad (5.8)$$

It can easily be demonstrated that on computing the cumulated charge, several z-terms cancel so that:

$$Q(N) = nkFA\left[(\rho_{\text{inn}} - \rho_{\text{surf}})z_N + \frac{\rho_{\text{surf}}}{1+\alpha}\left(\frac{z_N}{z_{\text{inn}}}\right)^{1+\alpha}\right] \qquad (5.9)$$

This equation predicts a potential variation of $Q(N)$ with z. As a particular case, if the density of the electroactive product increases linearly with depth, $\alpha = 1$ and Eq. (5.9) becomes:

$$Q(N) = nkFA\left[(\rho_{\text{inn}} - \rho_{\text{surf}})z_N + \frac{\rho_{\text{surf}}}{2}\left(\frac{z_N}{z_{\text{inn}}}\right)^{2}\right] \qquad (5.10)$$

b) Exponential growth model: this model assumes that the density of electroactive component decreases from the primary patina to the external surface following an exponential law. It can be expressed as:

$$\rho(z) = \rho_{\text{inn}} e^{-\beta(z - z_{\text{inn}})} \qquad (5.11)$$

In this equation, ρ_{inn} represents the density of the electroactive product in the core of the corrosion layers which is reached at a depth z_{inn} and β an adjustable parameter. Applied to our case of moderate copper/bronze corrosion, this quantity represents the cuprite density at the primary patina located at a depth z_{inn}. Then, the charge passed during the first voltammetric scan will be:

$$q(1) = nFkA \int_{z=0}^{z_1} \rho_{\text{inn}} e^{-\beta(z - z_{\text{inn}})} dz = nFkA\rho_{\text{inn}} - \frac{1}{\beta}(e^{\beta z_{\text{inn}}} - e^{-\beta(z_1 - z_{\text{inn}})}) \qquad (5.12)$$

Accordingly, the charge at the N scan will be:

$$q(N) = nFkA \int_{z_{N-1}}^{z_N} \rho_{\text{inn}} e^{-\beta(z - z_{\text{inn}})} dz = nFkA\rho_{\text{inn}} \left[-\frac{1}{\beta}\left(e^{-\beta(z_{N+1} - z_{\text{inn}})} - e^{-\beta(z_N - z_{\text{inn}})}\right) \right] \qquad (5.13)$$

Again, on computing the cumulated charge several z-terms cancel so that:

$$Q(N) = \frac{nFkA\rho_{\text{inn}}}{\beta} \left[e^{\beta z_{\text{inn}}} - e^{-\beta(z_N - z_{\text{inn}})} \right] \qquad (5.14)$$

c) Logarithmic growth: this can be derived from a density-depth function of the type:

$$\rho(z) = \frac{h\rho_{\text{inn}}}{h + (z - z_{\text{inn}})} \qquad (5.15)$$

where h is an adjustable length; i.e., assuming that the cuprite density decreases proportionally to the inverse of the distance to the more internal corrosion layer (primary patina). Then:

$$q(1) = nkFA\rho_{\text{inn}} \int_{z=0}^{z_1} h \frac{dz}{h + (z - z_{\text{inn}})} = -nkFAh\rho_{\text{inn}}\, ln\left(\frac{h + (z - z_{\text{inn}})}{h - z_{\text{inn}}}\right) \qquad (5.16)$$

$$q(N) = nkFAh\rho_{\text{inn}} \int_{z_{N-1}}^{z_N} \frac{dz}{h + (z - z_{\text{inn}})} = nkFAh\rho_{\text{inn}}\, ln\left(\frac{h + (z_N - z_{\text{inn}})}{h + (z_{N-1} - z_{\text{inn}})}\right) \qquad (5.17)$$

As before, several z-terms cancel so that the cumulative charge passed after N scans will be:

$$Q(N) = nFkAh\rho_{\text{inn}}\, ln\left(\frac{h + (z_N - z_{\text{inn}})}{h - z_{\text{inn}}}\right) \qquad (5.18)$$

As in the case of Eqs. (5.10) and (5.14), the precedent equation indicates that the cumulative charge after the N-scan is representative of the reached depth at this scan in the voltammetric experiment.

For our purposes, the relevant aspect to underline is that the parameters ρ_{surf}, ρ_{inn}, have a definite physical meaning and that the coefficients α, b in Eqs. (5.9, 5.10), and β in Eq. (5.14) are representative of the corrosion pattern, in turn depending on the composition and metallographic properties of the coin and its 'corrosion history', provided that any of these

functional relationships applies. To test the different models, one can introduce an additional simplifying assumption considering the depth as proportional to the scan number so that $z = \varepsilon N$. Accordingly, Eqs. (5.9), (5.10), (5.14), and (5.18) are converted to:

$$Q(N) = nkFA\left(\rho_{\text{surf}}\varepsilon N + \frac{b\varepsilon^{1+\alpha}}{1+\alpha}N^{1+\alpha}\right) \tag{5.19}$$

$$Q(N) = nkFA\left(\rho_{\text{surf}}\varepsilon N - \frac{b\varepsilon^{2}}{1+\alpha}N^{2}\right) \tag{5.20}$$

$$Q(N) = n\frac{Fk\varepsilon A\rho_{\text{inn}}}{\beta}\left[e^{\beta\varepsilon N} - e^{-\beta\varepsilon(N-N_{\text{inn}})}\right] \tag{5.21}$$

$$Q(N) = nFk\varepsilon Ah\rho_{\text{inn}}\, ln\left(\frac{h+\varepsilon(N-N_{\text{inn}})}{h-\varepsilon N_{\text{inn}}}\right) \tag{5.22}$$

N_{inn} representing the number of scans needed to reach the primary patina.

5.4. Considerations on the measurements

The previous theoretical modeling requires the disposal of a suitable method to measure the charges passed during the voltammetric runs. Since presumably slight variations in the composition/compaction/porosity/crystallinity of the corrosion patina are involved, the selected technique has to be highly sensitive. Another important advantage of VIMP is that the sampling results in the removal of few nanograms of sample which remains attached to the graphite surface. As previously noted, the disposal of so low amount of sample is convenient when dealing with historical objects, but the drawbacks of this method are: (i) the exact amount of transferred sample is unknown and (ii) the graphite surface becomes to some extent scratched

and, consequently, altered in its electrochemical behavior[16]. These features determine the appearance of uncompensated resistive and capacitive effects. As a result, the electrochemical methods yielding a direct estimate of the charge passed (linear potential scan voltammetry, controlled potential coulometry) do not produce satisfactory results because there is no possibility of subtracting a background current (i.e., the background current measured at unmodified graphite electrodes does not equal the "true" background measured in each voltammogram). Accordingly, in the developed strategy, it was exploited SWV, an intrinsic highly sensitive method that minimize the contribution of the charging current, in particular, when differential net SW component is considered. The problem is that the forward, backward, and net currents measured with this method do not provide a direct estimate of the charge passed under the voltammetric peak. In the case of a reactant immobilized onto the electrode surface experiencing a n-electron process, any of these currents can be expressed as $I = nFA\Gamma f \Psi$, where A is electrode surface area, Γ is initial surface concentration of the electroactive reactant, and f is SW frequency, Ψ is a dimensionless function representing intrinsic voltammetric features of a given electrode reaction, and the other symbols have their customary meaning. Since integration of Ψ cannot yield any result with a reasonable physical meaning, the integration of the current/potential SWV curves does not provide a real estimate of the charge passed. The same considerations can be applied to the peak currents, for which one can assume $I_{peak} = nFA\Gamma f\Psi_{peak}$. Then, the in-depth variation of the composition/porosity/compaction of the corrosion patina will be reflected but changes in $\Gamma$and Ψ_{peak} are measurable, in turn determining the variation of the peak currents in successive potential scans. It is pertinent to note that at solid electrodes, side electrochemical reactions frequently related to the electrochemical activity of the electrode surface itself contribute to the background current. This contribution dominates over the contribution of the charging current, which is negligible at the end of the pulse, in particular at

[16] F. Scholz, B. Meyer. In: A.J. Bard, I. Rubinstein (eds) Voltammetry of solid microparticles immobilized on electrode surfaces, electroanalytical chemistry, a series of advances, vol 20. Marcel Dekker, New York, 1–86, (**1998**).

low SW frequencies. This means that the contribution of the background current could be significant in both forward and backward SW components. However, assuming that the background current is quite comparable at the end of both forward and backward potential pulses, it normally cancels out effectively in the net current, which overall is another important advantage of SWV. In spite of this fundamental limitation, the use of SWV is favored in this case by two features: (i) the interest is focused on the relative amount of charge passed in successive scans rather than the absolute charge passed in each one of them and (ii) the observed electrochemical processes are dominated by the reduction of cuprite so that, along any given multiple-scan experiment, one can expect a slight variation of the parameter Ψ. The experimental data (*vide infra*) supported the use of this method. Accordingly, it was tentatively adopted SWV as a measuring technique resulting in the estimate of apparent charges, $Q_{app}(N)$, at the successive N^{th} scans.

5.5. Correlation between experimental data and data models

As previously noted, for each series of voltammograms, it was measured the net peak current and performed the integration of both the net current/potential and the forward current/potential curves using both Gaussian and diffusive peak modeling with equivalent results. The comparison of Eqs. (5.19-22) with experimental data for the studied coins revealed an excellent agreement in terms of the correlation coefficient between the logarithmic model for the first 3–4 scans accompanied by an also excellent agreement with the potential-linear model for the scans 4–6. Representative examples are shown in Figure 5.7. Here, the experimental $Q_{app}(N)$ vs. N data corresponding to three different spots taken in coin M32 (10 cts, Isabel II, Spain, 1840) are depicted. Similar results were obtained using the net current, ΔI (see Figure 5.8). Continuous lines correspond to the fit of the data from the first three voltammetric scans to a logarithmic function, while dotted lines correspond to the fit of data from the scans 4–6 to a

polynomial function of second degree. The corresponding statistical data are summarized in Table 5.2; here, one can see the excellent agreement with the previously indicated logarithmic and polynomial models.

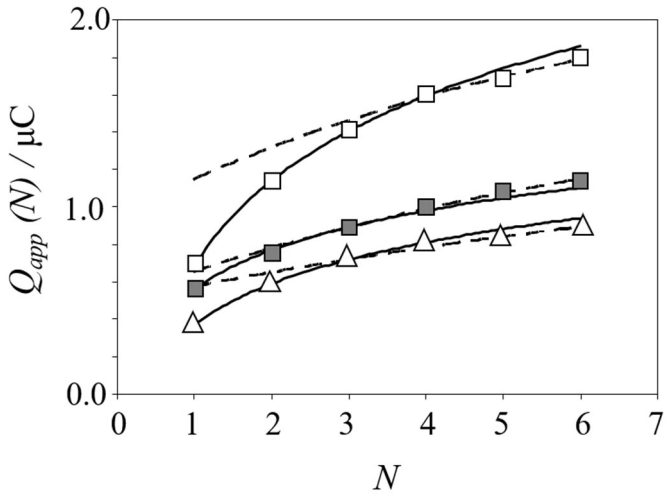

Figure 5.7: *Plots of Q_{app} (N) vs. N corresponding to three different spots taken in coin M32 (10 cts, Isable II, Spain, 1840). Continuous lines correspond to the fit of the data from the scans 1-3 to a logarithmic function; dashed lines correspond to the fit of data from the scans 4-6 to a polynomial function of 2nd degree.*

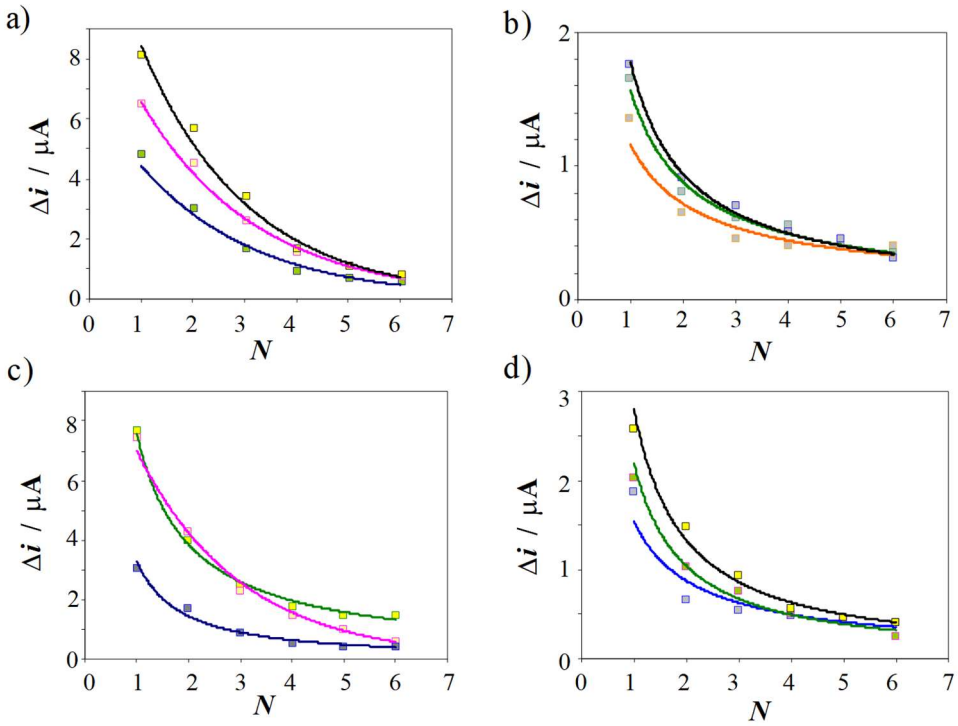

Figure 5.8. *Variation with the scan number N of the peak current difference of the signal C_1 (taken from series of SWVs) in three different spots for coins: a) M03 (Carolus IV, Spain, 1798); b) M30 (2nd Republic, Spain, 1937); c) M12 (Republique Française, 1904); d) M31 (Belgium, 1953). The continuous lines correspond to the fit of experimental points to a potential function taken N as a continuous variable.*

Table 5.2. *Statistical parameters corresponding to the fit of experimental data of cumulated charge in SWVs performed at sample-modified electrodes immersed into 0.25 M HAc/NaAc aqueous solution at pH 4.75. Potential scan initiated at 0.45 V in the negative direction. Potential step increment 4 mV; square wave amplitude 25 mV; frequency 5 Hz.*

Coin	Scans 1-3	Scans 4-6
M32	$Q_{app}(N) = 6.54\ln N + 6.87$; $r = 0.9991$ $Q_{app}(N) = 3.03\ln N + 5.60$; $r = 0.998$ $Q_{app}(N) = 3.18\ln N + 3.70$; $r = 0.997$	$Q_{app}(N) = 9.65+1.94N–0.095N^2$; $r = 0.9999$ $Q_{app}(N) = 5.14+1.44N–0.065N^2$; $r = 0.9999$ $Q_{app}(N) = 4.90+0.85N–0.030N^2$; $r = 0.9999$
M18	$Q_{app}(N)= 2.79\ln N + 4.56$; $r= 0.9998$ $Q_{app}(N)= 3.46\ln N + 4.78$; $r= 0.998$ $Q_{app}(N)= 1.96\ln N + 2.84$; $r= 0.9997$	$Q_{app}(N)= 4.69+1.14N–0.055N^2$; $r= 0.9999$ $Q_{app}(N)= 5.74+1.10N–0.055N^2$; $r= 0.9999$ $Q_{app}(N)= 3.09+0.72N–0.0350N^2$; $r= 0.9999$
M08	$Q_{app}(N)= 3.42\ln N + 2.99$; $r= 0.995$ $Q_{app}(N)= 10.67\ln N + 8.50$; $r= 0.998$ $Q_{app}(N)= 6.47\ln N + 6.60$; $r= 0.9999$ $Q_{app}(N)= 13.3\ln N + 6.28$; $r= 0.992$ $Q_{app}(N)= 18.4\ln N + 8.77$; $r= 0.992$	$Q_{app}(N)= 1.13+2.41N–0.157N^2$; $r= 0.9999$ $Q_{app}(N)= 5.45+6.08N–0.358N^2$; $r= 0.9999$ $Q_{app}(N)= 8.80+2.06N–0.123N^2$; $r= 0.9999$ $Q_{app}(N)= 1.47+7.48N–0.226N^2$; $r= 0.9999$ $Q_{app}(N)= 0.47+11.0N–0.276N^2$; $r= 0.9999$

Interestingly, the same two-region pattern is obtained if the experimental $Q_{app}(N)$ data recorded in different sampling spots of the same coin are plotted conjointly, adopting N as the total ordered number of $Q_{app}(N)$ values. Figure 5.9 compares the representation of $Q_{app}(N)$ vs. N corresponding to that combination of data for coins M16 (Seiseno Philipus V, Spain, 1709, squares), M04 (8 maravedís, Carolus IV, Spain, 1803, solid squares), and M30 (5 cts, Spanish Republic, 1937, triangles). The left region of the figure corresponds to the most external corrosion layers of the coins, whereas the right region corresponds to the internal ones. It is interestingly to note in Figure 5.9, that the variation of $Q_{app}(N)$ with N is more rapid in the oldest coins while in the internal region $Q_{app}(N)$ appears to tend to different limiting values increasing with age.

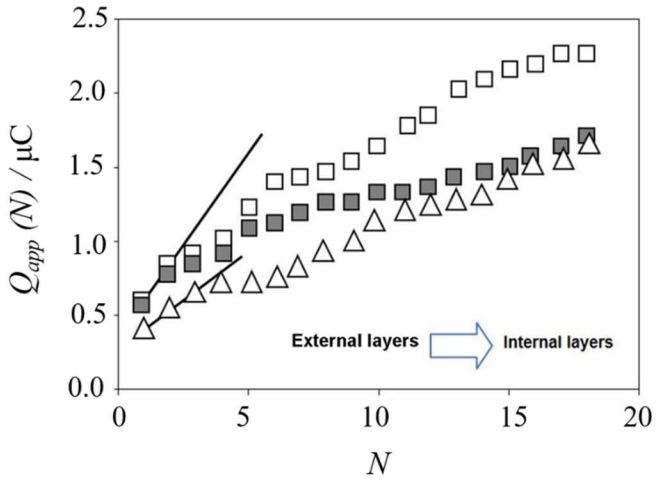

Figure 5.9: *Plots of Q_{app} (N) vs. N corresponding to the combination of data for three different spots taken in coins M16 (Philipus V, Spain, 1709, squares), M04 (Carolus IV, Spain, 1803, solid squares) and M30 (Spanish Republic, 1937, triangles).*

5.6. Implications for chronology

The previous set of considerations suggests that the studied voltammetric data are representative of the corrosion pattern of the coins, in turn depending on the conservation conditions, composition of the coin (copper or bronze), adherence of the corrosion products, etc.

On the other hand, inhomogeneities in the corrosion patina can produce differences in the voltammetric response depending on the region of sampling. In the studied samples, however, sampling in different points of the coins produced relatively low variability and, in spite of these drawbacks, it was obtained a correlation between the voltammetric pattern and the chronological order of the coins. Under uniform corrosion conditions, one can expect that the parameters ρ_{surf}, ρ_{inn}, α, etc. in Eqs. (5.19-22) should vary with the corrosion time following a defined variation for coins having identical composition and metallography. In these favorable conditions, these parameters should vary monotonically with time prompting the construction of calibration curves for age determination. However, a problem rising to this purpose, is that experimental data are dependent on the net amount of sample in the VIMP experiments, represented by the factor k in Eqs. (5.19-22). This problem can be avoided taking the ratios between the cumulated charges making the k-parameter cancelled. After testing different empirical ratios, the $Q_{app}(6)/Q_{app}$ (1) quotient, quite sensitive to the values of the parameters ρ_{surf}, ρ_{inn}, α, etc., was found to be reasonably representative of both the corrosion pattern and the age of the coins. The variation of $Q_{app}(6)/Q_{app}$ (1) (average value from 3-5 independent sampling spots on each coin) with the age of the studied coins is depicted in Figure 5.10a. Here, it is possible to note that the studied coins can be distributed into three tendency lines. The majority of the samples correspond to binary or ternary bronzes (see metal compositions approximated from EDX analysis listed in Table 5.1) with corrosion pattern such as in Figures 5.2a,b, the older displaying corrosion patterns such as in Figure 5.2d. These samples define a tendency line which can be fitted to a potential function (squares). Three coins presenting similar corrosion habit but having relatively high content of zinc fall in a different tendency line (solid squares). Finally, two coins composed of ternary bronzes (see Table 5.1) displayed a corrosion pattern characterized by a cassiterite-rich intermediate layer such as in Figure 5.2c defining a clearly different tendency line (triangles). Similar results were obtained using the ratio between the corresponding net peak

currents (see Figure 5.10b). The relevant aspect to emphasize is that the described multiple-scan voltammetry strategy permits the chronological ordering of the coins suffering low corrosion.

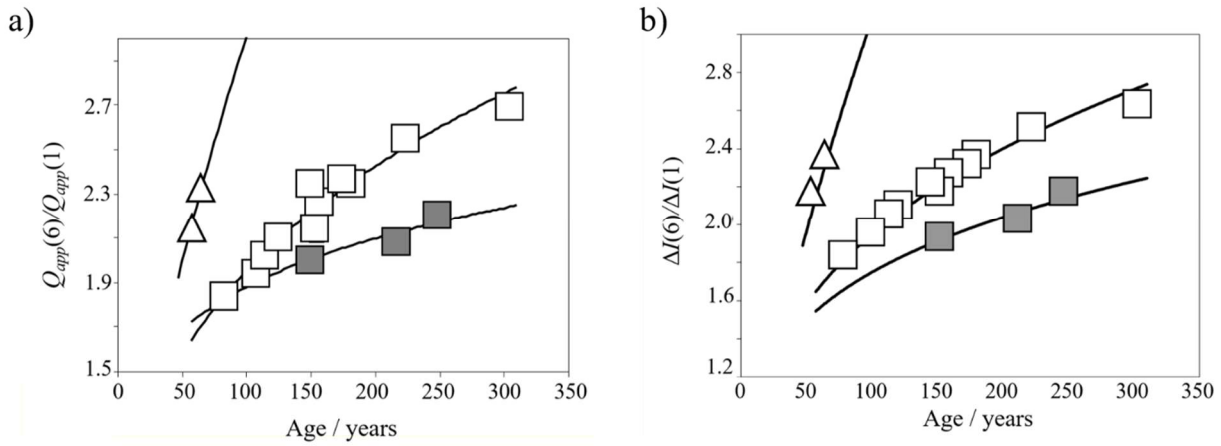

Figure 5.10: *Variation of a) the Q_{app} (6)/Q_{app} (1) ratio and b) the $\Delta I(6)/\Delta I(1)$ ratio versus the age of the studied coins grouped into binary or ternary bronzes corrosion pattern such as in Figs. 5.2a,b,d (white squares), ternary bronzes with relatively high Zn content (grey squares) and ternary bronzes with corrosion pattern such as in Fig. 5.2c (triangles).*

Chapter 6: Investigations on copper roof claddings

6.1. Voltammetric investigation on the interaction between Cu^{2+} ions and HC10

Copper has been extensively used in the past as base material for a wide variety of historic objects as coins, jewellery, kitchenware, sculptures and as construction material of architectural works as well. Unfortunately, its corrosion leads to the formation of corrosion layers, whose characteristics depend on the reactivity of the species present in the environments to which the copper objects are exposed. Previous studies have clearly shown that corrosion layers, formed upon exposure of copper to an urban environment for a significant time, are essentially composed by an inner layer of cuprite (Cu_2O), typically 5-10 μm thick, and a green external layer of brochantite ($Cu_4SO_4(OH)_6$, typically 45-50 μm thick[1,2,3]. The latter, often, displays great porosity and poor adhesion to the underlying cuprite layer[1]. In the field of preservation of historical and artistic materials, it is common practice not to remove the corrosion layer (the so-called patina, here referred to the one naturally formed), unless it compromises the stability of the objects themselves. In fact, the patina provides evidence of time passing and adds historical value to the objects; its colour (usually green for copper materials) is aesthetically pleasing and it protects, to a certain extent, the underlying metal from further corrosive processes[2]. However, there are some environmental conditions that may cause destabilization of the corrosion layers leading to the deterioration of the metal. This is why different strategies are adopted for the protection of metallic artefacts exposed outdoors by treating them with suitable corrosion inhibitors[4]. To this purpose, in recent years, a class of eco-friendly compounds, such as linear carboxylic acids, derivatives of fatty acids, extracted from vegetable oils, have received increasing

[1] D. de la Fuente, J. Simancas, and M. Morcillo, *Corros. Sci*. (**2008**) 50, 268–285.
[2] K. P. FitzGerald, J. Nairn, G. Skennerton, and A. Atrens, *Corros. Sci*. (**2006**) 48, 2480–2509.
[3] M. Morcillo, T.Chang, B.Chico, D.de la Fuente, I. Odnevall Wallinder, J.A.Jiménez, C.Leygraf, *Mater. Charact*. (**2017**) 133, 146–155.
[4] M. M. Antonijevic, M. B. Petrovic, Copper corrosion inhibitors. A review, *Int. J. Electrochem. Sci*. (**2008**) 3, 1 – 28.

attention[5,6,7,8,9,10]. In particular, decanoic acid has been used to protect a variety of copper substrates[5,6,7,8,10], especially of historic/artistic interest[10]. The treatment with the inhibitor is generally performed by soaking the samples for several hours in a medium containing HC10. The most used media are E/W mixtures (typically, 50% v/v), in which the carboxylic acid displays adequate solubility[10,11].

The voltammetric behavior of Cu^{2+} in ethanolic-aqueous solutions has been investigated earlier in a few reports by polarography[12,13,14] or voltammetry using bare solid copper[15], gold[16] and platinum electrodes[17], in the latter cases in the context of determining trace copper ions in ethanol fuels[14] or alcoholic beverages[17]. In these studies, it has been verified that, in general, the electrochemistry of copper ions in E/W solutions is similar to that observed in water media. For this reason, in the next paragraph, it will be briefly recalled the electrochemistry of copper ions in water media.

[5] E. Rocca, G. Bertrand, C. Rapin, J.C. Labrune, *J. Electroanal. Chem*. (**2001**) 503, 133–140.
[6] A. Elia, K. De Wael, M. Dowsett, A. Adrieaens, *J. Solid. State Electrochem*. (**2012**) 16, 143 – 148.
[7] G. Žerjav, I. Milošev, *Int. J. Electrochem. Sci*., 9 (**2014**) 2696 – 2715.
[8] T. Liu, S. Chen, S. Cheng, J. Tian, X. Chang, Y. Yin, *Electrochim. Acta* (**2007**) 52, 8003–8007.
[9] G Žerjav, A. Lanzutti, F. Andreatta, L. Fedrizzi, I. Milošev, *Materials and Corrosion* (**2017**) 68, 30-41.
[10] M. L'héronde, M. Bouttemy, F. Mercier-Bion, D. Neff, E. Apchain, A. Etcheberry, P. Dillmann, *Heritage* (**2019**) 2, 2640-2651.
[11] F.-J. Ruiz, S. Rubio, D. Perez-Bendito. *Anal. Chem*. (**2007**) 79, 7473 – 7484.
[12] I. V. Nelson, R.C. Larson, R. T. Iwamoto, J. Inorg. Nucl. Chem. 22 (**1961**) 279 – 284.
[13] I. V. Nelson, R. T. Iwamoto, Inorg. Chem. 1 (**1962**) 151 – 154.
[14] Z. Gorlich, M.J. Jaskula, E. Markiewicz, Electrochim. Acta, 30 (**1985**) 965 – 970.
[15] S. M. Kuz'min, S. A. Chulovskaya, V. I. Parfenyuka, Surface Engineering and Applied Electrochemistry 46 (**2010**) 589–595
[16] R. M. Takeuchi, A. L. Santos, M. J. Medeiros, N. R. Stradiotto, Microchimica Acta 164 (**2009**) 101–106.
[17] M. A. Baldo, S. Daniele, Electroanalysis 18 (**2006**) 633-639.

6.1.1. Voltammetric behavior of Cu^{2+} ions in aqueous solutions

A typical electrochemical behavior of a $CuSO_4$ water solution with 0.05 M Na_2SO_4 at a Pt microdisk electrode is reported in Figure 6.1.1.

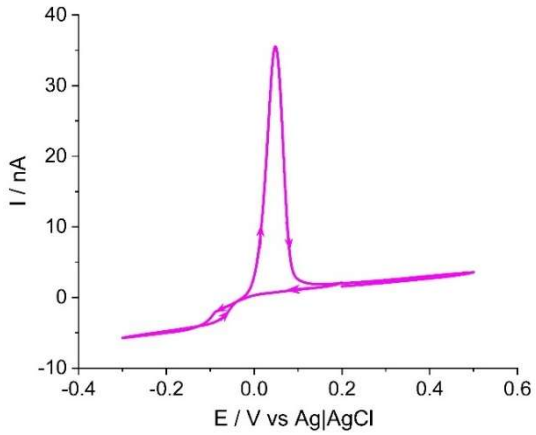

Figure 6.1.1*: CVs recorded in 1 mM $CuSO_4$ water solution containing 0.05 M Na_2SO_4 at a Pt microdisk 12.5 µm radius. Scan rate 5 mV s^{-1}.*

It has been previously reported that copper reduction takes place via cuprous ion intermediates[18,19,20] :

$$Cu^{2+} + e^- \rightleftharpoons Cu^+ \qquad (6.1.1)$$

$$Cu^+ + e^- \rightleftharpoons Cu^0 \qquad (6.1.2)$$

In solution containing electrolytes such as KNO_3 or Na_2SO_4, Cu^+ is unstable and gives rise to the disproportion reaction[18,19,20]:

$$2Cu^+ \rightleftharpoons Cu^0 + Cu^{2+} \qquad (6.1.3)$$

[18] E. Mattsson, J. O. M. Bockris, *Trans. Faraday Soc.* (**1959**) 55, 1586 – 1601.
[19] G. Gunawardena, G. Hills, I. Montenegro, *J. Electroanal Chem* (**1985**) 184, 357-369.
[20] S. Daniele, M.J. Pena, *Electrochim. Acta* (**1993**) 38, 165-174.

In the presence of Cl^- ions, Cu^+ can be stabilized to an extent that depends on the Cu^+/Cl^- ratio[19,20] as shown from the CVs recoded with 0.5 M (Figure 6.1.2a) and 0.01 M of NaCl (Figure 6.1.2b). The extent of the stabilization of Cu^+ with the increasing concentration of Cl^- ions is reflected in the shift of the cathodic peak process (6.1.2) towards more negative potentials, while the easier reduction of Cu^{2+} to Cu^+ is testified by the shift of the wave towards more positive potentials.

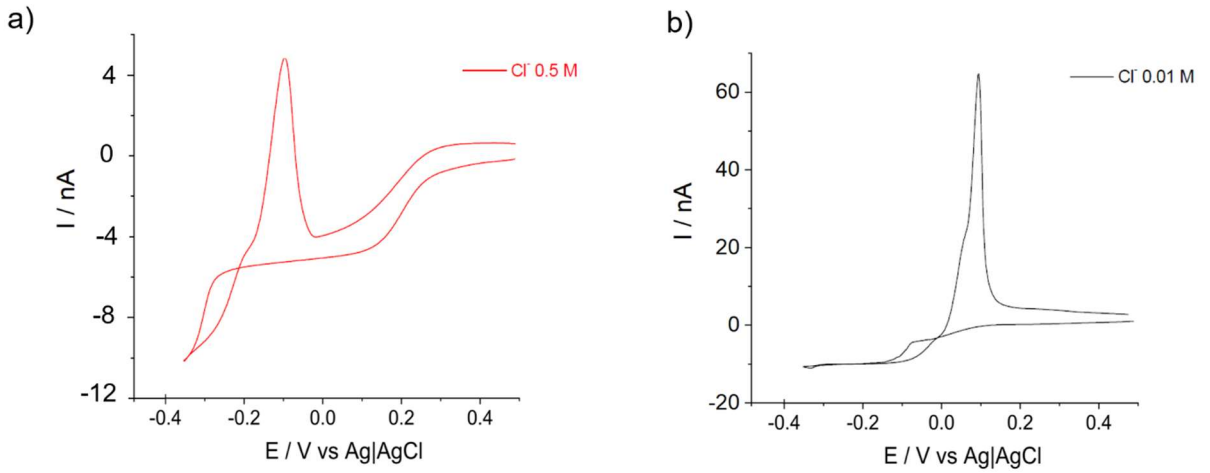

***Figure 6.1.2**: CVs recorded in 1 mM $CuSO_4$ water solution containing a) 0.5 M and b) 0.01 M of NaCl at a Pt microdisk 12.5 µm radius. Scan rate 20 mV s^{-1}.*

Although similar mechanisms have been proposed when ethanolic-rich media have been used as solvents, the voltammetric characteristics (i.e., peak position, current intensity and, in some cases, number of processes), due to Cu^{2+} reduction, have been found to depend on the E/W ratio of the mixture[13,14,17]. The presence of HC10 in the E/W media can further complicate the redox behaviour of Cu^{2+}, due to the formation of soluble copper carboxylate species[21]. Furthermore, the ternary system ethanol-water-HC10 can produce, in the bulk medium or near the electrode surface, colloidal systems (i.e., micelles, microemulsions or even coacervates[11]),

[21] N. Nordin, W. Z. Samad, E. Kardia, B. H. Yahaya, M. R. Yusop, M. R. Othman. *NANO: Brief Reports and Reviews* (**2018**) 13, 1850048.

which can also affect the electrochemistry of the copper species. Therefore, to shed light on some of the previous aspects and to gain information useful to better understand the mechanism involved in the formation of the inhibition coating layers and their stability over time, the voltammetric behavior of Cu^{2+} in a 50% (v/v) E/W mixture, without and with various amounts of HC10 and Cl^- ions, has been investigated.

6.1.2. Voltammetric behavior of the background E/W mixture containing 0.05 M Na_2SO_4 without and with HC10

A typical cyclic voltammogram (CV) obtained in the base electrolyte at 5 mV s^{-1} at the Pt microdisk over a potential window from -1.2 to +1.6 V (i.e., that available before the occurrence of the solvent discharge processes) is displayed in Figure 6.1.3. A featureless profile was recorded in the cathodic region up to the solvent discharge. In the anodic region, two main processes (at +0.4 and + 0.8 V) in the forward scan and a bell-shaped process (at + 0.24 V) in the backward scan were recorded (Figure 6.1.3, inset). These processes are due to the oxidation of ethanol at the Pt surface, involving dissociative adsorption of the molecule with the formation of intermediate poisoning species, which limit the ability of Pt to fully catalyze the oxidation of the organic molecule[22,23].

[22] J.M. Perez, B. Beden, F. Hahn, A. Aldaz, C. Lamy, *J. Electroanal. Chem*. (**1989**) 262, 251-261.
[23] Y. Mukouyama, K. Iida, T. Kuge, *Electrochemistry* (**2020**) 88, 178–184.

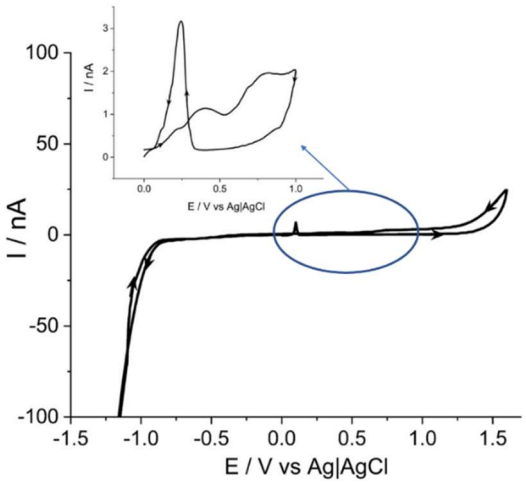

***Figure 6.1.3**: CVs recorded in 50% (v/v) E/W containing 0.05 M Na_2SO_4 at a Pt microdisk 12.5 µm radius. Inset: enlargement of the circled anodic region.*

In the presence of HC10, a sigmoidal wave, typical for microelectrode at which radial diffusion prevails[24], was recorded over the potential region from -0.5 to -0.8 V (Figure 6.1.4). The current of the wave increased by increasing the acid concentration. The half-wave potential ($E_{1/2}$) of the process varied from -0.550 to -0.597 V, as the HC10 concentration was changed from 1 to 16 mM.

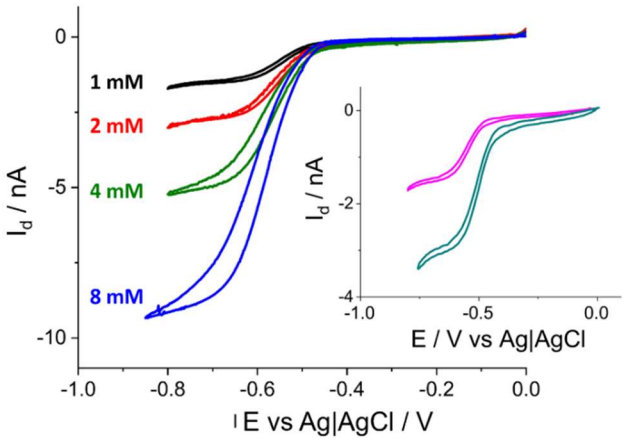

***Figure 6.1.4**: CVs recorded in 50% (v/v) E/W containing 0.05 M Na_2SO_4 at a Pt microdisk 12.5 µm radius with 1, 2, 4, 8 mM HC10 (black, red, green and blue lines, respectively). Inset: comparison between the CVs recorded in the E/W mixture containing 1 mM HC10 (magenta line) and 1mM HAc (cyan line). Scan rate 5 mV s^{-1}.*

[24] S. Daniele, G. Denuault in: Developments of Electrochemistry. Science inspired by Martin Fleishmann. D. Pletcher, Z-Q. Tian, D. Williams (Eds.), Wiley, Chichester, UK, (**2014**), 223.

The reduction of HC10 occurs, conceivably, through a CE mechanism (i.e., chemical reaction (6.1.4) preceding the electron transfer process (6.1.5))[25,26,27] :

$$HC10 \rightleftharpoons H^+ + C10^- \qquad (6.1.4)$$

$$H^+ + e^- \rightleftharpoons \tfrac{1}{2} H_2 \qquad (6.1.5)$$

Such a pathway was proposed on the basis of previous works performed at Pt microelectrodes in water solutions, containing a series of weak acids with low carbon chains, such as lactic and acetic acids[25,26]. In these studies, it was found that, at a given acid concentration, both diffusion limiting current (I_d) and half-wave potential ($E_{1/2}$) depended on pK_a of the weak acid. Specifically, I_d became lower, while $E_{1/2}$ shifted towards more negative potentials as the pK_a of the acid increased[25]. In Ref. [27], the voltammetric behavior of HAc was also investigated in detail in the 50% (v/v) E/W and, at 1 mM concentration, the sigmoidal wave was characterized by $E_{1/2}$ = -0.508 V. This value and relevant voltammetric behavior of HAc were confirmed using the same medium and electrode (inset in Figure 6.1.4, where the CV of HAc (cyan line) is compared with that of HC10 (magenta line)). The $E_{1/2}$ value of HC10 is 42 mV more negative than that of HAc, suggesting that, in the investigated E/W mixture, pK_a of HC10 is somewhat higher than that of HAc. For the latter, pKa = 5.73 was evaluated by linear interpolation from data reported in the literature for E/W mixtures in the range 0-60% (v/v) (Appendix A.2).

Since, to the best of our knowledge, no value is available for HC10 in the 50% (v/v) E/W medium, an estimate of its pKa was made starting from pKa = 4.90, value reported in water[28,29,30], and assuming that the acidity constant of HC10 changed by the same amount (ΔpKa) of that of

[25] S. Daniele, I. Lavagnini, M.A. Baldo, F. Magno. *J. Electroanal. Chem*. (**1996**) 404, 105-111.
[26] S. Daniele, M. A. Baldo, F. Simonetto. *Anal. Chim. Acta* (**1996**) 331, 117 – 123.
[27] M.A. Baldo, S. Daniele, C. Bragato, G.A. Manzocchin. *Electroanalysis* (**2001**) 13, 737-743.
[28] I.D. Robb, *Australian J. Chem*. (**1966**) 19, 2281 – 2284.
[29] G.H. Bell, *Chem. Phys. Lipids* (**1973**) 10, 1-10.
[30] J.F. Feehan, J. Monaghan, C.G. Gill, E.T. Krogha. *Environmental Toxicology and Chemistry* (**2019**) 38, 1879–1889.

HAc, passing from water to the E/W mixture. For HAc, pKa = 4.56 was reported in water at 0.1 M ionic strength[25], thus ΔpKa = 1.17 (i.e., 5.73 – 4.56). On the basis of these considerations, pKa = 6.07 was calculated for HC10.

Considering again the CVs of HC10 (Figure 6.1.4), it was found that its wave height increased linearly by increasing the acid concentration up to about 16 mM. The linear regression analysis of the experimental points provided the following relationship: $I_d\ (nA) = 0.98\ C_{HC10}\ (mM) + 0.56$ (R^2 = 0.978), indicating that the three-component mixture was homogeneous and that no microscopic phases involving HC10 (i.e., micelles or emulsions) were formed. Above 16 mM of HC10, the solution became slightly opalescent, conceivably due to the aggregation among the long aliphatic chains of the fatty acid molecules, which led to separation of microscopic phases[11,31]. It must be considered that a similar phenomenon was also observed, even at lower acid concentrations, when HC10 was added in the solid form directly in the 50% (v/v) E/W mixture. In these cases, a clear solution was obtained after prolonged and vigorous stirring. Colloidal systems also appeared when the % (v/v) of E/W ratio was below 40% (see paragraph 6.1.9). For these reasons, the suitable amount of HC10 was always added in the 50% E/W (v/v) medium, starting from concentrated solutions of HC10 dissolved in pure ethanol, in which HC10 was fully soluble[8,32].

As for the current plateau, I_d of 1.35 (±0.05) nA and 3.09 (±0.05) nA were found at 1 mM concentration in the E/W 50% (v/v) medium for HC10 and HAc, respectively. These values are, in part, congruent with the corresponding pKa of the two acids[21]. However, the smaller current found for HC10 can also be related to the value of diffusion coefficient (D_{HC10}) with respect to that of HAc (D_{HAc}).

[31] K. Bober, M. Garus, *Journal of Liquid Chromatography & Related Technologies* (**2006**) 29, 2787–2794.
[32] Handbook of Chemistry and Physics, 72nd edition, CRC press, Boca Raton, (**1991-1992**), 3-209.

6.1.3. Evaluation of the diffusion coefficient of HC10 in water and 50% (v/v) (E/W) mixture

The diffusion coefficient of HC10 in pure water $(D_{HC10})_0$ was calculated by assuming that HC10 and its conjugated base $C10^-$ share the same diffusion coefficient[26]. The diffusion coefficient of $C10^-$ in pure water $(D_{C10^-})_0$ was calculated by using equation (6.1.6), which relates the equivalent conductance at infinite dilution (λ_0) and the diffusion coefficient[33]:

$$(D_{C10^-})_0 = 8.96 \cdot 10^{-10} \cdot T \cdot \lambda_0/z \qquad (6.1.6)$$

where T is the temperature in Kelvin, z is the charge of the ion, (equal to 1 in the present case). At 298.13 K, λ_0 = 22. 51 S cm^2 mol^{-1} from Ref. [34]. Thus, $(D_{C10^-})_0 = (D_{HC10})_0 = 6.01 \cdot 10^{-6}$ cm^2 s^{-1} in water.

To account for the different viscosity of the 50 % (v/v) E/W medium with respect to pure water, the Stokes-Einstein equation (6.1.2) was employed[33]:

$$D = kT/ 6\pi\eta r_h \qquad (6.1.7)$$

where k is the Boltzmann constant, η is the dynamic viscosity and r_h is the hydrodynamic radius of the species. Viscosity values at 298.15 K, in water and the 50% (v/v) E/W were equal to 0.8914 and 2.3869 mPa s, respectively[35,36]. Assuming that no change in the hydrodynamic radius occurs passing from water to the ethanol/water mixture, the diffusion coefficient of HC10 in the solvent without electrolyte, $D_{0(HC10)E/W}$, is equal to $2.34 \cdot 10^{-6}$ cm^2 s^{-1}.

[33] J. O. Bockris, A. K. N. Reddy, Modern Electrochemistry, vol. 1, Plenum, New York, (**1970**) 384-386.
[34] Z. Kinart. *Journal of Molecular Liquids* (**2017**) 248, 1059-1064.
[35] I.S. Khatta, F. Bandarkar, M.A.A. Fakhree, and A. Jouyban, *Korean J. Chem. Eng.* (**2012**) 29(6), 812-817.
[36] M. Laliberté. *J. Chem. Eng. Data* (**2007**) 52, 321 – 335.

The variation of diffusion coefficient with ionic strength (J) in the presence of the supporting electrolyte was evaluated by the relationship[33]:

$$D = D_0(1 - \frac{A}{2}\sqrt{J}) \qquad (6.1.8)$$

where D and D_0 are the diffusion coefficients of the electroactive species at the given J and at infinite dilution, respectively, A is the Debye constant, which depends on both the nature of the medium and temperature[37,38]. For the 50% (v/v) E/W medium, at 293.15 K, A = 0.9804 $Kg^{1/2}$ $mol^{-1/2}$, [39] while J = 0.15 M (i.e., due to 0.05 M Na_2SO_4). Using equations (6.1.1–3) and the above values for the various parameters, $D_{(HC10)E/W}$ = 1.82 · 10^{-6} cm^2 s^{-1} was evaluated for HC10 in the 50% (v/v) E/W medium at J = 0.15 M.

6.1.4. Evaluation of the theoretical steady-state diffusion limiting currents for reduction of HC10 and HAc in the 50%(v/v) E/W medium

The validity of the above approaches used to calculate D_{HC10} and pKa of HC10 was assessed by comparing experimental current value (I_d) at 1 mM acid concentration with that predicted by equation (6.1.9), developed for reduction of a weak acid through a CE pathway, in which the preceding chemical reaction is fast[40]. For comparison, the theoretical I_d value for 1 mM acetic acid (HAc) was also calculated.

$$I_d = 4\, n\, F\, a\, [D_{H^+}\, C_{H^+} + D_{HA}\, C_{HA}] \qquad (6.1.9)$$

[37] F. Hernández-Luis, M.V. Vázquez, M.A. Esteso. *J. Mol. Liq*. (**2003**) 108, 283-301.
[38] F. Hernández-Luis, H. Galleguillos-Castro, M.A. Esteso. Fluid Phase Equilib. (**2005**) 227, 245-253.
[39] G. Pecchielan, M.A. Baldo, S. Fabris, S. Daniele. *J. Electroanal Chem*. (**2019**) 847:113-166.
[40] S. Daniele, I. Lavagnini, M.A. Baldo, F. Magno. *Anal. Chem*. (**1998**) 70, 285-294.

where D_{H^+} and C_{H^+} are the diffusion coefficient and bulk concentration at equilibrium of the hydrogen ion, while D_{HA} and C_{HA} stand for the diffusion coefficient and bulk concentration at equilibrium of the undissociated acid form (i.e., HC10 or HAc), n =1 and the other symbols have their usual meaning. $D_{H^+} = 3.01 \cdot 10^{-5}$ cm^2 s^{-1} and $D_{HAc} = 5.11 \cdot 10^{-5}$ cm^2 s^{-1} were reported in the literature[23]. By using the dissociation constant of HC10 (pKa = 6.07) and HAc (pKa = 5.73), C_{H^+} and C_{HA} at equilibrium were calculated. From equation (6.1.9), I_d of 1.39 nA and 3.15 nA were obtained for HC10 and HAc, respectively. These values compare well (i.e., within 2%) with those found experimentally.

6.1.5. Voltammetric behavior of Cu^{2+} in the 50%(v/v) E/W medium

Figure 6.1.4 (main picture) shows a typical CV recorded at 5 mVs^{-1} over the potential range from -0.3 to +0.5 V in the background solution containing 1 mM $CuSO_4$. The voltammogram displays the main features expected for the reduction of a metal ion to the metallic phase under nonplanar diffusion[41]. In the forward scan, a composite wave (onset potential at about -0.05 V) is observed. On reversal the potential sweep, a nucleation loop, typical for the growth of a metallic phase onto the solid electrode surface and a stripping peak due to the oxidation of metallic copper are observed[41,42]. In some cases, probably depending on the specific status of the Pt surface, a second small oxidation process at about 0.2 V, was also evident (Figure 6.1.5 b). This could be due to the oxidation of a thin layer of Cu_2O, adsorbed onto the electrode surface, formed during the oxidation of metallic copper. Comparative measurements, performed in Milli-Q water containing 1 mM $CuSO_4$ and 0.05 M Na_2SO_4, displayed, in general, similar voltammetric features (see inset in Figure 6.1.5a, magenta line). However, in the latter case, the current intensities of both cathodic and anodic responses were larger, while the onset of the

[41] M.A. Baldo, C. Bragato, G.A. Mazzocchin, S. Daniele. *Electrochim. Acta* (**1998**) 23, 3413-3422.
[42] B. Scharifker, G.J. Hills, *J. Electroanal. Chem*. (**1981**) 130, 81–97.

cathodic wave was about 40 mV more negative than that recorded in the 50%(v/v) E/W medium. The effect of the medium on the current intensities is, conceivably, due to the different viscosities (η_s) of water (0.8914 mPa s, at 25°C)[35,36] and 50% (v/v) E/W mixture (2.3869 mPa s, at 25°C)[35], which reflect on the diffusion coefficient of the Cu^{2+} ion[33]. Using the plateau current of the waves obtained in the two media and equation (5.2.9), diffusion coefficient values for Cu^{2+} of $2.45 \cdot 10^{-6}$ cm^2 s^{-1} and $6.22 \cdot 10^{-6}$ cm^2 s^{-1} were evaluated in the 50%(v/v) E/W and aqueous solutions, respectively. The corresponding Walden products ($D \cdot \eta$, D in cm^2 s^{-1}, η in mPa s)[43] were 5.85 and 5.54, respectively, which differ only by about 5%, confirming that the major effect on current intensity can be ascribed to the viscosity of the medium.

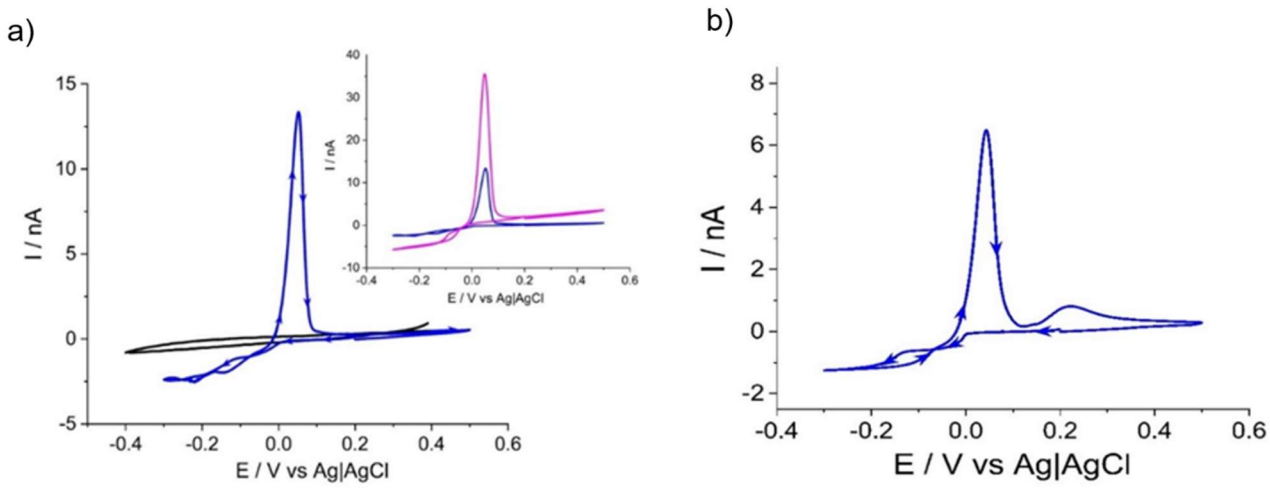

***Figure 6.1.5**: a) CVs recorded at the Pt 12.5 μm disk in the 50% (v/v) E/W containing 1 mM $CuSO_4$ + 0.05 M Na_2SO_4 (blue lines); background current (black line). Inset: comparison between CVs obtained 1mM $CuSO_4$ in the 50% (v/v) E/W (blue line) and H_2O+0.05 M Na_2SO_4 (magenta line); b) Conditions as in a) (main picture). Scan rate 5 mV s^{-1}.*

The potential onset at less negative potentials, observed in the E/W mixture with respect to the aqueous solution, can be related to a different solvation of Cu^{2+} ions in the two media or to the formation of a complex, whose reduction requires a smaller activation energy[14]. In fact, it was reported that the octahedral $Cu(H_2O)_6^{2+}$ species, which exists in pure water, can change into

a $Cu(H_2O)_5(C_2H_5OH)^{2+}$ in E/W solutions[43]. Similar findings on current intensity, shape and position of the waves, changing the medium from water to E/W mixtures, were also reported in Refs. [14,15], in which the reduction of Cu^{2+} ions was investigated by polarography[14] and at a copper film- modified platinum electrode[15] in E/W solutions up to an ethanol content of 30% (v/v).
The unexpected composite wave recorded in the forward scan, suggesting the occurrence of a multistep process, could also be due to trace of chloride ions present in the electrolyte, which stabilize the Cu^+ ion[44].

6.1.6. Voltammetric behavior of 1 mM Cu^{2+} in the base electrolyte without and with 10 mM KCl

Measurements performed in the 1 mM $CuSO_4$ 50% (v/v) E/W medium spiked with 10 mM KCl displayed a clear wave split (Figure 6.1.6), the first of which occurring at less negative value ($E_{1/2}$ = 0.1V). This can be ascribed to the formation of the cuprous $CuCl_2^-$ specie[44], similarly to what happens in aqueous solutions[20]. Indeed, in the presence of Cl^- ions, the reduction process of Cu^{2+} to Cu^0 occurs in two steps through the formation of the stable $CuCl_2^-$ species[20:]

$$Cu^{2+} + 2Cl^- + e^- \rightleftharpoons CuCl_2^- \qquad (6.1.10)$$

$$CuCl_2^- + e^- \rightleftharpoons Cu^0 + 2Cl^- \qquad (6.1.11)$$

This leads to the shift of the first reduction process towards less negative potentials and the nucleation process to metallic copper towards more negative values (Figure 6.1.6, red line).

[43] N.J. Friedman, R.A. Plane, *Inorg. Chem.* (**1963**) 2, 11-14
[44] S.E. Manahan, R.T. Iwamoto, *J. Electroanal. Chem.* (**1967**) 13, 411-417.

For this reason, the amount of copper deposited decreased, as was evident from the lower currents involved in the stripping peak recorded upon scan reversal. The formation of stable soluble $CuCl_2^-$ species was testified by the sigmoidal shaped wave recorded, when the scan was reversed from the plateau region of the first wave (Figure 6.1.6, inset), as expected for a diffusion-controlled process at a microelectrode.

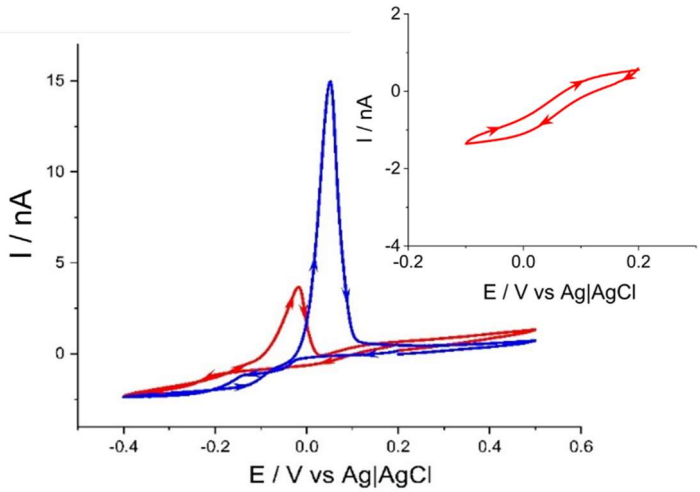

***Figure 6.1.6**: Comparison between CVs recorded at a Pt 12.5 µm in a 50% (v/v) E/W + 0.05 M Na_2SO_4, containing 1mM $CuSO_4$ (blue line) and 10 mM KCl (red line). Inset CV recorded by reversing the potential scan over the plateau region of the first wave. Scan rate 5 mV s^{-1}.*

6.1.7. Voltammetric behavior of Cu^{2+} in the base electrolyte containing HC10 at different concentrations

In the presence of HC10, the voltammetric behavior of Cu^{2+} changed to a different extent, depending on the HC10/Cu^{2+} ratio and the time left to the solution to equilibrate. Figure 6.1.7 (blue lines) shows typical CVs recorded in the 50%(v/v) E/W solution containing 1 mM each of Cu^{2+} and HC10. In general, composite waves were recorded in the forward scan, to which a stripping peak was associated on scan reversal. Current intensities of both cathodic and anodic processes decreased, while the positions of the corresponding wave and peak shifted towards

more negative and positive potentials, respectively, with respect to that obtained in the absence of HC10 (compare CVs in Figures. 6.1.5 and 6.1.7). It must be highlighted that the CV with the blue dashed line was recorded after about 30 minutes from the addition of HC10 to the Cu^{2+} solution. It changed to that shown in Figure 6.1.7 with the blue full line after 2 hours equilibration, denoting a further decrease of the current intensities of both cathodic and anodic processes, along with a further shift of the stripping peak towards a more positive potential.

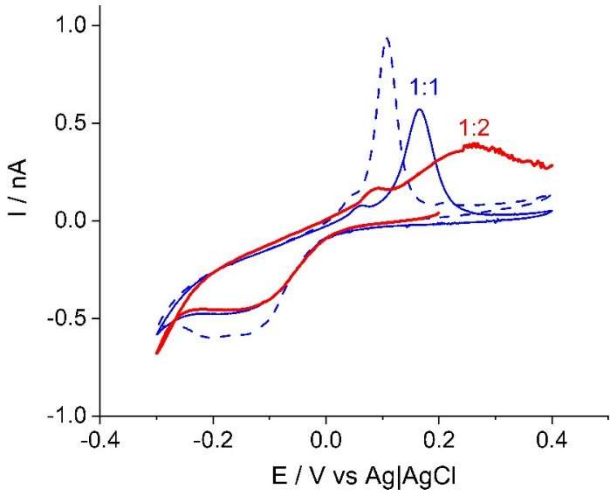

***Figure 6.1.7**: CVs recorded at the Pt 12.5 µm disk in the 50% (v/v) E/W + 0.05M Na_2SO_4 containing 1 mM (blue lines) and 2 mM (red line) (HC10). Scan rate 5 mV s^{-1}. CV with the blue dashed line was recorded after 30 min equilibration time; CVs with the blue and red full lines were recorded after 2 h equilibration time.*

These results suggest that HC10 interacts slowly with Cu^{2+} ions and that the oxidation process of metallic copper, deposited onto the electrode surface, is somewhat inhibited. The formation of a soluble (reaction 6.1.12)[21] or an adsorbed, onto the electrode surface (reaction 6.1.13)[6], Cu(II)-HC10 species can be responsible of the observed voltammetric behavior.

$$Cu^{2+} + 2\ HC10 \rightleftharpoons Cu(C10)_2 + 2\ H^+ \qquad (6.1.12)$$

$$Cu^{2+} + 2\ HC10 \rightleftharpoons Cu(C10)_{2ads} + 2\ H^+ \qquad (6.1.13)$$

In addition, the monomeric $Cu(C10)_2$ molecule, in the E/W mixture, can transform in a dimeric Cu-HC10 species[45,46]. To take into account the fact that the interaction between Cu^{2+} and HC10 was slow, in what follows, unless otherwise stated, the CVs displayed in the figures, were recorded after letting the solution to equilibrate for about 2 hours under stirring.

The stoichiometry of reactions (12)-(13) is 1:2; therefore, measurements were also performed in a solution containing Cu^{2+} and HC10 in the concentration ratio 1:2 (Figure 6.1.7, red line). Compared to that obtained in the Cu^{2+} and HC10 1:1 ratio, the cathodic wave decreased somewhat, while the stripping peak was lower and further shifted towards nobler potentials. These facts confirm that Cu^{2+} ions interact slowly with HC10, while the thin copper film, formed onto the electrode surface, is further passivated.

To investigate whether the decrease of the current, associated to the reduction process of Cu^{2+} to Cu^0, was due to the formation of stable, soluble and electroactive copper carboxylate complexes, the voltammetric investigation was extended in the negative potential region up to the solvent discharge. Figure 6.1.8 shows CVs recorded in solution containing Cu^{2+} and HC10 in the concentration ratio 1:1 (Figure 6.1.8a) and 1:2 (Figure 6.1.8b).

It is seen that in both cases, in the forward scan, apart from the above-mentioned processes occurring over the potential 0 to -0.3V, additional waves with $E_{1/2}$ at about -0.35 V, -0.70 and -0.87 V appear (details in the insets in Figure 6.1.8 a,b). On reversal the potential scan, a current crossover point, between the anodic and the cathodic branches of the CVs (at about -0.97 V) and a stripping peak at about 0.25 V are observed.

[45] Y. Hiromichi, K. Ryoji, K. Ikuo. *Bulletin of the Chemical Society of Japan* (**1983**) 56, 3302-3305.
[46] M. Kato, H.B. Jonassen, J. C. Fanning, *Chem. Rev*. (**1964**) 64, 99 – 128.

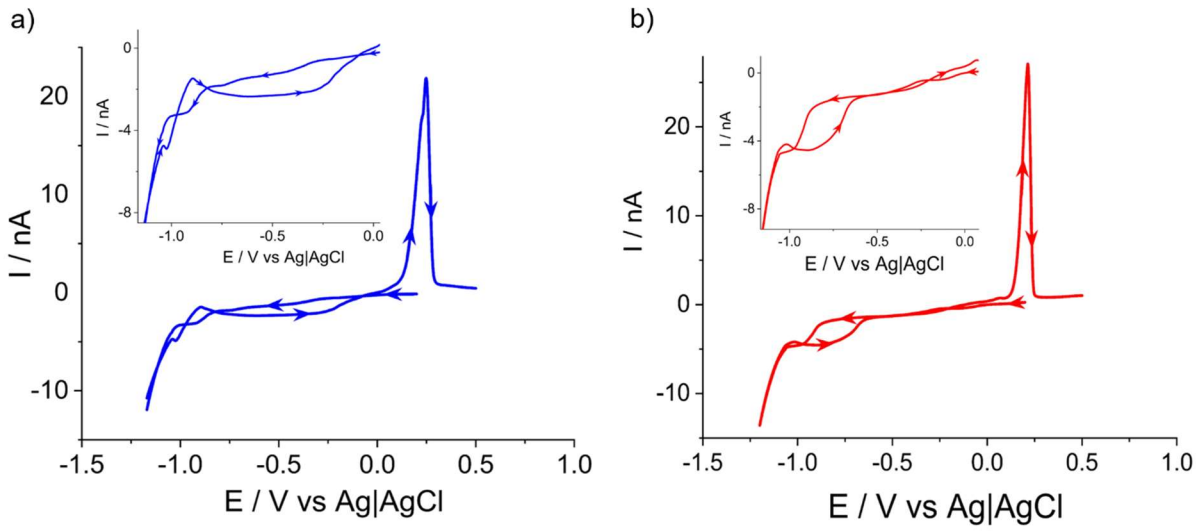

***Figure 6.1.8**: CVs recorded in a 50% (v/v) E/W + 0.05 M Na_2SO_4 solution containing 1 mM $CuSO_4$ and a) 1 mM and b) 2 mM HC10. Insets in the figures are enlargements of the cathodic zones. Scan rate 5 mV s^{-1}.*

The waves with $E_{1/2}$ of -0.35Vand -0.70 V can be assigned to the reduction of the monomeric and dimeric $Cu(C10)_2$ complexes. The reduction wave with $E_{1/2}$ = -0.90 V was assigned to the hydrogen evolution process due to the reduction of either H^+, released in reaction (6.1.12), or free HC10 (through the CE reactions (6.1.4) and (6.1.5)). The shift of hydrogen evolution process towards more negative potentials, can be explained considering that it occurred on a copper-coated Pt surface and, therefore, affected by a large overvoltage[47]. The current crossover point was instead related to the continuous nucleation and growth of metallic copper onto the microelectrode surface.

[47] X. Zhang, Y. Zhang, F. Lia, C.D. Easton, A.M. Bond, J. Zhang, *Applied Catalysis B: Environmental* (**2019**) 249, 227-234.

A further increase of the HC10 content in the medium (up to Cu^{2+}/HC10 concentration ratio of 1:10 (Figure 6.1.9) enhanced to some extent the changes in the CV features highlighted above.

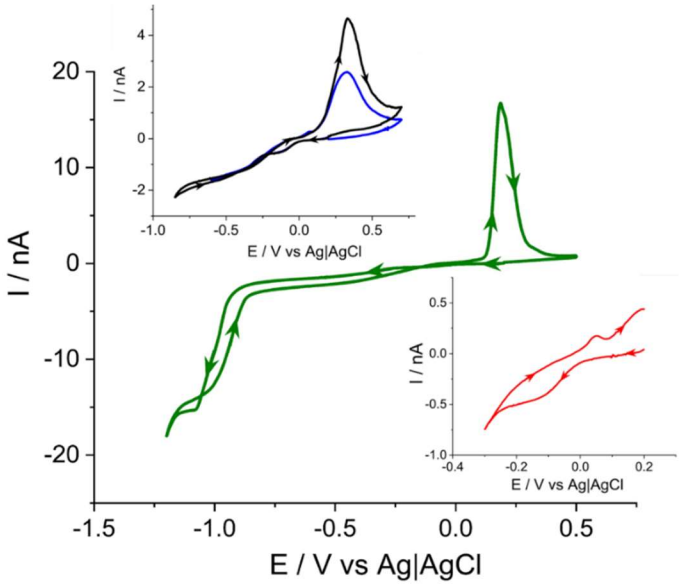

***Figure 6.1.9**: CVs recorded at a Pt microelectrode in the 1:10 Cu^{2+}/HC10 ratio (green line) in 50% (v/v) E/W + 0.05 M Na_2SO_4 mixture. Insets: potential scan reversal at -0.85V (black line), -0.6V (blue line) and -0.3 V (red line). Scan rate 5 mV s^{-1}.*

In fact, when the potential was scanned to more negative potentials, up to -0.6 and -0.85 V, where the $Cu(C10)_2$ species could be reduced to metallic copper, a current crossover and the stripping peak were recorded on scan reversal (blue and black lines in the inset of Figure 6.1.9). It is also noteworthy that, even with the excess of HC10, a small wave, due to the reduction of free Cu^{2+} ions, occurring over the potential range 0 ÷ -0.3 V, was still found (red line in inset of Figure 6.1.9). This would due to either the slow formation of the $Cu(C10)_2$ complex species, or to the fact that the apparent stability constants of the Cu(II)-C10 complex species were not high enough to make the amount of free Cu^{2+} ions negligible. A lower apparent stability constant is justified considering that the pH of the medium varied between 3.3 and 4.1 (depending on the amount of HC10 added in the solution), at which, based on the above calculated *pKa* value, undissociated HC10 is the prevailing form.

6.1.8. Voltammetric behavior of 1 mM Cu^{2+} without and with 10 mM KCl and HC10

The voltammetric behavior at Pt microelectrode of 1 mM Cu^{2+} in the base electrolyte was also studied in the presence of both KCl and HC10. The CVs shown in Figure 6.1.10a contrast the effect of the addition of 10 mM KCl (green line) and both 10 mM KCl and 1 mM HC10 (red line) in the 50% E/W medium, containing 1 mM Cu^{2+} and 0.05M Na_2SO_4.

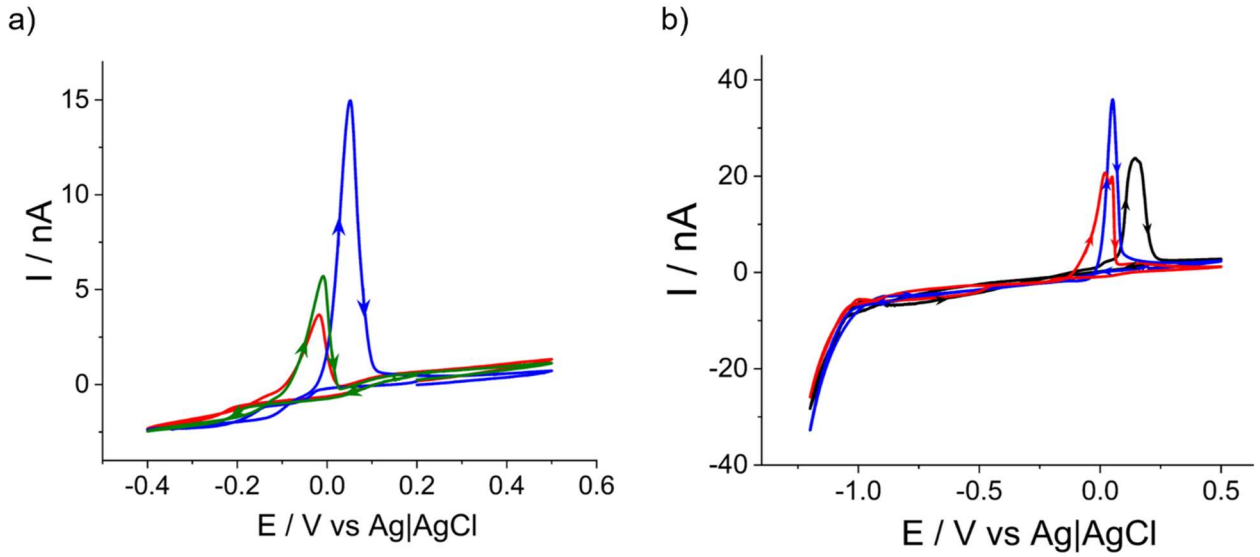

***Figure 6.1.10**: CVs recorded at a Pt 12.5 µm in a 50% (v/v) E/W + 0.05M Na_2SO_4, containing 1mM $CuSO_4$ (blue lines) and: a)10 mM KCl (green line) and 10 mM KCl + 1 mM HC10 (red line); b) 1 mM HC10 (black line) and 1 mM HC10 + 10 mM KCl (red line). Scan rate 5 mV s^{-1}.*

The addition of KCl provides the same effect, as discussed above (Figure 6.1.6, red line). The addition of 1 mM (HC10) leads to a small decrease of the wave/stripping peak due to the reduction/oxidation of the Cu^{2+}/Cu^0 system, indicating that HC10 interacts with Cu^{2+}, also in the presence of Cl^- ions. The CVs shown in Figure 6.1.10b compare the effect of 1 mM HC10 (red line) and a that of 1mM HC10 and 1 mM KCl (green line) on the Cu^{2+}/Cu^0 system over a wider potential window. It is evident that in the presence of HC10, the stripping peak is much more shifted towards positive potentials, indicating a passivation effect of the copper deposited onto the electrode surface. In the presence of Cl^-, the oxidation of metallic copper starts occurring at

less positive potentials, congruently with the greater tendency to corrosion[8]. Under these conditions, the Cu^{2+} reduction process shifted towards less negative potentials, due to the formation of the $CuCl_2^-$ species, the stripping peak decreased, while the passivation effect of the just deposited copper film, due to HC10, was less effective. These results are congruent with an enhanced corrosion process of copper materials in media containing Cl^- ions[48].

6.1.9. Effects of the water content increase

Series of CVs were performed in in a 25%/75% (v/v) E/W medium spiked with HC10, which can undergo coacervation[11]. In fact, when the E/W solution, containing 1 mM Cu^{2+} and 0.05 M Na_2SO_4, was spiked with 2 mM HC10, at the beginning, an opalescence appeared. This was followed by the slow formation of a pale blue precipitate. The latter can be due to $Cu(C10)_2$, which is sparingly soluble in water-rich media[21]. In fact, the solubility of $Cu(HC10)_2$ in pure water was reported to be $1.34 \cdot 10^{-5}$ M (at pH = 4.66)[49]; it can be higher in the E/W mixture and this was verified by running CVs in the colloidal medium. A typical response thus obtained is displayed in Figure 6.1.11 (black line). In the forward scan, a well-defined wave with $E_{1/2}$ = -0.47 V due to the reduction of a Cu(II)-HC10 species was recorded; the process at $E_{1/2}$ = -0.95 V, attributed to the hydrogen evolution reaction (see above) also appeared. In the reverse scan, the crossover point and the stripping peak, typical for nucleation/oxidation of metallic copper (see discussion above), confirmed the involvement of electroactive soluble copper species.

[48] Y. Zhang, Y. Chen, *Corrosion Engineering, Science and Technology* (**2019**) 54, 75 – 85.
[49] S. Mauchauffee, E. Meux, M. Schneider, *Ind. Eng. Chem. Res.* (**2008**) 47, 7533 – 7537.

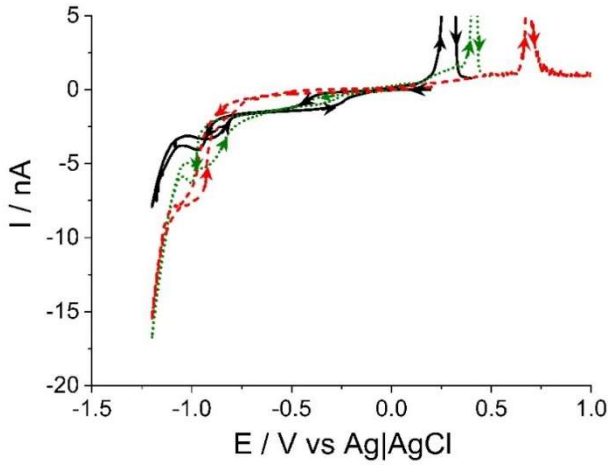

***Figure 6.1.11**: CVs recorded at a Pt microelectrode in a 25% /75% (v/v) E/W + 0.05 M Na_2SO_4 mixture, containing 1 mM Cu^{2+} and 2 mM (black line), 3 mM (green line) and 4 mM (green line) HC10. Scan rate 5 mV s^{-1}.*

Excess of HC10 in the solutions provided further changes in the voltammetric features, as is displayed in Figure 6.1.11, which sows CVs recorded after the addition of 3 mM (green line) and 4 mM (red line) HC10. The wave height of the process at -0.47 V, due to Cu(II)-species, decreased increasing the HC10 concentration, while the stripping peak shifted towards more positive potentials. This was associated to a decrease of the charge involved in the stripping peaks (i.e., 254.8, 217.4 and 91.6 nC by increasing the HC10 from 2 to 4 mM, respectively). These results are again congruent with the formation of solid Cu(II)-HC10 species, which separate from the homogeneous medium, as well as with an increasing inhibition effect of HC10 towards the oxidation of metallic copper deposited onto the electrode surface. The excess of HC10 in the medium provided also an increase of the wave due to the hydrogen evolution process at -0.95 V.

To confirm that the sparingly soluble product formed in the above experiments was due to $Cu(C10)_2$, the solid compound was filtered, rinsed with deionized water and then examined by FTIR. Figure 6.1.12 compares the spectra obtained for the blue precipitate and that for the pure HC10.

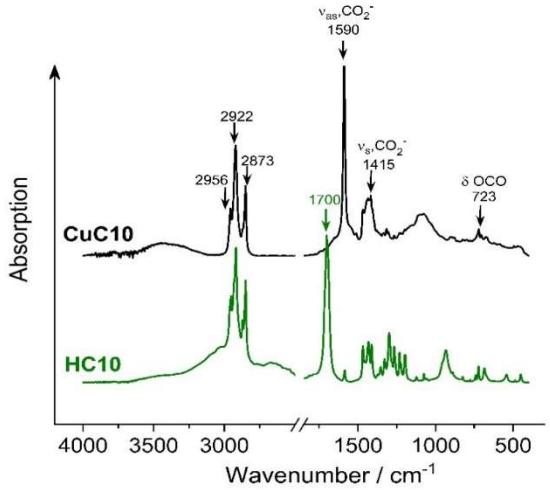

***Figure 6.1.12**: Comparison of the FT-IR spectra of $Cu(C10)_2$ (black line) and HC10 (green line).*

The spectra show absorption peaks at 2873, 2922 and 2956 cm^{-1}, which are related to the symmetric and asymmetric stretching vibrations of CH bonding[6,21,50,51,52,53]. These characterize the presence in both compounds examined of the alkyl chain of HC10. The absorption frequency of the COO^- stretching, which is highly sensitive to both the structure of the carboxylate group and the identity of the metal ion[6], allowed distinguishing between carboxylic acid and copper carboxylate[6,21]. In fact, the absorption band at 1590 cm^{-1} of the carbonyl group was due to the asymmetric COO^- stretching of copper decanoate (indicated as CuC10 in Figure 6.1.12), while the carbonyl group of HC10 occurred at 1700 cm^{-1}. [21]

[50] Y-T. Tao, W-L. Lin, G.D. Hietpas, D.L. Allara, *J. Phys. Chem. B* (**1997**) 101, 9732-9740.
[51] E.G. Papageorgiou, E.P. Kouvelos, E.P. Favvas, A.A. Sapalidis, G.E. Romanos, F.K. Katsaros, *Carbohydr. Res*. (**2010**) 345, 469-473.
[52] Y-T. Tao. *J. Am. Chem. Soc*. (**1993**) 115, 4350-4358.
[53] L. Chen, H. Meng, L. Jiang, S. Wang, *Chem. Asian J.* (**2011**) 6, 1757 – 1760.

6.1.10. Implications of the inhibition processes of HC10 on copper materials immersed in E/W media

As already mentioned, the inhibitory effect of HC10 on copper materials was explained as due, ultimately, to the formation on their surface of an insoluble layer of $Cu(C10)_2$. However, as suggested in previous works, the inhibition mechanism could involve the initial formation at the copper surface of either Cu^+ or Cu^{2+} ions, which in the solution can prompt react with the inhibitor to form copper(I) or copper(II) carboxylate species[5,6,7,8,10]. Based on our results, it appears that only soluble species of $Cu(C10)_2$ can be formed in the E/W mixture employed here, and it is likely that the same occurs in E/W mixtures with higher alcohol content[54]. Therefore, the inhibiting layer can be formed through a dissolution-precipitation mechanism involving mainly Cu^{2+}, formed initially by corrosion of the copper material, due to oxygen from air, followed by the reaction with HC10 to form the $Cu(C10)_2$. This compound can be slowly adsorbed onto the just corroded copper surface, preventing further release of Cu^{2+} ions. This view is congruent with the results obtained in Refs [53,54], in which copper inhibition measurements were performed in an ethanol solution containing various *n*-alkanoic acids, $CH_3(CH_2)_nCOOH$ (*n*= 1- 16). The formation of Cu(I)-carboxylate species was hypothesized in Refs [7,8], using a similar series of *n*-alkanoic acids, in ethanol rich solvents. Since, no evidence was found here on the formation of soluble Cu(I)-carboxylate species the latter can be formed directly on the solid material surface through Cu^+ diffusing from a Cu_2O surface film[8]. Cu_2O can actually be formed during the first stage of the copper corrosion process and it is favored in neutral or basic water media[6]. The Cu(I)-carboxylate species can be obtained after the formation of self-assembled monolayers of the *n*-alkanoic acids onto the surface of native Cu_2O[52]. It must be considered that Cu(I)-carboxylate complexes can gradually oxidize into the corresponding Cu(II)-complex

[54] S. Wang, L. Feng, H. Liu, T. Sun, X. Zhang, L. Jiang, D. Zhu. *ChemPhysChem* (**2005**) 6, 1475 – 1478.

species [55], which would agree with the circumstance that, essentially, adsorbed Cu(II)-carboxylate species were reported to be the final product of the HC10 inhibition process[5,6,7,8,9,53,54,55].

Finally, the results obtained in this section indicate that in the presence of relatively high concentrations of Cl^- ions (i.e., 0.1 M), $CuCl_2^-$ can be formed also in the E/W medium and its stability is little affected by the presence of HC10.

[55] M.M. Antonijevic, M.B. Petrovic, *Int. J. Electrochem. Sci.* (**2008**) 3, 1 – 28.

6.2. Comparative protective effects of HC10, NaC10 and BTA

For the protection of copper-based artefacts exposed outdoors, the most largely used inhibitor is benzotriazole (BTA), which has been considered for a long time as the reference corrosion inhibitor[1,2]. Its use in the field of conservation of archaeological and historical copper-based objects dates back to the 1960s[3]. However, since BTA is suspected of being toxic (i.e., because of its aromatic content in the molecule) and carcinogenic[4,5], in the last decades its use is discouraged, which results in an increase of studies on harmless inhibitors[6,7,8]. As eco-friendly and human-safe alternative, the protective effect of HC10 has been explained as due to the formation of a water-insoluble layer of copper decanoate inside the patina by using spectroscopic and Scanning Auger Microscopy techniques[8,9]. As seen in the previous section, for corrosion studies and corrosion mechanisms investigations, electrochemical techniques are fundamental to provide additional information on redox activity of the materials.

In this part of the PhD project, it was investigated the protective role of two non-toxic compounds, namely decanoic acid (HC10) and sodium decanoate (NaC10) compared to benzotriazole (BTA) on naturally corroded copper roof claddings.

[1] M. Finšgar, I. Milošev, *Corros. Sci*. (**2010**) 52, 2737–2749.
[2] M. Albini, P. Letardi, L. Mathys, L. Brambilla, J. Schröter, P. Junier, E. Joseph, *Corros. Sci*. (**2018**) 143, 84–92.
[3] H. Brinch Madsen, *Stud. Conserv*. (**1967**) 12, 163–167.
[4] D. Pillard, J. Cornell, D. Dufresne, M. Hernandez, *Water Res*. (**2001**) 35, 557–560.
[5] J.-W. Kim, K.-H. Chang, T. Isobe, and S. Tanabe, *J. Toxicol. Sci.* (**2011**) 36, 247–251.
[6] E. Rocca, G. Bertrand, C. Rapin, and J. C. Labrune, *J. Electroanal. Chem*. (**2001**) 503, 133–140.
[7] G. Žerjav, I. Milošev, *Int. J. Electrochem. Sci.* (**2014**) 9, 2696–2715.
[8] E. Apchain, Apport des traitements carboxylates à la protection des alliages cuivreux, Matériaux, Université de Cergy Pontoise (UCP) (**2018**).
[9] M. L'héronde, M. Bouttemy, F. Mercier-Bion, D. Neff, E. Apchain, A. Etcheberry and P. Dillmann, Heritage (**2019**) 2, 2640–2651.

6.2.1. Samples composition and treatment conditions

Bare copper samples employed were mainly constitute of copper. Samples of naturally corroded copper were cut (ca. 1×1 cm^2) from a larger copper plate (Figure 6.2.1). The plate was originally part of the roof cladding of St. Martin's Church in Metz (France) undergone long-term (>100 years) atmospheric corrosion. The samples consist of pure copper containing two types of micrometric inclusions: cuprite inclusions and inclusions containing lead and arsenic. The side exposed to the atmosphere is easily distinguishable by the characteristic pale green corrosion layer present on the top (Figure 6.2.1a).

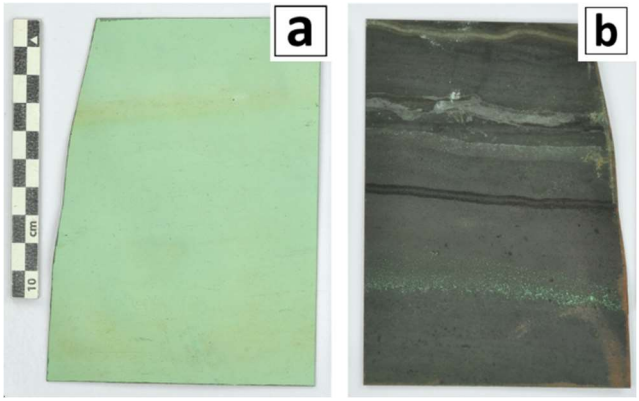

Figure 6.2.1*: Top view of the corroded copper roof cladding of St. Martin's Church in Metz. Front side (a) and back side (b).*

The treatment of both bare and naturally corroded copper samples was performed by soaking the samples for 2 hours in a solution containing each of the inhibitors studied: decanoic acid (HC10), sodium decanoate (NaC10) and benzotriazole (BTA) (see paragraph 4.4.1 of the Experimental for details). As references, both bare and naturally corroded copper samples were also tested without any treatment (labelled "untreated" samples). After the treatment the samples were left drying for 10/20 minutes to open air and then treated, as well as untreated, samples were immersed in acid rain for 24 hours (see paragraph 4.4.2 of the Experimental chapter).

6.2.2. Surface characterization by non-electrochemical methods

In order to understand the impact of the various treatments on historical materials the surface analyses were carried out exclusively on the corroded samples (both untreated and treated with the inhibitors) from the cooper cladding from the St. Martin's Church in Metz (France).

Color change

Colorimetric parameter data (L*, a*, b*) and global color changes (ΔE*) were computed using the color of the untreated sample as the reference. Results were calculated from the reflectance spectra and expressed in the CIEL*a*b* color space[10]; the color difference (ΔE) between untreated and treated samples was calculated as:

$$\Delta E = \sqrt{(\Delta L^*)^2 + (\Delta a^*)^2 + (\Delta b^*)^2} \qquad (6.2.1)$$

where, ΔL^*, Δa^* and Δb^* represent the differences for each color parameter (L*, a*, b*) before and after treatment with the various inhibitors. Results of the color measurements for each sample before and after treatment are summarized in Table 6.2.1.

As displayed in Table 6.2.1, the data confirm that the color of the untreated sample (before treatment) was uniform, as variations of L*, a* and b* parameters across three samples are relatively small (1.3% for L*, 5.7% for a* and 7.1% for b*). After the treatment with the inhibitors, all samples showed a change in color (ΔE>0). For the NaC10-treated sample, ΔE was the lowest, indicating that the treatment had only a minor effect on the original color of the corroded copper plate. The parameters a* and b* decreased, while lightness (L*) remained unchanged, resulting in a slight whitening of the overall surface.

[10] CIE 1976 L*a*b*Color Space, Commission Internationale de L'Eclairage, CIE Central Bureau: Vienna, Austria, (**2007**).

The treatments both with BTA and HC10 treatments caused an appreciable change in the color of the samples: ΔE being equal to 15.6 and 17.6 respectively. In the case of BTA, the decrease of the L* value reflected a shift in color towards dark-green, in agreement with observations reported in the literature[11,12]. As for HC10 the decrease of b* value reflected a color shift towards a blue hue.

Table 6.2.1*: Color measurements on the naturally corroded samples before (Untreated) and after each treatment. The SCI (specular component included) values are reported here.*

Sample	L*(SCI)	a*(SCI)	b*(SCI)	ΔE
Untreated	71.97	-12.23	14.1	-
BTA-treated	58.9	-18.5	16.1	15.6
HC10-treated	65.6	-24.4	4.8	17.6
NaC10-treated	70.5	-13	6.2	7.6

Surface morphology

When observed under an optical microscope (OM) (Figure 6.2.2), the untreated surface was characterized by the presence of craters of about 30 μm diameter, phenomenon previously observed on another historical copper roof cladding[13]; red and black stains were also visible. The stains may be due to external contamination incorporated into the surface. Both craters and stains were observed in the treated samples as well. The HC10-treated sample had a not uniform surface with patchy-colored zones.

[11] M. Albini, P. Letardi, L. Mathys, L. Brambilla, J. Schröter, P. Junier, E. Joseph, *Corros. Sci*. (**2018**) 143, 84–92.
[12] R.B. Faltermeier, *Stud. Conserv*. (**1998**) 44, 121–128.
[13] M. Morcillo, T.Chang, B.Chico, D.de la Fuente, I. Odnevall Wallinder, J.A.Jiménez, C.Leygraf, *Mater. Charact*. (**2017**) 133, 146–155.

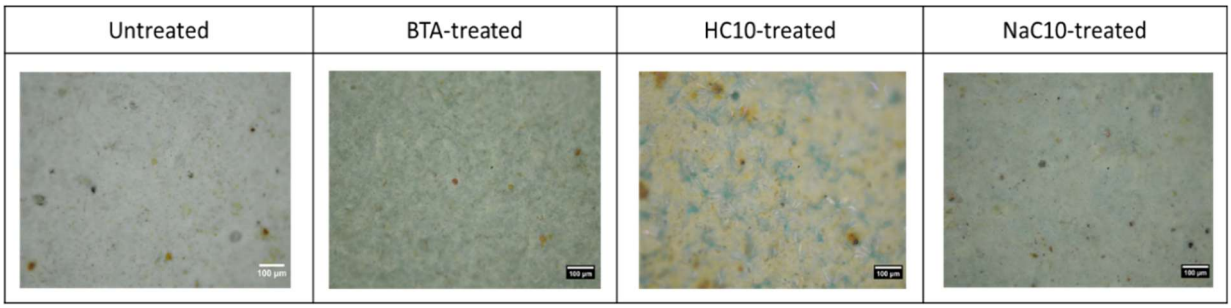

Figure 6.2.1*: Sample surface before (Untreated) and after each treatment observed by optical microscope (100X, bright field).*

In order to qualify the change in surface morphology at a higher magnification, are the SEM micrographs were taken in secondary electron mode. Figure 6.2.3 shows the main morphological modifications of the untreated (Figure 6.2.3a) and treated surfaces (Figure 6.2.3b-c).

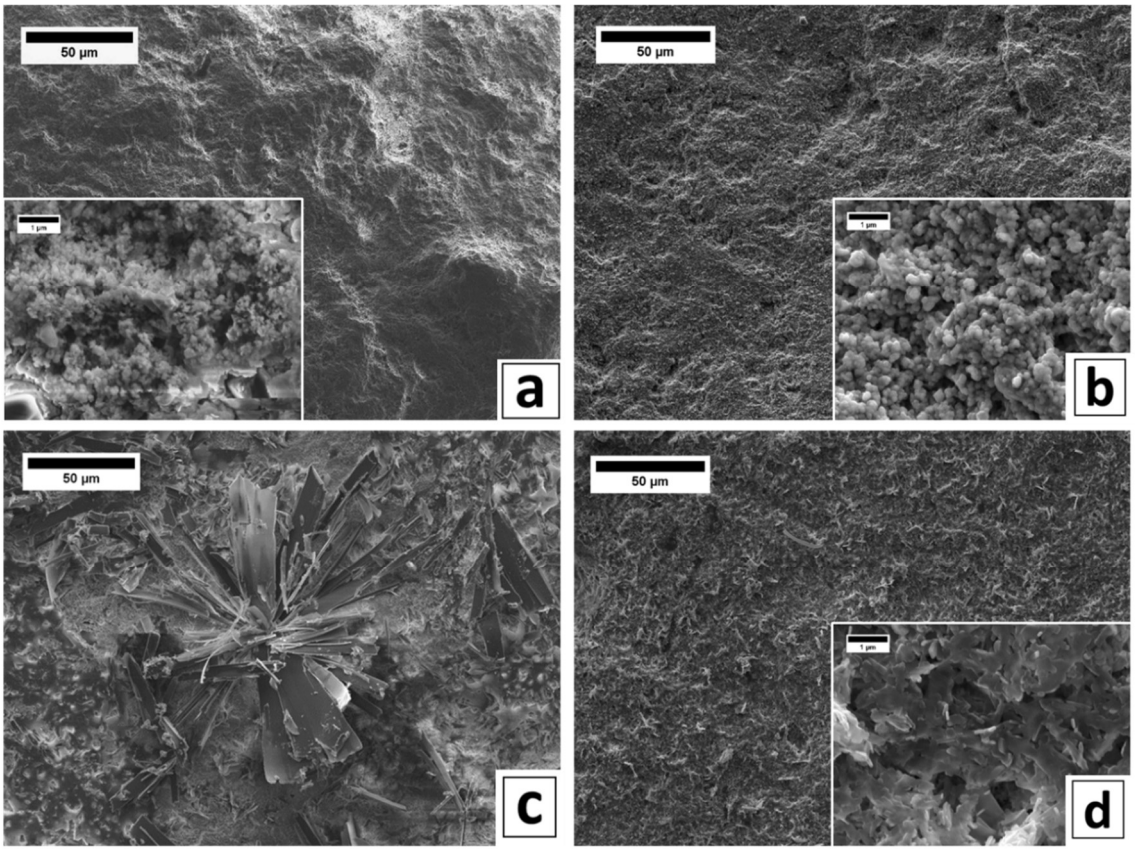

Figure 6.2.2*: Secondary electron images of the surfaces of (a) Untreated, (b) BTA-treated, (c) HC10-treated and (d) NaC10-treated samples.*

The untreated surface (Figure 6.2.3a) appeared covered by powdery aggregates (diameter <0.1μm). The BTA-treated sample showed well defined round-shaped aggregates (Figure 6.2.3b). The HC10-treated surface sample shows large elongated crystals forming flower-like clusters (Figure 6.2.3c). Such morphology was observed in previous studies on bare copper treated with long-chain carboxylic acids[14]. The distribution of the crystals is not uniform across the surface; crystals were more abundant in some areas.

In the case of the NaC10 treatment, the surface morphology was completely modified (Figure 6.2.3d). The surface was uniformly covered by irregularly-shaped, flake-like particles of homogeneous size (50-100 nm).

From OM and SEM observations, it appears that the surface morphology is most affected in the case of the two carboxylates treatment.

Surface tension

The surface tension was obtained by contact angle measurements; relevant results are summarized in Figure 6.2.4. The value of the contact angle of the untreated sample was around 20°, with a drastic change of the drop volume occurring in the first 10 seconds due to the hydrophilicity of the surface, for this reason, the contact angle value of the untreated sample is not reported. For the treated samples, stable contact angles higher than 90° were found in all cases. These results indicated that a hydrophobic layer formed on the sample surfaces after treatment with the three inhibitors. Interestingly, for the HC10- and NaC10-treated samples, the contact angles were close to 150°, the value typically observed for super-hydrophobic surfaces[15]. Both HC10 and NaC10 treatments show higher contact angle values compared to BTA-treated samples.

[14] S. Wang, L. Feng, L. Jiang, Adv. Mater. (**2006**) 18, 767–770.
[15] S. Wang, K. Liu, X. Yao, and L. Jiang, *Chem. Rev.* (**2015)** 115, 16, 8230–8293.

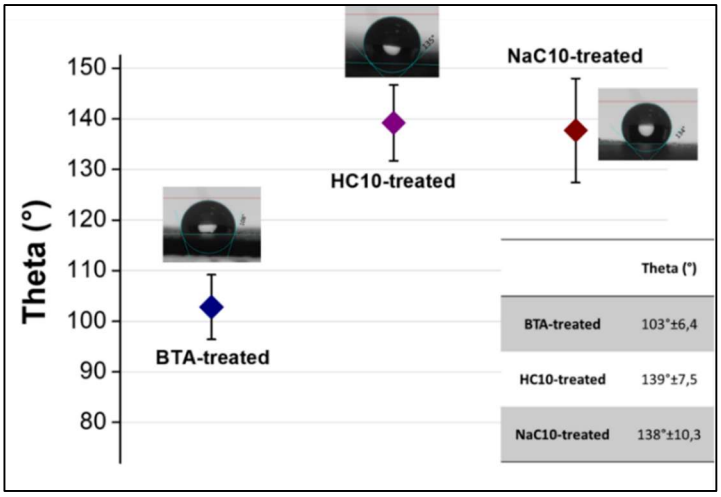

***Figure 6.2.3**: Contact angle measurements on the treated samples.*

Chemical modifications

The surface composition of the various samples was assessed by Raman spectroscopy (Figure 6.2.5). As expected, the main mineral phase found on the untreated sample (Figure 6.2.5a) was brochantite. This was inferred by the strong peak corresponding to the stretching of the SO_4^{2-} group at 973 cm^{-1} and the peaks due to -OH at 3587 cm^{-1} and 3563 cm^{-1} [16,17]; for comparison, a spectrum obtained from a specimen of synthetic brochantite is reported here (Figure 6.2.5a, red line).

The Raman spectra of the samples treated with the inhibitors are displayed in Figure 6.2.5b-d, which also include, for comparison, the reference spectra of the corresponding pure inhibitors (red lines). It must be noted that the band at 973 cm^{-1}, corresponding to the νSO_4^{2-}, could still be identified in all samples (Figure 6.2.5b-d, black lines) confirming that the brochantite was not fully transformed.

Regarding the BTA-treated sample (Figure 6.2.5b, black line), the reactivity of BTA on the surface chemistry was indicated by several differences in band positions when comparing the spectra of pure BTA and the BTA-treated sample. For the latter, there was a notable absence of

[16] M. Schmidt, H. D. Lutz, *Phys. Chem. Miner*. (**1993**) 20, 27–32.
[17] V. Hayez, V. Costa, J. Guillaume, H. Terryn, A. Hubin, *Analyst* (**2005**) 130, 550-556.

the -NH in plane bending mode at 1096 cm^{-1}, which is instead present in the spectrum of the pure BTA (Figure 6.2.5b, red line). This suggested that the –NH group interacted with species present on the sample surface to form, conceivably, the strong N-Cu chemical bond[18]. Other differences include the shift to higher wavenumbers of several bands observed in the spectrum on the treated sample as compared to the reference BTA spectrum. Indeed, the benzene ring breathing mode at 781 cm^{-1} in pure BTA shifted to 790 cm^{-1} on the sample surface and the strong composite band at 1386 cm^{-1} shifted to 1395 cm^{-1}.[19] In addition, the latter bands were broader, compared to those of pure BTA, indicating a lower crystallinity of the material formed on the sample surface[19]. The latter findings also suggested an interaction between Cu(II) species and the N1 atom in benzotriazole to form a Cu-BTA complex (either amorphous or having lower crystallinity compared to solid BTA) on the sample surface, likely mixed with brochantite, according to a previous study [20].

Concerning the sample treated with HC10, the Raman spectrum (Figure 6.2.5c, black line), recorded specifically on the flower-like clusters observed by SEM (Figure 6.2.3c), provided all the ν(Cu-O) modes at 236 cm^{-1}, 288 cm^{-1} and 400 cm^{-1}, which confirmed the presence of copper decanoate[21] on the sample surface (Figure 6.2.5c, blue line).

Controversial information was obtained from the Raman spectra of the sample treated with NaC10 (Figure 6.2.5d, black line). In fact, the band at 288 cm^{-1}, one of the bands that identifies copper decanoate, was generally weaker with respect to the HC10-treated sample (Figure 6.2.5c, black line) and only clearly discernible in certain localized spots of the sample. On the other, the presence of $\nu(CH_2)$ at high wavenumbers and, in particular, the band at 2881 cm^{-1} indicated that a decanoate-type compound was present throughout the sample surface. To shed light on these aspects, EDX analysis was performed on the NaC10-treated surface using a low acceleration

[18] A. Kokalj, S. Peljhan, M. Finsgar, I. Milosev, *J. Am. Chem Soc*. (**2010**) 132, 16657 – 16668.
[19] T. Kosec, A. Legat, P. Ropret, *J. Raman Spectrosc*. (**2014**) 45, 1085–1092.
[20] E. Ferrari, D. Neff, E. Apchain, in Metal 2019 - Proceedings of the Interim Meeting of the ICOM-CC Metals Working Group; Neuchatel (CH), (**2019**).
[21] L. Robinet, M. C. Corbeil, *Stud. Conserv*. (**2003**) 48, 23–40.

voltage (2 keV) in order to differentiate the Na Kα (1.04 eV) from the Cu Lα (0.9 eV). From these analyses was found 7.9 atomic% of sodium, which suggests the presence of some unreacted NaC10, but this information has to be considered as merely indicative.

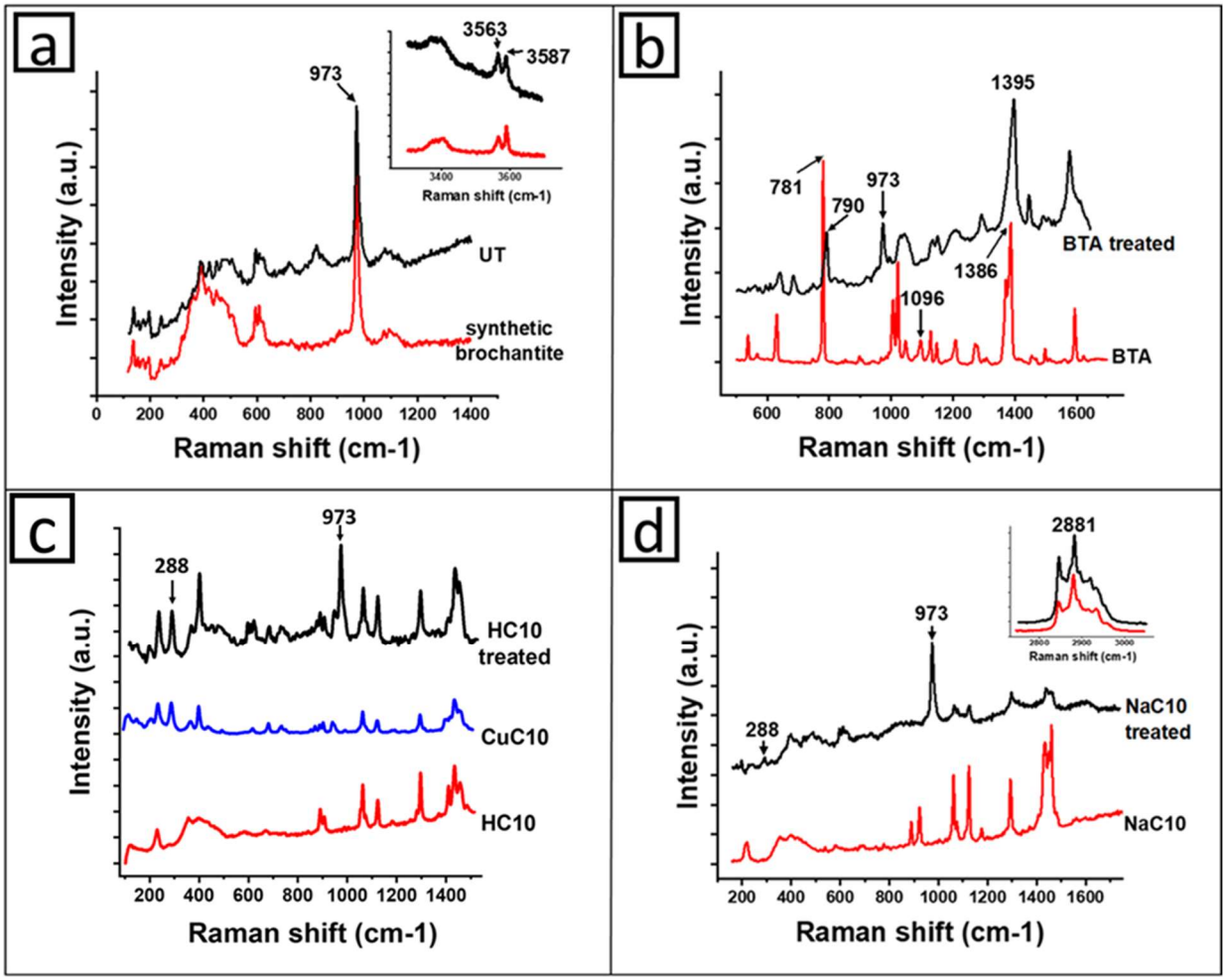

Figure 6.2.4*: Raman spectra recorded on the surface of the samples: a) untreated and treated with b) BTA, c) HC10 and d) NaC10. The black lines refer to the sample surface; the red lines refer to the corresponding reference compound; in c) the reference spectrum of copper decanoate is also presented (blue line).*

6.2.3. Electrochemical measurements

Open circuit potentials (OCP)

Open circuit potential responses for bare copper and naturally corroded samples, both untreated and treated with the various inhibitors, were recorded in synthetic acid rain; typical potential/time profiles obtained are shown in Figure 6.2.6. In all cases, stable OCP values, shown

in Tables 6.2.2 and 6.2.3, were achieved within approximately one hour from the immersion of the samples in the solution.

For the untreated bare copper sample, a constant potential value of 54mV (Table 6.2.2) was quickly reached. This could be due to deposition of passivating corrosion products on the copper surface which occurred shortly after immersion of the sample in the solution. The OCP profiles for the inhibitor-treated samples shifted significantly becoming either more positive, for the BTA-treated sample, or more negative, for both HC10- and NaC10-tretaed samples, conceivably due to a layer of the inhibitors adsorbed on the active corrosion sites of the copper. By comparing the final OCP values of the untreated and treated bare copper samples, BTA could be classified as a mixed-type inhibitor, whereas both HC10 and NaC10 behave like cathodic inhibitors[22].

The OCP profiles obtained for the naturally corroded copper (Figure 6.2.6b) were somewhat noisy, probably due to the porous nature of the corrosion layers. The OCP values (Table 6.2.3) were located positively with respect to the corresponding bare copper specimens, except for BTA. These results indicated that the corrosion layers themselves protected, to some extent, the underline metallic copper from further corrosion. In addition, all organic compounds acted as mixed-type inhibitors[22].

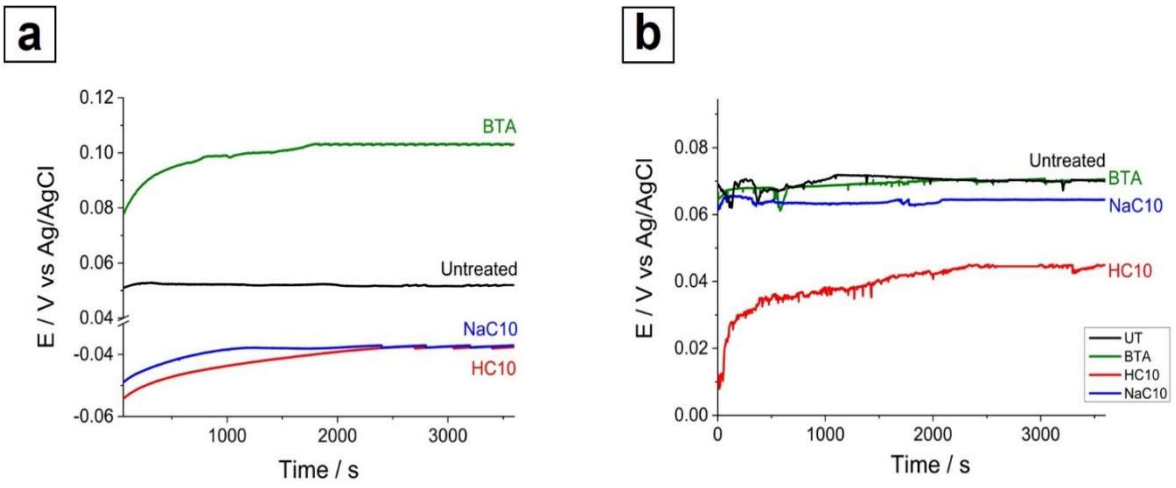

***Figure 6.2.1**: OCP curves of (a) bare copper samples and (b) real corroded samples untreated (black line) and treated with BTA (green line), HC10 (red line) and NaC10 (blue line).*

[22] O. L. Riggs Jr., Corrosion Inhibitors, 2nd ed., C.C. Nathan, Houston, (**1973**).

Potentiodynamic polarization (PDP)

The performances of each treatment on both bare copper and naturally corroded copper samples were evaluated by performing PDP measurements after 24 hours immersion in synthetic acid rain solution. Figure 6.2.7 shows typical PDP curves thus obtained, while Tables 6.2.2 and 6.2.3 summarize the associated electrochemical parameters: corrosion potentials (E_{corr}), corrosion current density (I_{corr}), Tafel slopes (anodic, β_a, and cathodic, β_c) and inhibition efficiency (IE%). The corrosion inhibition efficiency is determined according to the equation (6.2.2):

$$IE\% = [(I_{corrUT} - I_{corrINH}) / I_{corrUT}] \cdot 100 \qquad (6.2.2)$$

where I_{corrUT} and $I_{corrINH}$ are the corrosion current densities of the untreated and treated samples, respectively, determined by the Tafel method.

Data shown in Tables 6.2.2 and 6.2.3 are average values obtained from three different specimens of the same sample immersed in the same test solutions.

***Table 6.2.2**: Electrochemical parameters for bare copper samples untreated and treated with various inhibitors.*

	OCP (mV)	***E_{corr} (mV)***	***I_{corr} (µA)***	***βa (mV/dec)***	***-βc (mV/dec)***	***IE%***
Untreated	54 ± 3	45 ± 2	6.92 ± 0.2	38 ± 1	46 ±1	**-**
BTA	111 ± 3	107 ± 5	0.022 ± 0.005	51 ± 2	56 ± 3	**99.7**
HC10	-41 ± 2	-51 ± 3	0.28 ± 0.01	42 ± 2	60 ± 4	**92.8**
NaC10	-39 ± 3	-49 ± 4	0.29 ± 1.31	41 ± 2	53 ± 3	**92.5**

***Table 6.2.3**: Electrochemical parameters for naturally corroded samples untreated and treated with various inhibitors.*

	OCP (mV)	***E_{corr} (mV)***	***I_{corr} (µA)***	***βa (mV/dec)***	***-βc (mV)/dec***	***IE%***
Untreated	66 ± 2	51 ± 2	2.38±0.07	48 ± 3	73 ± 3	**65.6***
BTA	66 ± 2	56 ± 3	0.032±0.002	60 ± 4	62 ± 2	**98.8**
HC10	43 ± 3	39 ± 2	0.14 ±0.01	40 ± 3	52 ± 3	**94.2**

NaC10	62 ± 2	48 ± 3	0.84 ±0.03	42 ± 4	59 ± 5	**66.2**

*The IE% was evaluated considering $I_{corrUT,}$ as the value obtained from the bare copper sample (i.e., Table 6.2.2, third entry)

All polarization curves recorded for the copper samples (Figure 6.2.7a) showed a regular pattern, regardless of the inhibitor employed. A drop of the corrosion current density occurred with respect to the untreated sample for both the anodic copper dissolution and cathodic reduction reactions. These results suggest that all organic compounds employed exert a protective action against corrosion of metallic copper. However, the extent of the current decrease and, consequently, the inhibition efficiency, depended on the specific inhibitor employed, and it was the largest for BTA. This was also evident from *IE%* values shown in Table 6.2.2 (sixth entries). The average corrosion potential shifted positively for BTA (+62 mV) and negatively for both HC10 (-96 mV) and NaC10 (-94 mV), indicating that BTA treatment predominately controlled the anodic reaction, while both HC10 and NaC10 acted as cathodic type inhibitors[22], likely preventing the occurrence of the oxygen reduction process.

The values of *IE%* for BTA and HC10 found here (99.7% and 92.8%, respectively) are comparable to those reported in the literature for copper samples treated with the same inhibitors (i.e., *IE%* of about 98% and 90%, for BTA[23] and HC10 7, respectively) exposed to acid rain. Concerning NaC10, the *IE%* found here is similar to that of the HC10-treated sample. To the best of our knowledge, no information is available in the literature on inhibition efficiency for NaC10-treated copper samples in acid rain. However, a pronounced copper protection was previously reported[24] using potassium decanoate in an aqueous solution at pH 10.

Considering the potentiodynamic curves recorded with the naturally corroded samples (Figure 6.2.7b) and the associated electrochemical parameters (Table 6.2.3), it was evident that the corrosion potentials of the samples treated with the inhibitors did not change significantly with

[23] G. Žerjav, A. Lanzutti, F. Andreatta, L. Fedrizzi, and I. Milošev, *Mater. Corros*. (**2017**) 68, 30–41.
[24] E. Abelev, D. Starosvetsky, Y. Ein-Eli, *Langmuir* (**2007**) 23, 11281–11288.

respect to the untreated reference sample (i.e., not more than 13 mV). Therefore, from this perspective, it was harder to understand the predominant protection mechanism exerted by each treatment. However, corrosion currents dropped, though to a lesser extent than the corresponding bare copper samples, indicating that the investigated inhibitors, nevertheless, played a positive role in preventing the sample corrosion in the synthetic rain solution. The apparent lower current drop was conceivably due to the fact that the already existing patina on the corroded samples, itself exerted a protective effect against corrosion of the underlying metallic copper. The *IE*% of the untreated corroded sample (Table 6.2.3, sixth entry), calculated by using as I_{corrUT} the value of the untreated bare copper sample (Table 6.2.2, third entry), was equal to 65.6%. With respect to the untreated corroded sample, the *IE%* obtained for BTA- and HC10-treated corroded samples was considerably higher (98.8% and 94%, respectively), indicating a good protective action in acid rain. The lower *IE%* of the NaC10-treated sample (i.e., 66.2%), could be due to a pH effect of the synthetic acid rain on the coating materials formed on the sample surface (possibly on a copper-decanoate species).

Another specific feature of the potentiodynamic curves of the corroded samples was the presence of a double current plateau in the anodic region, the first occurring in the potential range from about 0.1 to 0.12 V. At higher potentials, the anodic current profiles increased and, for the samples treated with HC10 and NaC10, tended to overlap with that of the untreated one. The above behavior could be related to the fact that at potential slightly positive to E_{corr}, the oxidation of the underlying metallic copper led to the growth of a thicker passive Cu_2O layer, which at higher overpotentials oxidizes to $Cu(OH)_2$ and in turn to the formation of an insoluble layer of Cu(II)-carboxylate.

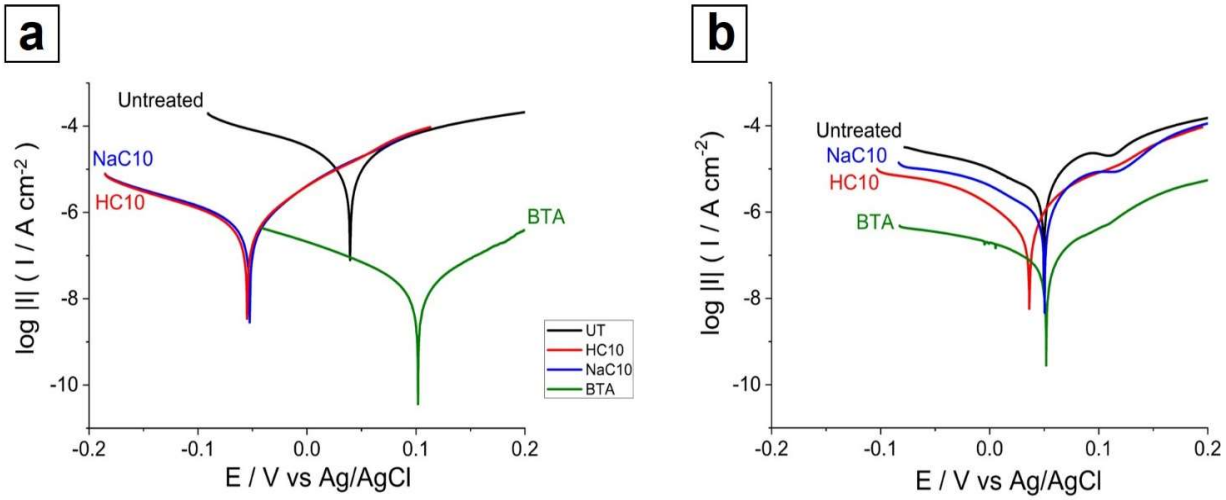

***Figure 6.2.2**: Representative potentiodynamic curves obtained for (a) bare copper untreated and treated with BTA, HC10, NaC10 for 2 h and immersed for 24h in acid rain; (b) real corroded samples untreated and treated with the same inhibitors.*

The above results are in line with what has been reported in the literature for other copper-based materials subjected to the action of acid rain[7,25,26]. In general, it was found that the corrosion mechanism depended on pH and the concentration of complexing species, such as Cl^- ions, present in the medium. In particular, it was reported that at pH ≥ 3.5, the rate determining step of corrosion proceeds through the following reactions[7,25,26,27]:

$$Cu \rightleftharpoons Cu^+ + e^- \qquad (6.2.3)$$

$$2Cu^+ + H_2O \rightleftharpoons Cu_2O + 2H^+ \qquad (6.2.4)$$

$$Cu^+ + Cl^- \rightleftharpoons CuCl_{(ads)} \qquad (6.2.5)$$

$$CuCl_{(ads)} + Cl^- \rightleftharpoons CuCl_2^- \qquad (6.2.6)$$

[25] M. Metikoš-Huković, R. Babić, I. Paić, *J. Appl. Electrochem*. (**2000**) 30, 617 – 624.
[26] S. Magaino, *Electrochim. Acta* (**1997**) 42, 377 – 382.
[27] S. Magaino, Y. Fukazawa, H. Uchida, *Corrosion Engineering* (**1995**) 44, 240-246.

Reactions (6.2.3 and 6.2.4) provide a cuprous oxide film, which in the presence of a large excess of Cl^- ions can partially be dissolved, due to the combined effects of reactions (6.2.5) and (6.2.6). For the Cl^- concentration and pH 3.1 of AR used here, the formation of Cu_2O onto the copper surface should prevail, while the film dissolution due the Cl^- should be negligible[7,25,26,27].

The inhibitory mechanism of BTA against copper corrosion is still debated and can be rationalized by the theory that combines two different processes, i.e., the direct adsorption of BTA on the metal copper surface to provide an hydrophobic layer of $Cu(BTA)_{ads}$, and the BTA adsorption on a surface of cuprous oxide, to provide a Cu(I)-BTA specie[1]. Therefore, the initial step could involve the adsorption of BTA on the metal surface (reaction (6.2.7)); copper slowly oxidises to Cu^+ (reaction (6.2.3)), which determines the subsequent growth of a polymeric Cu(I)-inhibitor film, which most likely lies on a thin Cu_2O inner layer (reaction (6.2.8))[1,7,28]:

$$Cu + BTA \rightleftharpoons Cu(BTA)_{ads} \qquad (6.2.7)$$

$$Cu_2O + BTA \rightleftharpoons Cu(I)\text{-}BTA \qquad (6.2.8)$$

In aerated media the following reactions could also occur:

$$Cu_2O + H_2O \rightleftharpoons 2CuO - 2e^- + 2H^+ \qquad (6.2.9)$$

$$Cu_2O + 3H_2O \rightleftharpoons 2Cu(OH)_2 - 2e^- + 2H^+ \qquad (6.2.10)$$

In addition, the Cu(I)-BTA films can oxidize rapidly to a Cu(II)-BTA species, upon removal of the sample from the liquid phase[1,29].

The cathodic reaction process coupled with copper corrosion involves the reduction of oxygen[1,7]:

[28] T. Liu, S. Chen, S. Cheng, J. Tian, X. Chang, Y. Yin, Electrochimica Acta 52 (**2007**) 8003–8007.
[29] D. Chadwick, T. Hashemi, *Corrosion Science*, (**1978**) 18(1), 39–51.

$O_2 + 4H^+ + 4e^- \rightleftharpoons 2H_2O$ (6.2.11)

Reactions (6.2.3 – 6.2.6) and (6.2.9 – 6.2.10) are conceivably involved also in the case of the copper samples treated with HC10 and NaC10. In fact, the inhibition mechanism could involve the initial formation of either Cu^+ or Cu^{2+} ions, which can prompt react with the inhibitor compounds to form a layer of copper(I) or copper(II) carboxylate species, depending on the specific medium. In Ref. [7], the inhibition mechanism, for a series of n-alkanoic acids, $CH_3(CH_2)_mCOOH$ (m= 2–18) in synthetic acid rain and sea-water, was proposed to occur through the formation of self-assembled layers of the n-alkanoic acids onto the surface of the native copper oxides, followed by the formation of Cu(I)-carboxylate compounds. Instead, in Ref [28], using an ethanol solution of n-tetradecanoic acid, $CH_3(CH_2)_{12}COOH$, a layer of Cu(II) carboxylate was obtained. The formation of the Cu^+ species, as stated above, is favored in solutions containing relatively high amounts of Cl^- ions. Since under the conditions employed here, the concentration of Cl^- is rather low, the formation of the Cu(II) carboxylate is likely to occur. Thus, the reaction mechanism involving HC10 can be described as follows:

$Cu + HC10 \rightleftharpoons Cu(C10)_{ads} + H^+ + e^-$ (6.2.12)

$Cu_2O + 2HC10 \rightleftharpoons 2Cu(C10)_{ads} + H_2O$ (6.2.13)

$Cu(OH)_2 + 2HC10 \rightleftharpoons Cu(C10)_{2ads} + 2H_2O$ (6.2.14)

Cu_2O and $Cu(OH)_2$ are formed through reactions (6.2.9) and (6.2.10).

A reaction sequence similar to (6.2.12 – 14) can be used to explain the reactions involving NaC10.

6.2.3.1. Considerations on the passivation mechanism on the roof cladding samples

From the above electrochemical measurements some considerations can be drawn for the inhibition mechanisms involved for the corroded samples, which conceivably follow similar schemes as those described in the literature for the bare copper[7,24,25,26,28,30], apart from the direct metal oxidation steps.

The mechanism of corrosion of copper in acid rain was reported in earlier articles[7,25,26]. It was found that it depended on pH and complexing species, such as Cl^- ions, present in the medium[28]. In particular, it was reported that at pH ≥ 3.5, the rate determining step of corrosion implied a film formation/dissolution process[7,25,26] involving the formation of insoluble CuCl, Cu_2O and, in aerated media, CuO or $Cu(OH)_2$ compounds. For the Cl^- concentration and pH 3.1 (i.e, conditions of the acid rain used here), the formation of copper oxides onto the copper surface should prevail, while the film dissolution due the Cl^-, to form soluble $CuCl_2^-$, should be negligible[7,25,26]. In the presence of the inhibitors, passivating hydrophobic layers are formed, consisting, conceivably of either Cu(I) or Cu(II) complexes containing BTA^1 or HC10 (or $C10^-$)[7,28]. Therefore, the formation of the hydrophobic layers on the corroded samples, which markedly decrease the wettability of their surfaces, impede the aggressive species present in acid rain from reaching, and then destroy, either the patina layer or the underlying metal surface.

6.2.4. General considerations on the overall experimental results

In view of the whole results above-reported, surface characterization and electrochemical measurements, led to drawn the following general considerations.

[30] M.A. Ameer, A.M. Fekry, *Prog. Org. Coat*. (**2011**) 71, 343–349.

From the PDP curves, it appeared that bare copper and naturally corroded copper showed different tendencies towards corrosion in the synthetic artificial rain solution. In particular, the naturally corroded copper exhibited a lower current density, with respect to the bare copper, with an inhibition efficiency, *IE%* of 65%. This is consistent with literature studies[13] and it is related to the presence of the protective corrosion layer that induces a decrease of the corrosion rate. The corrosion layer (previously described in Ref. [31]), composed of brochantite, in the external part, and cuprite at the interface with the metal, reflect the typical composition for long-term corroded copper samples in urban environment[13,32]. Since the brochantite layer is porous, the protective effect is explained by the presence of cuprite in contact with the metal, which provides a passivation of the copper substrate and controls the corrosion reactions.

The use of BTA to treat bare copper resulted in the inhibition of the corrosion reactions (i.e., in general the current density was reduced). The anodic role of BTA can be explained by the adsorption (chemisorption and/or physisorption) of the molecules on the surface during the treatment, thus blocking the anodic dissolution of the metal. The corroded samples treated with BTA displayed a substantial current density decrease, compared to the untreated sample, although no specific tendency could be inferred on which anodic or cathodic reaction mainly acted. As shown by Raman spectroscopy, the treatment on the naturally corroded copper led to the formation of a BTA-Cu complex on the surface and, as pointed out in a previous study[20], the complexation seemed to take place within the whole thickness of the brochantite layer. This surface complex, insoluble in water, is responsible for the color change of the surface and for surface tension increasing.

The use of HC10 and NaC10 for the treatments of bare copper samples also provided a substantial reduction of current density, compared to the untreated samples. In addition, from the PDP tests, it appeared that both inhibitors acted mainly towards the cathodic reactions. HC10

[31] D. de la Fuente, J. Simancas, and M. Morcillo, *Corros. Sci.* (**2008**) 50, 268–285.
[32] K. P. FitzGerald, J. Nairn, G. Skennerton, A. Atrens, *Corros. Sci*. (**2006**) 48, 2480–2509.

displayed similar effects also when employed for the treatment on the naturally corroded samples. The barrier effect prevails (shift to lower potentials) due to the formation of copper decanoate crystals on the surface as observed by SEM and Raman spectroscopy. The copper decanoate crystals gave to the surface the increased hydrophobic properties evidenced by contact angle measurements. On the contrary, lower protective effect and no barrier effect are found for the naturally corroded sample treated with NaC10. In fact, as observed by SEM, after the treatment, the surface clearly appeared modified. However, the precipitate on the surface had a different morphology compared to the one observed after HC10 treatment. The chemical structure of the compound formed onto the substrate surface was also unclear compared to that observed when HC10 was employed. In fact, an amorphous or a lower amount of crystalline copper decanoate forms were obtained after the treatment with NaC10. This could be related to the slight basicity of the hydroalcoholic solution (pH 8) containing 0.15 M of NaC10 inhibitor. Under the latter conditions, the amount of Cu^{2+} ions coming from the dissolution of brochantite decreased and, therefore, the complexation reaction between Cu^{2+} ions and NaC10 at the solid/solution interface might have been disfavored. This is contrary to the acid conditions (pH 3.6), which instead applies in the hydroalcoholic solution containing 0.17 M HC10. It can be said that in the case of NaC10, a protective surface layer can be formed, right after the sample treatment, as evidenced by the increase in surface tension measurements. It, however, was not stable enough after 24 hours immersion in the synthetic acid rain, thus lowering the inhibition efficiency of NaC10, compared to BTA and HC10.

Overall, the results obtained in this first part of the investigation on the roof cladding samples, allow to conclude that HC10 can represent an eco-friendly, human-safe and efficient alternative to the use of BTA, as corrosion inhibitor to maintain the actual conditions (in terms of naturally formed patina) of copper-based artworks exposed outdoors. However, a deeper investigation with a high spatial resolution, especially through the all stratigraphy of the corrosion

layers, seemed necessary in order to better understand the effect of the eco-friendly inhibitor on the naturally corroded copper roof cladding samples, as well as their protective action.

6.3. SECM investigation of the roof cladding untreated and treated with HC10 and BTA

The roof cladding specimens were also investigated by SECM. This allowed obtaining information on redox and chemical reactivity of the surface materials with high spatial resolution. To this purpose, the samples untreated and treated with the inhibitors HC10 and, for comparison, BTA were examined. The measurements were performed using, preliminarily, the redox mediators K_3IrCl_6 and $Ru(NH_3)_6Cl_3$, whose redox couples (i.e., ($[IrCl_6]^{2-}$ / $[IrCl_6]^{3-}$ and $[Ru(NH_3)_6]^{3+}$ / $[Ru(NH_3)_6]^{2+}$) are characterized by the half-wave potentials ($E_{1/2}$) of +0.74 V and -0.14 V *vs.* Ag/AgCl, respectively,(see Table 4.4 in the Experimental chapter) and, in principle, able to oxidize or reduce, respectively, redox specie of the sample surface or released from it. Both the top side and cross section of the samples were investigated (Scheme 6.3.1). In all cases, in the SECM configuration adopted here, the samples were kept unbiased. This allowed establishing conductivity or spontaneous reactivity of the investigated surfaces.

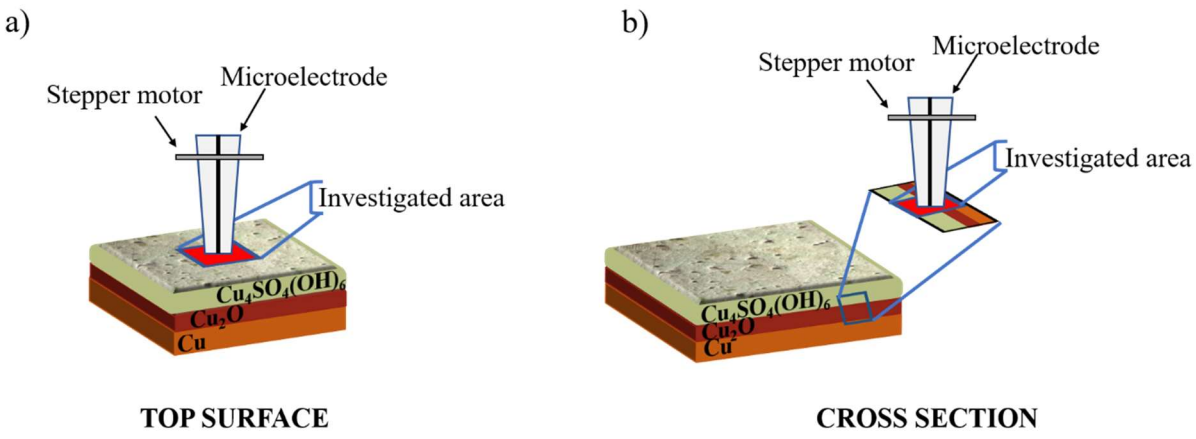

Scheme 6.3.1*: Scheme of the two SECM configurations employed to analyze the roof cladding samples from the top (a) and in cross section (b).*

6.3.1. Top Surface

Preliminarily, a series of a SECM measurements were performed in feedback mode by approaching the surface (at 1 μm s^{-1}) of the inhibitor-free sample, immersed in aqueous solutions containing, apart from the redox mediator, also different supporting electrolytes. In fact, because of the specific composition of the sample materials (i.e., copper compounds), their reactivity can be affected by the anion present in the solution, which can lead to the formation of soluble copper species through complexation or other chemical reactions (see below). The electrolyte employed were KNO_3 and KCl, both of them 0.1 M. The NO_3^- is a weak ligand towards both Cu^{2+} and Cu^+ ions, whereas Cl^- can form complexes with both ions and it is especially able to stabilize Cu^+ ions, as discussed in the above section 6.1, paragraph 6.1.1. Therefore, in the various media different effects on the stability of the patina layer should be expected.

Figure 6.3.1 shows typical approach curves obtained above different locations of the sample with $[Ru(NH_3)_6]^{3+}$ and $[IrCl_6]^{3-}$ (each 1 mM) in the 0.1 M KNO_3 solution. The microelectrode tip was biased at -0.3 V and +0.9V for $Ru(NH_3)_6^{3+}$ and $IrCl_6^{3-}$, at which the reduction or oxidation processes of the two mediators, respectively, are under diffusion control (see insets in the Figures 6.3.1a and 6.3.1b).

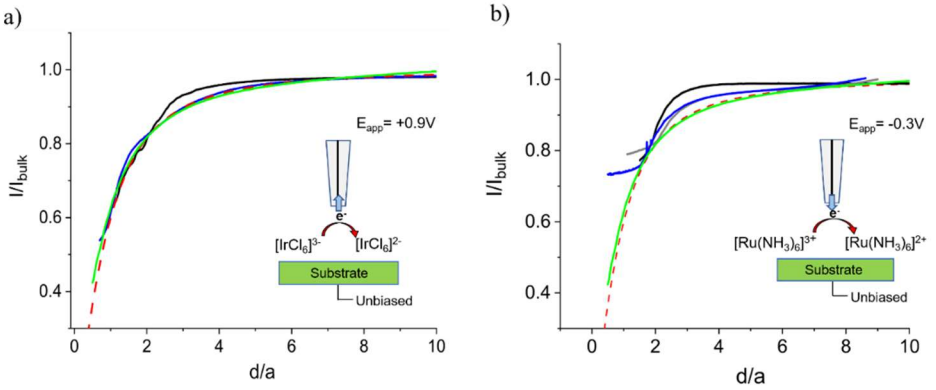

***Figure 6.3.1**: Feedback approach curves recorded in different spots over the roof cladding untreated sample in: (a) 1 mM K_3IrCl_6 + 0.1M KNO_3 and (b) 1mM $Ru(NH_3)_6Cl_3$ + 0.1M KNO_3. Theoretical negative feedback curve for RG=5 is reported (red dashed line) as well as the negative feedback over an insulating substrate (green lines).*

As is evident, both redox mediators provided negative feedback, indicating that the substrate surface behaves, essentially, as an inert and non-conductive material, congruently with the nature of the brochantite layer facing directly the solution. However, the degree of fitting of experimental approach curves with the theory for a diffusion-controlled process (red dashed lines) appears higher in the case of $IrCl_6^{3-}$. In addition, the normalized currents *(I/I_{bulk})* recorded with $[Ru(NH_3)_6]^{3+}$ flatten rapidly in the range 0.7 - 0.8 (Figure 6.3.1a), contrary to what happens for $[IrCl_6]^{3-}$ above the same substrate (Figure 6.3.1b, (i.e., $I/I_{bulk}$are around 0.4 - 0.6) or with the same microelectrode tip while approaching a fully insulating and inert material (Figure 6.3.1 green lines). Current flattening in SECM measurements generally indicates that the insulating part of the tip surrounding the Pt microdisk touches the substrate[1]. Because of the porous and rough nature of the sample investigated (see SEM image in Figure 6.2.3), the latter phenomenon likely occurs also here, regardless of the redox mediator employed. In addition, as reported for porous materials, the redox mediator trapped within the porous layer can diffuse through its structure, giving rise to a measurable current[2]. However, the marked different shape of the approach curves, observed in the two cases, would suggest that when the tip gets closer to the substrate, the electrode process involving $[Ru(NH_3)_6]^{3+}$can be affected by other chemical events occurring at the substrate/solution interface. In particular, it was hypothesized that, locally, a non-negligible amount of soluble copper ions species, due to the solubility of the brochantite[3], can be formed. In this case, at -0.30 V (i.e., the potential applied to the microelectrode), the reduction of Cu^{2+} to either Cu^{+} or Cu^{0}, concomitantly with the reduction of the redox mediator, can occur. This, in part, would increase the overall current at the microelectrode, while a metallic copper layer can accumulate on the microelectrode surface. These phenomena are, of course, not involved when $[IrCl_6]^{3-}$ is used as redox mediator, the microelectrode being poised at +0.9V,

[1]A.J. Bard, L.R. Faulkner. Electrochemical Methods - Fundamentals and and Applications, Wiley (**2001**).
[2] C. Kuss, N.A. Payne, J. Mauzeroll*, J. Electrochem. Soc.* (**2016**) 163**,** H3066-H3071.
[3]D. Marani, J.W. Patterson, P.R. Anderson, *Wat. Res*. (**1995**) 29, 1317-1326.

where no reduction process of Cu^{2+} to Cu^{0} or oxidation process of Cu^{2+} to Cu^{3+} can occur, the latter redox couple having a much higher standard redox potential (i.e., 2.4 V vs. NHE, compared to that of the $[IrCl_6]^{2-}$ / $[IrCl_6]^{3-}$ system (i.e., 0.8665 vs. NHE)[4], see below). Another explanation of the observed phenomena can be found considering that the redox mediator can be trapped within the porous layer and slowly released upon approaching the substrate with the microelectrode. Similar phenomena were observed and rationalized in recent papers regarding SECM measurements above porous substrates having a well-defined porosity[2,5,6].

The insulating nature of the substrate on larger zones was assessed by performing a series of line scans. In these experiments, the tip was positioned at about 10 μm, considering 0 the position at which the normalized current started to flatten. Typical line scans recorded across about 700 μm distance above the substrate with $[Ru(NH_3)_6]^{3+}$ are shown in Figure 6.3.2. The scans with black and red lines refer to two repetitions on the same line; the scan with the blue trace refers to a scan performed in a different direction. As can be seen, the current is almost constant over the entire range, apart from the spike observed at about 230 μm, probably due to the tip hitting high surface flakes. Line scans performed using $[IrCl_6]^{2-}$ (not shown) provided similar results. This confirms that the above-mentioned processes occur uniformly on the investigated surface.

[4]D.R. Lide. Handbook of Chemistry and Physics, 72nd edition, Boca Raton, (**1991-1992)**, 8-19.
[5] P. Dauphin-Ducharme, C. Kuss, D. Rossouw, N.A. Payne, L. Danis, G.A. Botton, J. Mauzeroll, *J. Electrochem. Soc.* (**2015**) 162, C677.
[6] J. Wang, L. Xie, L. Han, X. Wang, J. Wang, H. Zeng, *Journal of Colloid and Interface Science* (**2021**) 584, 103–113.

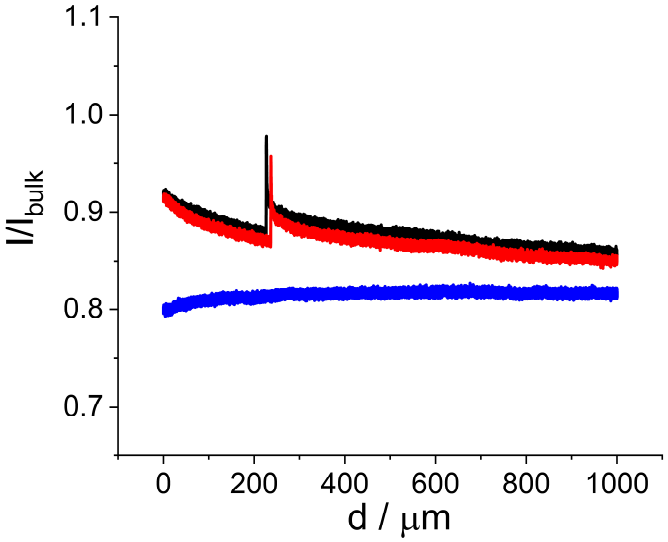

***Figure 6.3.2**: Line scans recorded in different zones over the roof cladding untreated sample in 1mM $Ru(NH_3)_6Cl_3$ + 0.1M KNO_3. The microelectrode tip was positioned at about 10 µm above the substrate.*

The formation of copper ions at the substrate/solution interface was investigated by performing linear sweep voltammetries (LSVs) and adsorptive stripping voltammetries (ASVs) (coupled with LSV) with the microelectrode positioned in the proximity of the substrate, which was approached by either $[Ru(NH_3)_6]^{3+}$ and $[IrCl_6]^{3-}$. LSV was used with $[Ru(NH_3)_6]^{3+}$, so that both the process due to the reduction of the redox mediator and oxidation of metallic copper deposited on the electrode surface could be revealed. ASV was employed when the surface was approached with $[IrCl_6]^{3-}$. Figure 6.3.3 with a black line shows a typical LSV recorded with the microelectrode positioned 30 µm above the substrate, starting from -0.3 V and scanning the potential at 50 mV s^{-1} towards positive potentials.

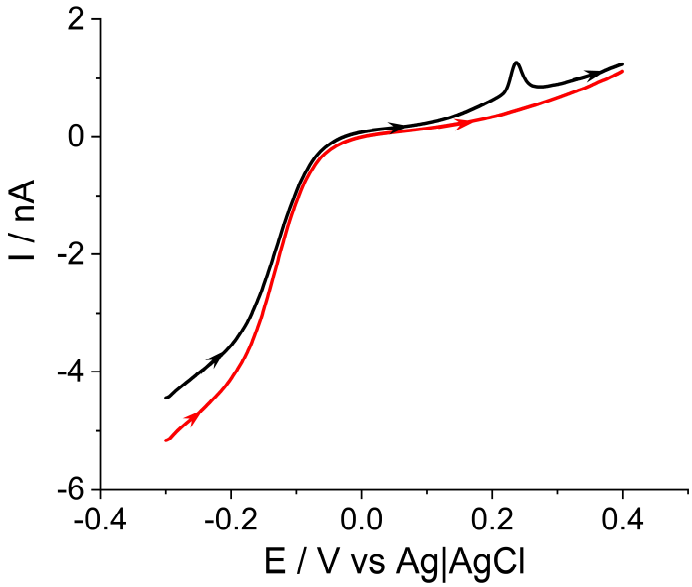

***Figure 6.3.3**: LSVs recorded over the roof cladding untreated sample in 1mM $Ru(NH_3)_6Cl_3$ + 0.1M KNO_3 with the microelectrode positioned at 30 µm above the substrate (black line) and in the bulk of the solution (red line). Scan rate: 0.05 V s^{-1}.*

As is evident in Figure 6.3.3, at -0.3 V a rather high current, mainly due to the reduction of $[Ru(NH_3)_6]^{3+}$ to $[Ru(NH_3)_6]^{2+}$ is observed; a bell shaped peak at +0.24 V appears, which, on the basis of shape and position, can be assigned to the oxidation of Cu^0 to Cu^{2+}. In fact, metallic copper can accumulate on the microelectrode surface while scanning the potential from -0.3 V up to the potential at which metallic copper oxidizes. This is typical for microelectrodes due to the high and steady flux that establishes rapidly at their surfaces. The effective deposition time (t_{eff}) can be calculated by the following equation[7,8]:

$$t_{eff} = t_d + \left(E_p - E_d\right)/v \qquad (6.3.1)$$

where t_d is the deposition time at the deposition potential E_d, E_p is the peak potential and v is the scan rate. The term in brackets represents the deposition time while scanning. A similar scan

[7]M.A. Baldo, S. Daniele, M. Corbetta, G.A. Mazzocchin, *Electroanalysis* (**1995**) 7, 980.
[8]M.A. Baldo, C. Bragato, G.A. Mazzocchin, S. Daniele, *Electrochim. Acta* (**1998**) 23, 3413-3422.

performed with the microelectrode positioned in the bulk solution (i.e., about 1 mm away from the substrate) did not provide any copper stripping peak (Figure 6.3.3, red line).

The release of Cu ions at the roof cladding untreated specimen/solution interface was also proved by using $[IrCl_6]^{3-}$ as redox mediator, which allowed to approach the surface with no interference due to reduction of copper ions. Moreover, to increase the sensitivity, ASV, with different accumulation times, was employed. Figure 6.3.4 shows typical ASVs obtained, again with the microelectrode positioned 30 µm above the substrate, and their variation with time elapsed from the sample immersion in the 0.1 M KNO_3 solution. As is evident, ASVs increases with the immersion time, due to the continuous release of copper ions, denoting, as expected under these conditions, a rather unstable patina layer.

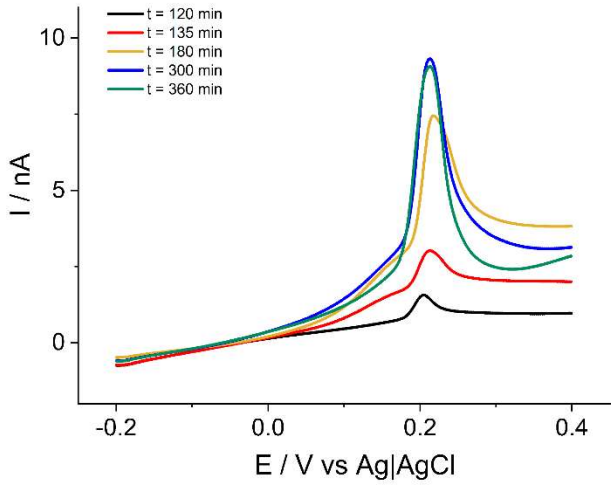

***Figure 6.3.4**: ASVs recorded over the roof cladding untreated sample in 1mM $[IrCl_6]^{3-}$+ 0.1M KNO_3 with the microelectrode positioned at 30 µm above the substrate at different times of immersion (as indicated). E_d = -0.2V; t_d = 150s; scan rate: 0.1 Vs^{-1}.*

The amount of Cu^{2+} released was evaluated from the charge associated to the ASV peaks and using a calibration plot obtained using synthetic solutions of $Cu(NO_3)_2$, as ion source, and KNO_3 as supporting electrolyte.

The linear regression analysis of the experimental *Q vs. C* values, evaluated over the concentration range 0.5 - 42 µM, provided the following equation:

$$Q(nC) = 0.748\, C(\mu M) - 0.015\,,\ R^2 = 0.998 \qquad (6.3.2)$$

It is important to stress that the ASV peaks and relative associated charges, recorded above the roof cladding samples, are instantaneous responses, as they slightly increased from one measurement to another, due to the continuous release of Cu^{2+} from the patina layers. The concentrations of Cu^{2+} ions, shown in Table 6.3.1, are therefore instantaneous values and congruent with the solubility of brochantite over the pH range 6.5 - 7.2 (i.e., 2.14 - 18.2 µM, respectively)[3].

Table 6.3.1*: Instantaneous concentration of Cu^{2+} ions evaluated at 30 µm above the roof cladding untreated sample immersed in an aqueous solution containing 0.1 M KNO_3.*

Time of immersion (min)	Charge of the ASV peaks (nC)	C (µM)
120	3.46	4.64
135	9.86	13.20
180	19.4	25.95
300	20.52	27.45
360	16.24	21.73

Series of analogous measurements, as those reported above in the 0.1 M KNO_3 medium, were carried out in the 0.1 M KCl solution. Typical approach curves recorded under these conditions with both $[Ru(NH_3)_6]^{3+}$ and $[IrCl_6]^{3-}$ are shown in Figure 6.3.5a and 6.3.5b, respectively. In the presence of chloride ions, rather different behaviors were observed with both mediators. In fact, with $[Ru(NH_3)_6]^{3+}$, approach curves displayed slight positive feedback effects, while both negative and positive feedback were recorded with $[IrCl_6]^{3-}$, depending on the specific

location of the microelectrode above the substrate and the time elapsed from one measurement to another.

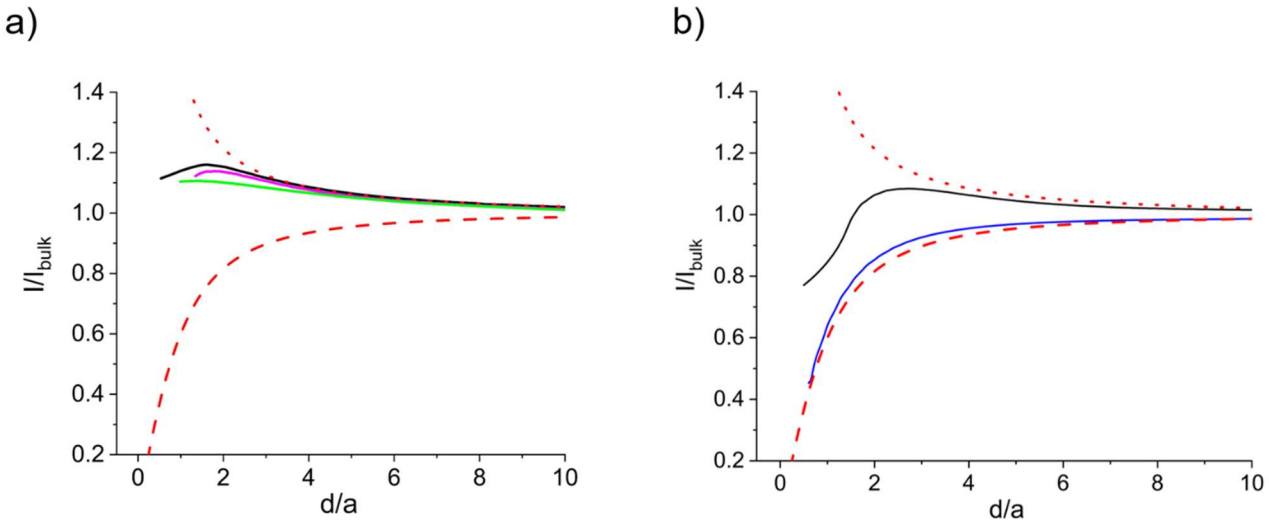

***Figure 6.3.5**: Feedback approach curves recorded in different spots over the roof cladding untreated sample in: (a) 1mM $Ru(NH_3)_6Cl_3$ + 0.1M KCl and (b) 1 mM K_3IrCl_6 + 0.1M KCl. Theoretical negative feedback curves (red dashed lines) as well as the positive feedback (red dotted lines) for RG=5 are reported.*

The different results obtained in the 0.1 M KCl solutions, compared to those in 0.1 M KNO_3, can be explained considering that the solubility of patina, other than involving the brochantite layer, can also involve the underlying cuprite layer, where Cu_2O can react with Cl^- to form the soluble and stable $CuCl_2^-$ complex[9]:

$$Cu_2O + 2H^+ + 4Cl^- \leftrightarrows 2CuCl_2^- + H_2O \qquad (6.3.3)$$

$CuCl_2^-$ can diffuse through the brochantite layer, where it can react with the redox mediators, (see below). The redox couples indicated in the reactions (6.3.4) and (6.3.5) are characterized by $E_{1/2}$ or nucleation potential (E_n) values, respectively, that depend on the Cl^-/Cu^+ concentration ratio ($[Cl^-]/[Cu^+]$)[10].

[9] D. Rui, L. Xiangbo, W. Jia, X. Likun, *Int. J. Electrochem. Sci.*, 8 (**2013**) 8, 5902–5924.
[10] S. Daniele, M.J. Pena,Electrochim. Acta 38 (**1993**) 165-174.

$$Cu^{2+} + e^- + 2Cl^- \leftrightarrows CuCl_2^- \quad (6.3.4)$$

$$CuCl_2^- + e^- \leftrightarrows Cu^0 + 2Cl^- \quad (6.3.5)$$

For reaction (6.3.4), $E_{1/2}$ is within 0.03 V ≤ $E_{1/2}$ ≤ 0.220 V, when 10 ≤ $[Cl^-]/[Cu^+]$ ≤ 500. For reaction (6.3.5), over the same concentration ratios range, E_n is -0.07 V ≥ E_n ≥ -0.280 V (Figure 6.3.6).

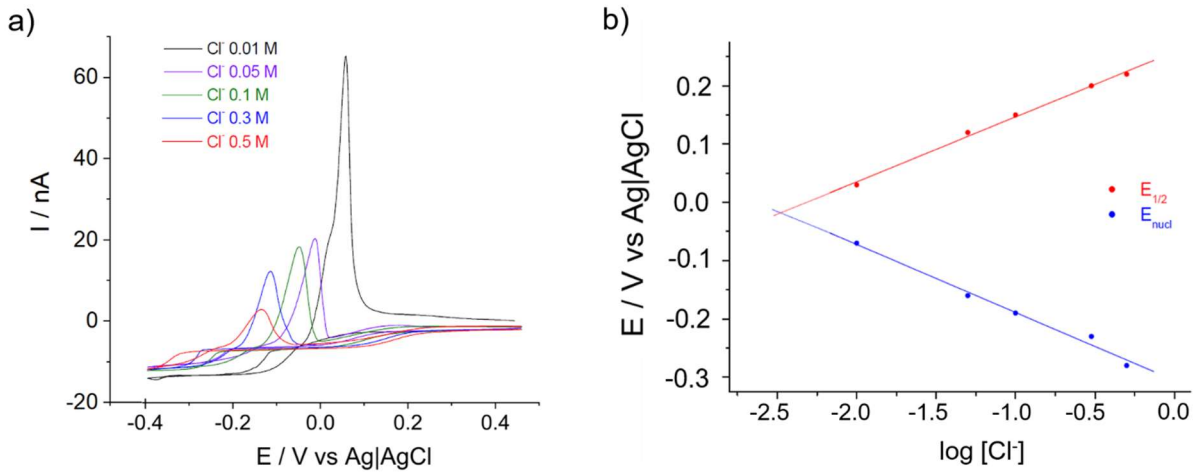

Figure 6.3.6*: a) CVs recorded in 1mM $CuSO_4$ with different concentrations of Cl^- ions. Scan rate 20 mVs^{-1}. b) Variation of $E_{1/2}$ ed E_{nucl} versus log[Cl^-], each potential datum refers to the average of three independent measurements (± 0.003 V).*

Therefore, if the overall amount of copper ions (i.e., both Cu(II) and Cu(I) chloro-complexes) formed at the interface is such that $[Cl^-]/[Cu^+]$ falls within the above ranges, $CuCl_2^-$ can undergo the following reactions within the gap formed between the microelectrode tip and substrate:

$$CuCl_2^- + [IrCl_6]^{2-} \leftrightarrows CuCl_2 + [IrCl_6]^{3-} \quad (6.3.6)$$

$$CuCl_2^- + [Ru(NH_3)_6]^{2+} \leftrightarrows Cu^0 + [Ru(NH_3)_6]^{3+} + 2Cl^- \quad (6.3.7)$$

These reactions can occur to a different extent depending on the local amount of copper ions generated at the interface and their kinetics. They are responsible of the redox mediator recycling as described in the scheme in Figure 6.3.7. This ultimately justifies the positive feedback effects observed under the investigated conditions.

It must be considered that when $[Ru(NH_3)_6]^{3+}$ is used as redox mediator, at -0.3 V, $CuCl_2^-$ can be formed not only through reaction (6.3.3), but also through reaction (6.3.4), due to the Cu^{2+} deriving from the brochantite. This is the reason why, with the latter redox mediator, positive approach curves were always obtained, while both positive and negative approach curves were recorded with $[IrCl_6]^{3-}$. In the latter case, at +0.9 V, only reaction (6.3.6), due to $CuCl_2^-$ formed locally from the dissolution of Cu_2O (i.e., reaction (6.3.3)) can occur. The kinetic of this reaction is probably slow and only when sensible amounts of $CuCl_2^-$ are accumulated at the interface, the positive feedback can be observed.

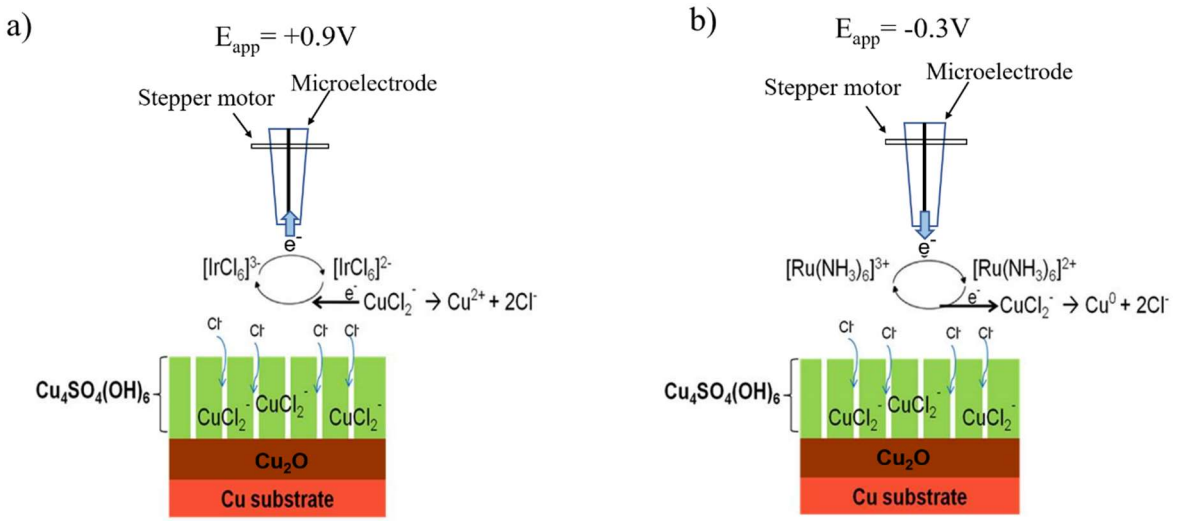

Figure 6.3.7*: Scheme of the processes occurring at the substrate/solution interface using: a) $[IrCl_6]^{3-}$ and b) $[Ru(NH_3)_6]^{3+}$ as redox mediators in the presence of Cl^- ions.*

Line scans performed using $[Ru(NH_3)_6]^{3+}$ and 0.1 M KCl as supporting electrolyte (Figure 6.3.8), again confirmed that the phenomena observed in given locations occurred also in larger zones of the substrate. In fact, apart from tilting effect, I/I_{bulk} are always larger than 1.

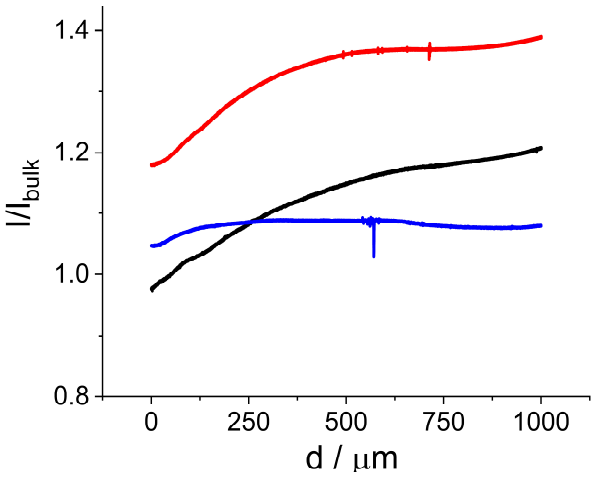

***Figure 6.3.8**: Line scans recorded in different spots over the roof cladding untreated sample in 1mM $Ru(NH_3)_6Cl_3$ + 0.1M KCl. The microelectrode tip was positioned at about 10 µm above the substrate.*

To confirm the occurrence of the above scenario, the release of Cu^{2+} in the 0.1 M KCl solution was investigated by using a similar approach employed for the KNO_3 medium. Figure 6.3.9 shows typical CVs in the bulk medium (red line) and at 30 µm above the substrate (black line), the latter distance achieved using $[Ru(NH_3)_6]^{3+}$ as redox mediator. As is evident, a stripping peak due to metallic copper oxidation appears at -0.05 V, that is, at less positive value, compared with that recorded in KNO_3. This suggests that copper oxidation involves the formation of $CuCl_2^-$ (see Figure 6.3.7b).

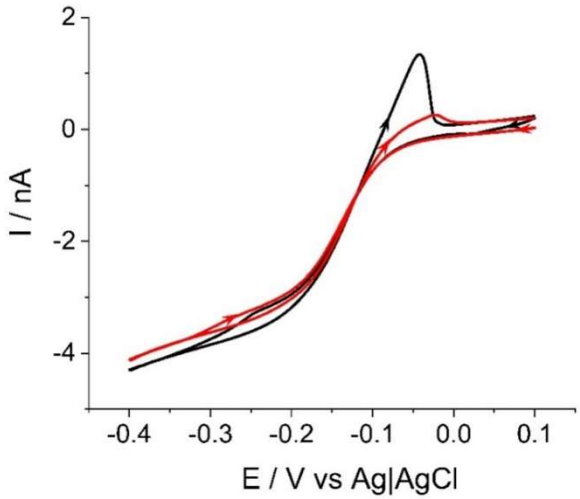

Figure 6.3.9*: CVs recorded over the roof cladding untreated sample in 1mM $Ru(NH_3)_6Cl_3$ + 0.1M KCl with the microelectrode positioned at 30 µm above the substrate (black line) and in the bulk of the solution (red line).*

The use of ASV, after approaching the substrate by means of $[IrCl_6]^{3-}$, provided responses as those displayed in Figure 6.3.10. Under these conditions, the ASV peaks are much better defined; moreover, the position of the peaks occurs at 0.15 V, still less positive than those recorded in KNO_3 solutions, but more positive than the that in Figure 6.3.4. The effect of the peak position in the presence of Cl^- is similar to that shown in Figure 6.3.6 a, and congruent with a literature report [11] for trace amounts of copper ions. It is attributable to the above mentioned $[Cl^-]/[Cu^+]$ ratio. Obviously, at a given Cl^- concentration, the greater is the amount of Cu accumulated onto the electrode surface, the lower is the $[Cl^-]/[Cu^+]$ ratio, formed during the stripping step, and, consequently, the lower is the $CuCl_2^-$ stability.

[11] M.A. Baldo, S. Daniele, P. Ugo, G.A. Mazzocchin, *Anal. Chim. Acta* (**1989**) 219, 9-18.

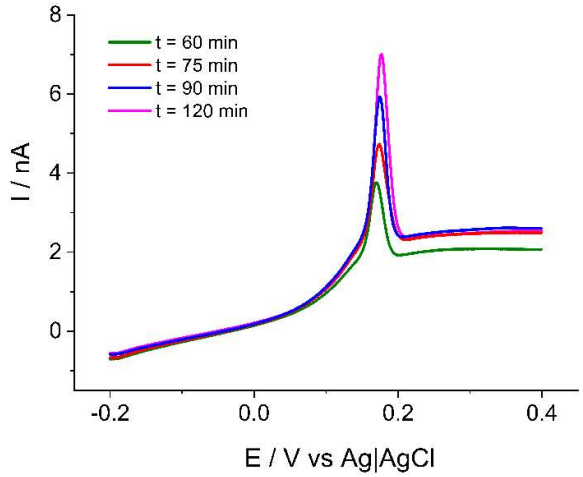

***Figure 6.3.10**: ASVs recorded over the roof cladding untreated sample in 1mM $[IrCl_6]^{3-}$ + 0.1M KCl with the microelectrode positioned at 30 µm above the substrate at different times of immersion (as indicated). E_d = -0.2V; t_d = 150s; scan rate: 0.1 Vs^{-1}.*

The quantification of total amount of copper ions released was difficult to obtain with accuracy, due to the complex mechanism occurring in the stripping step. However, a rough estimate of the amount of copper ions released was made by using the equation of the calibration plot (6.3.2). The instantaneous values obtained are shown in Table 6.3.2.

***Table 6.3.2**: Instantaneous concentration of Cu^{2+} ions evaluated at 30 µm above the untreated roof cladding sample immersed in an aqueous solution containing 0.1 M KCl.*

Time of immersion (min)	Charge of the ASV peaks (nC)	C (µM)
60	5.46	7.32
75	7.66	10.26
90	7.88	10.55
120	8.24	11.04

The values thus found, for similar immersion times of the samples (i.e., up to 120 min), are larger than those found in 0.1 KNO_3, which agrees with the known behavior of corrosion of copper in the presence of chloride ions[12].

To complete the investigation on the top surface of the roof cladding specimens, a series of SECM measurements were performed on the samples treated with the inhibitors HC10 and BTA. These measurements were performed using $[IrCl_6]^{3-}$ as redox mediator, in the solution containing 0.1 M KCl, i.e., a medium that revealed to be more aggressive than KNO_3. The successful of the coating of the patina layer with the inhibitors was initially explored, by performing SECM approach curves above the samples after they had been treated with the inhibitors in the 50% (v/v) E/W medium (see paragraph 4.4.1 in the Experimental chapter). Typical approach curves obtained are shown in Figure 6.3.11, and in both cases negative feedbacks (black lines) overlapping the theoretical curve (red dashed lines) are observed. Moreover, ASV analysis, performed at the substrate/solution interface (i.e., at 30 μm far from the substrate) to verify an eventually release of copper ions in the solution, provided responses as those shown in Figure 6.3.12. No stripping peak was in any case revealed, even after leaving the substrate immersed in the medium for about 3h. These results clearly indicated that a protective layer was formed onto the patina surfaces, in agreement with the OCP and PDP measurements reported in the paragraph 6.2.3 of the section 6.2.

The stability of the protective inhibitor layers was then investigated by SECM, after the samples were left immersed in acid rain for 24 h. The approach curves recorded above the substrate provided, again, negative feedback responses (Figure 6.3.11, green lines), confirming that the inhibitors still protected adequately the patina layer. In fact, no positive approach curves, as those recorded above the untreated samples (Figure 6.3.5) were recorded.

[12] Y. Zhang, Y. Chen, *Corrosion Engineering, Science and Technology* (**2019**) 54, 75 – 85.

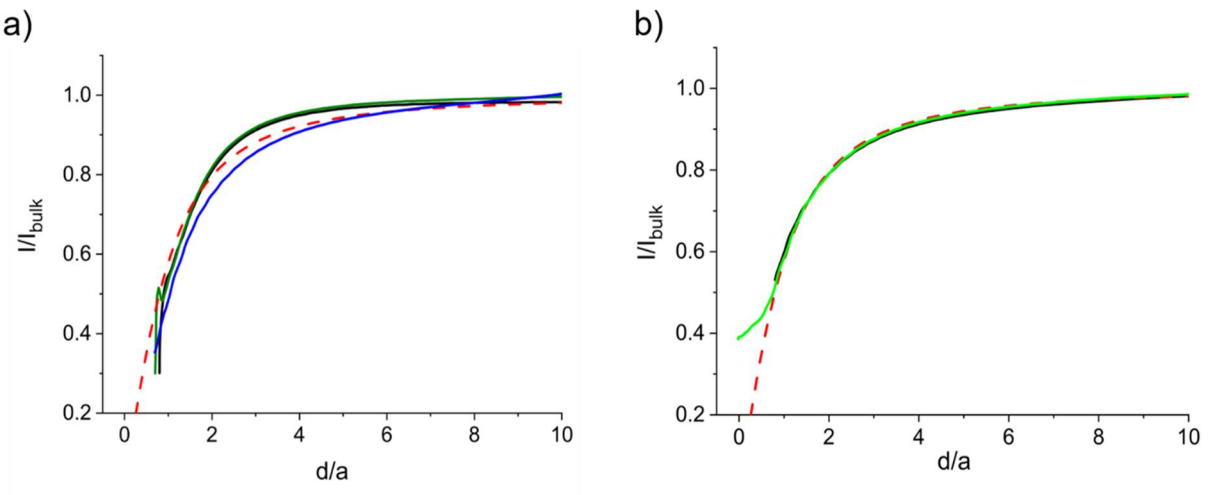

***Figure 6.3.11**: Feedback approach curves in 1mM of K_3IrCl_6 + 0.1M KCl over the roof cladding samples treated with (a) decanoic acid and (b) benzotriazole before (black lines) and after the immersion in synthetic acid rain (green and blue lines).*

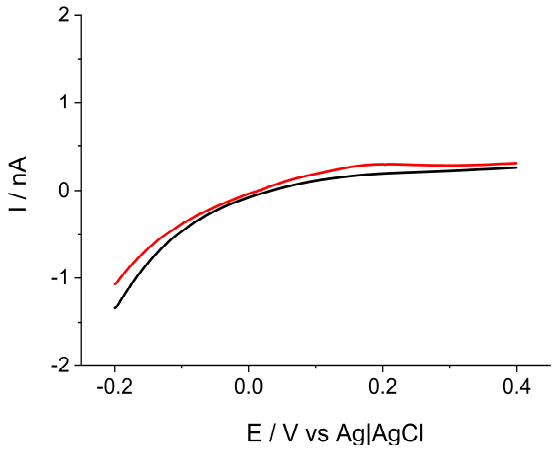

***Figure 6.3.12**: ASVs in 1mM of K_3IrCl_6 + 0.1M KCl over the roof cladding samples treated with decanoic acid (black line) and benzotriazole (red line). The microelectrode tip was positioned at 30 µm from the substrate. E_d = -0.2V; t_d = 150s; scan rate: 0.1 Vs^{-1}.*

The release of copper ions from the treated samples was also investigated by positioning the microelectrode at 30 μm away from the substrate surface and using the ASV technique. As is shown in Figure 6.3.13, stripping peaks due to copper species were recorded also for the inhibitor-treated samples, indicating that the acid rain destabilized to some extent the structure of both the treated-patina layers. However, using the same ASV parameters, it was verified that the stripping peaks recorded above the treated samples were much lower than those of inhibitor-free surface (Figure 6.3.13, black line).

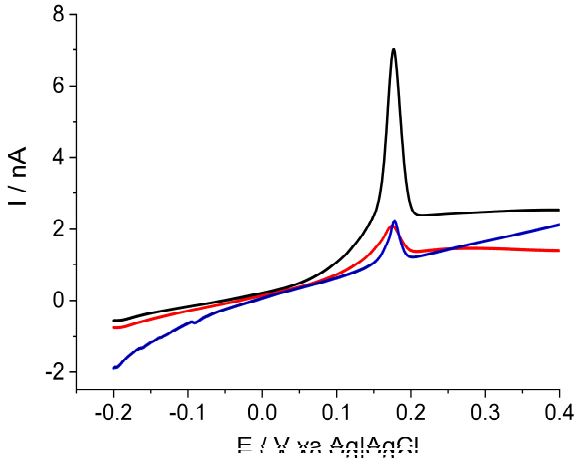

***Figure 6.3.13**: ASVs in 1mM of K_3IrCl_6 + 0.1M KCl over the roof cladding samples treated with decanoic acid (red line), benzotriazole (blue line) compared with the untreated one (black line). The microelectrode tip was positioned at 30 μm from the substrate. E_d = -0.2V; Scan rate: 0.1 Vs^{-1}; t_d : 150s.*

Peak height and relevant associated charged depended on the time elapsed from immersion of the sample in the solution, as well as on the deposition potential applied. Figure 6.3.14 shows series of ASV responses obtained at different times, using E_d = -0.5V. As is evident, as the immersion time increases also peak height increases. Shifting E_d from -0.2 V to -0.5 V also led to an increase of peak height. This was not due only to the increase of deposition time (i.e., based on equation (6.3.1)), but also to the reduction of soluble copper species, whose reduction potential is more negative than that of free copper ions. This is, for instance, the case of $Cu(C10)_2$, as evidenced in the study discussed in section 6.2. Soluble $Cu(BTA)_2$ species can also be involved for the BTA-treated sample.

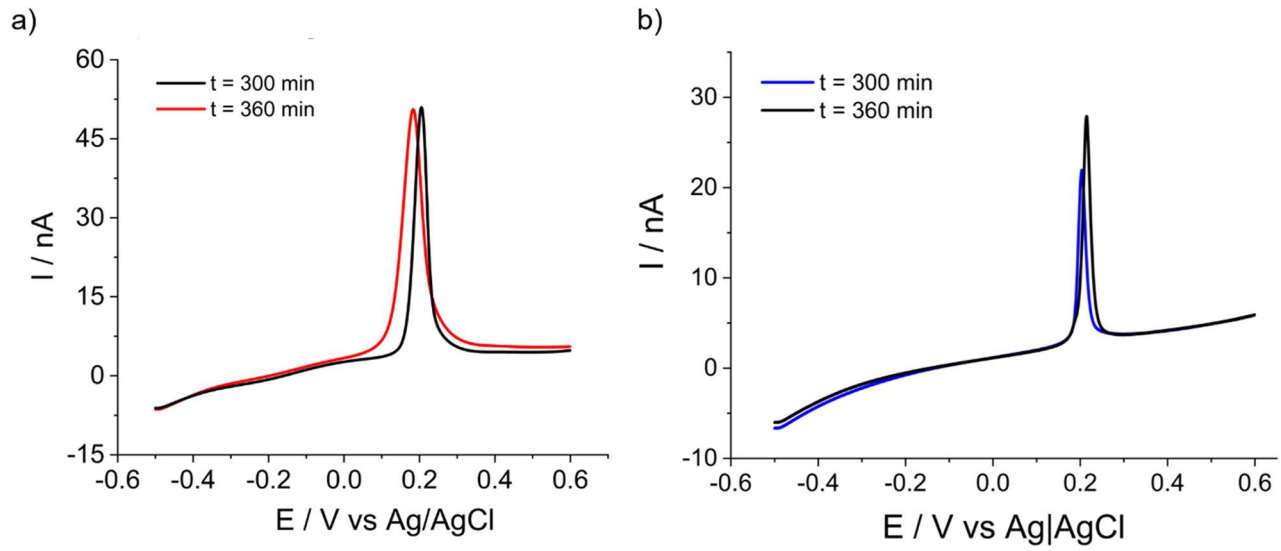

***Figure 6.3.14**: ASVs over the roof cladding samples treated with (a) decanoic acid and (b) benzotriazole after different times of immersion in 1mM of K_3IrCl_6 + 0.1M KCl (as indicated). The microelectrode tip was positioned at 30 µm from the substrate. E_d=-0.5V; t_d = 150s; scan rate: 0.1 Vs^{-1}.*

Comparing ASV responses obtained under similar voltammetric and other experimental conditions (i.e., time elapsed from the sample immersed in the 0.1 KCl solution, same microelectrode and tip-to-substrate distance, deposition time in the stripping step), the amount of copper ion released was lower in the BTA-treated samples, compared with HC10-treated ones (Figure 6.3.15). This result, again, indicates a better anticorrosion ability of BTA compared to that of HC10, congruently with the results obtained in section 6.2.

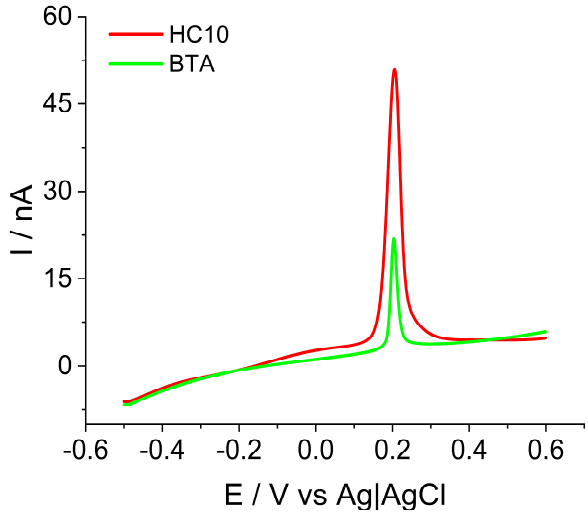

***Figure 6.3.15**: ASVs in 1mM of K_3IrCl_6 + 0.1M KCl over the roof cladding samples treated with decanoic acid (red line) and benzotriazole (green line) previously immersed for 24 h in synthetic acid rain. E_d=-0.5V; t_d = 150s; scan rate: 0.1 Vs^{-1}.*

An estimate of the amount of copper released was made by using the charge involved in the ASV peaks and equation (6.3.2). Relevant values are shown in Table 6.3.3.

***Table 6.3.3**: Instantaneous concentration of Cu^{2+} ions evaluated at 30 μm above the roof cladding samples treated with HC10 and BTA, after they were kept immersed 24 h in synthetic acid rain. ASV performed in an aqueous solution containing 1mM of K_3IrCl_6 + 0.1 M KCl.*

Inhibitor	Time of immersion (min)	Charge of the ASV peaks (nC)	C (μM)
HC10	300	19.4	26.0
	360	28.0	37.5
BTA	300	4.5	6.2
	360	5.8	7.8

6.3.2. Cross section

Figures 6.3.16 and 6.3.17 show optical images, respectively, of a typical cross section of the roof cladding samples as assembled for SECM measurements. The samples were firstly wrapped in a Paraloid B-72 film and then embedded in epoxy resin (see paragraph 4.4.3 of the Experimental chapter). The patina layers of the samples examined were either untreated or treated with the inhibitors. From the images, it appears that the surfaces of copper and patina, as expected, are rather rough.

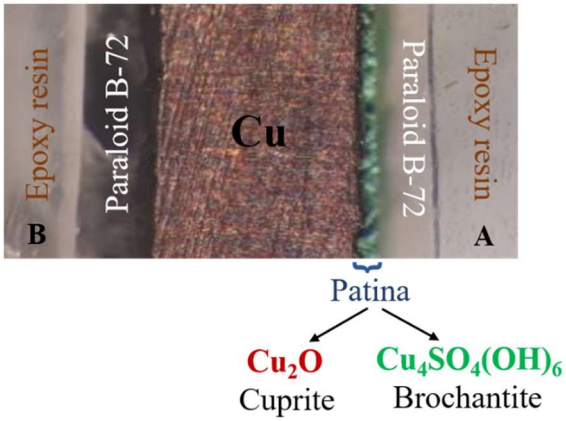

***Figure 6.3.16**: Photographic image of the roof cladding untreated sample in cross section under the optical microscope. The cross section presents from left to right: epoxy resin, Paraloid film, Copper core, cuprite, brochantite, Paraloid film and epoxy resin.*

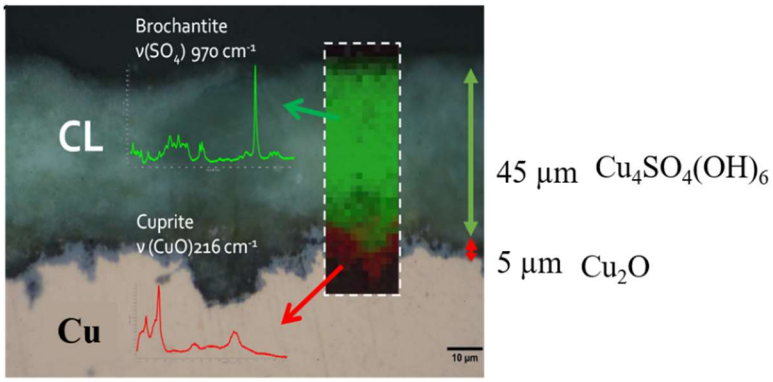

***Figure 6.3.17:** Cross section of the corrosion layers under the optical microscope with the corresponding Raman spectra. The arrows indicate the thickness of the layers measured by SEM.*

It is important to highlight that in this part of the investigation, differently from the previous one, a consistent amount of bare copper is also exposed to the solution, which may interfere with the analysis. For this reason, it was chosen to proceed with a different approach with respect to the previous one. After the preliminary examination on the top surface of the samples conducted with K_3IrCl_6 and $Ru(NH_3)_6Cl_3$ as redox mediators, in order to further improve the investigation with a more accurate and refined approach, for the SECM measurements on the cross section samples the redox mediator choose was FA^+. This redox mediator, whose counter ion is hexafluorophosphate instead of Cl^-, allowed to study the various layers of the samples

excluding any possible effects due to even relatively small amounts of chloride ions interacting with the copper. The aqueous electrolytes employed were either 0.1 M Na_2SO_4 or 0.1 M KCl, the latter to verify directly the stability of each layer of the patina and the copper core in the presence of a large amounts of Cl^- ions. The electrochemical cell was assembled in a two-electrode configuration, in which a Pt wire was used as pseudo-reference/counter electrode. The $E_{1/2}$ of FA^+, against the Pt wire, was equal to 0.21 and 0.19 V, in the Na_2SO_4 and 0.1 M KCl, respectively (see Table 4.4 in the Experimental chapter). The experimental scheme adopted in the measurements was similar to that followed to study the top surface of the samples. That is, the various strata were firstly investigated by performing approach curve, trying to positioning the microelectrode above each of the copper-containing layers and, for comparison, above the Paraloid film and the resin. Then, the interaction of each layer with the electrolyte, as well as the release of copper ions from the substrate in the solutions were evaluated by ASV. Moreover, the discussion that follows consider firstly the untreated samples and then those treated with the inhibitors.

6.3.2.1. Untreated sample

Figure 6.3.18 shows typical approach curves recorded in the 0.1 M Na_2SO_4 solution containing 1 mM FA^+ above: the epoxy resin -or over the Paraloid film- (green line), the patina (blue line) and the metallic copper core (magenta line). As expected, negative feedback responses, due to hindered diffusion, were obtained while approaching both resin or Paraloid (Scheme 6.3.2a); attenuated negative feedback was recorded over the patina layer (Scheme 6.3.2a), the latter being consistent with what has been extensively discussed in the previous

paragraph. Instead, positive feedback, involving recycling of the redox mediator, was obtained above the copper layer, congruently with the conducting nature of the material (Scheme 6.3.2b).

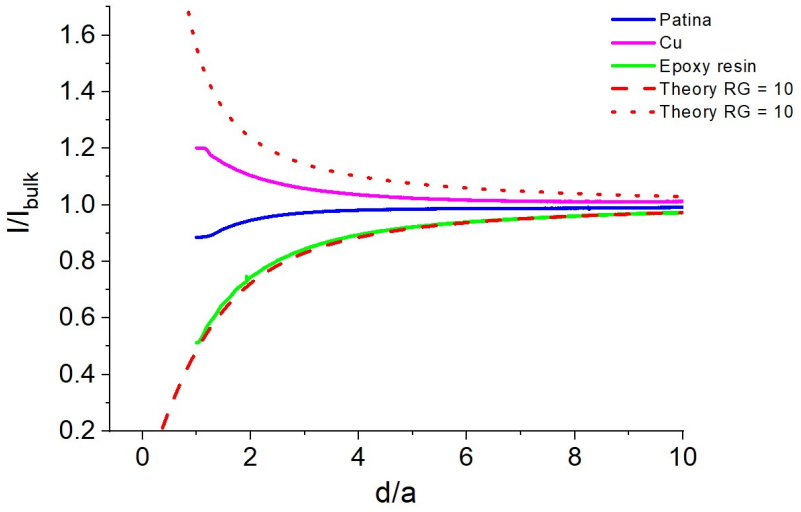

***Figure 6.3.18**: Approach curves recorded in 1mM FA^+ + 0.1M Na_2SO_4 over the untreated sample in cross section. Negative feedback curve over the resin (green trace) and attenuated negative feedback over the patina (blue trace) and positive feedback over the metallic copper core (magenta trace).*

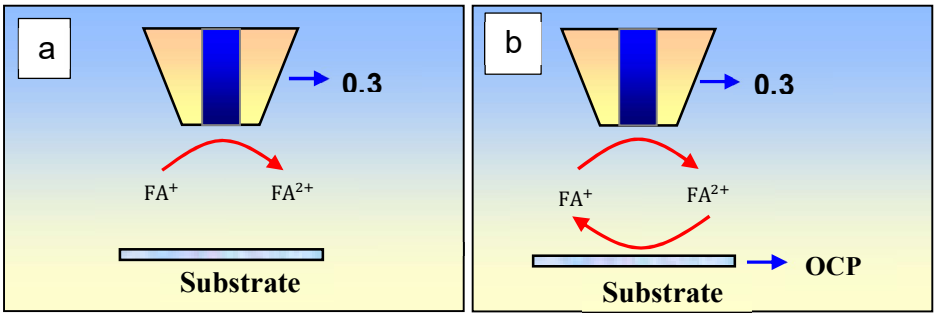

***Scheme 6.3.2**: Electrode processes occurring at the Pt microdisk and substrate: (a) insulating; (b) conducting.*

From Figure 6.3.18, it is evident that only the approach curves recorded above the Paraloid (or resin) insulating layer, fit the theory (see Figure 6.3.18, green line), as expected. The positive feedback curve recorded above the copper surface falls below the theoretical one. This can be explained, admitting that the copper surface, being immersed in an aerated aqueous solution, can be passivated by a thin layer of oxide films, formed by spontaneous corrosion of

the metal, and consequently characterized by a lower conductivity. Under these conditions and because the substrate was unbiased, the lateral electron transfer, responsible of the redox mediator recycling[13], could be somewhat inhibited.

As for the approach curve recorded above the patina layer, the behavior is similar to that discussed in section 6.3.1 for the top surface of the sample. Unfortunately, the size of the Pt microdisk employed for the above measurements (i.e., a 12.5 μm radius), being too big, did not allow achieving a sufficient high spatial resolution to distinguish the processes occurring above the two types of layers forming the patina (i.e., cuprite and brochantite).

In order to extend the observations to larger zones of the samples, line scans and bi-dimensional images were acquired. For these measurements, a microelectrode tip with a 10 μm radius (RG = 10) was employed. Figure 6.3.19 shows a typical line scan obtained by positioning the microelectrode 20 μm away from the substrate. The microelectrode was biased at +0.3 V *vs.* Pt, where the FA^+ oxidation is diffusion controlled (see Figure 4.2c in the Experimental chapter). The scan was started from a location (A) above one side of the resin and was completed to a location (B), above the other side of the resin (see the cross section in Figure 6.3.19). The overall distance travelled was 2500 μm, over which the I/I_{bulk} allowed distinguishing three zones. The first, extending by about 650 μm, characterized by low currents, indicating that the microelectrode travelled across the resin and Palaroid; the second zone extending by about 1100 μm in which the currents increased significantly in a hill shaped way, indicating that the microelectrode moved above both patina and copper core; the third zone, extending for about 750 μm, in which the currents dropped again, indicating the achievement of the second insulating layer, including the resin and the Palaroid.

[13]A.J. Bard, M.V. Mirkin, Scanning Electrochemical Microscopy, Marcel Dekker, Inc, New York, (**2001**).

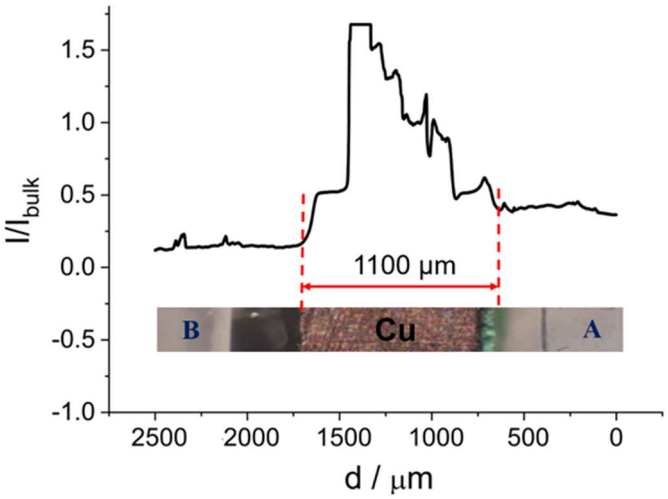

***Figure 6.3.19**: Linescan from the resin A to the resin B of the untreated sample in cross section obtained by using 1 mM FA^+ + 0.1 M Na_2SO_4 (E_{app}= +0.3 V) and a Pt microdisk (10 µm radius). The tip was positioned at 20 µm above the substrate.*

The current spikes observed over the entire line scan were conceivably related to roughness, grooves or bumps formed at the junction among the various layers of the materials. Tilting effects are also visible, comparing the normalized currents recorded when the microelectrode is located above the insulating layers A and B. A rough estimate of the tilt, based on the changes of normalized current and the theoretical approach curve for RG = 10, provided an overall value of 20 µm. Apart from the above problems, the spikes recorded on the active zones of the sample can also due to chemical processes, as for instance, etching, pitting/nucleation events. In fact, it must be considered that the measurements were performed under aerated conditions, which can promote the corrosion of copper and cuprite underlying the brochantite stratum. In addition, the FA^{2+}/FA^+ system could act as an oxidant towards cuprite (see below).

Bi-dimensional scans were performed on a surface region high enough to include the various zones of the same sample. In particular, starting from the Paraloid layer on the right side of Figure 6.3.16, the microelectrode was moved towards the patina layer up to rich the copper core layer. Figure 6.3.20 shows a typical bi-dimensional image thus obtained with the microelectrode positioned 10 µm above the substrate. As is evident, low, medium and high

normalized currents were recorded while moving the microelectrode from the insulator to the copper core, coherently with the result obtained by the line scan. It is interesting to note that between the green and red zone, a thin yellow stripe appears. It was hypothesized the latter be due to the cuprite layer (see below).

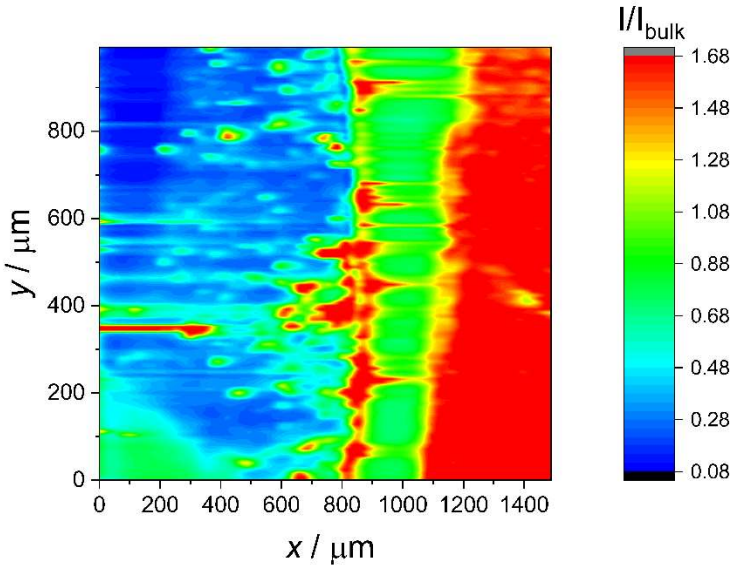

***Figure 6.3.20**: SECM image recorded over an area of the sample to include (from left to right) a stripe of resin and Palaroid in zone A, the patina layer and a stripe of the copper core. Redox mediator 1 mM FA^+ + 0.1 M Na_2SO_4. Pt microdisk 10 µm radius, biased at +0.3 V and positioned at 10 µm above the substrate.*

In order to get more detailed information over the boundary between patina and copper, a SECM image was recoded over a smaller zone (about 150 µm x 200 µm) of the substrate to include a copper stripe, the patina layer and a Palaroid stripe. To improve the resolution, the scan was performed by keeping the microelectrode above the substrate at about 5 µm. In this way, it was possible to heighten the contrast among the various currents and zones. A typical bi-dimensional image thus obtained is shown in Figure 6.3.21. The various zones can be better distinguished and they were characterized in the following four cases: i) high normalized currents (in red), corresponding to the copper core stripe; ii) lower normalized currents (in yellow), but still higher than 1, covering a stripe of thickness of about 10-16 µm, which could identify the cuprite layer; iii) normalize currents that are close or below 1 (green- light blue) of about 60-70

μm, which could correspond to the brochantite layer; iv) low normalized currents, i.e., < 0.7 (deep blue), which corresponds to the Palaroid stripe.

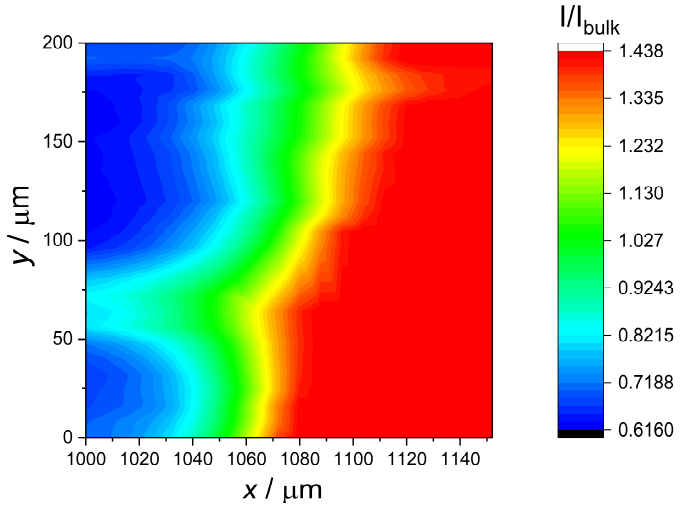

Figure 6.3.21: *SECM image recorded over an area of the sample to include (from left to right) a stripe of Palaroid in zone A, the patina layer and a stripe of the copper core. Redox mediator 1 mM FA^+ + 0.1 M Na_2SO_4; Pt microdisk 10 μm radius, biased at +0.3 V and positioned at 5 μm above the substrate.*

Apart from the obvious assignments of positive and negative effects, when the microelectrode travelled above the copper core and Palaroid zones, respectively, other assignments can be justified as follows. The cuprite layer could be revealed because of the following etching reaction involving the redox mediator:

$$Cu_2O + 2FA^{2+} + H_2O \rightleftharpoons 2Cu^{2+} + 2FA^{+}\ 2OH^{-} \qquad (6.3.8)$$

Reaction (6.3.8) can occur, as the FA^{2+}/FA^{+} system can act as oxidant with respect to Cu_2O, their redox potentials being 0.67 V [14] and -0.360 V [4], respectively. Therefore, FA^{2+}, formed at the Pt microelectrode, diffuses towards the substrate, where reaction (6.3.8) can occur, thus recycling the redox mediator (Scheme 6.3.2b). This justifies the I/I_{bulk} higher than 1.

[14] E. Coutouli-Argyropoulou, A. Kelaidopoulou, Christos Sideris,G. Kokkinidis, *J. Electroanal. Chem*. (**1999**) 477, 130–139.

However, the size of the yellow stripe in the SECM image (10-16 μm) is bigger than 5μm, as it was evaluated by SEM (Figure 6.3.17). The apparent discrepancy can be rationalized considering that the size of an object, as acquired by SECM, depends on several factors and, among others, on the tip-to-substrate distance. In Ref. [15] it was reported that the size of the object as detected by SECM, (indicated with s), is larger than its real size, (indicated with s_0), by the following distance-dependent term:

$$s = s_0 + 1.64\, d \qquad (6.3.9)$$

where d is the tip-to-substrate distance.

In our conditions, the tip-to-substrate distance could vary between 5 and 12 μm (due to the sample tilting in the investigated smaller zone). By using equation (6.3.9) and considering 5 μm as the real size, s_0, of the Cu_2O layer, the size of the cuprite layer detected by SECM, s, should vary between about 13 and 25 μm. In the images of Figure 6.3.21, the yellow-light green zone with $I/I_{bulk} > 1$, s actually extends over a distance of about 20 μm, which falls within the above two limits. From an imaging point of view, these blurry images are not desired and several strategies were adopted to avoid them[15]. In the specific situation investigated here, the diffusional broadening of the redox mediator allows characterizing the thin chemically active layer of cuprite, which otherwise would not have been possible to highlight.

The attenuated negative feedback recorded above the brochantite can also be an effect due to diffusion of the redox mediator occurring parallel to the sample surface. In fact, at the potential applied to the microelectrode, no interference due Cu^{2+} ions -which could come from solubility of brochantite, even if lowered by the sulfate ions of the supporting electrolyte- should

[15]K. Borgwarth, C. Ricken, D.G. Eblinget al., *Fresenius J Anal Chem* (**1996**) 356, 288–294.

occur. Nevertheless, copper ions can be released from the various layers of the substrate, as will be illustrated in detail below.

The release of copper ions and their diffusion in the solution was investigated by ASV using a similar approach as that described in the previous subsection 6.3.1. However, because the FA^+ oxidation occurs at potentials close to, but well separated from, the processes involving copper species, the tip-to-substrate distance and the responses related to copper were monitored simultaneously by combining ASV and linear sweep voltammetry (ASV-LSV). An example of the strategy employed is illustrated in Figure 6.3.22, which refers to the ASV-LSV responses obtained with the microelectrode positioned at different distances from and locations above the substrate. The microelectrode was biased at -0.5V for 120 s, which allowed detecting eventual trace of copper ions formed at the substrate/solution interface.

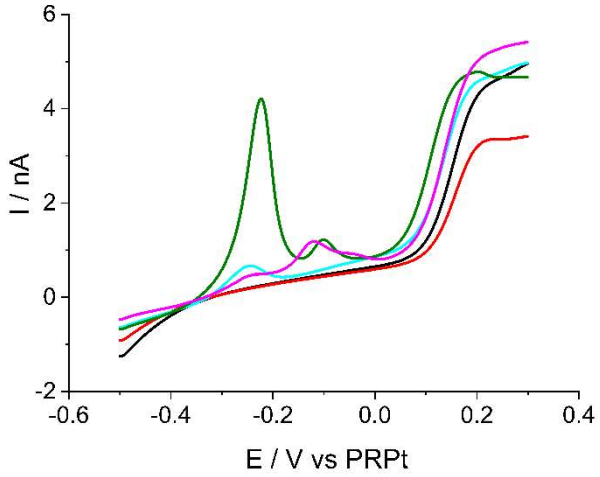

***Figure 6.3.22**: ASV-LSV registered after deposition at -0.5V for 120 seconds over the untreated sample in cross section in the bulk of the solution of 1 mM FA^+ + 0.1 M Na_2SO_4 (black trace), at 20 µm above the resin (red line), the patina (green and cyan lines) and the metallic copper core (magenta line). E_d = -0.5V; t_d = 120s; scan rate 50 mV s^{-1}.*

As is shown in Figure 6.3.22, when the microelectrode was positioned in the bulk solution (i.e., 700 µm away from the substrate), only the sigmoidal response due to FA^+ oxidation was recorded (Figure 6.3.22, black line). On the other hand, when the microelectrode was brought close to the surface (20 µm away) of the insulating resin, again only the response due to FA^+ was

obtained (Figure 6.3.22, red line), though, as expected, the limiting current was lower due to the hindered diffusion of redox mediator. Instead, when the microelectrode was brought close to the active part of the substrate, ASV signals due to oxidation of metallic copper, accumulated during the pre-concentration step of the ASV onto the microdisk surface, and FA^+ oxidation were recorded (Figure 6.3.22, cyan, magenta and green lines). Moreover, both ASV peak intensity and plateau current of the sigmoidal wave depended on the specific location and the time elapsed from the immersion of the sample in the solution. In particular, above the patina (including both the brochantite and cuprite layers), after 30 min immersion, an ASV peak at about -0.25 V was recorded (Figure 6.3.22, cyan trace); using the charge under the peak and equation (6.3.2), a concentration value of 1.7 μM was calculated. The current plateau of the sigmoidal wave was slightly higher than that recorded in bulk, conceivably due to a contribution of the mediator recycling due to the Cu_2O layer of the sample, i.e., through reaction (6.3.8). A larger ASV peak at -0.23 V, accompanied by a smaller one at about -0.1 V, similar to those observed in synthetic aqueous solutions, were recorded for longer immersion times (after about 210 min, ASV-LSV with the green line). From the charge involved in the ASV peak a copper ion concentration of 8.6 μM was calculated. Also in this case, the plateau current of the sigmoidal wave was slightly larger than in the bulk, again due to recycling of the redox mediator. The ASV-LSV response, obtained when the microelectrode was brought close to the copper core surface, also displayed two peaks, due to the stepwise oxidation of copper to Cu_2O and Cu^{2+}. The copper ions estimated from the charge involved in the ASV peaks was 3.5μM. In this case, the Cu^{2+} ions monitored could come from either the brochantite layer, reaching the copper surface through lateral diffusion, or from metallic copper itself through spontaneous corrosion. It must be considered that the ASV-LSV response was recorded after 90 min from the sample immersion, therefore a time long enough to allow sensible amount of Cu^{2+} ions to accumulate in the solution layer facing the substrate. The plateau current of the sigmoidal wave, higher than that recorded in the bulk

(Figure 6.3.22, magenta line), is mainly due to the recycling of the redox mediator above the conduction copper surface through lateral electron transfer (see Scheme 6.3.3).

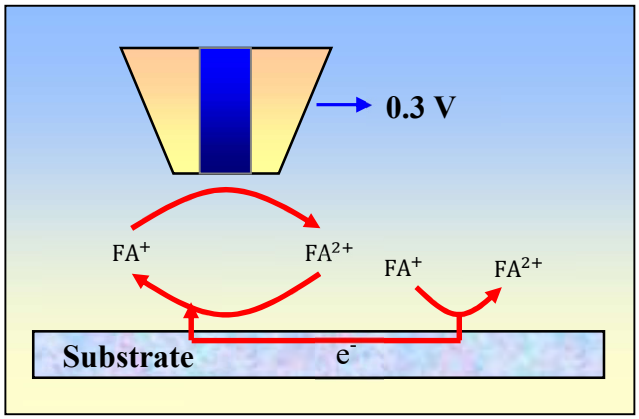

***Scheme 6.3.3**: Representation of the lateral electron transfer for unbiased substrates.*

The reactivity of the various layers of the cross-section was then investigated in the 0.1 KCl solution, and typical approach curves recorded above the insulating materials and active layers are are shown in Figure 6.3.23.

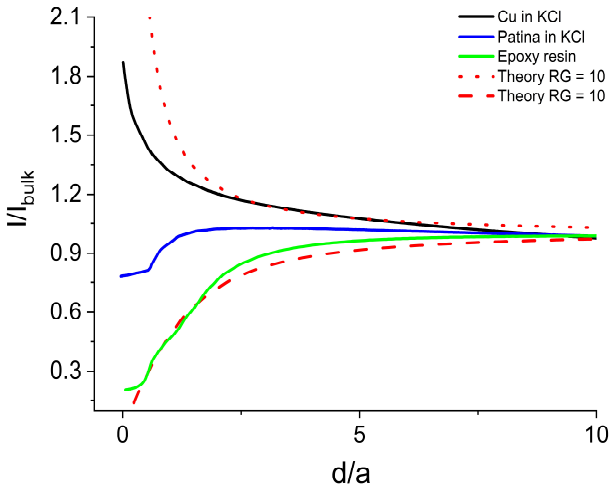

***Figure 6.3.23**: Approach curves recorded in 1mM FA^+ + 0.1M KCl over the untreated sample in cross section. Negative feedback curve over the resin (green trace) and attenuated negative feedback over the patina (blue trace) and positive feedback over the metallic copper (black trace).*

The general behavior is similar to that recorded in the 0.1 M Na_2SO_4 medium. That is, negative feedback, mixed positive-negative feedback and positive feedback responses were

obtained upon approaching the resin, the patina and the copper core layers, respectively. However, apart from the approach curve recorded above the insulating resin, whose I/I_{bulk} values fit the theory, in other cases, at a given d/a, I/I_{bulks} were higher in KCl, that that in Na_2SO_4 (see Figure 6.3.18). These results were rationalized by considering that the copper materials, in the presence of Cl^- ions, undergo enhanced corrosion processes[12]. In fact, copper oxides compounds, which can be formed on the copper surface by spontaneous corrosion, can be transformed in soluble copper chloro-complexes, thus providing a cleaner and more conductive copper surface. This should allow for more effective recycling of the redox mediator, through lateral electron transfer. On the other hand, Cu_2O of the patina can provide soluble $CuCl_2^-$ (reaction 6.3.10) and, in turn, to the reaction (6.3.11) with FA^{2+} generated at the microelectrode surface:

$$Cu_2O + 2H^+ + 4Cl^- \rightleftharpoons 2CuCl_2^- + H_2O \qquad (6.3.10)$$

$$CuCl_2^- + FA^{2+} \rightleftharpoons CuCl_2 + FA^+ \qquad (6.3.11)$$

This also provides the redox mediator recycling and, consequently, higher I/I_{bulk} values.

Line scans were performed to confirm the general behavior evidenced with the approach curves and Figure 6.3.24 shows typical current-distance profiles obtained starting from the insulator A going to B (red line) and viceversa (black line). The insulating zones, the conductive copper core and the reactive copper-containing materials can be clearly identified from the low, rapidly-growing and slowly-decaying normalized currents. The current depression within 125 µm $< d/a < 325$ was due to a Paraloid hump formed in close proximity of the copper core. This current depression and the entire current against distance profiles were quite reproducible as verified by repeating the scans several times. In addition, compared with the profiles recorded in the Na_2SO_4 solution, the current responses were smoother.

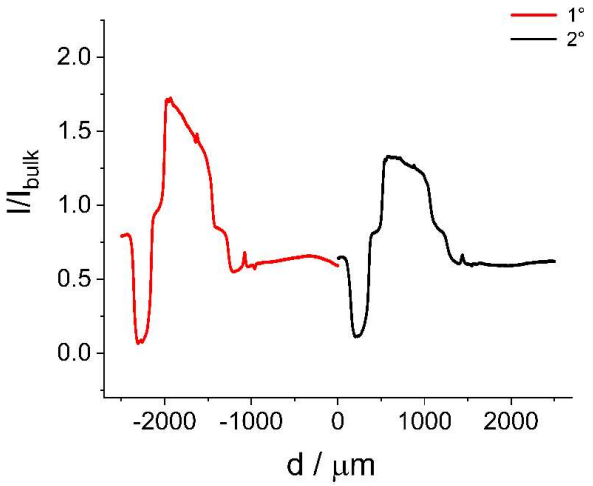

***Figure 6.3.24**: Linescans from the resin A to the resin B (red line) and viceversa (black line) of the untreated sample in cross section obtained by using 1 mM FA^+ + 0.1 M KCl (E_{app}= +0.3 V) and a Pt microdisk (10 µm radius). The tip was positioned at 10 µm above the substrate.*

Bi-dimensional scans were also performed (Figure 6.3.25) and the responses obtained provided similar information.

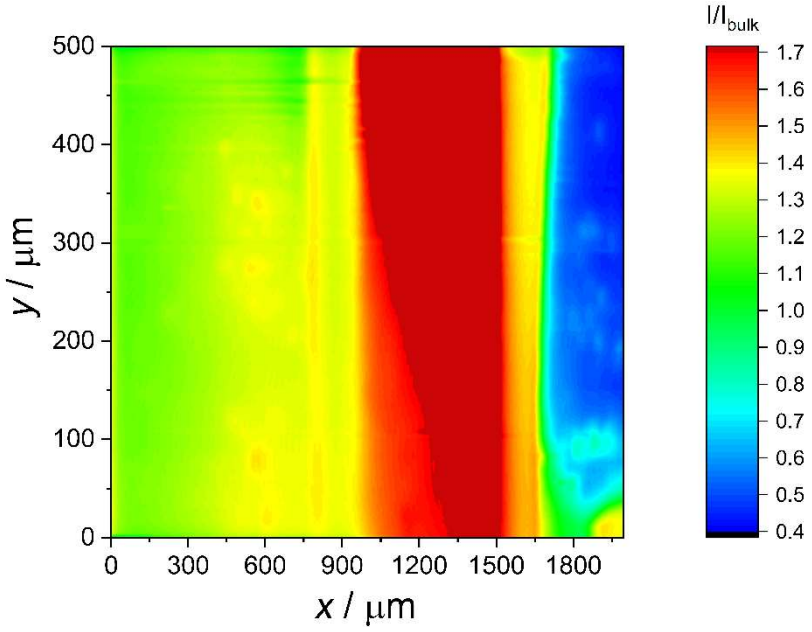

***Figure 6.3.25**: SECM image recorded over an area of the sample to include (from left to right) a stripe of resin and Palaroid in zone A, the patina layer and a stripe of the copper core. Redox mediator 1 mM FA^+ + 0.1 M KCl; Pt microdisk 10 µm radius, biased at +0.3 V and positioned at 20 µm above the substrate.*

To verify that copper ions were released from the various copper layers of the cross section, series of ASV-LSV measurements were performed by positioning the microelectrode in different points of the sample (indicated with numbers in the optical image in Figure 6.3.26) and different tip-to-substrate distances. Because of the continuous copper corrosion, the amount of copper ions released varied with the time elapsed from the sample immersion in the solution.

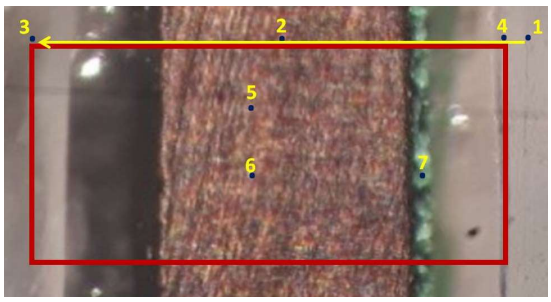

Figure 6.3.25*: Photographic image of the roof cladding untreated sample in cross section under the optical microscope. The numbers indicate the points where the SECM analysis were performed (1,3 and 4 over the resin, 2,5 and 6 over the Cu and 7 over the patina). The arrow indicates the position of the linescans and the red rectangle indicates the area of the bi-dimensional map.*

Initially, control measurements were performed to ascertain that no copper ions were present in the solution when the measurements were started. To this purpose ASV-LSV measurements were performed in the bulk solution (about 1000 µm away from the substrate), and under these conditions only the sigmoidal wave due to the oxidation of FA^+ was recorded. The microtip was then brought above the substrate in different points and different tip-to-substrate distances by using the FA^+ redox mediator. Once positioned at a precise location, CVs or ASV-LSV were performed. Figure 6.3.26 shows a typical CV (black line) performed in point **5**, above the copper layer. The potential range explored was from 0 V to -0.8 V in the forward scan and after reversal the potential was scanned up to + 0.3 V.

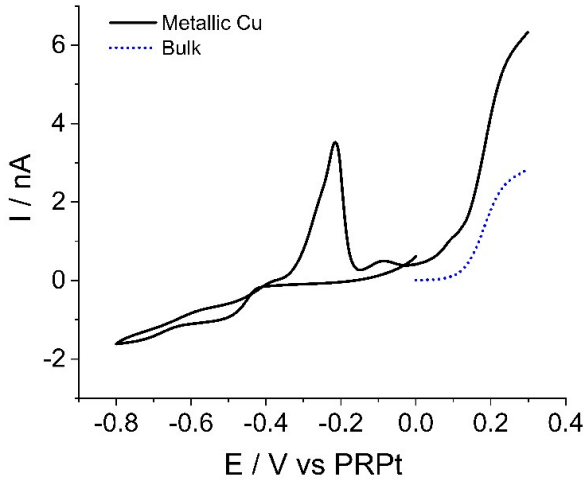

Figure* 6.3.26: CVs recorded over the untreated sample in cross section in 1mM FA^+ + 0.1M KCl above metallic copper in point 5 and in the bulk of the solution (dotted blue line). Scan rate 5mV s^{-1}.*

In the negative potential region, the typical features for the reduction/stripping process of the Cu^{2+}/Cu^0 system (see section 6.1) was recorded; in the anodic potential region, the oxidation wave due to FA^+ was observed as well. It was higher than that of the bulk (Figure 6.3.26, dotted blue line), due to recycling of the redox mediator. The current plateau of the latter wave normalized for that obtained in bulk was used to establish the correct tip-to-substrate distance. In the case of Figure 6.3.26, a *d/a* value of 0.7 was evaluated. The above result indicated that copper ions were formed at the copper/solution interface. Because the reduction wave occurred at rather negative potentials, it is likely that the wave observed was due to the reduction of $CuCl_2^-$ trough reaction (6.3.5), congruently with the stability of the latter species in the presence of high Cl^- concentrations.

Series of CVs as the previous one, were made by changing the tip-to-substrate distance and Figure 6.3.27 shows typical series thus obtained. These were recorded after about 120 min from immersion of the sample in the solution. Moreover, the negative going scan was limited to -0.6 V, to avoid including the small feature occurring at -0.7 V (in Figure 3.3.26), conceivably due to the oxygen reduction.

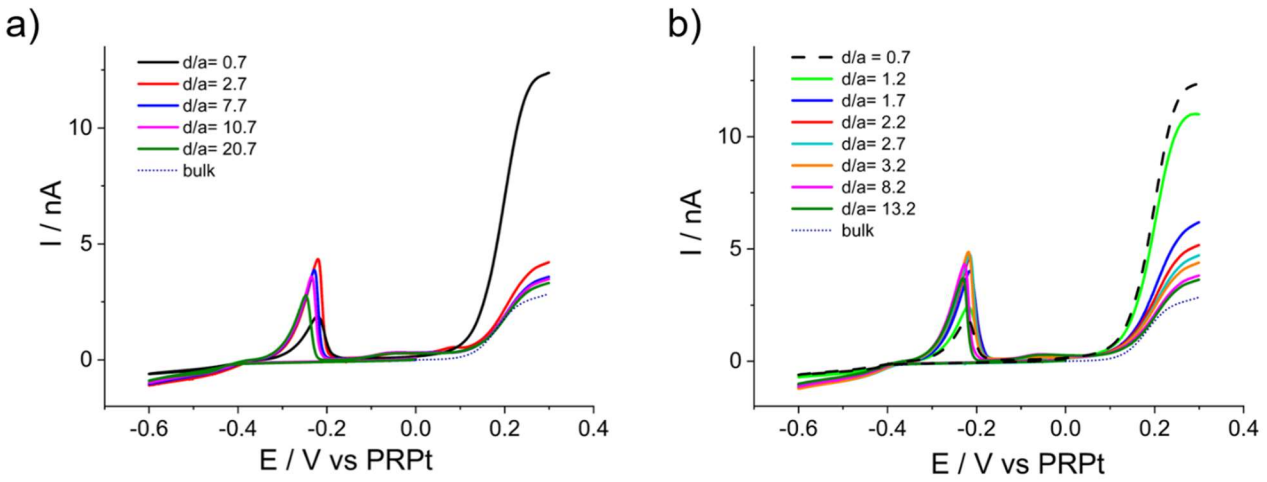

Figure 6.3.27: *CVs recorded over the untreated sample in cross section in 1mM FA^+ + 0.1M KCl with the microelectrode positioned at different distances approaching the metallic Cu substrate (a) and retracting from the substrate (b). The CV recorded in the bulk of the solution is also reported (dotted blue line). Scan rate 5mV s^{-1}.*

From Figure 6.3.27, it is evident that the amount of Cu^+ recorded depends on the tip-to-substrate distance, probably related to a concentration profile that generates at the metal/solution interface. The current intensity (I_c), corresponding to the plateau of the cathodic wave due to the reduction of $CuCl_2^-$ (when it could be clearly discerned from the background), the charge involved in the stripping peak (Q_a) and the I/I_{bulk} of the FA^+ were plotted against d/a. Relevant trends are shown in Figure 6.3.28a,b,c, respectively. As is evident, while the microelectrode approaches the surface (i.e., d/a decreases), I/I_{bulk} increases (Figure 6.3.28c, black symbols). Both I_c and Q_a (Figure 6.3.28a and 6.3.28b, respectively) increases up to d/a = 2, then decreases abruptly. This tailing peak shaped profile can be justified considering that that $CuCl_2^-$, released from copper corrosion, produced a dynamic concentration profile, the concentration being larger

in close proximity of the generating material. The apparent anomalous values of I_c and Q_a found at d/a < 2, can be related to a diffusion hindering, due to the substrate itself, which impedes somewhat the mass transport of $CuCl_2^-$ towards the microelectrode surface. In other words, when the microelectrode is positioned very close to the copper material, the depletion of $CuCl_2^-$ at the microelectrode surface (due to its reduction to Cu^0) was not quickly replenished from corrosion of copper. This view was supported by the fact that once the microelectrode was retracted from the copper surface towards the bulk solution, CVs of the $CuCl_2^-/Cu^0$ system provided the inverse behavior displayed while approaching the surface (Figure 6.3.28b,c red symbols). Instead, the I/I_{bulk} vs. d/a provided the positive feedback as that recorded during the approach step (Figure 6.3.28a). It is interesting to note that the point-by-point approach curve fully overlaps the theory (Figure 6.3.28a, red dashed line), contrary to that obtained at the beginning of the measurements (Figure 6.3.23, black line). This suggested that the redox mediator recycling could occur by either at the conducting copper surface or by reaction (6.3.11), when the amount of $CuCl_2^-$ in the solution is high enough to supply the extra current needed.

From the above result, it was assumed that for d/a ≥ 2, the effect of the substrate on the $CuCl_2^-$ diffusion towards the microelectrode surface was negligible.

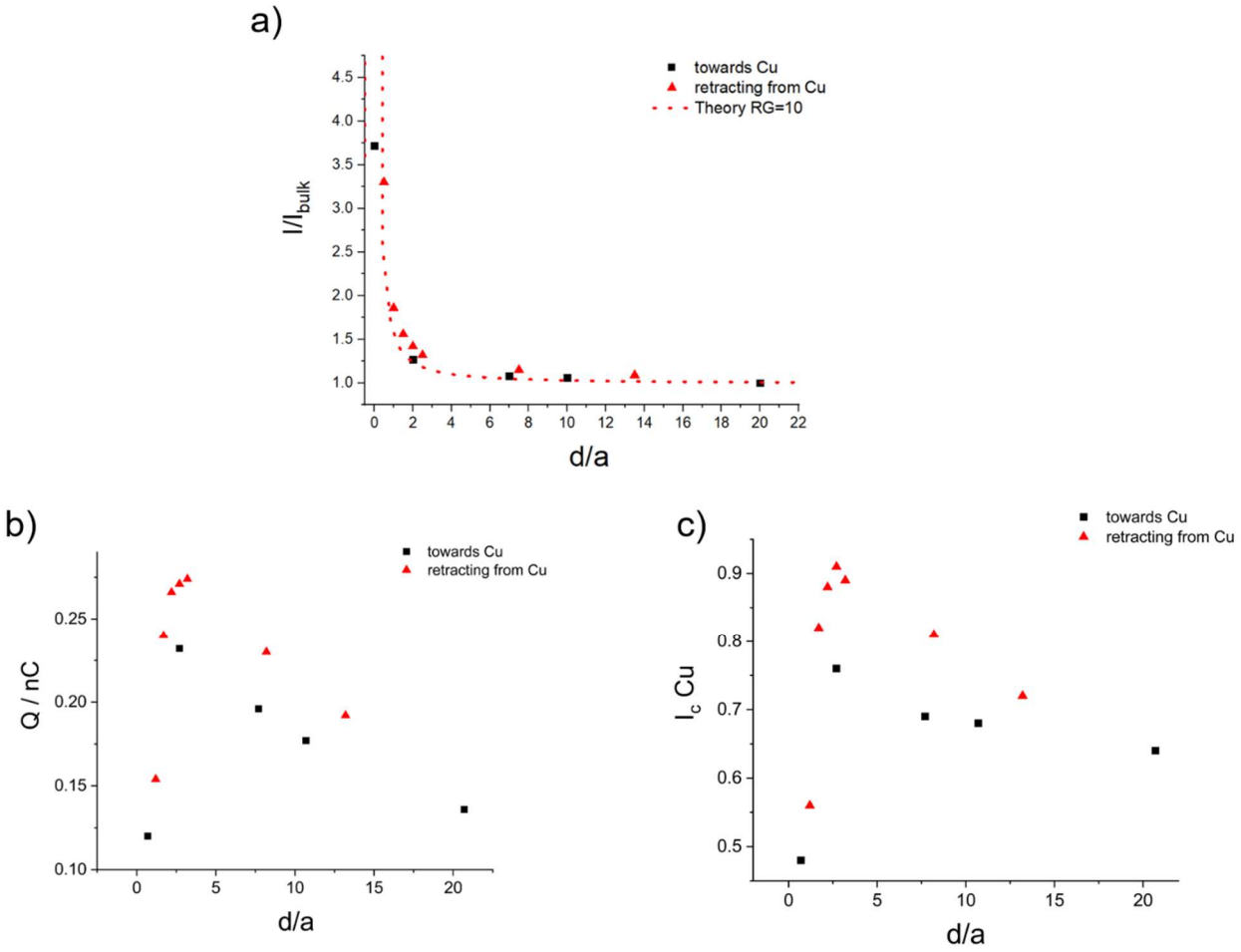

***Figure 6.3.28**: Normalized currents of FA^+ limiting currents (a), charge of the copper oxidation (b) and cathodic currents of copper reduction versus normalized distances taken from CVs of Figure 6.3.27a,b recorded over the untreated sample in cross section approaching (black squares) and retracting (red triangles) from the metallic Cu substrate. Theoretical curve for RG=10 is also reported (a, dotted red line).*

In order to verify to what extent copper ions diffuse laterally also over both patina and resin layers, and whether it was possible to distinguish between the regeneration of FA^+ through reactions (6.3.8) or (6.3.11), CVs measurements were performed in different points (highlighted with numbers in bold in Figure 6.3.25) of the cross section.

Figure 6.3.29a compares the CVs recorded in point **1** above the resin and that obtained at the same tip-to-substrate distance, specifically at about 200 µm away, in point **2** above the copper. The distance between the two points, as determined by the step motor was of 700 µm. From the CVs, it is clear that above the resin, the current intensities associated to the $CuCl_2^-/Cu^0$ system

are lower than those above the copper. This result indicated that $CuCl_2^-$ depleted significantly when passing from the copper surface to that of the resin.

Figure 6.3.29b compares CVs obtained recorded on point **7**, above the patina, and **6,** above the copper. To improve the resolution, these measurements were performed at a *d/a* of about 0.7. As is evident from the figure, the current intensities associated with the $CuCl_2^-/Cu^0$ system are similar in both positions. This suggested that the copper ions released from the copper core, likely, spread to the very close patina layer; this conceivably hidden the amount of copper ion released from the cuprite layer (trough reaction 6.3.8). Instead, as expected, the current due to the oxidation of FA^+ is much larger on copper, due to the efficient recycling of the redox mediator, compared to that exerted by the patina.

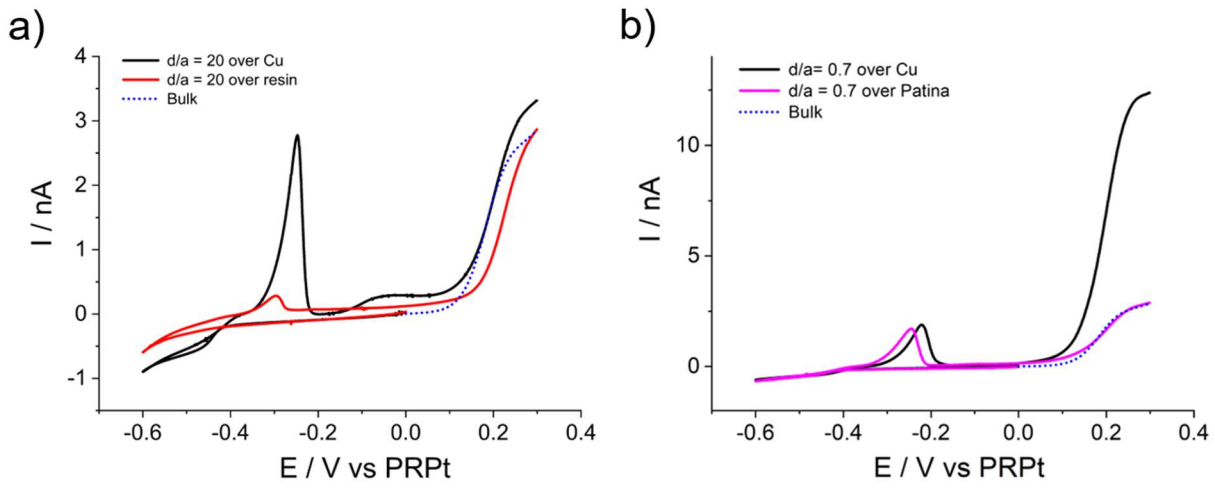

***Figure* 6.3.29**: *CVs recorded over the untreated sample in cross section in 1mM FA^+ + 0.1M KCl after 120 minutes of immersion with the microelectrode positioned at: a) d/a=20* over *the metallic Cu core (black line) and over the resin (red line); b) d/a=0.7 over the metallic Cu core (black line) and over the patina (magenta line). The CV recorded in the bulk at the beginning of the experiment is also reported (blue dotted line). Scan rate 5 mV s^{-1}.*

6.3.2.2. Samples treated with the inhibitors

The cross section of the roof samples treated with the inhibitors considered here are actually the same as those examined in the previous subsections. That is, only the top layer of the brochantite was directly in contact with solutions containing the inhibitors during the treatment. The inhibitors, however, could diffuse through the porous top layer inside the inner material, even down to the cuprite layer and the adjacent metallic copper. Therefore, the SECM results should, eventually, differ from those obtained for the untreated sample only when the measurements are carried out above the patina stratum.

The procedure employed in this investigation was similar to that described for the untreated sample. To better follows the reasoning, an image of the cross section is given in Figure 6.3.30 with indications on the specific points in which approach curves were recorded or the directions for line scans or bi-dimensional directions. The image represents both the samples treated with BTA and HC10.

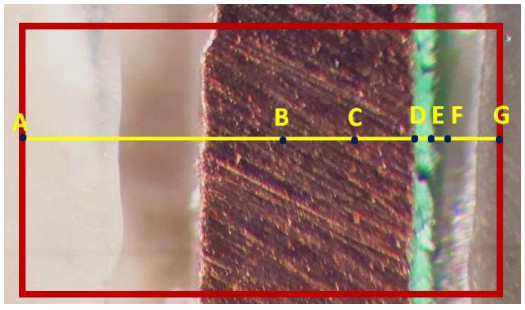

Figure 6.3.30: *Photographic image of the roof cladding treated samples (with both BTA and HC10) in cross section under the optical microscope. The capital letters indicate, roughly, the points where the SECM analysis were performed (A,G,F over the resin, B, C over the core copper and D and E over the patina). The yellow line indicates the direction of the linescans and the red rectangle indicates the area of the bi-dimensional image acquired by SECM.*

Figure 6.3.31 shows typical approach curves recorded in the various points (indicated with capital letters in Figure 6.3.30), in a solution containing 1 mM FA^+ and 0.1 M Na_2SO_4. The Pt microdisk (a = 12.5 μm) used in these experiments had an RG = 5. As is shown, above the

copper core (point B) and resin (point G), as expected, positive and negative feedback responses, respectively, overlapping the theoretical curves, were recorded. Above the patina layer (point E) negative feedback responses, also overlapping the theoretical curve, were obtained for both BTA- and HC10-treated samples, indicating that the patina layer was almost completely insulated. However, in point D, which was closer to the copper core, attenuated negative feedback approach curves were obtained. This can be due to the fact that because of the microelectrode size, a region including both patina and core copper were approached.

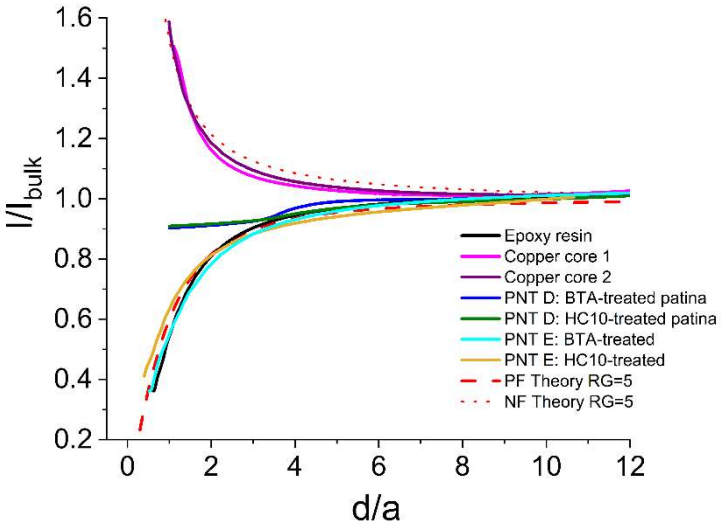

***Figure 6.3.31**: Approach curves recorded in 1mM FA^+ + 0.1M Na_2SO_4 over the roof cladding samples in cross section treated with HC10 and BTA. Negative feedback curve over the resin (black trace) and the points E; attenuated negative feedback over the patina in the points D, and positive feedback over the metallic copper (magenta and purple lines). Theoretical curves are also reported for a RG=5 (dotted and dashed red lines).*

To confirm the above observations on larger zones of the samples and to improve, to some extent, the resolution, line- and bi-dimensional scans were recorded above both kinds of treated samples, using a Pt microtip having a = 10 µm and RG = 5. Figures 6.3.32 shows line scans acquired by positioning the microelectrode 15 µm away from the substrate, starting from point G and moving the tip towards point A. As is evident the features of the scans obtained above both types of treated samples reflect the conductivity/reactivity of the various layers, i.e.,

low normalized currents above the insulating Palaroid and patina layers, high normalized current above the metallic copper.

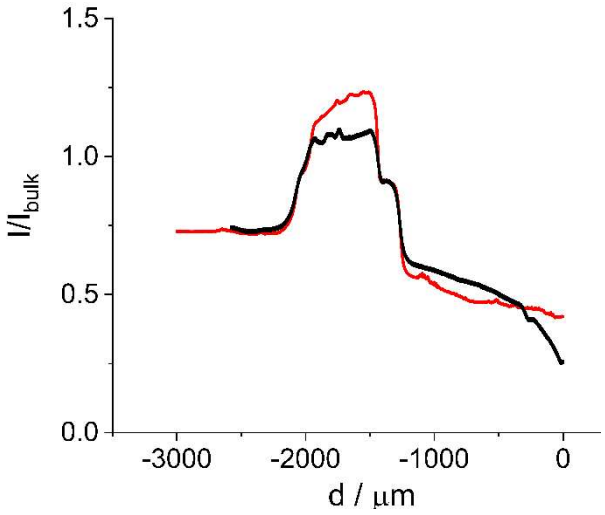

***Figure 6.3.32**: Linescans from the resin G to the resin A of the roof cladding samples in cross section treated with decanoic acid (black trace) and benzotriazole (red trace) obtained by using 1 mM FA^+ + 0.1 M Na_2SO_4 (E_{app}= +0.3 V) and a Pt microdisk (10 µm radius). The tip was positioned at 15 µm above the substrate.*

Similar results were obtained by bi-dimensional scans (Figure 6.3.33). In this case, the Pt microtip had a = 12.5 µm and RG = 5 µm. The scan was initiated from the copper core and moved towards the insulating Paraloid and refer to the HC10-treated sample. A similar image (not shown) was recorded above the BTA-treated sample.

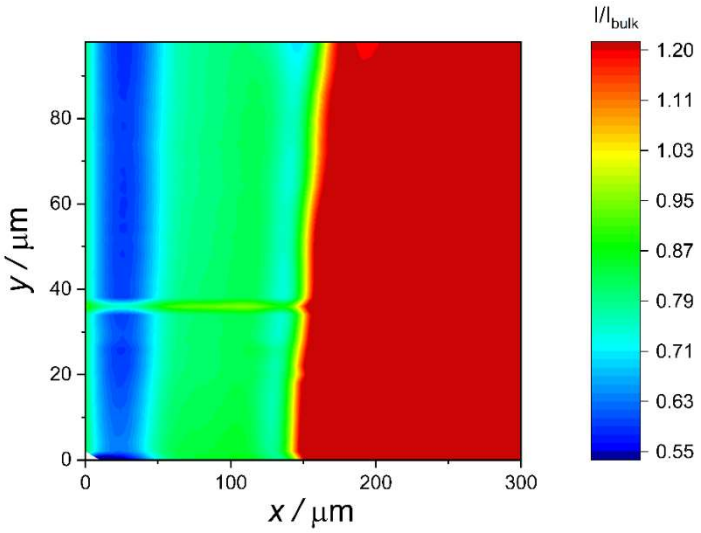

***Figure 6.3.33**: SECM image recorded over an area of the roof cladding HC10-treated sample to include (from left to right) a stripe of Palaroid in the point F, the patina layer and a stripe of the copper core. Redox mediator 1 mM FA^+ + 0.1 M Na_2SO_4; Pt microdisk 12.5 µm radius, biased at +0.3 V and positioned at 20 µm above the substrate.*

With respect to the images recorded across the inhibitor-free samples, in the treated samples the I/I_{bulk} on the right side of the image appears smoother and extends slightly closer to the copper layer. In fact, from the bi-dimensional image, the size of the yellow stripe was about 4 µm, indicating that the redox reaction between FA^{2+} and Cu_2O took place to a very low extent, indicating that also this layer was somewhat passivated.

In order to assess that the inhibitors also decreased the reactivity of the materials in terms of copper ions released, ASV-LSV measurements were performed at the substrate solution interface. Above the copper core, sensible amounts of copper ions were found, similar to those obtained for the inhibitor-free samples. Instead, above the patina layer, in both types of inhibitors treated-samples, negligible amounts of copper could be monitored. This is clearly evident from the ASV-LSV shown in Figure 6.3.34 (for BTA-, black line, and HC10-, blue line, treated samples, respectively).

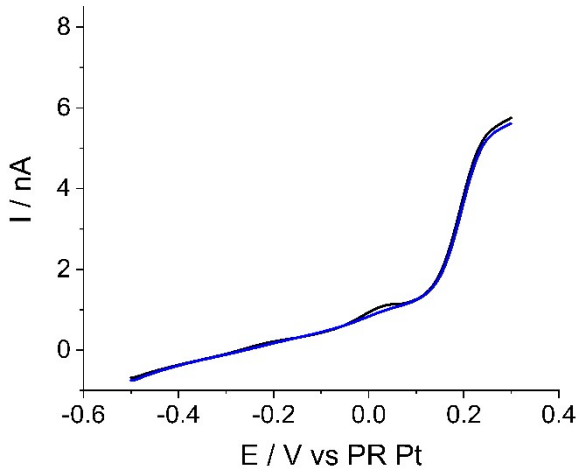

***Figure 6.3.34**: ASVs recorded over the roof cladding BTA- and HC10-treated samples (black and blue lines, respectively) in 1 mM FA^+ + 0.1 M Na_2SO_4 with the microelectrode positioned at 30 µm above the patina. E_d = -0.5V; t_d = 120s; scan rate 50 mV s^{-1}.*

Analogous series of SECM measurements, using the roof cladding samples treated with the inhibitors, were performed in a solution containing 0.1 M KCl.

The approach curves recorded above the BTA-treated sample (Figure 6.3.35a) displayed similar results, as those obtained in 0.1 M Na_2SO_4. That is negative feedback and positive feedback responses were recorded above the patina and the copper core respectively, both overlapping the theoretical curves. Shifting the position of the microelectrode from the patina layer towards copper, attenuated negative feedback approach curves were recorded (as seen in Figure 6.3.31). These results indicated that BTA formed a stable layer above the patina.

Approach curves recorded above the HC10-treated samples provided somewhat different results in 0.1 M KCl. Figure 6.3.35b shows a series of such measurements, moving the microtip from the patina layer to the copper core layer (from point F to point B in Figure 6.3.30). In this case approach curves varying from negative feedback to fully positive feedback responses are observed. Positive feedback approach curves are also recorded in points between the patina and the copper core layer. This would suggest the occurrence of the redox mediator regeneration through the reaction involving $CuCl_2^-$, formed at the substrate/solution interface, and FA^{2+} generated at the microelectrode surface.

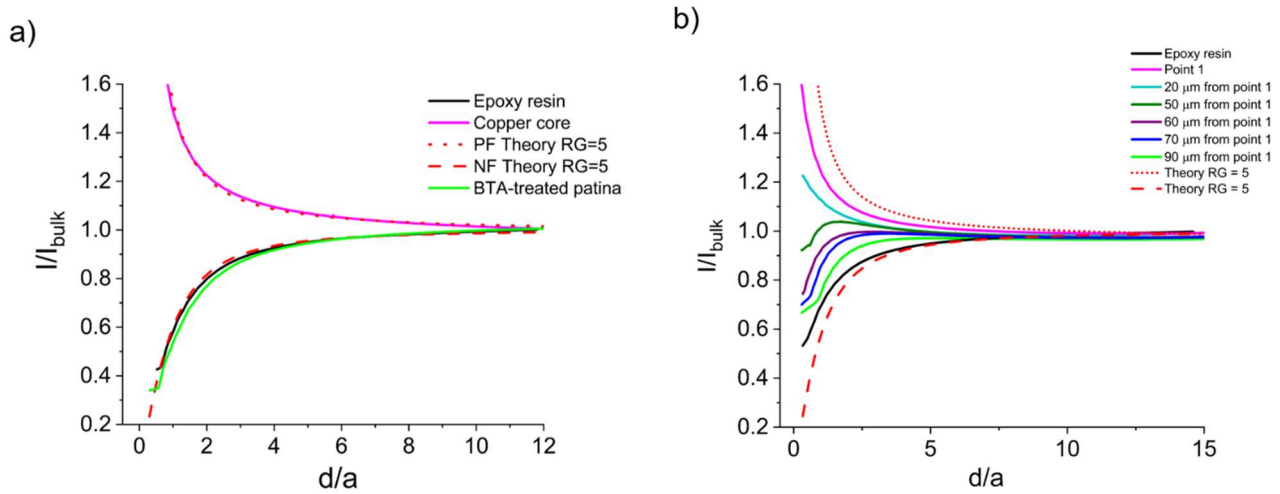

Figure 6.3.35: *Feedback approach curves recorded in different spots over the roof cladding (a) BTA-treated and (b) HC10-treated samples in 1 mM FA^+ + 0.1M KCl. Theoretical negative feedback curves (red dashed lines) as well as the positive feedback (red dotted lines) for RG=5 are reported.*

The higher reactivity of the HC10-treated sample, compared to the BTA-treated one, was also confirmed by recording line- and bi-dimensional scans (Figure 6.3.36 and Figure 6.3.37a,b respectively).

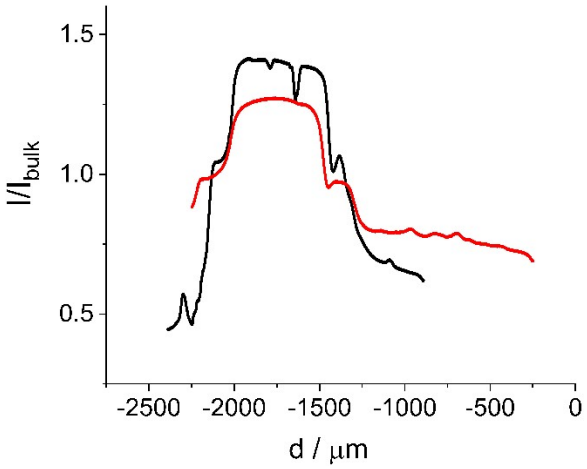

***Figure 6.3.36**: Linescans from the resin G to the resin A of the roof cladding samples in cross section treated with decanoic acid (black line) and benzotriazole (red line) obtained by using 1 mM FA^+ + 0.1 M KCl (E_{app}= +0.3 V) and a Pt microdisk (12.5 µm radius). The tip was positioned at 20 µm above the substrate.*

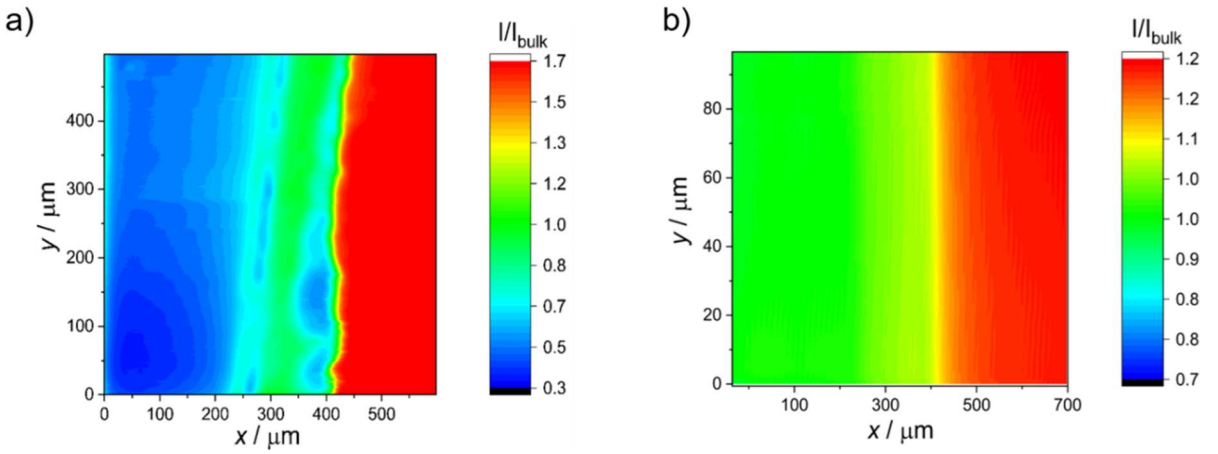

***Figure 6.3.37**: SECM image recorded over an area of the roof cladding (a) HC10-treated and (b) BTA-treated samples to include (from left to right) a stripe of Palaroid in the point F, the patina layer and a stripe of the copper core. Redox mediator 1 mM FA^+ + 0.1 M KCl; Pt microdisk 12.5 µm radius, biased at +0.3 V and positioned at 20 µm above the substrate.*

Finally to prove that the BTA-tretaed sample is less reactive than the HC10-treated one, ASV-LSV measurements were performed above the copper and the patina lyers.

Figure 6.3.38 shows ASV-LSV obtained above the copper core (point B in Figure 6.3.30) as a function of the time elapsed from the immersion of the sample in the solution. As is evident relative high ASV peaks are recorded, indicating a rather high amount of copper ions released in the solution (compare the ASV peak heigths with the sigmoidal wave of the FA^+).

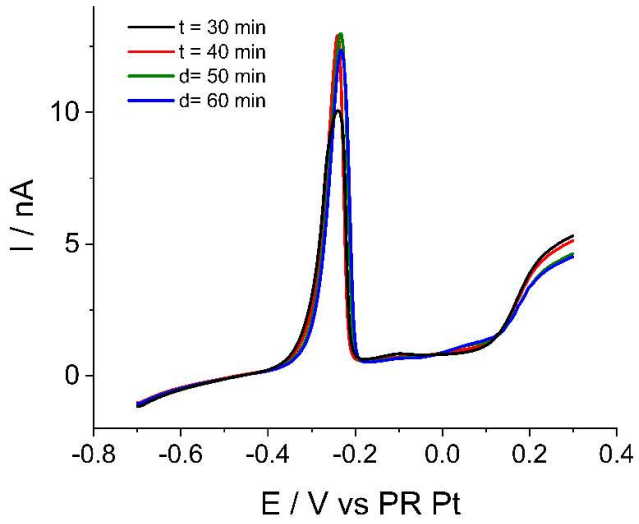

***Figure 6.3.38**: ASV-LSVs recorded over the copper core of the roof cladding BTA-treated samples in 1 mM FA^+ + 0.1 M KCl with the microelectrode positioned at 30 µm above the substrate. E_d = -0.7V; t_d = 120s; scan rate 50 mV s^{-1}.*

Above the two-treated patina layers (between D-F, in Figure 6.3.30), ASV-LSV measurements performed under similar experimental conditions, provided rather different results (Figure 6.3.39a for HC10, and Figure 6.3.39b for BTA). In fact, in both cases, the ASV peaks were much lower than those recorded above the copper core of Figure 6.3.38 (compare the ASV peak relative heigths with the sigmoidal wave of the FA^+). In addition, the ASV peaks above the BTA-tretaed sample are somewhat lower than the HC10-treated sample. These results confirm that, overall, both BTA and HC10 are useful to inhibit the corroded layers of the patina, and

agreed with data obtained in the previous sections in the study performed on the top layers of the samples.

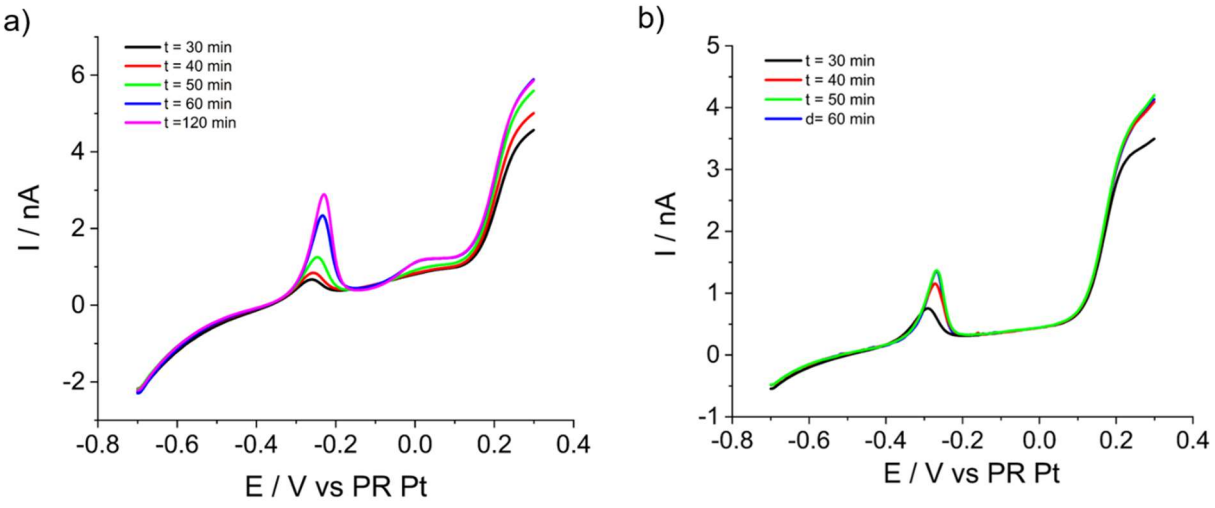

***Figure 6.3.39**: ASVs recorded over the patina layer of the roof cladding HC10- and BTA-treated samples (a and b, respectively) in 1 mM FA^+ + 0.1 M KCl with the microelectrode positioned at 30 µm above the patina. E_d = -0.7V; t_d = 120s; scan rate 50 mV s^{-1}.*

6.3.3. Final considerations

Finally, considering the results obtained in this chapter by SECM, together with those obtained in section 6.2, using potentiodynamic measurements, and the spectroscopic analysis of the sample-inhibited surfaces, can be concluded that, although BTA seems to be slightly more effective than HC10 in preventing corrosion phenomena and protecting the patina layer, because of the above-mentioned toxicity concerns of BTA, HC10 could represent an attractive eco-friendly and human-safe alternative as inhibitor to be used for treating copper-based materials of cultural heritage interest.

Chapter 7: Hydrogel-Filled Micropipette Contact Systems

7. Hydrogel-Filled Micropipette Contact Systems

Polymeric gels (PGs) prepared by biopolymers (BPs), such as starch, pectin or agar, have been extensively used in different areas including biology[1] and food industry[2,3]. PGs have also been frequently used in electrochemical devices such as batteries, accumulators[4,5], solar cells[6] and sensors[7]. In the latter field, biopolymeric gels (BPGs) have been used to avoid adverse effects arising from organic matter, which can adsorb onto the electrode surface[8], to minimize contribution due to natural convection in the mass transport[9], and to accommodate nanomaterials within its matrix for sensor applications[7]. Recently, BPGs have found applications to construct contact electrochemical cells for solid surface analysis by using electrochemical impedance spectroscopy[10,11,12,13,14]. These systems were employed for studying corrosion processes and characterize in-situ large surface areas (i.e., over cm^2 sizes) of patinas and protective coatings of cultural heritage materials. Miniaturized hydrogel-integrated systems for studying localized electrochemical events by voltammetry or potentiometry have also been reported. In Refs. [15,16], a layer of chitosan has been electrodeposited on microdisk electrodes and the gel has been loaded with suitable redox species to perform voltammetric[15] or potentiometric[16] measurements. In Ref. [17], a pyramid-shaped tip, composed of agarose, has been fabricated from a master prepared by

[1] S. Mohanty, S. Mishra, P. Jena, B. Jacob, B. Sarkar, A. Sonawane, *Nanomedicine: Nanotechnology, Biology, and Medicine* (**2012**) 8:916–924.
[2] A.L. Incoronato, G.G. Buonocore, A. Conte, M. Lavorgna, M.A. Del Nobile, *Journal of Food Protection* (**2010**) 73(12):2256–2262.
[3] J.W. Rhim, L.F. Wang, S.I. Hong, *Food Hydrocolloids* (**2013**) 33:327-335.
[4] J. Wu, J.J. Black, L. Aldous, *Electrochimica Acta* (**2017**) 225:482–492.
[5] L. Cao, M. Yang, D. Wu, F. Lyu, Z. Sun, X. Zhong, H. Pan, H. Liuc, Z. Lu, *Chem. Commun*. (**2017**) 53:1615-1618.
[6] M. Kaneko, T. Nomura, C. Sasaki, *Macromolecular Rapid Communications*, (**2003**) 24:444-446.
[7] Dhanjai, A. Sinha, P.K. Kalambate, S.M. Mugo, P. Kamau, J. Chen, R. Jain, *Trends in Analytical Chemistry* (**2019**) 118:488-501.
[8] C. Belmont-Hébert, M.L. Tercier, J. Buffle, G.C. Fiaccabrino, N.F. De Rooij, M. Koudelka-Hep, *Anal. Chem*. (**1998**) 70:2949-2956.
[9] M.H. Lee, Y.T. Kim, *Electrochemical and Solid-State Letters* (**1999**) 2:72-74.
[10] E. Cano, A. Crespo, D. Lafuente, B.R. Barat, *Electrochem. Commun.* (**2014**) 41:16-19,
[11] B.R. Barat, E. Cano, *Electrochimica Acta* (**2015**) 182:751-762.
[12] B.R. Barat BR, Cano, P. Letardi, *Sensors and Actuators B* (**2018**) 261:572 – 580.
[13] F. Di Turo, P. Matricardi, C. Di Meo, F. Mazzei, G. Favero, D. Zane, *Journal of Cultural Heritage* (**2019**) 37:113–120.
[14] F. Di Turo, C. De Vito, F. Coletti, F. Mazzei, R. Antiochia, G. Favero, *Microchemical Journal* (**2017**) 134:154–163.
[15] L. Liu L, M. Etienne, A. Walcarius, *Anal. Chem*. (**2018**) 90 :8889−8895.
[16] N. Dang N, M. Etienne, A. Walcarius, L. Liu, *Electrochem. Commun*. (**2018**) 97:64-67.
[17] H. Kang, S. Hwang, J. Kwak, *Nanoscale* (**2015**) 7:994-1001.

conventional photolithography and subsequent anisotropic etching. The hydrogel tip has been then filled with an electrolyte through an equilibrium process by soaking the gel-pyramid in the electrolyte solution. These probes, combined with a scanning system, other than probing the surface reactivity, have allowed to image the topography of the substrate or to fabricate, by electrodeposition, 3D nanostructures.

This part of the research project was devoted to the development of an alternative gel-integrated electrochemical microprobe for contact electrochemical measurements, exploiting the principle of the microcapillary-based technique[18,19,20].

7.1. Hydrogel-filled micropipette

The system proposed here employs a micropipette (Figure 7.1.1a), which is filled with an ionically conductive hydrogel made by mixing a polysaccharide and an aqueous solution containing an electrolyte. A thin layer of the formed hydrogel protrudes outside the micropipette extremity. A two-electrode micro-electrochemical cell can be formed by a pseudo-reference/counter electrode (usually a Pt or Ag wire), immersed in the hydrogel medium within the micropipette, and a working electrode made by the small portion of the conducting substrate that comes into contact with the gelled meniscus (Figure 7.1.1b).

Agarose has been chosen as polysaccharide because it provides an uncharged matrix thus mimicking molecular solvents, in which free diffusion electroactive species can occur, regardless of whether they are charged or not[21]. In addition, the agarose hydrogel brings the advantage of being cheap, biodegradable, non-toxic and can be easily prepared. The system proposed here can

[18] N. Ebejer, A.G. Guell, S.C.S. Lai, K. McKelvey, M.E. Snowden, P.R. Unwin, *Annu. Rev. Anal. Chem*. (**2013**) 6:329–351.
[19] R.M. Souto, J. Izquierdo, J. Santana, S. Gonzalez, *Eur. J. Sci. Technol.* (**2013**) 9:71-89.
[20] V. Vignal, H. Krawiec, O. Heintz, R. Oltra, *Electrochim. Acta* (**2007**) 52:4994-5001.
[21] H.L.T. Ho, R.A.W. Dryfe, *Langmuir* (**2009**) 25(21):12757-12765.

be useful to make electrochemical measurements on surfaces which suffer from direct contact with liquid electrolytes as can be materials of historical/artistic interest.

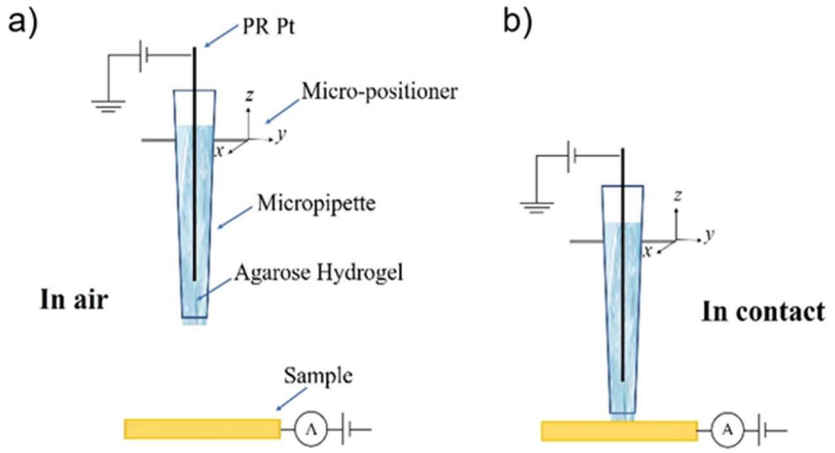

***Figure 7.1**: Scheme of the developed hydrogel-filled micropipette system. a) Micropipette approaching the substrate while it is in air; b) gelled meniscus landed on the substrate forming the electrochemical cell.*

7.2. Potential windows and open circuit potentials in the bulk of the agarose hydrogels

Preliminarily, cyclic voltammograms (CVs) were recorded in the bulk of the aerated hydrogels to establish the potential windows available at a Pt microdisk electrode. Figure 7.2 shows typical responses obtained in the hydrogels containing 0.1 M KNO_3 (blue line) or 0.1 M KCl (black line). In the cathodic scan, waves with half-wave potential ($E_{1/2}$) of -0.50 V (in 0.1 M KCl) and -0.60 V (in 0.1 M KNO_3) were observed (inset in Figure 2). These were assigned to the oxygen reduction process, as the solutions were not de-aerated. The onsets of the cathodic limits occurred at about -1.1 V and -1.2 V in the medium containing KCl and KNO_3, respectively. In the anodic scan, a featureless voltammogram up to the onset of the background discharge, taking place at about 1.4 V, was recorded in 0.1 M KNO_3. Instead, in 0.1 M KCl, prior the onset of background discharge that occurred also at about 1.4 V, a wave with $E_{1/2}$ equal to 1.2 V,

conceivably due to the Cl^- oxidation[22], was observed. These results therefore indicate that, within the above limits, no process due to the organic matter, present in the medium, occurs.

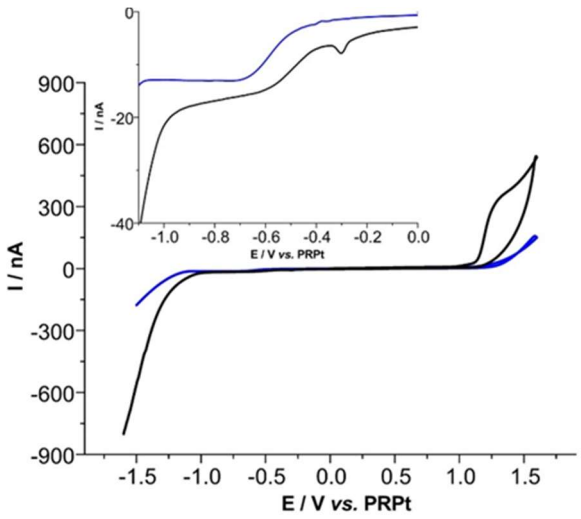

***Figure 7.2**: Cyclic voltammograms recorded at a Pt 12.5 µm radius in agarose hydrogel containing 0.1 M KNO_3 (blue line) and 0.1 M KCl (black line). Scan rate: 100 mV s^{-1}.*

The stability of the ionic hydrogel and the effect of agarose at the electrode/hydrogel interface was also investigated by performing open circuit potential (OCP) measurements. It was observed that stable OCPs were achieved after about 90-100 s and set at -22 (± 5) mV and -80 (± 15) mV in the 0.1 M KCl and 0.1 M KNO_3 media, respectively. The higher reproducibility observed in the KCl medium was probably due to the adsorption strength of chloride ions, higher than that of other anions, onto platinum electrode surfaces[23]. This, presumably, provided a more stable Pt/hydrogel interface, which prevented, to some extent, the possible formation of an agarose layer on the electrode surface, due to adsorption phenomena, as often happens to Pt electrodes, in the presence of organic matter[24].

[22] E.L. Littauer, L.L. Shreir, *Electrochimica Acta* (**1966**) 11:527 – 536.
[23] G. Horányi, G. Vértes, *Journal of electroanalytical chemistry and interfacial electrochemistry* (**1973**) 45(2):295-299.
[24] S. Daniele, D. Battistel, S. Bergamin, C. Bragato, *Electroanalysis* (**2010**) 22:1511–1518.

Similar measurements performed in the above media containing also the redox probes (1mM) produced slight changes in the OPC values, i.e., of about 50 mV and 13 mV towards less negative potentials in the presence of $Ru(NH_3)_6^{3+}$ and $Fe(CN)_6^{4-}$, respectively.

7.3. Voltammetric behavior of soluble redox probes in the bulk of aqueous and agarose hydrogel media

Preliminarily, mass transport characteristics of the redox probes $[Ru(NH_3)_6]^{3+}$ and $[Fe(CN)_6]^{4-}$ in the 2% (w/v) agarose were obtained in the bulk media, using the Pt microelectrode. For comparison, measurements were also performed in the corresponding gel-free aqueous media. These measurements were limited to the hydrogel/electrode systems containing 0.1 M KCl as supporting electrolyte, which was employed for microcapillary measurements (see next paragraph).

Figure 7.3 (full lines) contrasts typical CVs obtained at 5 mV s^{-1} in 1 mM each of $[Ru(NH_3)_6]^{3+}$ (Figure 7.3a) and $[Fe(CN)_6]^{4-}$ (Figure 7.3b) aerated aqueous and agarose-gel media. In both cases, sigmoidal waves, typical for microelectrodes working under steady-state conditions, are evident[25]. The lack of a well-defined current plateau for $Ru(NH_3)_6^{3+}$ was due to the presence of oxygen, whose reduction process, at potential negative to -0.4 V, partially overlapped with that of the redox probe. This effect was less marked in the agarose hydrogel, probably because of the lower diffusion coefficient of O_2 in the gel (i.e., $9.18 \cdot 10^{-6}$ cm^2 s^{-1})[26] with respect to water solutions (i.e., $2.12 \cdot 10^{-5}$ cm^2 s^{-1})[27]. Indeed, in de-aerated aqueous media, using the same Pt microelectrode, the reduction of $Ru(NH_3)_6^{3+}$ provided a better-defined current plateau (Figure 7.3a, red dashed line).

[25] A.J. Bard, L.R. Faulkner, Electrochemical Methods: Fundamentals and Applications. John Wiley & Sons, (**2001**)
[26] M. Zhang, L. Xiong, R.G. Compton, *Anal. Methods* (**2013**) 5:3473–3481.
[27] C. Bragato, S. Daniele, M.A. Baldo, G. Denuault, *Ann. Chim*. (**2002**) 92:153 – 161.

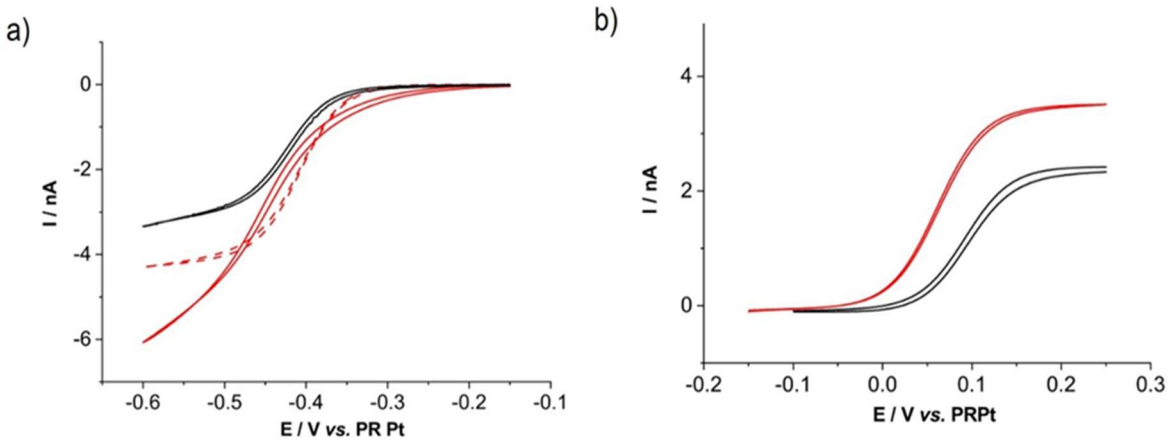

Figure 7.3: *Cyclic voltammograms recorded at a Pt microdisk 12.5 µm radius in (a) 1 mM $[Ru(NH_3)_6]^{3+}$ and (b) 1 mM $[Fe(CN)_6]^{4-}$ solutions. Black and red full lines refer to the aerated agarose hydrogel and aqueous media, respectively; the red dashed line in (a) refers to the de-aerated aqueous solution.*

From the steady state limiting currents, and the Equation (7.1), diffusion coefficient values for both redox probes were calculated and are shown in Table 7.1.

$$I_{ss} = 4\, n\, F\, D\, C^b\, a \qquad (7.1)$$

In the hydrogel, diffusion coefficients (D_{gel}) are lower than those in aqueous solution (D_{aq}), the D_{gel}/D_{aq} ratios being 0.76 and 0.68 for $[Ru(NH_3)_6]^{3+}$ and $[Fe(CN)_6]^{4-}$, respectively. For $[Ru(NH_3)_6]^{3+}$, D_{gel}/D_{aq} found here is consistent with 0.80 reported in [28] (where a 0.5% (w/v) agarose hydrogel + 0.1 M KCl medium was investigated), though absolute diffusion coefficient values in both media were larger than those shown in Table 7.1 (i.e., $D_{gel} = 7.84 \cdot 10^{-6}$ cm^2 s^{-1} and $D_{aq} = 9.78 \cdot 10^{-6}$ cm^2 s^{-1}).

[28] B. Csoka, G. Nagy, *J. Biochem. Biophys. Methods* (**2004**) 61:57–6.

***Table 7.1**: Diffusion coefficient values of the redox probes in aqueous solution (D_{aq}) and in 2% (w/v) agarose hydrogel (D_{gel}), both media containing 1 mM of the electroactive specie and 0.1 M KCl.*

Redox probe	D_{aq} ($\cdot 10^6$ cm^2 s^{-1})*	D_{gel} ($\cdot 10^6$ cm^2 s^{-1})*	D_{gel}/D_{aq}
$[Fe(CN)_6]^{4-}$	6.52 (± 0.11)	4.43(± 0.13)	0.68
$[Ru(NH_3)_6]^{3+}$	7.45 (± 0.14)**	5.66(± 0.14)	0.76
Ag^+	15.1(± 0.2)	11.3(± 0.2)	0.75

*Average values from three replicates. **Obtained in de-aerate aqueous solution.

7.4. Microcapillary voltammetry using the micropipette filled with hydrogel and aqueous solutions

Microcapillary contact measurements were performed with the micropipettes filled with either the hydrogel or the corresponding agarose-free aqueous solution, containing 1 mM $[Fe(CN)_6]^{4-}$ and 0.1 M KCl; an Au-coated glass surface was employed as substrate. The micropipette was mounted on the micro-positioning system and moved towards the substrate (Figure 7.4a, initially, at 10 μm s^{-1} and subsequently more finely at 0.1 μm s^{-1}. The substrate was held at +0.4 V and the current flow was monitored continuously. Upon contact of the meniscus at the end of the pipette with the substrate, a current spike was observed (see as an example Figure 7.4a), and the approach was automatically stopped. The pipette was held in place and series of CVs were run at different scan rates, over the range 5-75 mV s^{-1}. Typical CVs obtained with the micropipette filled with the hydrogel and the aqueous solution are shown in Figures 7.4b and 7.4c, respectively. It is worth to note that the two series of measurements were performed using the same micropipette having an opening radius of 30 μm. As is evident from Figures 7.4b-c, in both media, peak-shaped responses, typical for planar diffusion, were obtained. This is different from the features observed with the microelectrode in the bulk media and is related to the fact that, for the size of the meniscuses involved in these measurements, the current is

essentially dominated by the linear diffusion through the capillary. This behavior agrees with previous reports[29]. The analysis of the forward peak current (I_p) against the square root of the scan rate (v), (Figure 7.4b,c, insets), provided linear trends, consistently with Equation (7.2) that holds for planar diffusion[25]:

$$I_p = 2.69 \cdot 10^5 \; n^{3/2} A D^{1/2} C v^{1/2} \qquad (7.2)$$

where A is the surface area of the substrate wet by the meniscus; the other symbols have their usual meanings. Linear regression analysis of the experimental data provided the following relationships: $y\ (nA) = 21.22\ (\pm 0.45.)\ v^{1/2}\ (v, V\ s^{-1}) + 0.05$ ($\pm$.0.02) (R^2 = 0.997) and $y\ (nA) = 394.19$ ($\pm$ 14.71) $v^{1/2}\ (v, V\ s^{-1}) + 1.15$ ($\pm$ 0.24) (R^2 = 0.993) for the hydrogel- and aqueous-filled micropipette, respectively. Further analysis of the CV responses provided $E_{1/2}$ = 0.014 ($\pm$ 0.003) V *vs.* PRPt and a cathodic- to -anodic peak separation (ΔE_p) of 68 ($\pm$ 3) mV regardless of the scan rate, for the hydrogel-filled micropipette, indicating, essentially, the occurrence of a reversible electrode process. For the pipette filled with the aqueous solution, $E_{1/2}$ = 0.045 ($\pm$ 0.003) V *vs*. PRPt and ΔE_p values varying from 65 mV to 230 mV, upon varying the scan rate from 5 to 75 mV s^{-1}, were instead found.

The gradual change in shape of voltammograms (i.e., more drawn-out responses) at higher scan rates could be due to ohmic drop effects[30]. However, considering the relatively small currents involved in the measurements, the occurrence of a more complex mass transport condition cannot be excluded[31]. These effects could be related to the fact that with the aqueous-

[29] D. Battistel, G. Pecchielan, S. Daniele, *Chem.ElectroChem* (**2014**)1:140-146.
[30] R.S. Nicholson, *Anal. Chem*. (**1965**) 37: 667 – 671.
[31] K.J. Aoki, J. Chen, Y. Liu, B. Jia, *J. Electroanal. Chem.* (**2020**) 856:11369.

filled microcapillary, the electrolyte spread around the micropipette orifice leading to an increase of the active surface area on the substrate.

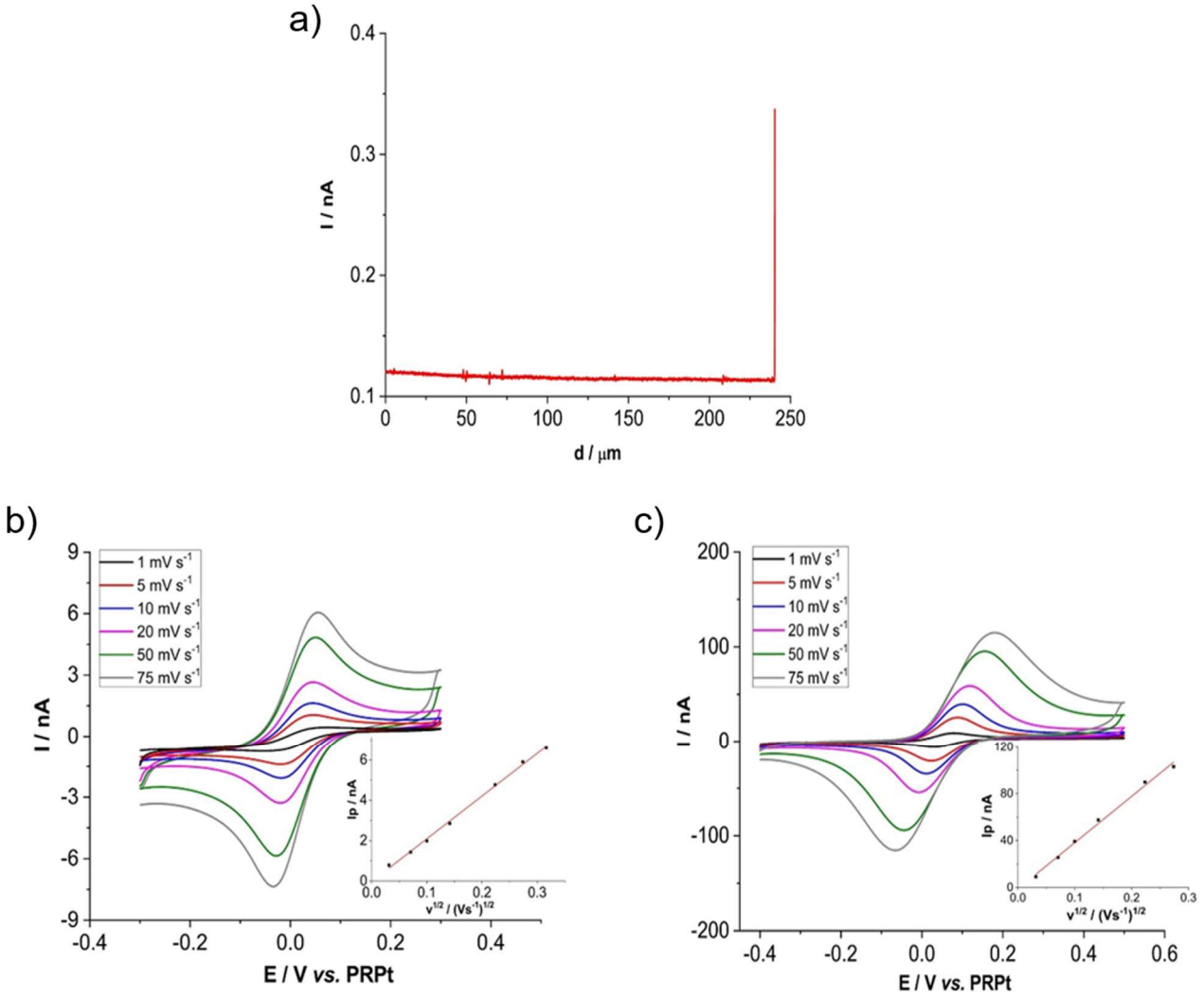

***Figure 7.4**: (a) Typical approach curve obtained with the hydrogel-filled micropipette towards a conducting substrate. (b) and (c) CVs obtained at different scan rates, as indicated, with the micropipette filled with hydrogel and aqueous solution, respectively, containing 1 mM $[Fe(CN)_6]^{4-}$ and 0.1 M KCl. Insets: I_p vs. $v^{1/2}$ plots.*

The surface area, and consequently, the diameters of the meniscuses contacting the substrate were estimated by using equation (7.2), the slopes of the I_p *vs.* $v^{1/2}$ plots and the diffusion coefficients shown in Table 7.1 for $[Fe(CN)_6]^{4-}$. The contact radii thus found were 33 (± 2) µm and 139 (± 5) µm, for the pipette filled with the hydrogel and aqueous solution, respectively. These results clearly indicated that, while the gelled meniscus remained essentially confined to

the micropipette extremity, the aqueous meniscus spread onto the substrate. Indeed, it is known that to ensure the confinement of protruding aqueous meniscuses, the outer walls of the micropipettes need to be silanized (typically, with dimethydicholosilane[32,33]. As previously stated in the experimental section, this kind of treatment was not applied to the micropipettes used here.

The stability of the gelled meniscus with time was then investigated, and Figure 7.5 shows, as an example, two CVs recorded at 50 mV s^{-1} right after the meniscus had landed on the substrate (black line) and after it was held in place for about 1 h (red line). As is evident the two CVs almost overlap, indicating a good stability of the meniscus with time. This result supports the observation that the hydrogel-filled micropipette prevents the spreading and leakage of electrolyte.

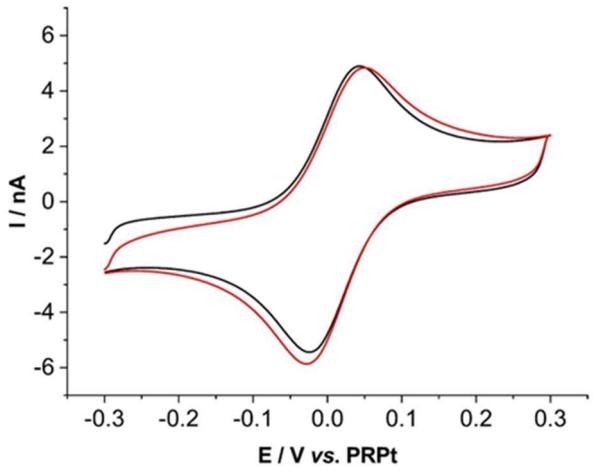

***Figure 7.5**: CVs recorded at 50 mV s^{-1} with the hydrogel-filled micropipette containing 1 mM $[Fe(CN)_6]^{4-}$ and 0.1 M KCl, just after it had landed onto the substrate (black line) and after 1h it was held in place (red line).*

Measurements as those discussed above were also performed by using micropipettes characterized by smaller orifices, i.e., below 30 μm radius, containing $[Fe(CN)_6]^{4-}$ as redox probe. The results obtained were similar to those described above (that is, peak shaped CVs), provided that the orifices, and the corresponding contact meniscuses, were larger than about 5

[32] Y. Shao Y, M.V. Mirkin, *Anal. Chem*. (**1998**) 70:3155-3161.
[33] J.V. Macpherson, P.R. Unwin, *Anal Chem*. (**1999**) 71(20):4642-4648.

μm radius. With smaller micropipettes and contact radii (i.e., 2 μm), mixed planar-radial or radial diffusion prevailed, and sigmoidal CV responses (depending on the scan rate), similar to those recorded in the bulk media with the 12.5 μm radius Pt disk, could be recorded. As an example, Figure 7.6 shows two CVs recoded at 5 mV s^{-1} with the same micropipette (1.5 μm radius) filled with the hydrogel (red line) and aqueous (black line) solutions, respectively. This behaviour is congruent with literature works, where pipettes having just a few micrometres or sub-micrometres dimensions were reported[34]. It must be considered that also in these cases the CVs recorded with the aqueous-filled micropipette provided larger currents than expected (i.e., about twice), conceivably due to spreading and leakage of solution on the substrate surface.

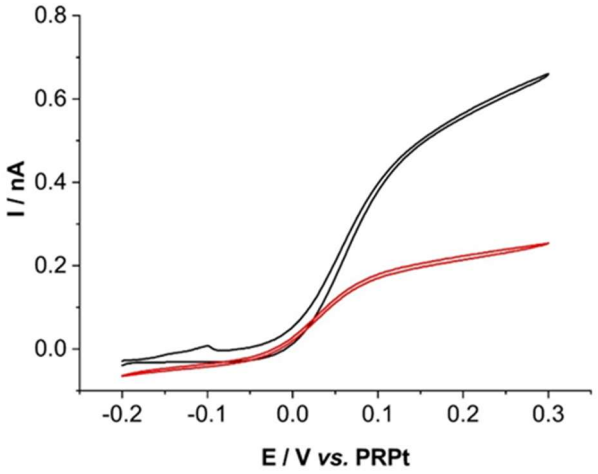

Figure 7.6: *CVs recorded at 5 mV s^{-1} with the micropipette filled with hydrogel (red line) and aqueous solution (black line) containing 1 mM $[Fe(CN)_6]^{4-}$ and 0.1 M KCl.*

7.5. Microelectrode and micro capillary voltammetry of Ag^+ ions in agarose hydrogel and water media

The voltammetric behaviour of Ag^+ ions in the agarose hydrogel and, for comparison, in the corresponding aqueous medium, was investigated both in the bulk media and in the capillary

[34] C.G. Williams, M.A. Edwards, A.L. Colley, J.V. Macpherson, P.R. Unwin, *Anal. Chem*. (**2009**) 81: 2486–2495.

contact mode. The measurements were performed in the media containing 1 mM $AgNO_3$ and to avoid the formation of sparingly soluble AgCl, 0.1 M KNO_3 was used as supporting electrolyte. The electrode process involved is:

$$Ag^+ + e^- \rightleftarrows Ag^0 \qquad (7.3)$$

Figure 7.7 contrasts CVs recorded at 5 mV s^{-1} in bulk hydrogel and water solution with the microelectrode. In both cases, the CVs display the characteristic signatures of metal electrodeposition at the surface of microelectrodes, involving nucleation and growth of a new metallic phase, and dissolution of the metal deposited from the electrode surface[29,35,36].

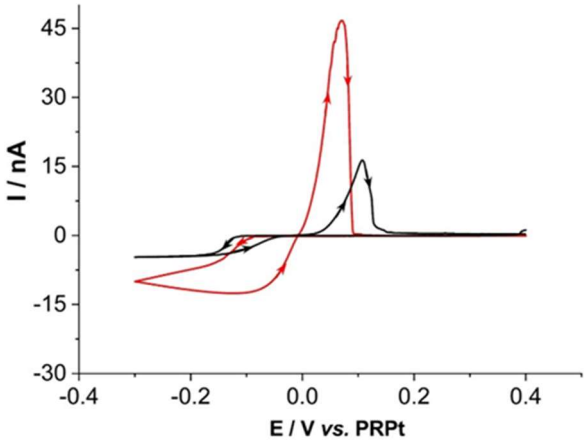

***Figure 7.7**: CVs recorded at a Pt microdisk 12.5 µm radius in solution containing 1 mM $AgNO_3$ + 0.1 M KNO_3 in: (black line) hydrogel and (red line) aqueous solution. Scan rate: 5 mV s^{-1}.*

In fact, waves achieving quasi-steady-state current values are obtained in the cathodic sweep, while characteristic nucleation loops, followed by stripping peaks, are evident on reversal of the sweep. However, a nucleation overpotential of about 50 mV, a shift of the stripping peak

[35] B. Scharifker, G.J. Hills, *J. Electroanal. Chem.* (**1981**) 130:81–97.
[36] M.A. Baldo, C. Bragato, G.A. Mazzocchin, S. Daniele, *Electrochim. Acta* (**1998**) 43:3413 – 3422.

towards more positive potentials (i.e., of 35 mV) and lower current intensities of waves/peaks (depending on the sweep direction) were found in the hydrogel with respect to the aqueous solution. These differences can be accounted for considering, from one side, the effect of agarose on the nucleation/dissolution process of the Ag^+/Ag^0 system on/from the surface of a platinum electrode[37]; from the other side to the different diffusion coefficients of Ag^+ (D_{Ag+}) that, conceivably, applies in the two media. From the current plateaus recorded in the forward scan of the CVs and Equation (7.1), D_{Ag+} values were evaluated and included in Table 7.1. The D_{Ag+} found here in the aqueous solution compares well with literature reports[29,38,39]. To the best of our knowledge, no data was available in literature for Ag^+ ions in 2% (w/v) agarose hydrogel. However, the D_{gel}/D_{aq} ratio of 0.75 (Table 7.1) is within those found for the above investigated soluble species, indicating that no specific interaction exists between Ag^+ ions and the agarose hydrogel structure.

A further distinctive difference, between the features of the CVs obtained in the two media, was the charge involved in the anodic peak (Q_{an}) with respect to that involved in the cathodic-going scan (Q_{ca}). In fact, while in the water phase the Q_{an}/Q_{ca} ratio was 0.94 ± 0.04 (from three replicates), in the hydrogel, it was lower (from about 0.3 to 0.4 times). Since the total amount of charge under the waves/peaks is related to the amount of silver plated or dissolved, respectively, the above results suggest that in the hydrogel, apparently, only a fraction of the metallic silver deposited is stripped from the electrode surface. We actually believe that part of metallic silver deposited (probably as nanoparticles[40] detaches from the electrode surface and diffuse in the hydrogel. This can also be related to the growth mode of silver electrodeposits, which, in agarose-containing solutions, result in a less stable open branched pattern that behaves as a surface and mass fractal[37].

[37] M.A. Pasquale, S.L. Marchiano, A.E. Bolzán, A.J. Arvia, *Journal of Applied Electrochemistry* (**2003**) 33:431 – 441.
[38] C. Xiang, Q. Xie, J. Hu, S. Yao, *J Electroanal Chem* (**2005**) 584: 201-209.
[39] G. Pecchielan, M.A. Baldo, S. Fabris, S. Daniele, *J Electroanal Chem* (**2019**) 847: 113166.
[40] U. Hasse, F. Scholz, *J Solid State Electrochem* (**2006**) 10: 380–382.

Capillary contact measurements were performed with a 2 µm diameter pipette filled with either the hydrogel or the corresponding aqueous solution, containing 1 mM $AgNO_3$, and typical CVs recorded taken at 50 mV s^{-1} are shown in Figure 7.8a. Because of the smaller size of the pipette orifice, the forward cathodic current is almost independent on scan rate over the range 5 - 100 mV s^{-1} (Figure 7.8b), whereas the anodic stripping peak, being a surface process, increases with the scan rate[36].

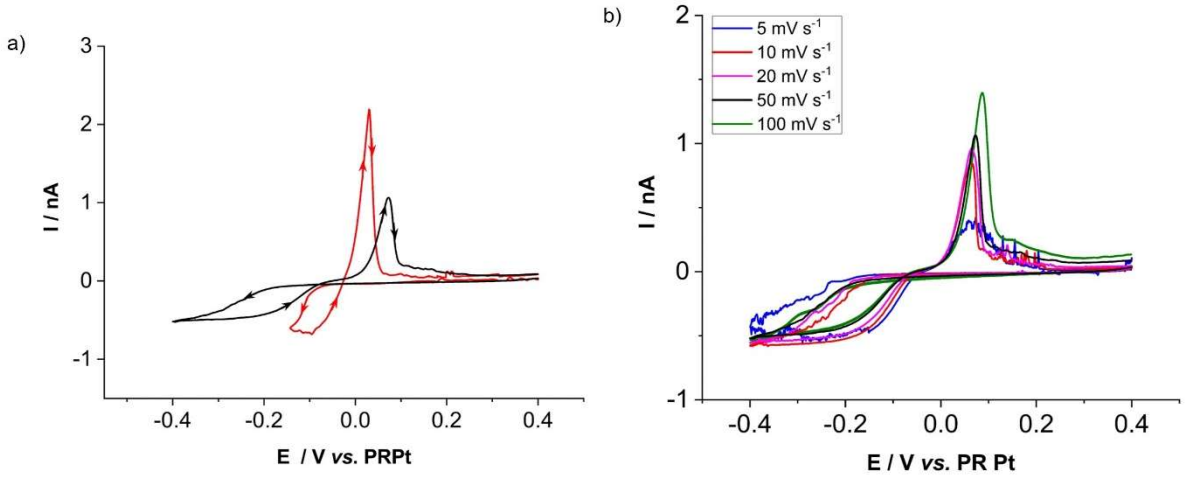

***Figure 7.8**: (a) CVs recorded at 5 mV s^{-1} with a hydrogel- (black line) and aqueous- filled (red line) micropipette (1 µm radius) containing 1 mM $AgNO_3$ + 0.1 M KNO_3. (b) CVs recorded at different scan rates, as indicated, with the hydrogel-filled micropipette having the same composition as in (a).*

From the quasi steady-state current recorded in the hydrogel at 5 mV s^{-1} and equation (7.1), using the D_{Ag+} shown in Table 7.1, contact meniscuses of 1.1 µm and of 1.5 µm radius were evaluated with the micropipette filled with the hydrogel and aqueous solution, respectively. Again, also in this case the aqueous meniscus resulted larger than that of the hydrogel, likely due to the same phenomenon described above for the soluble redox probe.

Evaluation of the charge involved in the cathodic and anodic branches revealed a similar behavior as that observed with the Pt microelectrode in the bulk media. That is, Q_{an}/Q_{ca} was of about 0.5 and 0.9 for the micropipette filled with the hydrogel and aqueous solution, respectively, again in accordance with the observations made above in the bulk media.

7.6. Hydrogel microcapillary measurements on paper-based materials

Proof-of-concept hydrogel-capillary measurements were performed to distinguish the presence of metallic silver deposited on a graphite-on-paper based material, realized through simple pencil strokes as described in the next paragraph.

7.6.1. Preparation of silver deposits on graphite-on-paper based material

A pencil-drawn paper support material[41] was prepared by hand drawing a 20 mm long × 6 mm wide line on a piece of Whatman no. 1 paper sheet using a Bic #2 graphite pencil forming a graphite-on-paper layer necessary to make the electrical contact of the whole sample with the external circuit (see Scheme 7.1 in the next paragraph). 50 μL of an $AgNO_3$ 0.1 M aqueous solution was cast on the graphite layer and the solvent was allowed to evaporate overnight in a controlled environment, avoiding exposure to light. Afterward, the spot was treated with a 1:1 (v/v) Na_2CO_3 (5 g in 100 mL H_2O) and formaldehyde (37 % CH_2O, 5 mL in 100 ml H_2O) solution to allow the reduction of silver ions[42]. The excess of the reagents was eliminated by rinsing the sample with milli-Q water. Finally, the spot was dried in a controlled environment.

7.6.2. Hydrogel microcapillary measurements

In these measurements, a micropipette (orifice 5 μm radius) filled with the agarose hydrogel, containing only 0.1 M KNO_3, was employed. Initially, the micropipette was brought

[41] N. Dossi, R. Toniolo, A. Pizzariello, F. Impellizzieri, E.G. Piccin, G. Bontempelli, *Electrophoresis* (**2013**) 34:2085–2091.
[42] D. Battistel, G. Pecchielan, S. Daniele, *Chem.ElectroChem* (**2014**) 1(1):140–146.

above the graphite layer to establish the electrical contact with the substrate biased at +0.4 V *vs*. PRPt (as depicted in Scheme 7.1).

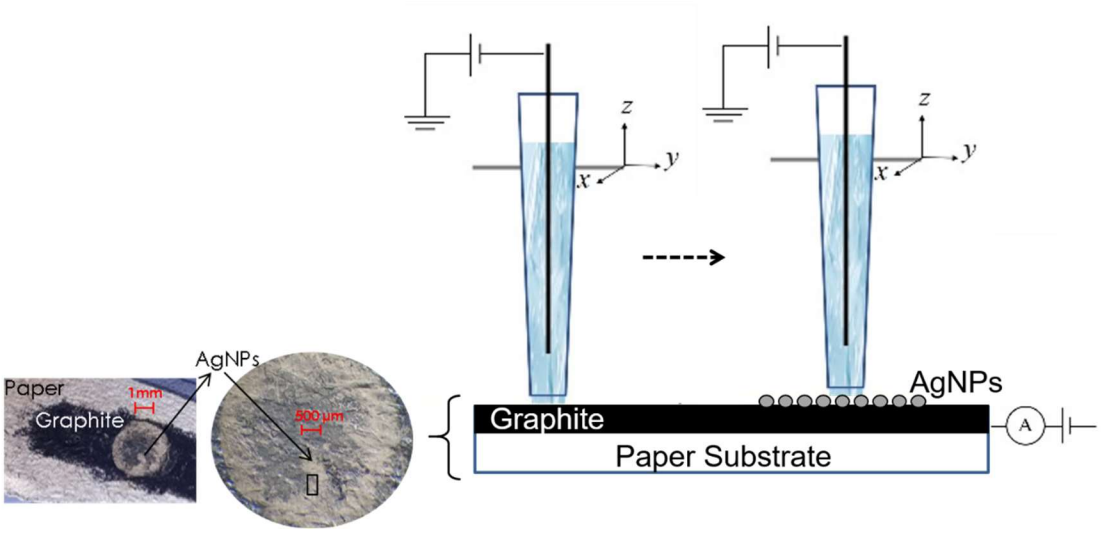

Scheme 7.1*: Representation of the graphite-on-paper layer coated with silver nanoparticles and the hydrogel-filled micropipette scanning the surface.*

Afterward, repetitive retraction-approaching processes were performed to detach the probe from a given measuring point, move it laterally to the next point and approach the substrate again. In this way a line scan at the boundary between the Ag-free and Ag-coated graphite layer was performed. Each time the micropipette had landed on the substrate, continuously biased at +0.4 V, the current was monitored for 5 s. and the value corresponding at 5s (I_{5s}) was plotted as a function of the lateral distance (d), as shown in Figure 7.9.

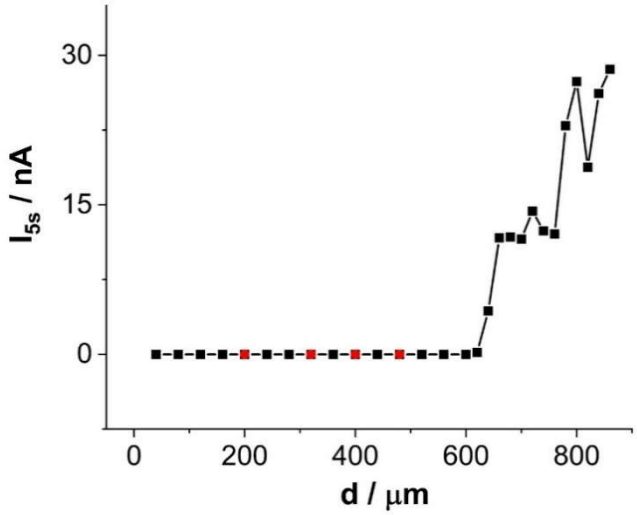

Figure 7.9*: Current-distance plot obtained above a graphite-on-paper based substrate, coated with silver deposits. The substrate was biased at 0.4 V vs. PRPt. The plot was recorded using a micropipette filled with the agarose hydrogel, containing 0.1 M KNO_3. Black square symbols refer the forward lateral scan, while red symbols refer to control measurements performed by moving back the micropipette on the Ag-free graphite layer.*

In this way, negligible currents, essentially due to the background, were obtained when the micropipette landed on the Ag-free graphite zone, whereas much larger currents were recorded above the Ag-coated graphite layer. In fact, at +0. 4 V, the oxidation process of metallic silver could occur (see Figures 7.7 and 7.8) and the current was enhanced to an extent that depended, conceivably, on the amount of metallic silver coating the sample. To confirm this view, control experiments were performed by moving back the micropipette above the Ag-free graphite zone, where again negligible currents were recorded (see red symbols in Figure 7.9). Therefore, the results shown in Figure 7.9 reflect the distribution of metallic silver is on the pencil-graphite layer as well as its relative amount.

7.7. Hydrogel microcapillary measurements on a copper substrate

Preliminary measurements with micropipette filled with agarose hydrogel containing 0.1 M Na_2SO_4 were also done on a bare copper substrate. The pipette orifice size, preliminarily determined as described above, using $Ru(NH_3)_6^{3+}$ as redox probe, provided a radius of 30 (± 5) µm a radius. Figure 7.10 shows OCP (a) and PDP (b) profiles obtained upon the meniscus of the micropipette landed to three different locations of the substrate; relevant corrosion parameters are summarized in Table 7.2. The measurements were performed using a Pt wire as pseudo-reference electrode.

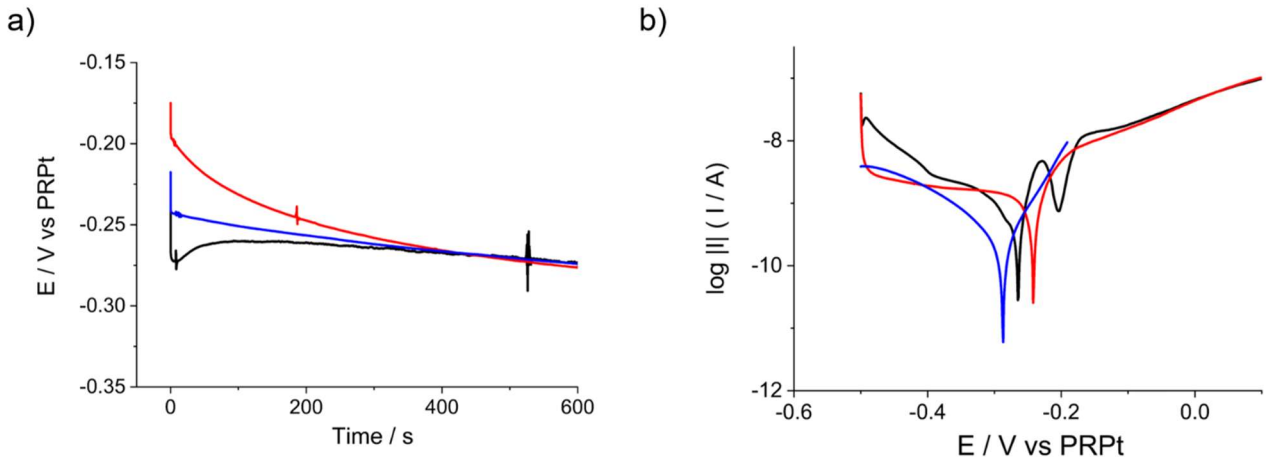

***Figure 7.10**: a) OCP and b) PDP on bare copper substrate using a micropipette filled with the agarose hydrogel, containing 0.1 M Na_2SO_4. Different colors refers to three different points.*

From Figure 7.10a it is evident that OCP starts from different initial values and converge, after about 600 s, at an average value of 274 (±2) mV. The shape of the PDP profiles (Figure 7.10b), as well as E_{corr} and I_{corr} (Table 7.2) differ to some extent, highlighting that the local status of the material can present some heterogeneity in terms of resistance towards corrosion behavior.

***Table 7.2**: OCP values and PDP parameters on bare copper substrate using a micropipette filled with the agarose hydrogel containing 0.1 M Na_2SO_4.*

Position	OCP (mV)	E_{corr} (mV)	I_{corr} (µA cm^{-2})
1	-274	-285	5.7
2	-276	-241	2.5
3	-273	-265	1.1

Similar measurements performed on the top layer of the patina of a roof cladding sample resulted in undetermined OCP values and no current flows, in agreement with the non-conducting and passivating nature of the brochantite layer, as also evidenced by previous reported SECM measurements.

Overall, these results suggest that the MC filled with hydrogel can also be used to imaging small surface area of precious metallic objects, containing randomly distributed corroded particles.

Chapter 8: Characterization of inherently chiral oligomeric films

8. Characterization of inherently chiral oligomeric films

Among natural resins, triterpenoid resins, such as mastic and dammar, used on their own or mixed with wax and oils, were the most used varnishes by artists (and restorers) on easel paintings both for protective and aesthetic purposes[1]. In the past, it was a common practice to apply a varnish layer to protect the paint film against dirt and mechanical damage and, at the same time, providing the pigments excellent adhesive properties. Varnishes were used not only to protect paintings but also wooden musical instruments or other objects from moisture, dust, and biological agents[2]. Terpenoids possess electroactive and chiral properties, which could be the target for their selective determination in complex matrices[3,4]. With these prospective, conducting chiral polymers or oligomers could be electrodeposited over a microelectrode surface to perform local SECM or, more in general, electrochemical measurements similarly to what has been recently shown using other types of polymers or gels with no chiral characteristics[5,6,7]. In addition, following a similar scheme adopted in chapter 7, chiral compounds may also be inserted inside the glass capillary micropipettes to function as chiral polymeric probes.

In view to develop in the next future strategies to investigate chiral surfaces, using an approach similar to the one described in section 7.6.2, in this chapter, the preparation and characterization by voltammetry and SECM of conducting chiral oligomers are described.

[1] M.P. Colombini, F. Modugno, S. Giannarelli, R. Fuoco, M. Matteini, *Microchemical Journal* (**2000**) 67, 385-396.
[2] M. Clausi, G.M. Crisci, M.F. La Russa, M. Malagodi, A. Palermo, S.A. Ruffolo*, J. Cult. Herit*. (**2011**) 12, 28–33.
[3] Z.A. De los Santos, C. Wolf, *J. Am. Chem. Soc.* (**2020**) 142, 4121−4125.
[4] C. Wolf, K.W. Bentley, Chem. Soc. Rev. (**2013**) 42, 5408.
[5] L. Liu, M. Etienne, A. Walcarius, *Anal. Chem.* (**2018**) 90, 15, 8889–8895.
[6] N. Dang, M. Etienne, A. Walcarius, L. Liu, *Electrochemistry Communications* (**2018**) 97, 64–67.
[7] N. Dang, M. Etienne, A. Walcarius, L. Liu*, Anal. Chem.* (**2020**) 92, 9, 6415–6422.

Conducting polymers (CPs) or oligomers consist of repeating units of conjugated electroactive organic molecules. CPs display high chemical stability and conductivity[8]. They can mediate reactions while in their conductive state, making them viable as electrode materials. In addition, CPs are widely used as electrode modifiers to fine-tune the performance and quality of a variety of substrates[9]. In this regard, considerable attention has been devoted to the preparation of CP-modified electrodes to be employed as chemo- and bio-sensors to enhance sensitivity and selectivity in electroanalytical applications[9,10,11]. Among other desired sensing properties, enantiomer discrimination and quantification are fundamental for chiral compounds of interest in pharmaceutical, food, fragrance and environmental fields. Chirality is often introduced into CPs by attaching chiral pendants to the monomers to be (electro)oligomerized to yield the CP conjugated backbone[12], but other alternative approaches have also been proposed[13]. Outstanding chirality properties have been recently observed with electroactive films electrosynthesized from "inherently chiral" electroactive monomers, designed so that chirality and electroactivity originate from the same element, coinciding with the main molecular backbone featuring a tailored torsion on account of an atropisomeric or helical building block with associated high racemization barrier; this results in powerful chirality manifestations, possibly also electrochemically modulated[13]. The so far best studied example of inherently chiral monomer is 2,2'-bis(2,2'-bithiophene-5-yl)-3,3'-bibenzothiophene (BT_2T_4) (Scheme 8.1), featuring a 3,3'-bibenzothiophene atropisomeric core (with sterically hindered rotation between its two halves); its C2 symmetry results in propagation and amplification of its outstanding chirality properties in macro- and supramolecular structures[14].

[8] J. Heinze, B.A. Frontana-Uribe, S. Ludwigs, Chem. Rev. ***(2010)*** *110, 4724–4771*.
[9] V. Tsakova, R. Seeber. *Anal. Bioanal. Chem*. (**2016**) 408, 7231–7241.
[10] H. Tan-Phat, P.S. Sharma, M. Sosnowska, F. D'Souza, W. Kutner, *Prog. Polym. Sci.* (**2015**) 47, 1–25.
[11] D. Bottari, L. Pigani, C. Zanardi, F. Terzi, S.V. Paturca, S.D. Grigorescu, C. Matei, C. Lete, S. Lupu, *Chemosensors* (**2019**) 7, 65.
[12] L.A.P. Kane-Maguire, G.G. Wallace, *Chem. Soc. Rev*. (**2010**) 39, 2545–2576.
[13] S. Arnaboldi, S. Grecchi, M. Magni, P. Mussini, *Curr. Opin. Electrochem*. (**2018**) 7, 188–199.
[14] F. Sannicolò, S. Arnaboldi, T. Benincori, V. Bonometti, R. Cirilli, L. Dunsch, W. Kutner, G. Longhi, P.R. Mussini, M. Panigati et al., *Angew. Chem. Int. Ed.* (**2014**) 53, 2623–2627.

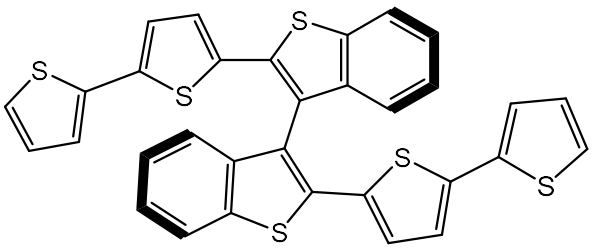

(*S*)-BT_2T_4

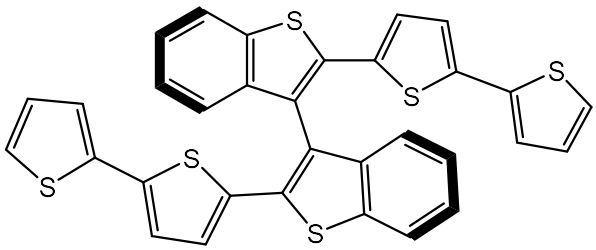

(*R*)-BT_2T_4

***Scheme 1**: The (S)- and (R)-enantiomers of the inherently chiral BT_2T_4 monomer.*

Because these monomers are electroactive and with high electrooligomerization ability, they represent suitable starting reagents for the electrodeposition of inherently chiral oligomers onto electrode surfaces[13,14,15]. Chemically produced oligomers can also be drop-casted onto the electrode surface [16] . These oligomer-modified electrodes have displayed outstanding enantiodiscrimination ability for chiral electroactive probes in terms of large potential differences in voltammetric experiments[13,14,16,17].

In previous works, the electrochemical characterization of these electrodes has been performed considering voltammetry, spectroelectrochemistry and in-situ conductance techniques[13,14,15,16,17,18]. These techniques normally provide information on the whole and bulk material. Further knowledge of the chemical and electrochemical phenomena involved in such systems can be obtained by high spatial resolution electrochemical techniques, such as SECM[19]. In the context of conducting polymers, SECM has been used to characterize

[15] S. Arnaboldi, D. Vigo, M. Longhi, F. Orsini, S. Riva, S. Grecchi, E. Giacovelli, V. Guglielmi, R. Cirilli, G. Longhi, et al., *ChemElectroChem* (**2019**) 6, 4202–4214.

[16] F. Sannicolò, P.R. Mussini, T. Benincori, R. Cirilli, S. Abbate, S. Arnaboldi, S. Casolo, E. Castiglioni, G. Longhi, R. Martinazzo, et al. *Chem. Eur. J.* (**2014**) 20, 15298–15302.

[17] S. Grecchi, S. Arnaboldi, M. Korb, R. Cirilli, S. Araneo, V. Guglielmi, G. Tomboni, M. Magni, T. Benincori, H. Lang, H., et al., *ChemElectroChem* (**2020**) 7, 3429–3438.

[18] T. Benincori, S. Gàmez-Valenzuela, M. Goll, K. Bruchlos, C. Malacrida, S. Arnaboldi, P.R. Mussini, M. Panigati, J.T. López Navarrete, M.C. Ruiz Delgado, et al. *Electrochim. Acta* (**2018**) 284, 513–525.

[19] A.J. Bard, M.V. Mirkin, (Eds.) Scanning ElectrochemicalMicroscopy, 2nd ed.; CRC Press: Boca Raton, FL, USA, (**2012**).

poly(alkylterthiophene) films[20] and polypyrrole[21], to establish semiconducting surfaces and to study lateral charge transfer inside molecular films[22]. To the best of our knowledge, no SECM study exists dealing with the characterization of chiral polymers or oligomers.

In this chapter, for the first time, it is reported a SECM study to characterize the enantiopure (S)-BT_2T_4 oligomer, electrodeposited onto the surface of a gold disk electrode, starting from the corresponding *(S)*-BT_2T_4 monomer. In particular, the study aims at establishing whether: i) the oligomer film acts as a porous membrane, with resulting electron transfer occurring at the underlying metal electrode; ii) the electron transfer is localized at the oligomer/solution interface with the conducting oligomer film behaving as a conductive electrode material; iii) a catalytic electron-transfer process occurs between the conducting polymer and a redox couple present in the bathing solution. In addition, the investigation aims at establishing how the chiral properties of the film affects the redox process of chiral compounds. To this purpose, voltammetric and SECM measurements were performed using different redox mediators charged and uncharged, without and with chiral properties.

8.1. Electrosynthesis and voltammetric characterization of the oligomeric BT_2T_4 film

For the electrosynthesis of the oligo-(*S*)-BT_2T_4 film, a polycrystalline gold disk 2 mm diameter, embedded in a PTFE rod, was employed as working electrode; a platinum spiral and an Ag/AgCl (KCl, saturated) were employed as counter and reference electrode, respectively. The enantiopure (*S*)-BT_2T_4 monomer was used for the electro-synthesis of the oligomer, following a protocol analogous to those reported in literature[15,16,17]. In brief, repeated oxidative

[20] M. Tsionsky, A.J. Bard, D. Dini, F. Decker, *Chem. Mater*. (**1998**) 10, 2120–2126.
[21] M. Arca, M.V. Mirkin, A.J. Bard, *J. Phys. Chem*. (**1995**) 99, 5040–5050.
[22] D. Mandler, P.R. Unwin, *J. Phys. Chem. B* (**2003**) 107, 407–410.

potential cycling at 0.2 V s^{-1} was performed over the potential region 0 - 1.4 V *vs* Ag/AgCl, in a CH_3CN solution containing 0.5 mM (*S*)-BT_2T_4 and 0.1 M $TBAPF_6$, as supporting electrolyte. The first and fortieth cycles are displayed in Figure 8.1 (with black and red line, respectively).

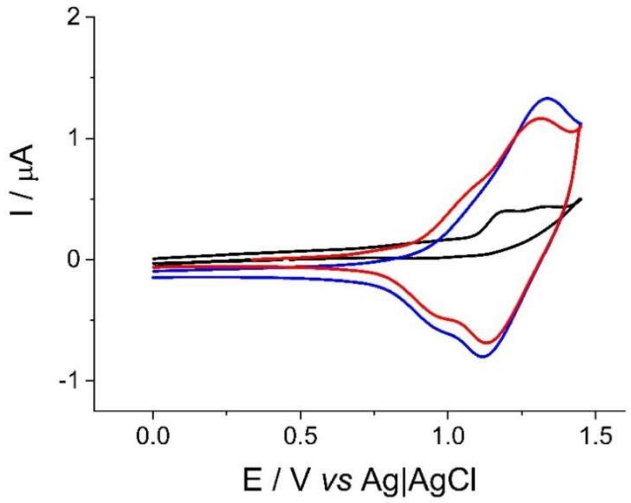

Figure 8.1: *CVs in a 0.5 mM (S)-BT_2T_4 CH_3CN solution + 0.1 M $TBAPF_6$ at Au disk electrode: first cycle (black line); fortieth cycle (red line). CV recorded at the oligomer-modified Au disk electrode in a (S)-BT_2T_4-free CH_3CN solution + 0.1 M $TBAPF_6$ (blue line). Scan rate 0.2 Vs^{-1}.*

In the first cycle a two-peak process was observed, the first of which is due to the oxidation of the terthiophene moiety; the second corresponds to a further oxidation process of an electroactive product formed by a chemical follow up reaction, since it disappears at increasing scan rates. Instead, in less polar CH_2Cl_2, a first oxidation system is observed consisting of two nearly merging peaks accounting for the two molecule moieties behaving as interacting equivalent redox centers[14]. In the second and following cycles, a shift of the first oxidation peak at less positive potential and an overall current increase were observed. The potential shift points to an increased effective conjugation as a consequence of the coupling of terthiophene π systems, resulting in electroactivity features close to a linear hexathiophene[23]. The current increase, by increasing the number of CV cycles, together with the presence of ill-

[23] E. Quartapelle Procopio, T. Benincori, G. Appoloni, P.R. Mussini, S. Arnaboldi, C. Carbonera, R. Cirilli, A. Cominetti, L. Longo, R. Martinazzo, et al. *New J. Chem.* (**2017**) 41, 10009–10019.

defined cathodic peaks, recorded upon potential scan reversal, indicate the deposition of a solid, electrochemically active product on the electrode surface. According to earlier works, the deposited material is made of oligomers, from open and cyclic dimers to higher terms, with dimers largely prevailing in high-resolution laser desorption ionization (HR LDI) spectra[14,15,16]. The stability of the deposited film was verified by performing CV measurements with gold-modified electrode in a (*S*)-BT_2T_4-free acetonitrile solution and in the same potential window. The CV thus recorded displayed, essentially, the same features of that obtained in the medium containing the monomer (Figure 8.1, blue line). The presence of the oligomer onto the electrode surface was also verified by SEM (Figure 8.2 a,b) and relevant EDX analysis (Figure 8.2, c,d,e,f) which shown the presence of gold together with carbon and sulphur.

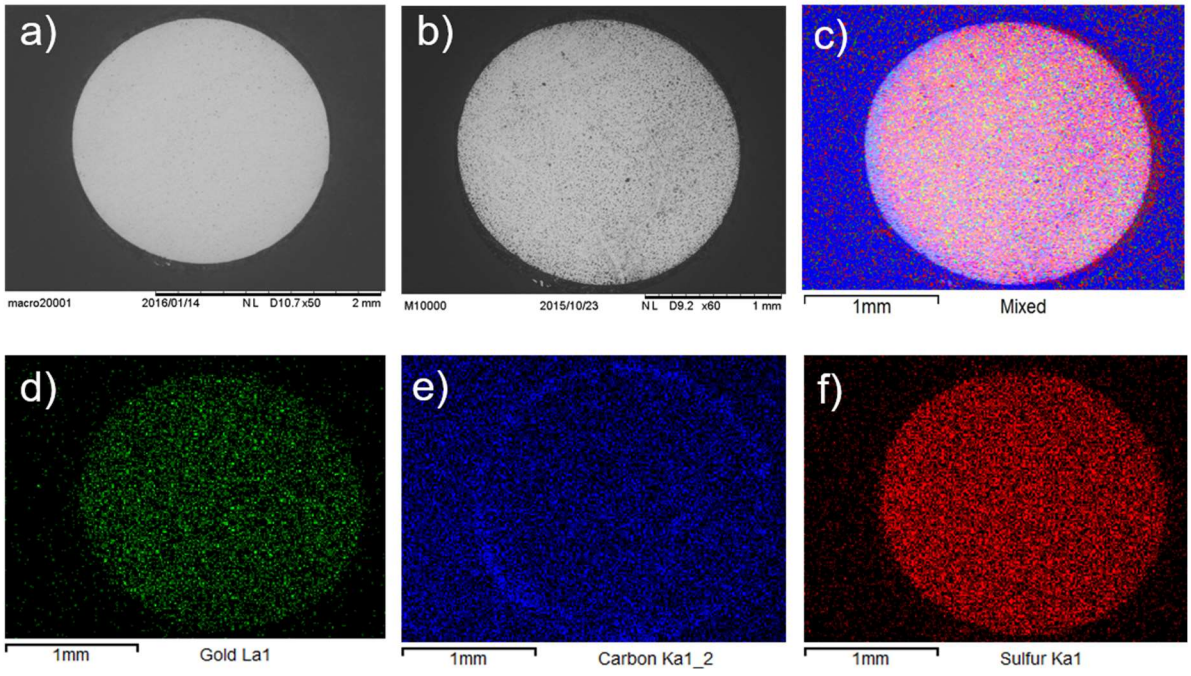

***Figure 8.2**: SEM images of the naked (a) and oligomer-modified (b) polycrystalline gold electrode and EDX mapping: c) mixed elements, d) gold (green), e) carbon (blue), f) sulphur (red).*

The enantio-recognition ability of the oligomer-modified gold electrode (oligo-(*S*)-BT_2T_4-Au) was assessed by CV in acetonitrile solutions containing the chiral probes (*S*)-(-), (*R*)-(+) and racemate ((*S*)-FcEA, (*R*)-FcEA and *rac*-(±)FcEA, respectively), as shown in Figure 8.3a. For comparison, the CVs of the same probes were performed using the bare Au-disk electrode (Figure 8.3b).

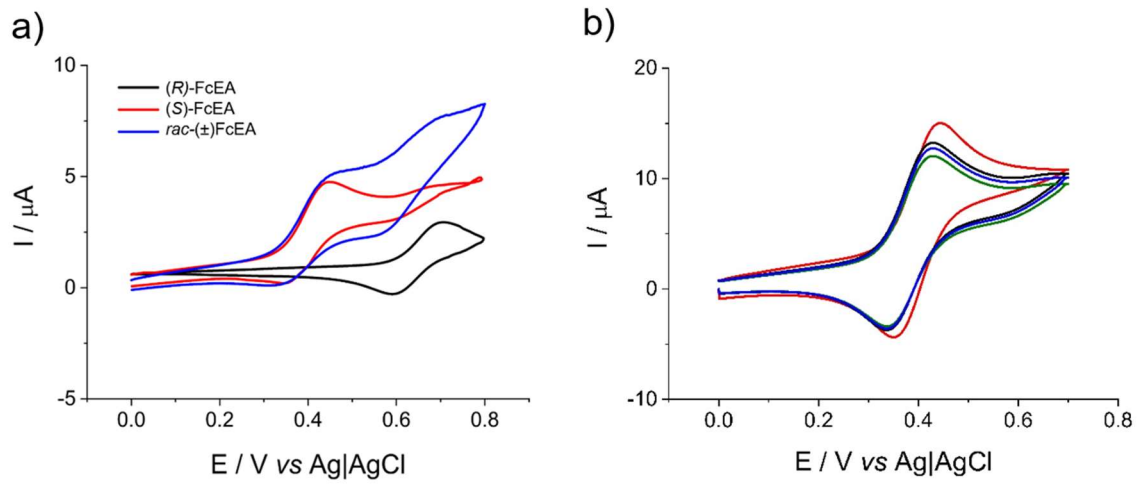

Figure 8.3: *a) CVs recorded at an oligo-(S)-BT_2T_4- Au electrode in a CH_3CN + 0.1 M $TBAPF_6$ solution containing 1 mM (S)-FcEA (red line), 2 mM rac-FcEA (blue line) and 0.6 mM (R)-FcEA (black line); b) CVs recorded at the bare Au electrode in the same base electrolyte solution containing 1 mM each of Fc (red line), (S)-FcEA (black line) and (R)-FcEA and rac(±)-FcEA probes. Scan rate 50 mV s^{-1}.*

It is seen that at the oligo-(*S*)-BT_2T_4-Au a clear separation of the half-wave potentials ($E_{1/2}$) (obtained by the half sum of the anodic ($E_{p,a}$) and cathodic ($E_{p,c}$) peak potentials, $E_{1/2} = (E_{pc} + E_{pa}) / 2$) [24], of about 240 mV, exists between the (*S*)-FcEA and (*R*)-FcEA probes when present in solution either alone or in the racemic mixture. It must be outlined that no such potential separation was observed at the naked Au electrode, where $E_{1/2}$ values are identical (within ± 5 mV, experimental error) regardless of the probe enantiomer configuration (Figure 8.3b). Thus, as in previous cases[14,25], the combination (*S*)-oligoBT_2T_4 + (*S*)-FcEA (or specularly (*R*)+(*R*))[14,25]

[24] A.J. Bard, L.R. Faulkner, (Eds.) Electrochemical Methods, Fundamentals and Applications, 2nd ed.; Wiley:Hoboken, NJ, USA, (**2001**).
[25] S. Arnaboldi, T. Benincori, R. Cirilli, W. Kutner, M. Magni, P.R. Mussini, K. Noworyta, F. Sannicolò, *Chem. Sci*. (**2015**) 6, 1706–1711.

results in a less positive potential respect to (*S*)-oligoBT_2T_4 + (*R*)- FcEA (or, specularly, (*S*)+(*R*))[14,25]. It is however worthwhile recalling that no particular meaning should be given to such absolute configuration combinations, since the (*R*) and (*S*) stereodescriptors are assigned according to rules with no direct link to physical properties[26].

8.2. SECM characterization of the bare Au surface and oligo-(S)-BT_2T_4-Au substrate

SECM measurements were performed using platinum microdisk electrodes of 12.5 μm radius with *RG* varying between 5 and 8 (see paragraph 4.7.4.1 of the experimental section). The redox mediators employed were: $[Fe(CN)_6]^{4-}$, $[Fe(CN)_6]^{3-}$ in aqueous solutions containing 0.1 M KCl; ferrocene (Fc) and the chiral (*S*)-FcEA, (*R*)-FcEA and *rac*-FcEA molecules in CH_3CN solution containing 0.1 M $TBAPF_6$. Steady-state voltammograms obtained at the platinum microelectrode for all redox mediators employed are shown in Figure 4.3 and the corresponding $E_{1/2}$ are summarized in Table 4.4 in the Experimental chapter.

Preliminarily, the surface status of the bare gold substrate (1 mm radius) for the electrodeposition of the oligo-(*S*)-BT_2T_4 film, was investigated by SECM in feedback mode (see theory, paragraph 3.6.1.2). In these experiments, the microelectrode tip was always biased at a potential at which the steady-state diffusion limiting current of each redox mediator was achieved. Instead, the substrate was either unbiased or biased at a potential at which the inverse of the reaction occurring at the SECM tip took place (see Scheme 8.2, which refers to a generic reaction *O/R* redox system). The substrate under investigation is immersed in a solution

[26] G.P. Moss, *Pure Appl. Chem*. (**1996**) 88, 2193–2222.

containing the electroactive specie *R*, which at the microelectrode can undergo the following reversible redox reaction (8.1):

$$R \rightleftharpoons O + e^- \qquad (8.1)$$

At the SECM tip, a high positive potential is applied (i.e., more positive to the halfwave potential, $E_{1/2}$, of the *O*/*R* couple), such that *R* is oxidized to *O* at a diffusion control rate (see Scheme 8.2a).

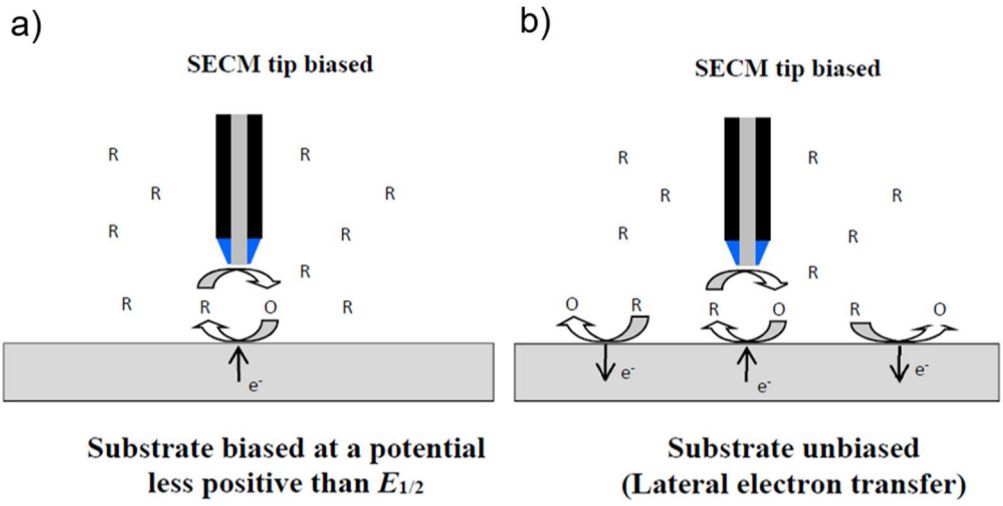

Scheme 8.2: *Representation of the redox mediator regeneration for a generic species O and its reaction product R to a substrate biased at a potential less positive than* $E_{1/2}$ *(a) and to a substrate unbiased trough lateral electron transfer (b).*

The redox mediator regeneration can also occur at the unbiased substrate (Scheme 8.2b). This is because a significant area of the substrate below the tip, and away from it, is bathed by

the solution whose concentration has not been perturbed by the tip-reaction.[19,27,28,29,30,31] Thus, in the latter zone, the substrate is poised at a potential established by the species *R* in the bulk solution and, at open circuit, its value is negative to the halfwave potential ($E_{1/2}$) of the *O/R* couple. When the tip approaches the substrate, the portion of the substrate directly under the tip is exposed to the electrode reaction product, *O*, and at a more positive potential. In this case, the localized reduction current at the portion of the substrate under the tip is driven by the oxidation of *R* at those portions of substrate away from the tip region[30]. This provides a lateral electron transport through the conducting material. It must be noted that the potential of an unbiased substrate is also perturbed by current flow, which is required for recycling the mediator[28]. Thus, the feedback response can also be perturbed by finite heterogeneous electron-transfer kinetics[28]. In general, the lateral electron transport of Scheme 8.2b is operative in a conductive substrate whose surface area is larger than that of the micro-tip counterpart. In these SECM experiments, the latter condition is fulfilled only at the bare gold electrode. Apparently, it was not the case for the measurements performed at the oligo-(S)-BT_2T_4-Au.

Since in the case of the bare Au electrode, all redox mediators provided similar responses, in what follows, the results obtained for the redox system Fc^+/Fc are discussed. Typical normalized approach curves, *i.e.*, normalized current, (I/I_b) (I is the current at given tip-to-substrate distance d, I_b is the current in the bulk solution), against normalized distance (d/a) (a is the radius of microelectrode) obtained above the active metal surface and, for comparison, above the surrounding insulating material, are shown in Figures 8.4a and 8.4b, respectively. Above the Au surface, regardless of whether the substrate was biased or not, a positive feedback current (*i.e.*, current increases as the tip-to substrate distance decreases), overlapping the

[27] P. Liljeroth, D. Vanmaekelbergh, V. Ruiz, K. Konturri, H. Jiang, E. Kauppinen, B.M. Quinn, *J. Am. Chem. Soc*. (**2004**) 126, 7126–7132.
[28] A.L. Whitworth, A.L.; D. Mandler, D.; P.R. Unwin, *Phys. Chem. Chem. Phys*. (**2005**) 7, 356–365.
[29] D.O. Wipf, A.J. Bard, *J. Electrochem. Soc*. (**1991**) 138, L4–L6.
[30] S.B. Hocevar, S. Daniele, C. Bragato, B. Ogorevc, *Electrochim. Acta* (**2007**) 53, 555–560.
[31] A.J. Bard, Fu-Ren F. Fan, J. Kwak, O. Lev, *Anal. Chem*. (**1989**) 61, 132-138.

theoretical curve for a diffusion-controlled process, was obtained (Figure 8.4a). This accords with the regeneration mechanism of the redox mediator characteristic for a conductive substrate,[19,27,28,29,30,32] (inset in Figure 8.4a). The positive feedback response, also obtained at the unbiased substrate, is due to the above-mentioned phenomenon of the lateral electron transfer,[19,27,28,29,30,32] (Scheme 8.2).

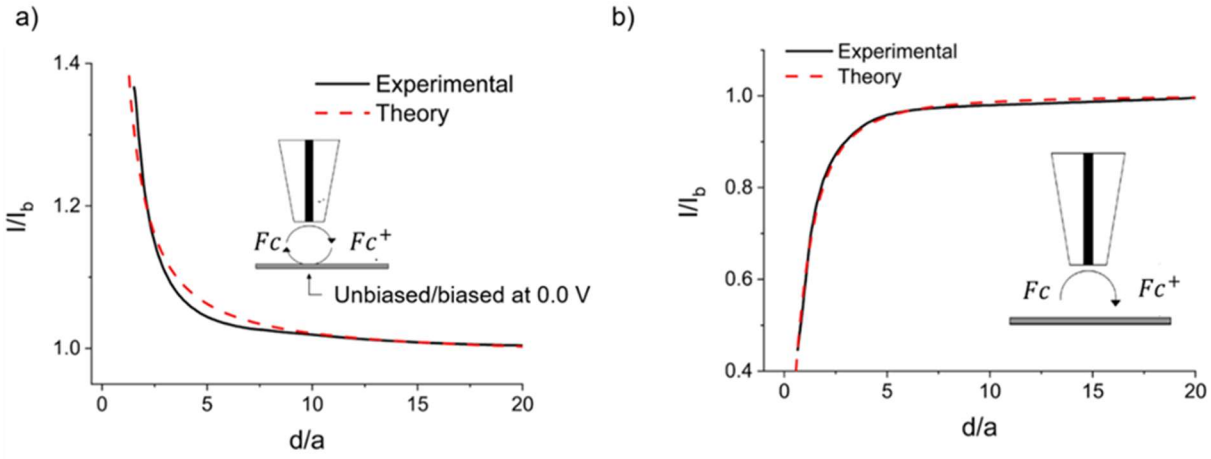

Figure 8.4: *Approach curves recorded using Fc as redox mediator with a Pt microdisk 12.5 µm radius, above the bare gold surface (a) and the surrounding PTFE insulator (b). Red dashed lines refer to theoretical diffusion-controlled processes. The tip was biased at 0.4 V and the substrate was either unbiased or biased at 0.0 V.*

Above the insulator, the approach curves provided negative feedback (*i.e.*, current decreases as the tip-to substrate distance decreases) overlapping that for a diffusion-controlled process. This behaviour is related to the hindered diffusion of the redox mediator towards the microelectrode surface (see inset in Figure 8.4b). Approach curves like those described above were also recorded by performing measurements above different locations of both Au disk and insulator.

The uniformity of the responses across the substrate was also assessed by performing linear (1-D) and bi-dimensional (2-D) scans. In these experiments, the microelectrode was

[32] A.J. Bard, M.V. Mirkin, P.R. Unwin, D.O. Wipf, *J. Phys. Chem*. (**1992**) 96, 1861–1868.

initially located at 10 µm above the substrate and the scans were started with the microelectrode positioned above the insulator. Then, it was moved towards the active metal surface. Typical 1-D and 2-D scans are shown in Figure 8.5. Insulating (or not active) and conducting (or active) materials correspond to the zones with lower and higher currents, respectively. The abrupt current changes, from low to high values (or vice-versa in Figure 8.5a), indicate the transition from the insulating to the conducting zone of the material (or vice-versa). Current spikes and oscillations over the active zone (see inset in Figure 8.5a) reflect, conceivably, the high roughness of the substrate.

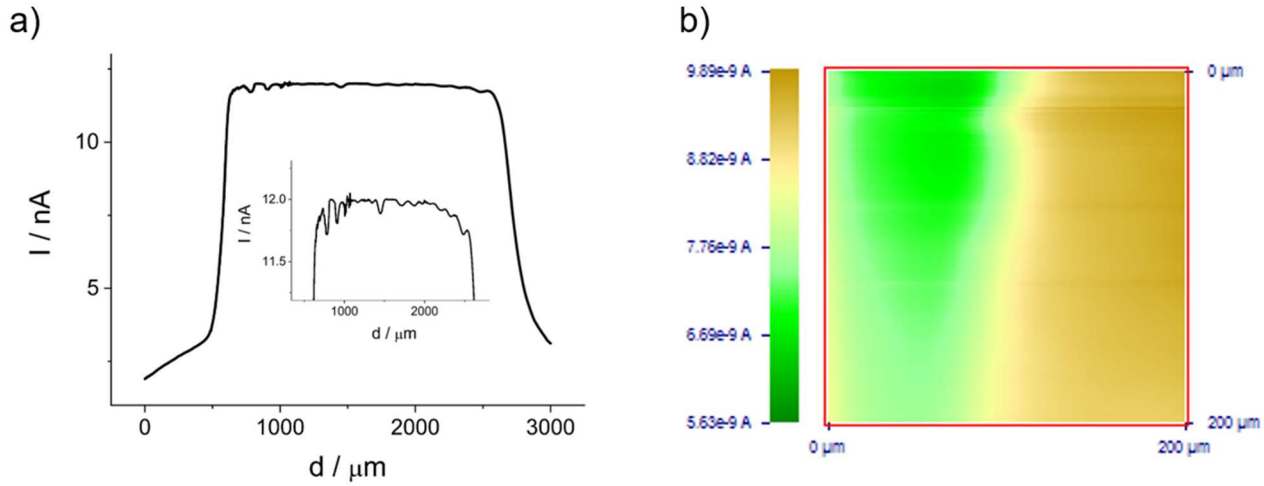

Figure 8.5: *1-D (a) and 2-D (b) scans obtained by using Fc as redox mediator and a Pt microdisk with 12.5 µm radius. The tip was positioned at 10 µm above the substrate.*

The surface roughness profiles of the bare gold and oligo-(*S*)-BT_2T_4-Au surfaces were evaluated by using the current oscillations obtained in the 1-D scans. The current values were preliminarily normalized for the bulk current obtained for the specific redox mediator employed. The arithmetic mean current value (R_I) measured along a line was evaluated by using the Equation (8.2):

$$R_I = \frac{1}{N}\Sigma_{i=1}^{N}|I_i| \qquad (8.2)$$

The amplitude of the current oscillation between the maximum peak ($\max_i I_i$) and minimum valley ($\min_i I_i$) were also evaluated. The maximum peak to valley height (R_{Imax}) was then established by the following Equation (8.3):

$$R_{Imax} = \max_i I_i - \min_i I_i \qquad (8.3)$$

The values thus established were interpolated to the theoretical approach curves to transform current in normalized distance, *d/a*. By the knowledge of the microelectrode radius, roughness average (R_a) of 1.5 μm and maximum peak to valley height (R_{max}) of 2.6 μm were evaluated.

Series of SECM measurements, as those described above, were performed using the oligo-(*S*)-BT_2T_4-Au substrate in feedback and competition mode; in the latter case, the applied potentials at both SECM tip and substrate were such that the same process of the redox mediator (oxidation or reduction) occurred. In addition, to differentiate between general (conductivity, permeability and topography) and enantiomeric properties of the oligo-(*S*)-BT_2T_4 film, the results obtained with the conventional (*i.e.,* achiral) and chiral redox mediators are discussed separately.

8.3. Achiral redox mediators

Typical approach curves obtained at the unbiased oligo-(*S*)-BT_2T_4-Au are shown in Figure 8.6. As is evident, all redox mediators provide I/I_b vs. *d/a* profiles that fit the theory for negative feedback responses. Comparative measurements, performed above the insulating material surrounding the Au surface, gave similar responses (not shown).

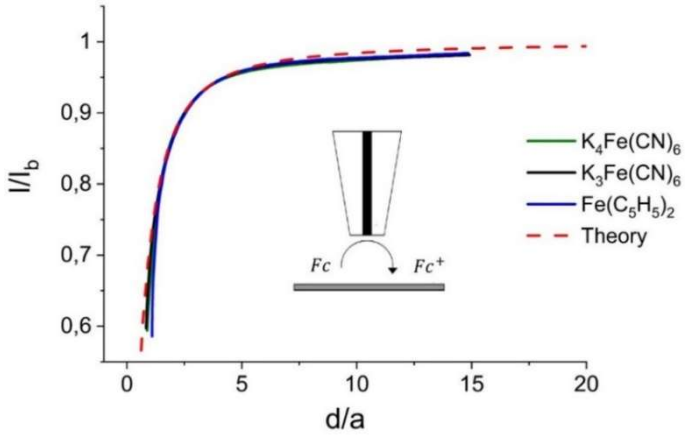

Figure 8.6: *Approach curves recorded with the indicated redox mediator above the unbiased oligo-(S)-BT_2T_4-Au. The scheme shown in the inset represents, as an example, the process occurring using Fc as redox mediator.*

These results suggest that, under the above conditions, the oligomer film acts as an insulating membrane and that no ion exchange process takes place between ion species, eventually trapped within the oligomer, and the charged redox mediators in solution. This can be because the oligomer film was in its uncharged state. On the other hand, based on the $E_{1/2}$ values shown in Table 4.4 (Experimental chapter), the above results are congruent with the circumstance that the various redox mediators were not able to locally inject or subtract electrons, *i.e.*, to act as reductant or oxidant, towards the oligo-(*S*)-BT_2T_4-film, whose oxidation or reduction processes occur at higher (Figure 8.1) or much lower potentials[23]. The latter occurrence would have involved the regeneration of the redox mediator at the oligomer/solution interface, which would manifest through positive feedback currents. Permeation of the redox mediators

within the oligomer film down to the underlying gold surface (whose open circuit potential would be defined by the solution redox species) cannot be excluded. However, even if this were the case, the I/I_b vs. d/a responses in Figure 8.6 would indicate that the local portion of the substrate surface bathed by the redox mediator solutions, and therefore participating in the feedback loop, was not large enough to support any substantial current enhancement.[27,28,30,32]. It must be noticed that the lack of current enhancement could also be related to both the thickness of the oligomer film, which could be too thick for redox mediator regeneration at the Pt microdisk surface[20,21]. and the actual closest tip-to-substrate distance, which could be achieved to avoid film penetration. As for the latter aspect, from the approach curve in Figure 8.5, and considering the I/I_b value of 0.4 (approximately corresponding to the closest d/a achieved while bringing the tip towards the substrate), an average tip to- substrate separation of about 8 μm was estimated. In fact, attempts to bring the SECM tip closer led to a flattening of the tip current, indicating that the tip came into contact with the oligomer film. Possible explanations for such behavior include a significant roughness of the substrate material and lack of precise perpendicular alignment of the tip above the substrate. Clearly, the above circumstances limited to some extent the resolution of the measurements and can in part explain the observed negative feedback effects.

The effect of the application of the potential to the oligo-(*S*)-BT_2T_4-Au was then investigated. The case of $Fe(CN)_6^{3-}$ redox mediator is discussed in detail as, unlike Fc and $Fe(CN)_6^{4-}$, at the microelectrode, a diffusion limiting current is achieved by applying a potential negative to its $E_{1/2}$ value and the experiments provided somewhat different results. In the measurements, the microelectrode tip was biased at 0.0 V, at which the reduction of $Fe(CN)_6^{3-}$ to $Fe(CN)_6^{4-}$ is under diffusion control (see Schemes 8.3a-c). The substrate was biased at

different potentials over the range 0 - 1.2 V at which either the competitive reduction (Scheme 8.3a) or the regeneration (Scheme 8.3b) of the redox mediator could occur.

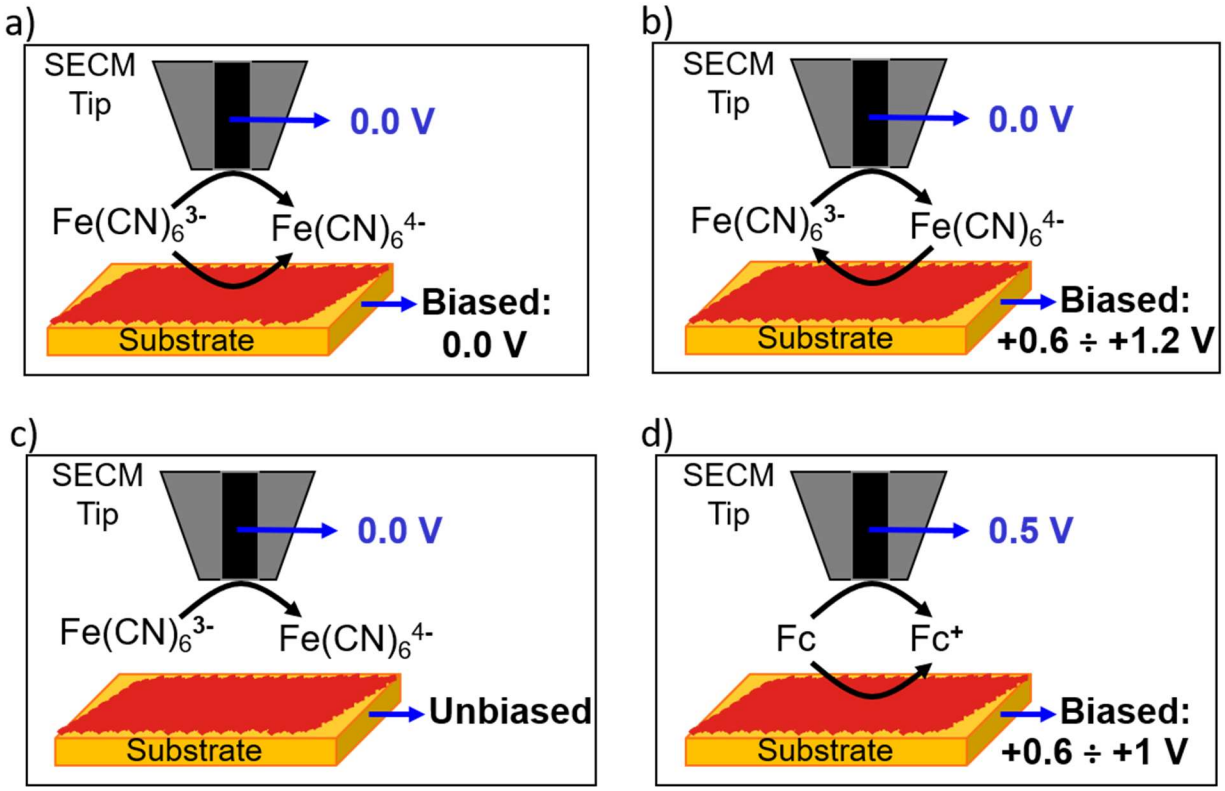

Scheme 8.3: *Scheme of the redox processes occurring at the microelectrode tip and substrate at different potentials applied at the substrate. a)-c) and d) refer to $Fe(CN)_6^{3-}$ and Fc redox mediator, respectively. Potential applied to the tip and substrate as indicated.*

Typical approach curves thus recorded are displayed in Figure 8.7.

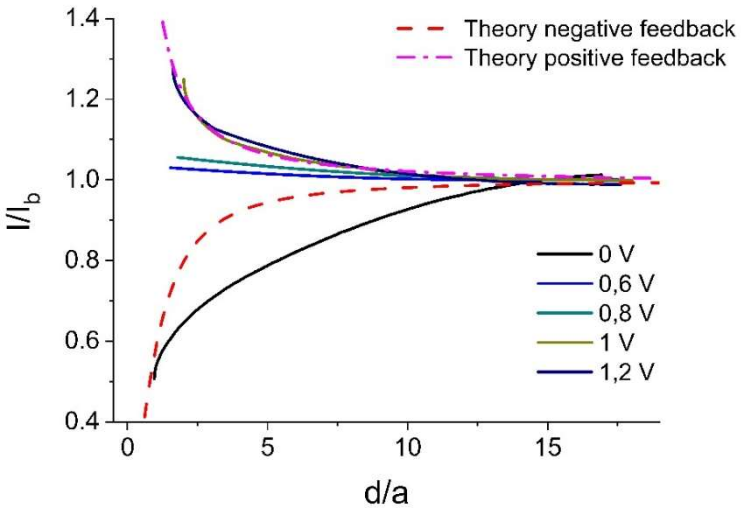

Figure 8.7: *Approach curves recorded in a 2 mM $K_3Fe(CN)_6$ + 0.1 M KCl water solution with the microelectrode tip biased at 0.0 V, above the oligo-(S)-BT_2T_4-Au biased at different potentials as indicated.*

When the substrate is biased at 0.0 V, the tip current decreases, starting far away from the substrate. This is because the redox mediator is reduced competitively at both microelectrode and substrate, as illustrated in Scheme 8.3a. The redox process at the substrate, conceivably, occurs at the underlying Au surface, through permeation of $[Fe(CN)_6]^{3-}$ within the film or through film defects and porosity. Therefore, the I/I_b *vs. d/a* profile follows the depletion of the concentration of $Fe(CN)_6^{3-}$ within the diffusion layer that grows in the solution above the substrate. At higher applied potentials, the I/I_b *vs*. *d/a* profile changes from negative into positive feedback, indicating the occurrence of the redox mediator regeneration, as illustrated in Scheme 8.3b. However, over the potential region 0.6 - 0.8 V, the current increase (Figure 8.7 with blue and green line) is below the diffusion-controlled process for positive feedback (Figure 8.7, magenta dashed line). This can be due to the fact that the location of the electron transfer can be at the underlying gold surface, which being coated by the oligomer film can work as a partially blocked electrode, at which the electron transfer process can be somewhat inhibited[28,30]. Notably, the problem of Au surface availability is here more important respect to the above case of competition mode, since to obtain positive feedback the mediator should both diffuse to the Au surface to be oxidized and retro-diffuse out of the porous layer to reach the tip. It is also worthwhile noting that, unlike in the above case of competition mode, in this case only the surface below the microelectrode tip is involved[19,28,30,32]. Moreover, over the latter potential range, the oligo-(*S*)-BT_2T_4 begins to be doped (see Figure 8.1), the film can acquire semiconductive properties and the process can occur at the oligomer/solution interface (or within the film). At potentials above 0.8 V, the conductivity of the oligomer remarkably increases18, with the film behaving as a metal electrode. In fact, at 1.0 and 1.2 V, the experimental approach curves almost fit the theory. The positive feedback current can also be due to a catalytic electron-transfer process between the oxidized oligomer (reaction (8.4) and the reduced form of redox

mediator (reaction (8.5)), formed at the microelectrode tip and diffusing towards the oligo-(*S*)-BT_2T_4 film:

$$\text{oligo-(}S\text{)-}BT_2T_4 \rightleftharpoons \text{oligo-(}S\text{)-}BT_2T_4^{n+} + ne^- \qquad (n = 1 \text{ or } 2) \qquad (8.4)$$

$$\text{oligo-(}S\text{)-}BT_2T_4^{+} + [Fe(CN)_6]^{4-} \rightleftharpoons \text{oligo-(}S\text{)-}BT_2T_4 + [Fe(CN)_6]^{3-} \qquad (\text{for } n= 1) \qquad (8.5)$$

The latter sequence, however, would include, in reaction (8.4), an anion exchange process, in which the redox mediator itself might be involved although the supporting electrolyte anion is smaller and at higher concentration. This would limit the overall kinetic of the process.

The uniformity of the properties of the oligo-(*S*)-BT_2T_4-Au was established by performing 1-D and 2-D scans across the substrate surface, using $Fe(CN)_6^{3-}$ as redox mediator. For the 1-D scan, the microelectrode was initially located at 10 μm above the insulating zone and then moved towards the oligo-(*S*)-BT_2T_4-Au material. The 2-D scans were instead made on a 150 μm x 150 μm square zone above the oligomeric film and at a tip-to substrate distance of 10 μm. The tip was always biased at 0.0 V, while the substrate was either unbiased or biased at 1.0 V. Under these conditions, the oligo-(*S*)-BT_2T_4-Au behaved as an insulating or an active material, respectively, at which the electrode processes illustrated in Scheme 3c and 3b, respectively, occurred. Typical 1-D and 2-D images thus obtained are shown in Figures 8.8 and 8.9.

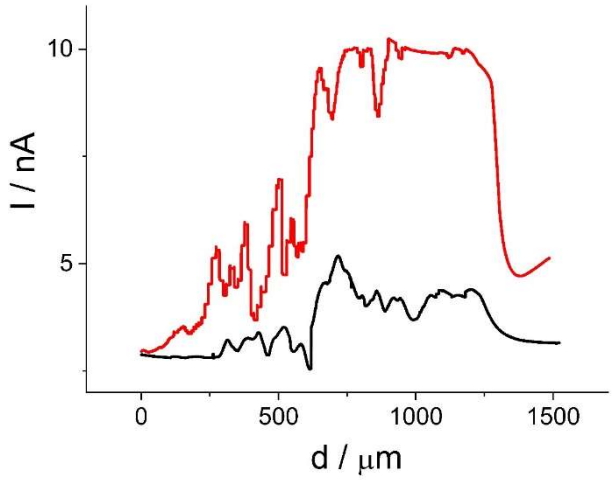

Figure 8.8: *1-D scans recorded recorded in a 2 mM $K_3Fe(CN)_6$ + 0.1 M KCl water solution with the microelectrode tip located at 10 μm above the oligo-(S)-BT_2T_4-Au. Microelectrode tip biased at 0.0 V substrate unbiased (black line) and biased at 1 V (red line).*

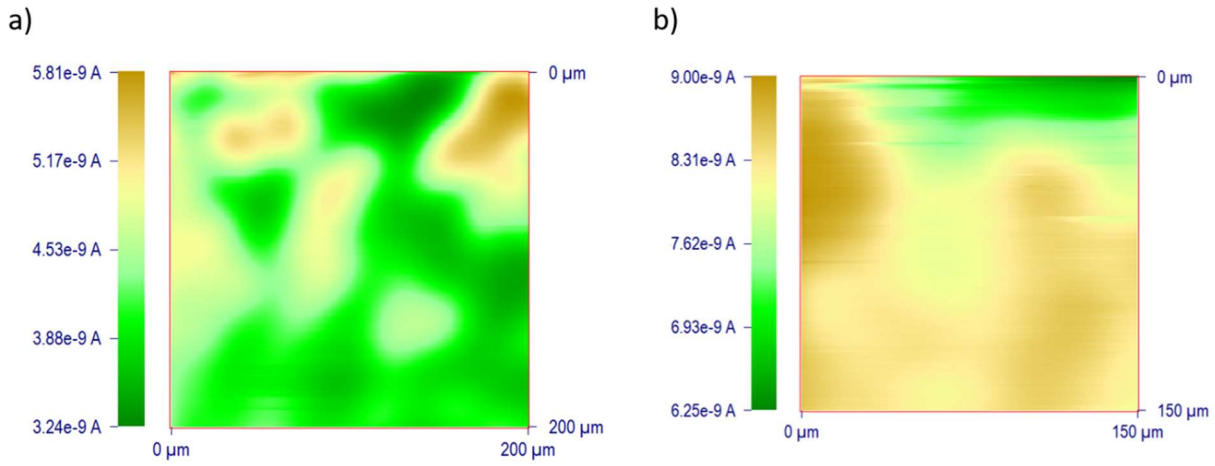

Figure 8.9: *2-D scans recorded in a 2 mM $K_3Fe(CN)_6$ + 0.1 M KCl water solution with the microelectrode tip located at 10 μm above the oligo-(S)-BT_2T_4-Au. Microelectrode tip biased at 0.0 V substrate unbiased (a) and biased at 1 V (b).*

The *I* vs. *d* profile in Figure 8.8 with the black line and the image in Figure 8.9a, both characterized by relatively low currents, reflect, essentially, the topography of the material; the current spikes in Figure 8.8 are conceivably due to the surface roughness (including defect in the film), which as mentioned above, seems to be rather high. The scan displayed with the red line

in Figure 8 and the image in Figure 8.9b, characterized by larger currents, reflect both activity (*i.e.,* conductivity) and topography of the oligo-(*S)*-BT_2T_4 film. The current spikes, again, are due to the rather rough topography of the investigated material. An estimate of the roughness of the oligo-(*S)*-BT_2T_4 film was made by the analysis of the current oscillations of the 1-D scans, using the same approach employed above for the bare Au surface. *Ra and* R_{max} values were 2.1 and 4.1 μm, respectively, indicating a higher roughness with respect to the bare Au surface, as also appears from SEM images shown in Figure 8.2.

The above scenario concerning the general characteristics (conductivity and topography) of the oligomer film was also supported from SECM measurements performed with both Fc and $Fe(CN)_6^{4-}$ as redox mediators. In these experiments, the substrate was also kept either unbiased or biased over the same potential window as above. At the microelectrode tip, the potential applied was 0.55 and 0.4 V for Fc and $Fe(CN)_6^{4-}$, respectively, to achieve steady-state diffusion limiting currents. Again, with both redox mediators, a negative feedback current was recorded above the oligo-(*S*)-BT_2T_4-Au substrate (same as in Figure 8.6), kept either unbiased or biased at potentials less positive than the corresponding $E_{1/2}$ of the two redox mediators. This was due to the above mentioned less availability of the underlying gold surface and to the diffusion and retro-diffusion of the redox mediator couple through the oligomer film. Instead, a competitive oxidation process of the redox mediators occurred at both microelectrode tip and substrate (see, for example, Scheme 8.3d for Fc), when the latter was biased at a potential more positive than the $E_{1/2}$ values of Fc and $Fe(CN)_6^{4-}$. The I/I_b vs. *d/a* profiles (not shown for the specific cases) were as that displayed in Figure 8.7 with the black line. In fact, under the latter conditions, the oxidation of the two redox mediators occurs at both substrate (either at the underlying Au surface or at the oligomer/solution interface, the electroactive film being now conductive) and the microelectrode tip.

8.4. Chiral redox mediators

Figure 8.10 shows typical approach curves obtained with the different chiral redox mediators while the microelectrode tip was positioned above the unbiased (Figure 8.10a) and biased (Figure 8.10b,c) oligo-(*S*)-BT_2T_4-Au substrate. Apparently, the results obtained by using the enantiomers of the chiral redox mediator are qualitatively similar to those described above for Fc. This is not surprising as, at the microelectrode tip, they share as expected the same $E_{1/2}$ value (within experimental error, see Table 4.4 in the experimental section) and, as discussed above, the oligomer film behaved as an insulating porous membrane when it was in its uncharged form. Thus, at the unbiased substrate, negative feedback currents were recorded, regardless of the configuration of the chiral redox mediator (Figure 8.10a). Similarly, when the substrate was biased at 0.0 V, negative feedback currents were obtained (black lines in Figure 8.10b-c), due to both the limited active substrate area below the microelectrode tip and the relatively high *d/a* at which the microelectrode could be brought above the substrate (see above discussion). At higher applied potentials, the typical I/I_b *vs*. *d/a* responses for competitive oxidation of the redox mediators at both microelectrode tip and substrate occurred (blue, green and magenta lines in Figure 8.10b-c). However, in these cases, a careful analysis of the SECM responses allowed verifying that the decrease of I/I_b, at same *d/a*, was larger for (*S*)-FcEA with respect to (*R*)-FcEA, indicating a clear discriminating ability of the oligo-(*S*)-BT_2T_4 film towards the two probe enantiomers. For instance, when the substrate was biased at 0.45 V, at which only (*S*)-FcEA could be oxidized (Figure 8.3a), I/I_b were about 0.65 and 0.77, at *d/a*=2 and 4, respectively; the corresponding values (*i.e.,* at same *d/a*) for (*R*)-FcEA were 0.78 and 0.92, respectively. As the substrate potential was shifted further towards more positive values (*i.e.*, 1 V), the oxidation of

both (*S*)-FcEA and (*R*)-FcEA was under diffusion control, and I/I_b vs. d/a acquired very close profiles.

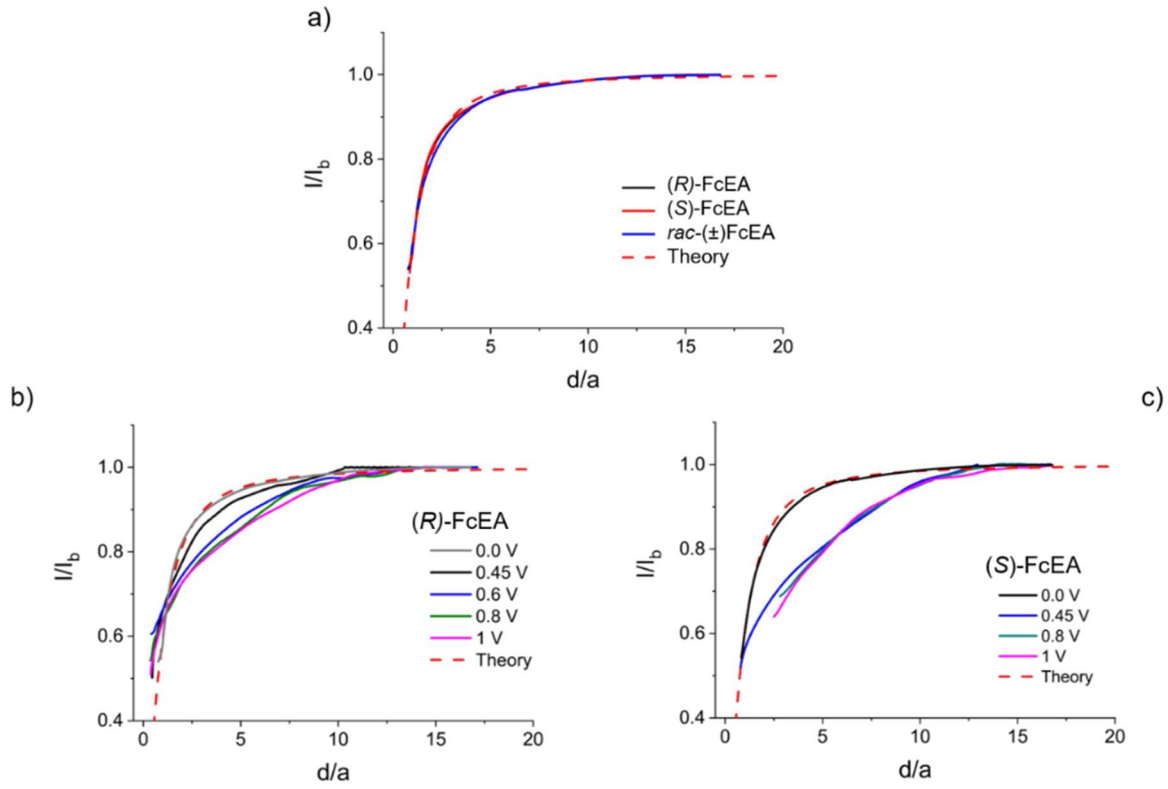

Figure 8.10. *Approach curves recorded in 2 mM of (S)-FcEA or and 1 mM (R)-FcEA CH_3CN solution with a Pt microdisk 12.5 µm radius, biased at 0.5 V, above the unbiased oligo-(S)-BT_2T_4-Au (a) and biased at different potentials (b) and (c) as indicated. Approach curves with dashed red lines refer to the theory for negative and positive feedback.*

To further support the above view, 1-D scans were performed above the oligo-(S)-BT_2T_4-Au substrate using *rac*-(±)FcEA, as redox mediator (Figure 8.11). The microelectrode tip was biased at 0.55 V, while the substrate was either unbiased (blue line) or biased at 0.45 V (red line) and 1 V (black line). Again, the scans were started from the insulating portion of the substrate and the microtip moved towards the entire section of oligo-(*S*)-BT_2T_4-Au. At the unbiased substrate, current spikes, conceivably due to the substrate topography (see above discussion), were recorded. When the substrate was biased at 0.45 V only (*S*)-FcEA could be oxidized (Figure 8.3a) and the current decreased to a significant extent, due to the consumption of the probe at the underlying gold surface. The current decrease was much more marked when the substrate was

biased at 1 V, at which both (*S*)-FcEA and (*R*)-FcEA could be oxidized. These results therefore confirm the enantiodiscrimination ability of the oligo-(*S*)-BT_2T_4 film and that the phenomenon occurred, essentially, evenly across the entire substrate surface.

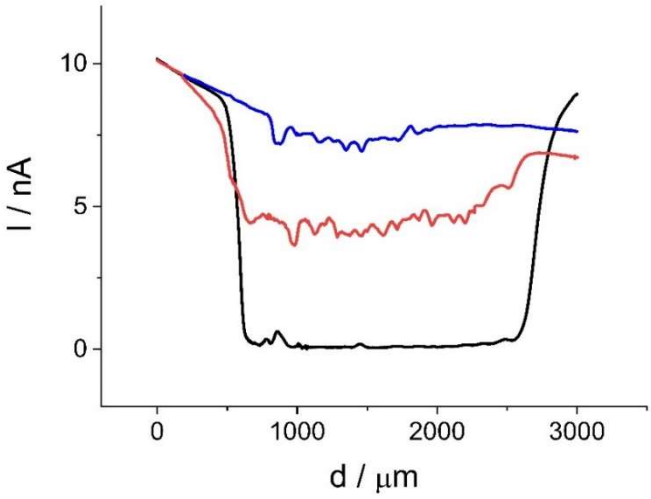

Figure 8.11: *1-D scans recoded recorded in 2 mM rac-(±)FcEA acetonitrile solution, with a Pt microdisk 12.5 µm radius, biased at 0.55 V, above the oligo(S)-BT_2T_4-Au: unbiased (blue line), biased at 0.45 V (red line) and at 1 V (black line). Tip to substrate distance 10 µm.*

In perspective, and in relation to the field of cultural heritage, these chiral conducting oligomers could be deposited on microelectrodes or inserted inside the glass capillary micropipettes for the selective determination of chiral compounds, i.e., natural resins, mainly composed by terpenoids, often employed as final protective films in paintings.

Chapter 9: Conclusions

9. Conclusions

In this thesis a series of investigations, based on the use of various electroanalytical techniques and devices, have been performed for studying and characterizing different types of substrates and materials of historic/artistic interest. The main achievements and relevant concluding remarks are summarized below for each specific chapter.

Chapter 5 – Dating copper-based coins by multiple-scan voltammetry

The application of the VIMP technique to nanosamples from the corrosion layers of slightly corroded copper/bronze artifacts attached to graphite electrodes yields to well-defined signatures associated to the reduction of cuprite. The application of a multiple-scan voltammetry protocol permits to record the voltammetric features of increasingly deeper regions in the corrosion patina whose variation can be interpreted in terms of the in-depth variation of the cuprite crystallinity and/or porosity. This methodology has been applied to a set of 16 copper/bronze coins produced between 1709 and 1962. Voltammetric data, complemented with FIB-FESEM and HRFESM-EDX reveal the existence of different corrosion patterns which are sensitive to the composition of the base metal, in particular to the presence of Zn. The presented results suggest the possibility of establishing a chronological ordering of the coins, and hence to add this multiple-scan strategy to the existing electrochemical dating methods.

Chapter 6 – Investigations on copper roof claddings

In this chapter a comprehensive study has been performed on copper roof cladding samples coming from Saint Martin church in Metz (France), which underwent long-term (>100 years) atmospheric corrosion. The investigation has dealt with different aspects of the chemistry

of metallic copper and its oxides and ions in the presence of various species, such as corrosion inhibitors and complexing agents present in aqueous or mixed ethanolic/aqueous solutions. The samples have been studied in different conditions and using a variety of techniques as specified in detail below.

Section – 6.1. Voltammetric investigation on the interaction between Cu^{2+} ions and HC10

Here, the electrochemical properties of the ternary system ethanol-water-decanoic acid, without and with Cu^{2+} ions, has been investigated by cyclic voltammetry using a platinum microdisk electrode. In particular, a 50% (v/v) E/W mixture has been considered as the main solution. The latter is often employed to dissolve the corrosion inhibitors n-alkanoic acids for treating copper materials to prevent their corrosion. HC10 has been chosen as corrosion inhibitor, as it has recently found applications in coating copper-based materials of cultural heritage interest. The study provided the following main information:

- in the three-component homogeneous system ethanol-water- HC10, a reduction process, involving hydrogen ions released from the weak acid (i.e., through a CE mechanism), has been identified. The half-wave potential and the diffusion limiting current have allowed evaluating pKa = 6.07 for HC10, datum not available before for the specific medium considered;

- the reduction of Cu^{2+} to Cu^{0} in the E/W mixture occurs essentially in a single two-electron process; it proceeds in two steps, in the presence of Cl^- ions, due to the formation of the stable $CuCl_2^-$ species;

- Cu^{2+} interacts slowly with HC10 under the acidic conditions ensuing by the acid dissociation itself, and provides soluble copper(II)-carboxylate species. These can be

reduced at potentials more negative than the one due to the reduction of the free Cu^{2+} ions.

- the metallic copper layer, formed onto the Pt electrode surface, upon reduction of the various soluble Cu(II)-carboxylate species, is passivated by the excess or unreacted HC10 in the medium;
- the decrease of the ethanol content in the E/W mixture below 40%(v/v), and over the HC10 concentration range 1 – 16 mM, causes the formation of both colloidal structures and a sparingly soluble compound, identified as $Cu(C10)_2$ by FTIR s analysis;
- the inhibition mechanism of copper samples treated with HC10 in E/W mixtures is rather complex and involves several steps such as dissolution, complexation, surface adsorption and precipitation, which are often antagonistic to each other.

Overall, the above results resulted useful for the understanding some of the processes involving the copper-based materials treated with inhibitors or when they interact with aggressive media such as acid raid.

Section 6.2 – Comparative protective effects of HC10, NaC10 and BTA

In this section, the protective action of the eco-friendly inhibitors HC10 and NaC10 on copper roof claddings has been investigated and compared with that obtained using the classical inhibitor BTA, which has recently risen toxicity concerns. The effects of the various inhibitors on the naturally-formed corrosion layers have been compared with those obtained on bare copper samples. The investigation has been carried out by using a set of complementary spectroscopic, surface analysis and electrochemical techniques. The efficacy of the inhibitors towards the material protection against corrosion has been evaluated in synthetic acid rain (pH 3.1). The results obtained indicated that HC10 proved efficient as well against corrosion for both bare

copper and naturally corroded materials. This was verified by potentiodynamic measurements which provided inhibition efficiency higher than 90%. The good protective action could be related to the formation of a highly hydrophobic copper decanoate film on the sample surface, having a crystals structure, clearly established by contact angle, SEM and Raman spectroscopy measurements. However, the formed layer was responsible of a color variation, which from pale green turned towards blue hue. NaC10 proved efficient when applied on bare copper (inhibition efficiency higher than 90%, obtained by PDP), whereas it was less effective on the naturally corroded roof claddings (inhibition efficiency around 60%, obtained by PDP), despite the fact that on the latter material a hydrophobic layer without significant color change was established by contact angle and colorimetric measurements. The lower stability of the hydrophobic layer formed using NaC10 in the synthetic acid rain, could be related to the different morphology of the coating layer, as verified by SEM and Raman spectroscopy measurements.

Overall, the results obtained in this work, allowed to conclude that HC10 can represent an eco-friendly and efficient alternative to the use of BTA, as corrosion inhibitor to maintain the actual conditions (in terms of naturally formed patina) of copper-based artworks exposed outdoors.

Section 6.3 – SECM investigation of the roof claddings untreated and treated with HC10 and BTA

In this section, a detailed investigation was performed by using SECM, which enabled to investigate and monitor chemical corrosion phenomena with high spatial resolution and to assess the stability of the copper roof cladding samples in their pristine conditions and after they underwent treatments with inhibitors. SECM was also used for imaging the local reactivity of the entire sample stratigraphy and also to get information of chemical species released. From the results obtained the following main conclusions can be drawn.

The roof cladding samples untreated with the inhibitors, if immersed in solutions containing electrolyte characterized of low (i.e., KNO_3 and Na_2SO_4) or high (i.e., KCl) complexing ability, resulted rather unstable and after relatively short times (i.e., 20 min), released sensible amounts of copper ions. The instability was related to either corrosion of the copper core, even if protected to some extent by the patina layer, or to the solubility of the brochantite and cuprite that compose the patina layer. These phenomena were enhanced in the media containing Cl^- ions, due to the formation of very stable $CuCl_2^-$ complex.

The samples treated with both BTA and HC10 allowed to retard and thus protect the samples from corrosion, though to a different extent, BTA being more effective than HC10. Relevant information on the stability and passivating ability of the two inhibitors have gained by using SECM in feedback mode and by substrate generation-tip-collections. Under the first condition, approach curves, line and bi-dimensional scans were acquired using various redox mediators, characterized by a different redox potential. The amount of copper ions released were evaluated by using SECM coupled with ASV. The above measurements were performed both on the top layers and the cross-sections of the samples.

Chapter 7 – Hydrogel-filled micropipette contact system

In this chapter, for the first time, it was developed a new system based on the MC techniques, which exploits micropipettes filled with a conducting hydrogel to perform local solid contact electrochemical measurements on solid substrates. The hydrogel employed was made of 2% (w/v) agarose in water solutions, which displays the advantageous characteristic of being eco-friendly. In particular, it was shown that micropipettes having orifices of radii over the range 1 – 30 μm, filled with the hydrogel containing the electroactive species $[Fe(CN)_6]^{4-}$ or Ag^+ ions, provide electrochemical responses, which are in accordance with theory developed for

microcapillary voltammetry. The microsystems employed here can be used to probe small areas of solid surfaces containing different active materials and to produce micrometers and sub-micrometers metallic structures by electrodeposition. These can be associated to a specific advantage offered by the gelled meniscus produced at the end of the micropipettes. In fact, they could overcome the limitations of the corresponding aqueous systems, with which the spreading of the electrolyte droplet on the sample surface is difficult to be controlled. Finally, the use of gelled media within the pipette opens new roads for the characterization, from an electrochemical point of view, of micro areas on surfaces, which suffer from direct contact with liquid electrolytes as well as on precious metallic objects.

Chapter 8 – Characterization of inherently chiral oligomeric films

The voltammetric and SECM behavior of the chiral (S)-BT_2T_4 oligomer, electrodeposited onto the surface of a gold disk electrode, was investigated by using a range of redox mediators with different characteristics (i.e., charged and uncharged, racemate and enantiopure antipodes). The results obtained with all achiral redox mediators have indicated that the oligomeric film, as produced, was uncharged. Using $[Fe(CN)_6]^{3-}$ in the SECM experiments allowed establishing the local properties of the fabricated oligomeric film in terms of topography and conductivity. Thus, it has been verified that the oligomeric film behaved as a porous insulating membrane, presenting a rather rough surface exposed to the bathing solution, when the substrate was biased at potentials below about 0.6 V vs. Ag/AgCl. This was inferred from the approach curves, which have displayed essentially negative feedback effects. The film acquired semiconducting properties over the potential region 0.6 ÷ 0.8 V vs. Ag/AgCl, while it became fully conductive at 1.0 and 1.2 V vs. Ag/AgCl. Under these conditions, the approach curves have displayed positive feedback effects. In addition, SECM measurements, performed in competition mode, using chiral probes, have allowed assessing the discriminating ability of the oligo-(*S*)-BT_2T_4 film towards the

(*S*)-FcEA and (*R*)-FcEA redox mediators, thus confirming results obtained by cyclic voltammetry. Thanks to the high spatial resolution of SECM, it has also been shown that the enantiomeric discriminating ability of the oligo-(*S*)-BT_2T_4 occurred evenly across the entire substrate surface. Improvements in the spatial resolution of the SECM measurements can be obtained by using smaller microelectrode tips (e.g., at sub-micrometer levels). However, this would also require the use of smoother oligomer films, which in principle can be obtained by decreasing the number of CV cycles during the electrodeposition step and smoother surfaces of the underlying electrode material. These aspects will be addressed in future investigations as well as these conducting oligomers for the selective determination of chiral compounds, i.e., natural resins, mainly composed by terpenoids, often employed as final protective films in paintings.

Appendix

A1

Table A.1: *Numismatic data of the studied coins.*

Ref.	Country	Issuer	Date	Denomination	Mint	Obverse	Reverse	Weight (g)	Ø(mm)
M16	Spain	Felipe V	1709	*Seiseno*	Valencia	HISPANIARVM □ REX □ 1709 V	PHILIPVS □ V □ DEI □ GRAT	5.07	26
M14	Sovereign Military Order of Malta	Emmanuel of Rohan	1776	10 *grani*	-	M □ M □ H □ F. EMMANUEL DE ROHAN	FIDES □ NON □ AES □ SED □	4.44	22
M03	Spain	Carlos IV	1798	4 *maravedís*	Segovia	CAROLUS IIII □ D □ G □ HISP □ REX □ 1798 □	Don Pelayo cross with castles and lions sorrounded by a laurel crown	5.06	26

M04	Spain	Carlos IV	1803	8 *maravedís*	Segovia	CAROLUS IIII □ [D □ G □ HISP □ REIX □ 1803]	Don Pelayo cross with castles and lions sorrounded by a laurel crown	10.69	31
M20	Spain	Isabel II	1849	2 *maravedís*	Jubia	ISABEL 2º POR LA G • DE DIOS Y LA CONST.1849	REYNA DE LAS ESPAÑAS	2.42	22
M07	France	Napoleon III	1864	5 *centimes*	Burdeos	NAPOLEON III EMPEREUR 1864	EMPIRE FRANÇAIS CINQ CENTIMES	4.92	25
M15	Spain	Gobierno Provisional	1870	2 *céntimos*	Barcelona	Lion with shield	DOS GRAMOS 1870	1.92	20
M05	Spain	Ángel Monreal	1889-1890	20 *pesetas* imitation	Zaragoza	FUNERARIA ECONOMICA. D. JAIME I. 8. ZARAGOZA.	ANGEL MONREAL.	4.48	24
M13	Portugal	Carlos II	1892	20 *reis*	-	CARLOS I REI DE PORTUGAL •1892•	20 reis	11.57	30
M12	France	Republique Française	1904	5 *centimes*	Paris	REPUBLIQUE FRANCAISE	LIBERTE EGALITE FRATERNITE	4.74	25

M06	France	Republique Française	1916	5 *centimes*	Madrid	REPUBLIQUE FRANCAISE	LIBERTE EGALITE FRATERNITE	4.97	25
M08	France	Republique Française	1916	10 *centimes*	Madrid	REPUBLIQUE FRANCAISE	LIBERTE EGALITE FRATERNITE	10.08	30
M18	Swiss	Government of Swiss	1962	1 rappen	-	HELVETIA 1962	1	1.5	16
M30	Spain	República Española	1937	50 *céntimos*	Madrid	REPUBLICA ESPAÑOLA	50 CENTIMOS	6	23
M31	Belgium	Balduino I	1953	50 *centimes*	Brussels	Bust of the King	BELGIQUE 50 CENTIMES	2.75	19
M32	Spain	Isabel II	1840	2 *maravedís*	Madrid	ISABEL 2º POR LA G • DE DIOS Y LA CONST.1840	REYNA DE LAS ESPAÑAS	2.42	22

A2

Evaluation of the *pK*a of acetic acid (HAc) in the 50% (v/v) *E/W* mixture

pKa values of HAc in E/W mixtures were reported in the literature[1,2], over the range 0 – 100 % (w/w)[1] and 0-55% (w/w) E/W, and as is displayed in Fig. 3, a linear relationship between *pKa* and %(w/w) E/W was found over the range 0 – 60 %(w/w) E/W. The linear regression equations found were:

pKa = 0.023 (± 0.002) *%(w/w) E/W* + 4.693 (± 0.063) from data reported in Ref. [1]

pKa = 0.025 (± 0.002) *%(w/w) E/W* + 4.641 (± 0.069) from data reported in Ref. [2]

At 25° C, the 50% (v/v) E/W mixture, employed in the present work, corresponds to 44.06 % (w/w) E/W. On the basis of these equations, the linear interpolation provided the average *pka* = 5.725.

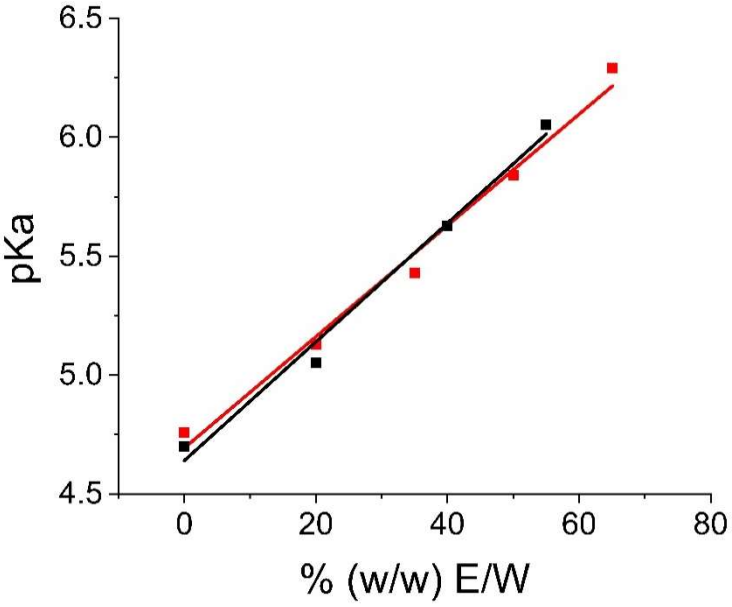

Figure A.1*: pKa vs. %(w/w) E/W %. Data obtained from Refs. [1] (red squares) and [2] (black squares).*

[1] E. Grunwald, B. Berkowitz. *J. Am. Chem. Soc.* (**1951**) 773, 4939 – 4944.
[2] H. A. Azab, I. T. Ahmed, M. R. Mahmoud., *J. Chem. Eng. Data* (**1995**) 40, 523—525.

List of Acronyms

AR	Acid rain
ASV	Adsorptive stripping voltammetry
ATR/FTIR	Attenuated total reflection – Fourier transform infrared
BTA	Benzotriazole
CV	Cyclic voltammetry
DPV	Differential pulse voltammetry
EC-SERS	Electrochemical – surface-enhanced Raman spectroscopy
EIS	Electrochemical impedance spectroscopy
E/W	Ethanol/water mixture
FIB-FESEM	Focused ion beams – field emission scanning electron microscope
FT-IR	Fourier transform – infrared
HAc	Acetic acid
HC10	Decanoic acid
HPLC	High performance liquid chromatography
HRFESM-EDX	High-resolution field emission scanning electron microscopy
ICP-AES/MS	Inductively coupled plasma / atomic emission spectrometry – mass spectrometry
LIBS	Laser induced breakdown spectroscopy
LSV	Linear sweep voltammetry
MC	Microcapillary
NaC10	Sodium decanoate

PRPt	Pseudo-reference of Platinum
Py/GC-MS	Pyrolysis/gas chromatography –mass spectrometry
VIMP	Voltammetry of immobilized particles
SECM	Scanning electrochemical microscopy
SEM-EDS	Surface-enhanced Raman spectroscopy
SERS	Scanning electron microscope – energy dispersive X-rays spectrometry
SWV	Square Wave Voltammetry
XRD	X-rays diffraction
XRF	X-rays fluorescence

Acknowledgements

Scientific research does not come without commitment, efforts and dedication that must be acknowledged. I would like to thank my supervisor, Professor S. Daniele, who gave me the possibility to learn, make mistakes and learn again. I'm grateful for his patience and commitment despite, often, our points of view were far apart.

I express my acknowledgements to Professor A. Doménech-Carbó who supervised the research activity carried out at the Universitat de Valencia, who shares with me the same big passions for cultural heritage and science. I'm very grateful for involving me in the scientific investigations he was leading, and for welcoming me as if I were his granddaughter.

I thank Dr. D. Neff of the Laboratoire Archéomatériaux et Prévision de l'Altération (LAPA) who accepted my proposal for a fruitful collaboration which made possible very interesting research studies.

I would like to express my immense gratitude to Professor M.A. Baldo who always stood on my side, supporting and encouraging me in the hardest moments. Good results are inextricably linked to a happy and healthy life; you helped me to find the balance to arrive until the end of an uphill path, since the beginning. Thank you for having always believed in me and rooting for me, always giving me the best advices and treating me like if I was your second daughter; I consider you a second mom.

If I held on these three years, between smiles and tears, it was also for the support of my colleagues and friends. Maria Sole wiped off my tears with her immense positiveness; I'm very happy to have you in my life. Impossible to forget trips, chats, teas, coffees, thoughts, feelings and a gigantic list of other things shared in these years. Thank you for having always beautiful words towards everyone; never lose this amazing quality, Sole.

I would like to thank Thomas, Sara, Davide, Andrea, Claudio, Dido, the “Tortellini group”, for always having me heard my breakouts, for bringing my smile back after the hardest times; for the dinners, gossip moments, talks and scientific suggestions we shared in these years. Although we are now spread all over the world, I hope to keep our friendship alive.

Thank you, Davide. No words express my biggest gratitude for always standing by my side, (also in the very literal sense!), sustaining me and giving me useful advices. I wish you to have a fruitful career; you deserve it.

Thank you, Simone, for your true and genuine friendship, for your moral and high-tech support. Thank you, Chiara, for supporting me, I know how much you empathise with my situation.

A big thank to all the other colleagues and professionals with who I shared good moments during these three years. It is impossible to list everyone, but thanks to Francesca, Gregorio, Marco, Matteo, Aurora, Ettore, Nicolò, Giulia Mazzon, Giulia Moro, Vincenzo, Eelin, Erika, Najmeh, Ligia, Sabrina and Angela. Thanks to Irene, Silvia, Valentina, Sonia; you are a part of me.

I am grateful to my family who supported me all along my university career, always supporting me in all my choices. My aunt Gina and Valentina, always rooting for me.

And the last, but not least, huge and lovely thank to Claudio, who encouraged me, supported me and loved me. We have been through very difficult moments, but we always became much stronger and much closer after them. Thank you for having patiently waited these three years to embrace each other again and, finally, start our life together. I love you.

With all my heart,

Margherita